ENHANCED BONE TISSUE REGENERATION ENABLED WITH TISSUE-ENGINEERED

INTERLOCKING NANOCLAY SCAFFOLDS AND BONE MORPHOGENIC PROTEINS

A Dissertation
Submitted to the Graduate Faculty
of the
North Dakota State University
of Agriculture and Applied Science

By

Krishna Kundu

In Partial Fulfillment of the Requirements
for the Degree of
DOCTOR OF PHILOSOPHY

Major Program:
Materials and Nanotechnology

July 2022

Fargo, North Dakota

North Dakota State University
Graduate School

Title

ENHANCED BONE TISSUE REGENERATION ENABLED WITH
TISSUE-ENGINEERED INTERLOCKING NANOCLAY SCAFFOLDS
AND BONE MORPHOGENIC PROTEINS

By

Krishna Kundu

The Supervisory Committee certifies that this ***disquisition*** complies with North Dakota

State University's regulations and meets the accepted standards for the degree of

DOCTOR OF PHILOSOPHY

SUPERVISORY COMMITTEE:

Kalpana. S. Katti
Chair

Dinesh R. Katti
Co-Chair

Xuefeng Chu

Chad Ulven

Approved:

November 15, 2022   Erik Hobbie
Date   Department Chair

ABSTRACT

About 6 million bone fractures occur annually in the US; 30% require bone grafting transplants to aid bone healing. Well-established clinical therapy techniques for bone regeneration suffer from limited availability, higher infection risk, donor site morbidity, and poor transplant integration. Delay in healing or nonunion of critical-sized defects is another concern in orthopedics. This dissertation focuses on constructing an interlocking scaffold structure to speed bone regeneration. In this thesis, a BMP-2 & 7 coated PCL-nanoclay-hydroxyapatite interlocking scaffold was developed to accelerate bone regeneration. Developed nano clay polymer interlocking scaffolds retain the scaffold's structural integrity and provide a large surface area while allowing for media interaction. Mesenchymal stem cells (MSCs) and osteoblast cells seeded at a 1:1 ratio boost cell viability and enable calcium deposition on day three and collagen production on day 7 with BMP-2 and BMP-7 coated scaffolds. In addition, BMPs, interlocking, and co-culturing of osteoblasts and MSCs promote osteogenic differentiation. In this dissertation, The long-term effect of BMP-2/BMP-7 on in-vitro utilizing interlocking scaffold blocks was evaluated. Changes to the nanomechanical properties of scaffolds and bone tissue during osteogenesis with the progression of ECM formation were reported. Gene expression results and Alizarin Red S staining images indicate a significant increase in mineralized bone nodules with BMPs coated samples compared with uncoated samples. Results suggest BMPs played a critical role in mineralized ECM production, which increased the scaffolds' elastic modulus. This research provides valuable insight into understanding how BMPs affect bone growth. In this dissertation, polymer clay nanocomposites fibers were constructed utilizing a pressured gyration setup and observed improved cell viability, osteogenic differentiation, ECM development, and collagen formation for PCL HAP MMT-Clay nanocomposite fiber scaffolds compared to pure PCL fibers.

In this dissertation, the in-silico design of the unnatural amino acids modified clays and fabricated unnatural amino acids modified scaffolds were reported for application as cancer testbeds. This dissertation also reported the design of the in situ hydroxy apatite and tri-calcium phosphate incorporated nano clays polymer scaffolds for bone tissue engineering applications. These studies represent a new opportunity to design manufacturable composite nanoclay polymer scaffolds for bone tissue engineering applications.

DEDICATION

This dissertation is lovingly dedicated to my mother, Late Nirmala Rani Kundu. Her

encouragement, support, and constant love have sustained me throughout my life.

TABLE OF CONTENTS

LIST OF TABLES

LIST OF FIGURES

LIST OF ABBREVIATIONS

MSCs...Mesenchymal Stem Cells.

RUNX2 ....Runt related transcription factor 2.

DLX5 ....Distal-less homeobox 5.

OSX..Osterix.

BSP ....Bone sialoprotein.

OCN ....Osteocalcin.

COL I ....Collagen Type I.

RANKL...Receptor Activator of Nuclear factor Kappa B Ligand.

VEGF ....Vascular Endothelial Growth Factor.

OPN..Osteopontin.

TGF-β...Transforming growth factor-β.

HAP..Hydroxyapatite.

2D...Two-dimensional.

3D...Three-dimensional.

PLG..Poly-lactide-co-glycolide.

PCN..Polymer-Clay Nanocomposite.

Na-MMT..Sodium Montmorillonite.

Chi/PgA..Chitosan-Polygalacturonic acid.

PCL ....Polycaprolactone.

LRP-5/6..Low-density lipoprotein receptor-related protein 5/6.

FZD..Frizzled.

CK1..Casein Kinase 1.

GSK-3β ....Glycogen Synthase Kinase-3β.

APC...Adenomatous Polyposis Coli.

AFM...Atomic Force Microscopy.

ATCC...American Type Culture Collection.

DMEM ....Dulbecco's Modified Eagle Medium.

EMEM...Eagle's Minimum Essential Medium.

PBS ....Phosphate Buffered Saline.

UV..Ultraviolet.

SC...Sequential Culture.

ALP...Alkaline Phosphate.

SEM ....Scanning Electron Microscope.

DAPI ....4', 6-diamidino-2-phenylindole.

ELISA ....Enzyme-Linked Immunosorbent Assay.

PCR...Polymerase Chain Reaction.

GAPDH...Glyceraldehyde 3-Phosphate Dehydrogenase.

ECM...Extracellular Matrix.

TCPS...Tissue Culture Polystyrene.

PFA ....Paraformaldehyde.

ARS..Alizarin Red S.

PVA..Poly (Vinyl Alcohol).

PEG..Poly (Ethylene Glycol).

FBS ....Fetal Bovine Serum.

CHAPTER 1. INTRODUCTION

1.1. Bone tissue engineering

Tissue engineering is a multidisciplinary field constantly expanding and provides a structured way to produce three-dimensional scaffold constructs by combining engineering and life science to replace or repair the functions of wounded or lost organs[1]. Bone grafting's significance has substantially increased over the years because of the rising incidence of bone-related injuries and disorders. In the United States alone, 600,000 cases of bone grafting are performed annually [2]. The market for bone grafts and substitutes is anticipated to increase from USD 2.5 billion in 2020 to USD 4 billion by 2040[2]. According to a newly released estimate, the frequency of fractures in men is anticipated to increase by 310% and in women by 240% by 2050[2]. Around the world, women over 50 years old are more prone to have osteoporosis, a widespread bone condition that alone causes 8.9 million fractures yearly[3, 4]. These investigations demonstrate the significant need for bone graft substitutes that can replace damaged bone and rebuild natural human components. Autografts, allografts, xenografts, and metallic implants are examples of conventional tissue restoration techniques that have limitations. Autograft transplant techniques involving tissue harvesting from a patient's body are limited by the availability of such tissue grafts and the risk of harm to the spot where the tissue was harvested. When significant amounts of tissue are required to repair the lesion, utilizing autografts becomes exceedingly challenging. The use of tissue from another healthy donor in allograft transplant procedures carries the danger of immunological rejection, infection transfer, and immune rejection. Immune rejection and the transmission of pathogens limit xenograft transplantations involving tissue from an animal donor. Metallic implants have a limited functional life and have been linked to issues including stress shielding that weakens the surrounding bone (10-15 years).

Due to their fragile nature, ceramic implants could fail quickly, and polymeric implants could degrade over time. Tissue engineering has the ability to overcome these constraints since it utilizes cell-scaffold interactions to encourage the natural regeneration of new tissue. In addition, there is a good chance that the new tissue formed through tissue engineering possesses structural and functional features similar to those of healthy, natural tissue. In tissue engineering, cells, scaffolds, and growth factors are the three key elements (Fig. 1.1). Each element of tissue engineering is a topic of intriguing research in science and engineering areas. Since the early 1990s, scaffolds and cells have been the primary focus of various studies on the development of tissue engineering, these studies have created the groundwork for spreading tissue engineering concepts beyond tissue regeneration. Depending on the specific tissue that needs to be generated, a specific cell type can be employed. Immune rejection is less likely when the patient's cells are used. Induced pluripotent stem cells, which may be stimulated with the right amount of growth factors to develop the desired tissue, can be used as an alternate source for tissue regeneration. Scaffolds are porous three-dimensional matrices that enable growing tissues, and intracellular architectures provide mechanical support. Depending on the type of tissue regeneration, cells are cultured on a synthetic biodegradable substrate that serves as a template and stimulus for tissue regeneration. With proper nutrients and growth factors, cell growth is observed over time for the optimum tissue engineering application. The scaffold should degrade with the tissue generation into non-toxic degradation products[1, 5]. The in vitro regeneration of tissues, such as nerves, liver, bone, heart valves, blood arteries, and kidneys, is currently being studied globally. This dissertation uses bone tissue engineering to create polymer composite scaffolds for accelerated bone regeneration. This research also includes experimental investigations of the interactions between human osteoblasts cells (hFOB) and human mesenchymal stem cells (hMSCs) with these scaffolds, the effect of bone

morphogenic proteins (BMP-2 and BMP-7), and changes in the nanomechanical properties of the bone tissue over time and the effect of wingless/integrated pathway (wnt pathway) in bone regeneration.
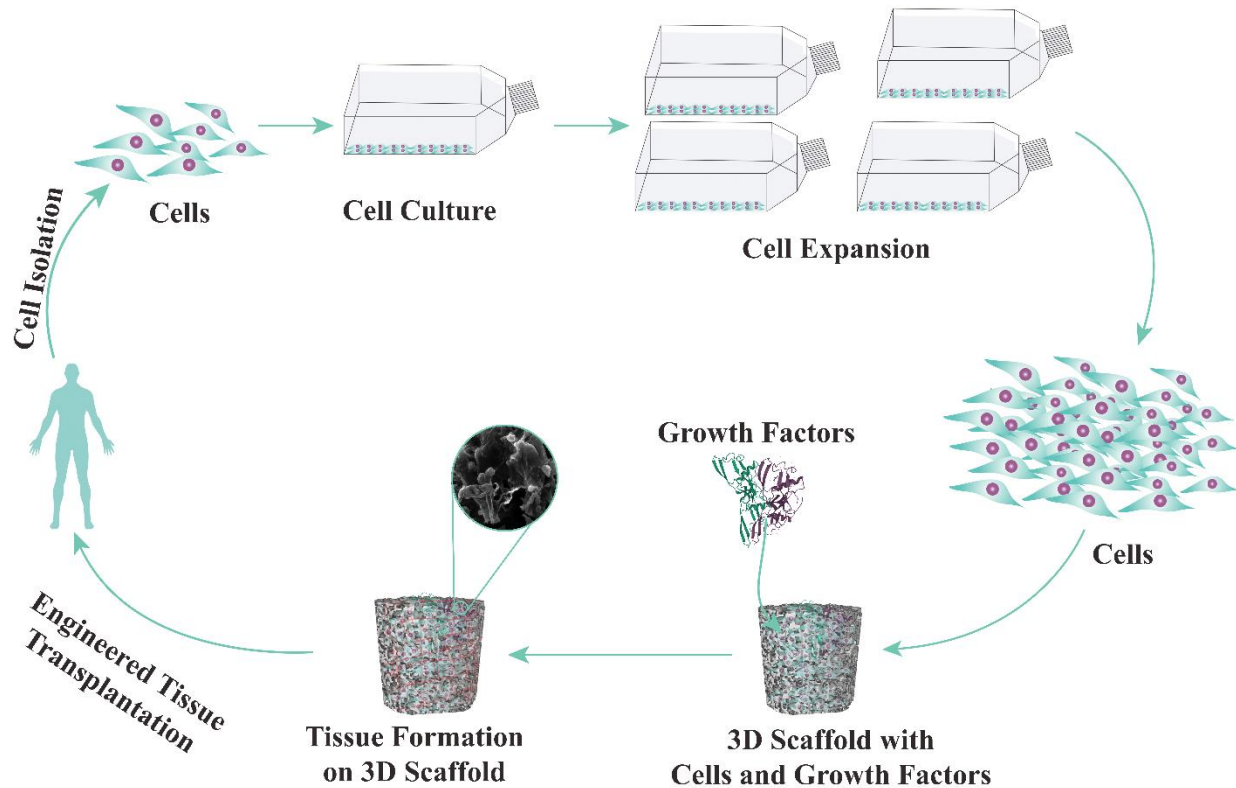
Fig. 1.1. Schematic representation of the Bone tissue engineering.

1.2. Scaffolds for bone tissue engineering

Bone consists of both cells and extracellular matrix (ECM). The ECM comprises a remarkable variety of proteins and polysaccharides arranged in a nonwoven mesh in close proximity to the cells that create them. Different structural shapes result from variations in the relative numbers of various ECM macromolecules as well as in how they are arranged. These structural configurations are all appropriate for the functional requirements of the various tissues. The ECM is thought to be a dynamic, hierarchically organized nanocomposite (from the molecular to the macroscale) that gives the cells mechanical support[6]. In cellular processes such

as adhesion, migration, proliferation, differentiation, and morphogenesis, the extracellular matrix provides the cells with a highly interacting environment. The ECM contains protein fibers with nanoscale dimensions (both structural and functional) (10 to several hundred nanometers). Therefore, it is believed that a cell's activity can be significantly influenced by a setting composed of components with nanoscale dimensions[7].

Additionally, cells are sensitive to the mechanical and chemical stimuli that are present in their immediate surroundings. The creation of three-dimensional porous scaffolds with properties similar to the ECM found in a particular tissue is thus one of the main areas of attention in tissue engineering. Because of its hierarchical structure (Fig. 1.2) from the nanoscale to the macroscale, bone is viewed as a complex, nanocomposite material[8]. Bone provides structural support, protects key organs, stores calcium, and phosphate-based minerals, and facilitates movement. Its hierarchical structure is thought to be responsible for bone's mechanical characteristics. A fundamental problem in bone tissue engineering is creating scaffolds with enough mechanical characteristics to withstand biomechanical pressures at defect sites while new tissue grows and matures. Scaffolds for bone tissue engineering are more complex to construct because they must satisfy parameters relating to porosity, pore size, and biodegradability while simultaneously providing the cells with a suitable environment for tissue creation. Furthermore, cells transform mechanical cues from their surroundings into biochemical signals[9]. Therefore, the mechanical characteristics necessary at the macroscale to support biomechanical loads may differ from those required at the sub-micron/molecular scale to influence cell function. Mechanical characteristics of bone tissue engineering scaffolds should therefore be sufficient to give suitable mechanical cues for bone tissue creation and support biomechanical stresses at the defect site in vivo or the growing bone (in the case of in vitro bone regeneration).
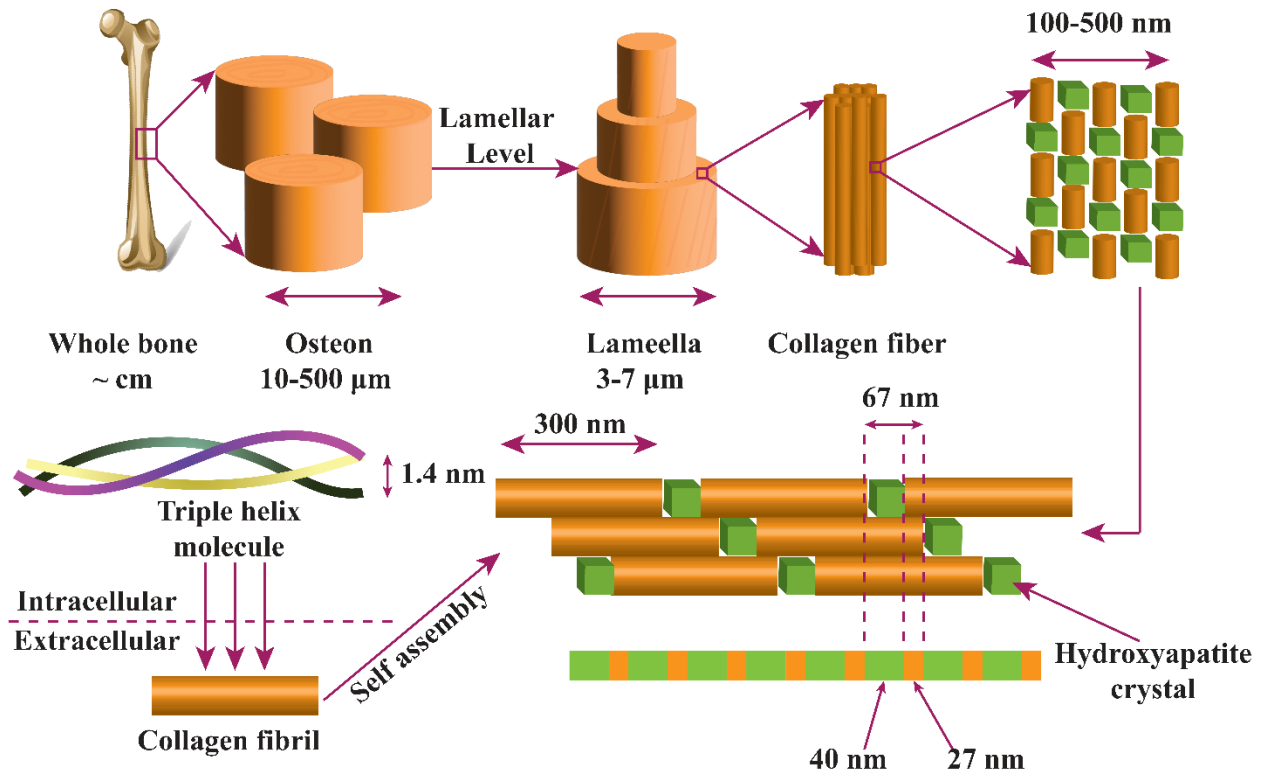
Fig. 1.2. Schematic representation of the hierarchical structure of bone.

Consequently, the challenge associated with scaffold's mechanical characteristics appears to extend from the molecular to the macroscopic scale. It is anticipated that scaffolds used in tissue engineering will offer cells a microenvironment resembling that seen in the extracellular matrix (ECM) in vivo. It is possible to provide cells with the proper cues for tissue regeneration (or engineering) by designing scaffolds with a microenvironment analogous to the ECM in normal, healthy tissue. 3D Scaffolds utilized in tissue engineering experiments are thought to give the cells a more physiological environment than two-dimensional (2D) substrates. The ability of three-dimensional (3D) scaffolds to present a more physiological environment aside from their dimensionality component has recently been recognized and studied extensively [9]. When grown in a 3D environment, cells exhibit a distinct shape, organization, and function. Although the impact of cell spreading and cell geometry on cellular functions has been thoroughly investigated in the

context of 2D substrates, it has been suggested that these effects differ from those seen in a 3D environment.

In contrast to 2D substrates, generally unrestricted, these differences result from the steric restrictions cells must overcome in a 3D environment to spread/expand and migrate. Furthermore, local mechanical characteristics and topography are expected to influence cell attachment in a 3D environment. This may also cause changes in cell-matrix adhesions in a three-dimensional environment. Since 3D cells experience physical restrictions during deformation and have a different morphology and organization than 2D cells, how force is communicated to cells in 3D environments may differ from that of 2D substrates. Additionally, diffusion-dependent gradients of soluble components in media and oxygen are more likely to be experienced by cells grown in a three-dimensional (3D) environment. The 3D environment of scaffolds can also offer chances for storing soluble components and coordinating when they are released with how they are presented spatially to the cells[10].

1.3. Materials for scaffold fabrication

Bone tissue engineering scaffolds are made of both organic and inorganic materials. In contrast to typically utilized inorganic materials like hydroxyapatite, tricalcium phosphate, and silicates, organic materials like natural or synthetic polymers can be employed to construct composite scaffolds. The effectiveness of these materials depends on their ability to reproduce the extracellular matrix's subtleties in nature accurately.

The mineral hydroxyapatite (HAP) makes up the majority of the inorganic phase of bone. It is known to be bioactive, osteoconductive, non-toxic, and non-immunogenic, and its natural or synthesized forms have a crystal structure comparable to the HAP found in bone tissue. Nano-HAP is more effective than micro-HAP due to its superior surface characteristics, such as increased

surface roughness, lower contact angles, and smaller pore size. Nano-HAP improves cell adhesion, differentiation, and development by increasing protein adsorption[11]. Adhesive proteins' unfolding is more effectively influenced by Nano-HAP, which increases the quantity of arginine-glycine-aspartic (RGD) acid sequences available to cell surface receptors[11]. Numerous techniques, including wet-chemical, hydrothermal, solid-state, mechanochemical, and microwave, have been utilized to fabricate nano-HAP. Numerous research has employed nano-HAP to produce nanocomposites for bone tissue engineering. Nano-HAP has been integrated into polymers[12-19] to prepare polymer nanocomposites for bone tissue engineering applications. These research show that nano-HAP can be used to generate nanocomposites that can be used for bone regeneration.

For the aim of creating nanocomposites with enhanced mechanical characteristics, permeability, and flammability as well as improved biodegradability[20] for bone tissue engineering applications, silicates, such as montmorillonite (MMT) clays[21-25], have been employed. Bone tissue engineering involves the creation of biocompatible scaffolds, still a challenging aspect, that can bear the stresses of the in-vivo environment without compromising the surrounding tissue's ability to function normally. Scaffolds utilized for bone tissue engineering offer an opportunity to take advantage of MMT clays' potential to enhance the mechanical properties of composites. Studies have demonstrated that MMT clays can improve the mechanical properties of bone tissue engineering composites[26-32].

Bone is a nanocomposite with an inorganic phase as its principal component; hence the inorganic phase may be important when constructing nanocomposites for bone tissue engineering, however, hierarchical structure gives bone its mechanical characteristics. This structural hierarchy is challenging to reproduce in bone tissue engineering nanocomposites. So, when creating nanocomposites for bone tissue engineering, accurate organic phase selection becomes just as

crucial as the inorganic phase. In addition to mimicking ECM properties, the organic phase should have a reasonable biodegradation rate for tissue regeneration. Additionally, the degradation byproducts should not interfere with enzymatic reactions in the cells and their environment. It must have appropriate mechanical properties to support developing tissue without eliciting an immunological response. Natural and synthetic polymers can be employed in bone-regeneration composite scaffolds. Natural polymers are derived from sources such as plants and animals. Biomolecules or biomolecule sequences in these polymers promote cell adhesion and differentiation[33]. These polymers are analogous to biological macromolecules, can be broken down by enzymes or hydrolysis, and might not cause an immunological reaction. Uncontrolled biodegradation, batch-to-batch fluctuation in mechanical characteristics, scale-up challenges[33], and infection risk for animal-derived polymers like collagen are some of their downsides. Because of varying enzymatic activity, it's difficult to forecast or estimate these polymers' in vivo biodegradation rate. Synthetic polymers can have their biodegradation rate controlled by grafting functional groups onto the polymeric chain or by using appropriate monomers. Using the appropriate polymer synthesis technique, the molecular weight can be controlled as well as the mechanical properties of synthetic polymers. However, these polymers can cause insistent inflammation and a lack of desired cell response because they lack the natural biomolecule sequences that stimulate cell attachment and proliferation. Collagen is present in most connective tissues and deposited by fibroblasts in the extracellular matrix. Collagen maintains ECM's structural integrity and performs biological activities. There are currently 28 identified types of collagen. Bone, cartilage, skin, and muscle contain collagen types I, II, III, and V[34]. Type I collagen is derived from animal or human skin, tendons, and ligaments for tissue engineering. It's biocompatible, strong, and can be crosslinked to adjust its mechanical and degrading

properties[35]. Kikuchi et al. [36] discovered that glutaraldehyde increased the mechanical strength of crosslinked collagen/hydroxyapatite nanocomposites. In vivo investigations of crosslinked nanocomposites implanted in rabbit, tibias showed that osteoclastic resorption decreased with increasing glutaraldehyde content without deleterious effects. Kim et al.[37] produced microspheres of collagen-apatite nanocomposites and evaluated the in vitro response of rat bone marrow stem cells on these microspheres. In vitro tests demonstrated that rat bone marrow stem cells could attach and grow on these nanocomposite microspheres, indicating that they can be employed for bone tissue regeneration. Several other studies [38-42] that have used collagen have also shown how important it is for bone regeneration.

Aliphatic polyesters, including poly (glycolic acid) (PGA), poly (lactic acid) (PLA), poly (lactic-co-glycolic acid) (PLGA), and polycaprolactone (PCL), are employed for bone tissue engineering. The monomer units of these polymers determine their characteristics. PGA has intermediate crystallinity, a high melting point, low solubility in organic solvents, and the capacity to degrade hydrolytically. Although the potential for local pH fluctuations caused by its breakdown products forces the consideration of using PGA in places with a buffering capacity or a system for swift removal of the degradation wastes, it has been suggested that PGA can be employed in instances where an initially faster degradation rate is required. When it comes to electrospinning, the fact that PLA is more soluble in organic solvents than PGA is likely to benefit the process. It is possible to alter the characteristics of PLGA by changing the lactic acid/glycolic acid ratio. A semicrystalline material, PCL has a low melting point, good solubility in organic solvents, and degrades slower than PGA and PLGA. Numerous investigations into bone tissue engineering have made use of aliphatic polyesters. A better PLLA/MMT scaffold for bone tissue engineering has been developed by Lee et al. [43]. Adding titania nanoparticles into PLGA can reduce the extent

of pH reduction by working as a buffer and is found to be beneficial for cells[44, 45]. The microstructure and compressive strength of PLLA/HAP nanocomposites produced by Nejati et al.[46] were comparable to those of cancellous bone. Serrano et al. [47] used murine fibroblasts to study the biocompatibility of PCL and found that PCL acts as an excellent substrate for fibroblast attachment. Using an extrusion approach, Shor et al.[48] created PCL/HAP scaffolds with controlled microstructures capable of promoting mineralization when seeded with fetal bovine osteoblasts. Erisken et al. [49] made graded nanocomposites scaffolds from PCL and -tricalcium phosphate that might produce mineralized extracellular matrix (ECM). Additionally, a number of studies [50-54] have demonstrated the value of aliphatic polyesters as a material for bone tissue engineering. It is possible to construct nanocomposites from a vast array of synthetic polymers that are valuable for tissue engineering applications. The growing understanding of polymerization mechanics has boosted the possibility of constructing synthetic polymer systems for bone tissue engineering.

1.4. Cells for bone tissue engineering

Tissue engineering relies heavily on cells, particularly when the large defect size. Cells employed for tissue engineering must possess the ability to differentiate into the correct phenotype[55] when stimulated by the right signals, organization through structural support from the environment, and also the capacity to produce an extracellular matrix (ECM) that is appropriately structured[55, 56]. To reduce immunological rejection, cells must also create the necessary cytokines (or cell signaling molecules)[56], exhibit structural and mechanical compatibility with the native cells around them, and integrate with those cells[55]. These cells can come from autologous (the patient's) sources, allogenic (human donors other than the patient), and xenogenic (animal) sources, all of which have drawbacks. Autologous cells are best due to reduced

immunological rejection; however, getting enough is challenging without damaging the donor location. Immune rejection and pathogen transmission are concerns linked with allogenic and xenogenic cells. Tissue explant-derived primary (mature) cells exhibit a limited ability to proliferate, form tissue, and express phenotypes. Cell-related features such as osteogenic and vasculogenic potential, the ability to govern differentiation into the osteogenic lineage, and sustained expression of osteogenic phenotype to minimize "non-specific" tissue creation[57] are critical for bone formation. Research that has been conducted extensively as well as newly developing research over the past few years has demonstrated that mesenchymal stem cells (MSCs), embryonic stem cells, and induced pluripotent stem cells are all viable alternatives to traditional cell types.

Osteoblasts are generated from osteoprogenitor stem cells (MSCs). When osteoblasts mature, they express more of the homeobox protein distal-less homeobox 5 (Dlx5) and bone matrix proteins such as bone sialoprotein (BSP) I/II, osteocalcin (OCN), and collagen type I (COL I) as well as higher levels of the transcription factors runt-related transcription factor 2 (Runx2) and osterix (Osx)[58-62]. In the course of bone remodeling, osteoblasts can be found around the bone's surface, where they are involved in the deposition and mineralization of the bone matrix. Pre-osteoclasts are formed by the fusion of mononuclear cells from the hematopoietic stem cell lineage, which give rise to osteoclasts[58]. M-CSF and RANKL, produced by osteoblasts, osteoprogenitor mesenchymal cells, and other stromal cells, induce preosteoclasts to develop into multinucleated, active osteoclasts that resorb bone during bone remodeling[63, 64]. On the other hand, osteoporosis can be caused by an abnormally high level of osteoclast activity in the absence of new bone production[65]. This condition affects the bones and is characterized by a dysfunctional bone matrix with a low mechanical stability level. Osteocytes are one of the abundant cells in the

bone matrix generated from mature osteoblasts[66]. Up to 50 cytoplasmic dendritic extensions per cell connect to nearby osteocytes, osteoblasts, and bone surface lining cells[62, 67]. In this way, osteocytes serve as a mechanosensory and enable bone to adjust its microarchitecture, shape, or mass in response to mechanical loads[62].

1.5. Nanoclay-based scaffolds for bone tissue engineering

Tissue engineering focuses on developing materials that promote tissue growth and regeneration. Scientists from different parts of the world have been working continuously to develop composite systems with polymers and nano/micro-sized fillers to tailor polymer properties, such as biodegradability, bioactivity, biocompatibility, surface roughness, and mechanical strength, for use in tissue engineering. In PCNs, the dispersed phase is clay particles with at least one dimension in the nanometer range in the polymer matrix [20, 68]. In the preparation of nanocomposites, clay modification has been found to play an important role due to its ability to influence their final properties. To better understand the modification of sodium montmorillonite (Na-MMT) clay with various organic modifiers, the "altered phase" model was developed. This model demonstrates the influence of interactions between polymer, clay, and organic modifiers on crystallinity and nanomechanical properties of PCNs[69]. Furthermore, backbone chain length and functional groups in modifiers have been shown to influence crystallinity and nanomechanical properties[70] of PCNs in a related study. In light of these findings, we began using synthetic amino acids to modify clay, which elevated the interlayer d-spacing while enhancing its biocompatibility[71]. Biomineralization of HAP into intercalated nanoclay galleries produced in situ HAPclay from a subsequent study. When preparing chitosan-polygalacturonic acid (Chi/PgA) and polycaprolactone (PCL) composites, in situ HAPclay is used as a reinforcement filler[24, 72]. Incorporating in situ HAPclay improved composites'

mechanical and bioactive properties[24, 72]. A number of studies from our group have shown that human mesenchymal stem cell differentiation in situ on HAPclay-scaffolds does not require osteogenic supplements. Calcium-rich vesicles were found on nanoclay-based composites produced by MSCs facilitated by nanocomposite. Following further investigation, it was discovered that the Ca/P ratio in these vesicles was lower than the stoichiometric Ca/P ratio of HAP, indicative of the formation of new bone and the remodeling of existing bone[73].

1.6. Bone morphogenetic proteins

As part of the TGF- family, bone morphogenetic proteins (BMPs) play an important role in cell proliferation, differentiation, and bone formation. By simulating a series of cellular processes connected to the formation of embryonic bone, they impart a significant role during the development of the skeleton and adult fracture healing. Over 30 structurally similar BMPs have been identified, and some may have roles beyond bone[74]. There are four groups of BMPs with proven osteogenic properties: BMP2/BMP4, BMP5/BMP6/BMP7, BMP9/10, and BMP12/13/BMP14. For the first time, Marshall Urist demonstrated that demineralized bone could generate new bone when implanted at ectopic sites, known as bone formation by auto induction[75]. Demineralized bone matrix induces mesenchymal cell recruitment, proliferation, and differentiation into cartilage-forming cells[76]. The BMPs-induced ectopic bone formation may involve progenitor cells[77]. BMPs implantation site and the surrounding microenvironment affect how the body reacts to the BMPs. Using BMPs increases the number of pluripotent cells, making them more efficient. Skeletal progenitor cells in bone injuries come from various tissue compartments, including the injured periosteum, endosteum, vascular tissue, and the surrounding musculature, and they work together to aid in skeletal healing[[78]. As both periosteal bone and a surrounding microenvironment do not contain osteoclasts, the addition of a BMPs on an

13

appropriate carrier together with uncoupled osteoblast precursor cells results in bone formation. Canonical Smad-dependent pathways (ligands, receptors, and Smad) and non-canonical Smad-independent pathways are involved in the BMPs signaling pathway. Runx2 gene expression is induced by canonical Smad-dependent (Fig. 1.3) and non-canonical Smad-independent signaling pathways to regulate osteogenesis. For BMPs signaling to take place, specific type I and type II serine/threonine kinase receptors must form a heteromeric complex together. This receptor was
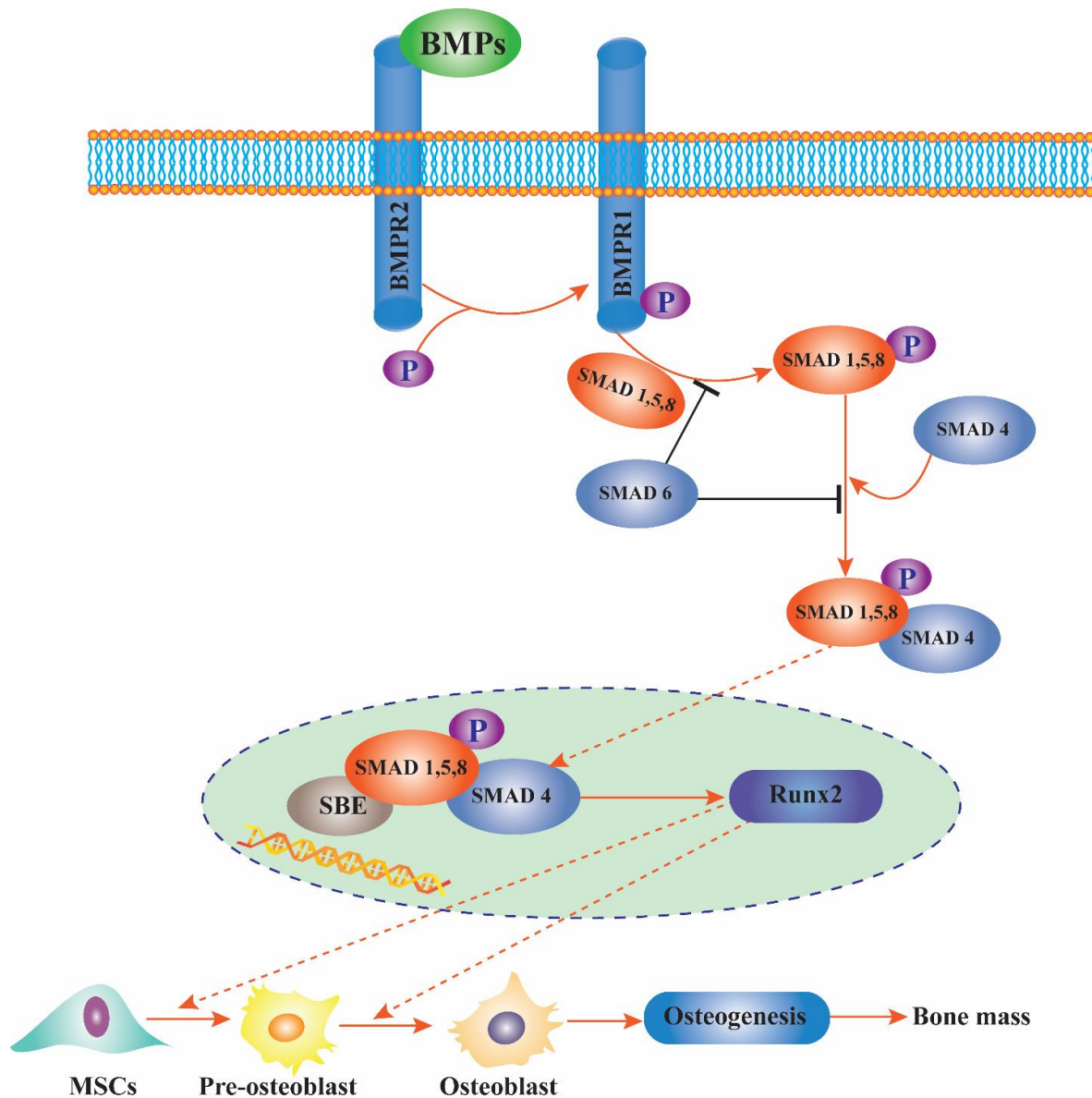
Fig. 1.3. Schematic representation of the BMPs pathway for bone regeneration.

triggered by the presence of another type II receptor[79]. In response to the activation of type I receptors, phosphorylation occurs, resulting in intracellular signaling through R-Smads. Complex interactions between activated R-Smads and co-Smad and Smad4 in the nucleus allow the expression of target genes (Dlx5, Runx2, and Osx) in osteoblasts[80]. Smad6 inhibits activation of Smad1/5/8 by attaching to type I BMP receptor simultaneously. The TAK1 signaling system, which is not dependent on Smad, promotes bone formation by expressing the same genes[81].

Signaling via the Wnt and bone morphogenic protein (BMP) pathways is critical for numerous biological processes. Wnt and BMP ligands complement each other in several biological processes, but they can operate independently of each other[82]. BMP-2 induces Wnt, which activates the β-catenin signaling pathway (Fig. 1.4) and governs the early stages of chondrogenesis and osteogenesis[83]. BMP-2 increases LRP5 expression and stabilizes β-catenin by downregulating β-Trcp[84]. BMP-2 promotes a Wnt ligand-dependent increase in β-catenin levels, and BMP-2 imparts its role through this mechanism[85]. β-catenin deficiency reduces bone formation significantly. Overexpression of DKK-1 or conditional deletion of β-catenin inhibits BMP-2's bone-forming function[83, 86, 87]. In conjunction with the BMPs signaling system, the Wnt/β-catenin signaling pathway is essential for osteogenesis and bone regeneration. It is important to note that bone remodeling depends on the local cytokine signaling environment and systemic hormones concerning osteoblast-osteoclast coupling in the bone shaft. Experimental animals' ectopic bone growth is induced in vivo by BMP2 and BMP7, which enhance the development of diverse osteoblast-like cells. Delivery of osteogenic growth factors to an ectopic location in an uncoupled cell environment or near the periosteum or muscle will aid bone formation and repair. BMPs and Wnt signaling pathways are stimulated in the presence of calcium phosphate-based biomaterials[88], which alters the quality of new bone.
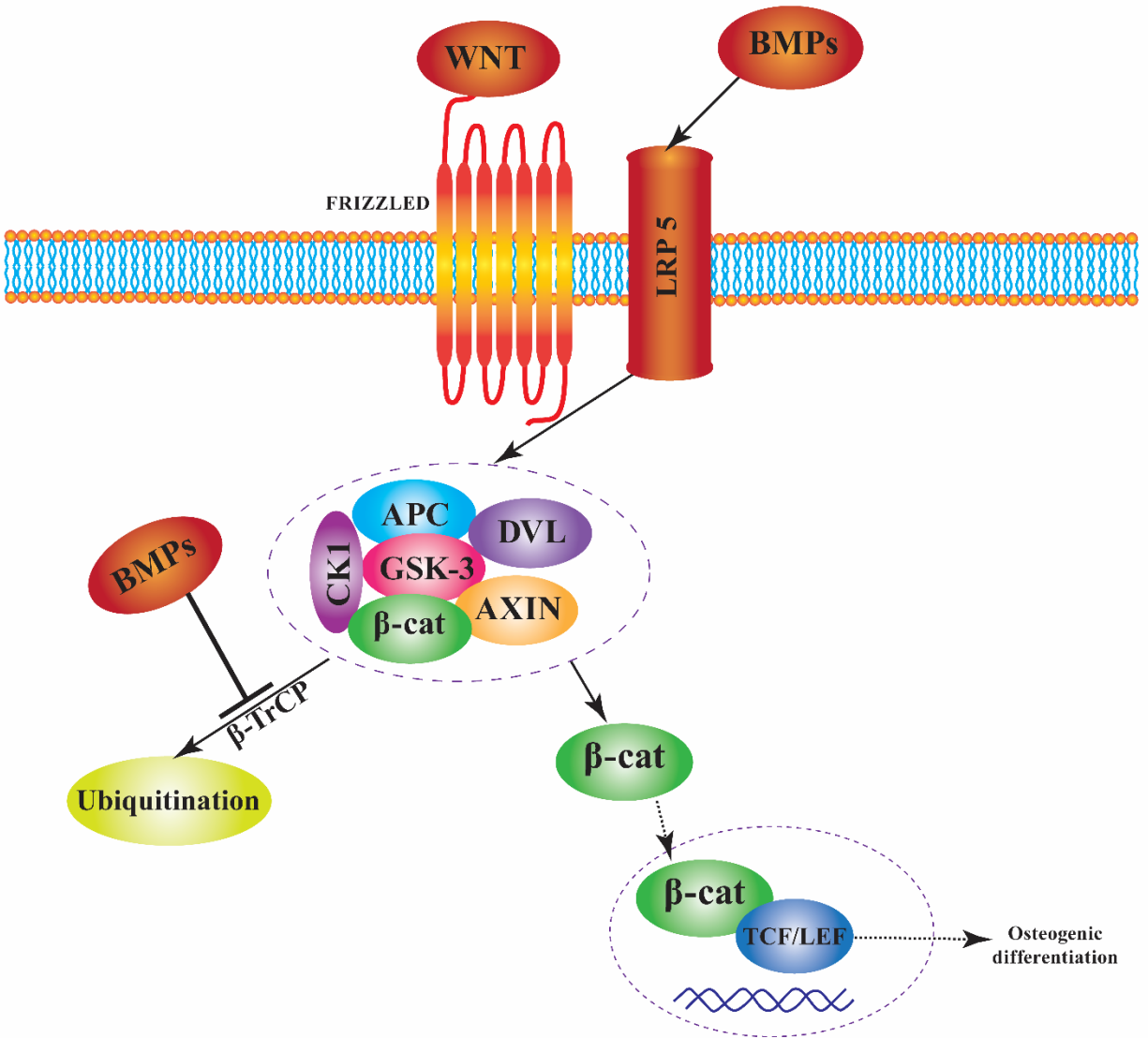
Fig. 1.4. Schematic representation of the BMPs activated wnt-pathway for osteogenesis.

Bone development during embryogenesis is replicated and confirmed by healing fractures in the adult bone, indicating the same cell types and chemicals that drive this process. An early inflammatory phase, a repair phase, and a late remodeling phase have historically been used to classify the bone healing process[89]. Fractures that are not properly stabilized result in secondary or indirect healing, culminating in ossification and callus production in the damaged tissue. Chondrogenesis, the primary ossification process in the endochondral system, begins within the first few days of injury, and the process of intramembranous bone formation overlaps with that.

During this early stage of injury to the periosteum, BMP 2, 4, and 7 are all substantially increased. BMP signaling is involved in intramembranous and endochondral ossification[76]. Early healing allows fracture stability, endochondral bone growth, and MSCs-dependent chondrogenesis[90]. BMPs enhance the development of MSCs into chondroblasts and osteoblasts. Cartilage is replaced by the woven bone, which undergoes remodeling to facilitate normal bone function in the late stages of recovery when adequate angiogenesis is available. Between days 14 and 28 following fracture, immunostaining of BMP2, 4, and 7 in newly produced trabecular bone revealed their presence in osteoclast-like cells[91]. BMPs have a critical function in osteoprogenitor chemotaxis. Because successful fracture healing relies on BMP signaling pathways, BMP antagonists for bone repair have been postulated as a potential clinical application[92]. Human callus recovered from patients undergoing surgery for bone fracture was the first to show BMP signaling[93]. During endochondral ossification, more BMP2 and BMP4 were detected in the matrix between the newly formed osteoid, as shown by immunohistochemical labeling. In the new osteoid tissue, osteoblasts expressed BMP3 and 7. Osteoclasts did not display considerable BMP expression, which is widely regarded as an inhibitor of typical BMP effects. BMPR-IA and BMPR-IB were found in all cells of interest, primarily fibroblasts, osteoblasts, chondroblasts, and osteoclasts, although BMPR-II staining was weaker in osteoblasts and cartilaginous tissue. Endochondral ossification-related BMP2 and BMP4 expression, as well as Noggin and Chordin, were found in healing tissue in this phase of bone repair. In a non-union, BMPs and BMP inhibitors are expressed differently than in routine fracture healing[94]. In non-unions, chondrocytes' BMP2 expression was drastically reduced, and BMP7 expression was completely missing, while mature osteoblasts showed normal BMPs expression. Bone non-union may result from elevated BMP antagonist concentration or insufficient BMP levels, but further clinical trials and carefully planned animal investigations,

including knockout mice and selective suppression of BMP antagonists, are needed to clarify this issue. Since the FDA approved BMP2 and BMP7 in 2002 and 2004, numerous studies have been conducted to examine their safety and effectiveness[95-99]. In addition, rhBMP2 and BMP7 were utilized in various studies, some of which included investigations into fractures of the scaphoid, distal radius, and cervical regions[100, 101]. However, during clinical studies for both rhBMP2 and 7, significant side-effects linked to overdosage have been observed[95, 96].

1.7. Nanomechanics

Biodegradable polymer nanocomposites, osteoprogenitor cells, and growth factors are used in bone tissue engineering to produce functional tissue. While the scaffold deteriorates at a controlled rate, maintaining cell-scaffold contact is necessary for developing healthy tissue until it develops adequate mechanical strength. The physical, chemical and mechanical properties of biomaterials affect signal transduction pathways that govern tissue regeneration and the progression of biological events. Tissue engineering applications require a better understanding of proteins, cells, and cell-substrate interactions on synthetic biodegradable substrates. An important aspect of our research is developing an innovative nanoindentation approach that uses significant deformation to induce a composite response from the cells, newly formed bone tissue, and the deteriorating scaffolds. In this dissertation, changes in the nanomechanical properties during osteogenesis and bone tissue formation in porous scaffolds over extended periods and correlated the nanoindentation response from cells, tissue, and scaffolds to understand the long-term effect of BMPs has been reported.

1.8. Research objectives

The present study's particular goals are as follows:

1. To develop an interlocking scaffolds system combining the synergistic combination of nanoclay-based 3D scaffolds, MSCs, osteoblast, and BMP-2/7 for the accelerated regeneration of critical size bone defects.

2. To understand the long-term effect of BMPs in bone regeneration.

3. To study the influence of BMPs on cellular nanomechanics during bone tissue formation.

4. To develop and characterize composite nanoclay polymer fiber scaffolds for bone tissue engineering applications

5. To develop unnatural amino acid modified Na-MMT clay PCL *in situ* HAP scaffolds for cancer testbed.

6. To study the effect of different compositions of bioactive ceramics on mechanical and biochemical properties of the scaffold toward bone tissue engineering.

1.9. Organization of dissertation

This dissertation is organized into different chapters as follows:

1. Chapter 1: This chapter gives an introduction to tissue engineering. It also gives a brief overview of the different materials used for fabricating bone tissue engineering scaffolds. This chapter also discusses Bone morphogenic proteins (BMPs), the BMPs pathway for bone regeneration, the importance of BMP activated wnt pathway and the potential of BMPs for non-union bone defect repair. Afterward, it describes the importance of nanomechanical response over time to understand the effect of BMPs on cellular response.

2. Chapter 2. This chapter describes the development of a tissue-engineered interlocking block for accelerated bone regeneration.

3. Chapter 3. This chapter describes the mechanisms of the BMPs associated with bone tissue formation and the effect of BMPs on the nanomechanical properties of the newly formed tissue.

4. Chapter 4. This chapter describes the fabrication and characterization of polymer nanoclay composite fiber prepared by the pressure gyration method for bone tissue engineering application.

5. Chapter 5. This chapter describes the in-silico design of the unnatural amino acids modified clays and discusses the potential of these nano clay incorporated polymer scaffolds as cancer testbeds.

6. Chapter 6. This chapter describes the development of different bioactive ceramics nanoclay-based scaffolds and discusses the effects of different compositions of bioactive ceramics on the mechanical and biochemical properties of the scaffold toward bone tissue engineering.

7. Chapter 7. This chapter presents summary and major conclusions of the research presented in this dissertation and future directions for the research in this field.

1.10. References

[1] R. Langer, J.P. Vacanti, TISSUE ENGINEERING, Science 260(5110) (1993) 920-926.

[2] J.A. Singh, S.H. Yu, L. Chen, J.D. Cleveland, Rates of Total Joint Replacement in the United States: Future Projections to 2020-2040 Using the National Inpatient Sample, Journal of Rheumatology 46(9) (2019) 1134-1140.

[3] O. Johnell, J.A. Kanis, An estimate of the worldwide prevalence and disability associated with osteoporotic fractures, Osteoporosis international 17(12) (2006) 1726-1733.

[4]   R. Keen, Osteoporosis: strategies for prevention and management, Best Practice &
       Research Clinical Rheumatology 21(1) (2007) 109-122.

[5]   R. Langer, D.A. Tirrell, Designing materials for biology and medicine, Nature 428(6982)
       (2004) 487-492.

[6]   M. Goldberg, R. Langer, X. Jia, Nanostructured materials for applications in drug delivery
       and tissue engineering, Journal of Biomaterials Science, Polymer Edition 18(3) (2007)
       241-268.

[7]   M.M. Stevens, J.H. George, Exploring and engineering the cell surface interface, Science
       310(5751) (2005) 1135-1138.

[8]   R. Murugan, S. Ramakrishna, Development of nanocomposites for bone grafting,
       Composites Science and Technology 65(15-16) (2005) 2385-2406.

[9]   A. Buxboim, I.L. Ivanovska, D.E. Discher, Matrix elasticity, cytoskeletal forces and
       physics of the nucleus: how deeply do cells 'feel'outside and in?, Journal of cell science
       123(3) (2010) 297-308.

[10]   B.M. Baker, C.S. Chen, Deconstructing the third dimension–how 3D culture
       microenvironments alter cellular cues, Journal of cell science 125(13) (2012) 3015-3024.

[11]   C.K. Chan, T.S.S. Kumar, S. Liao, R. Murugan, M. Ngiam, S. Ramakrishman,
       Biomimetic nanocomposites for bone graft applications, Nanomedicine 1(2) (2006) 177-
       188.

[12]   W.W. Thein-Han, R.D.K. Misra, Biomimetic chitosan–nanohydroxyapatite composite
       scaffolds for bone tissue engineering, Acta biomaterialia 5(4) (2009) 1182-1197.

[13]   K.S. Katti, D.R. Katti, R. Dash, Synthesis and characterization of a novel chitosan/montmorillonite/hydroxyapatite nanocomposite for bone tissue engineering, Biomedical Materials 3(3) (2008) 12.

[14]   X. Cai, H. Tong, X. Shen, W. Chen, J. Yan, J. Hu, Preparation and characterization of homogeneous chitosan–polylactic acid/hydroxyapatite nanocomposite for bone tissue engineering and evaluation of its mechanical properties, Acta biomaterialia 5(7) (2009) 2693-2703.

[15]   J. Huang, Y.W. Lin, X.W. Fu, S.M. Best, R.A. Brooks, N. Rushton, W. Bonfield, Development of nano-sized hydroxyapatite reinforced composites for tissue engineering scaffolds, Journal of Materials Science: Materials in Medicine 18(11) (2007) 2151-2157.

[16]   C.R. Kothapalli, M.T. Shaw, M. Wei, Biodegradable HA-PLA 3-D porous scaffolds: Effect of nano-sized filler content on scaffold properties, Acta biomaterialia 1(6) (2005) 653-662.

[17]   S.M. Cool, B. Kenny, A. Wu, V. Nurcombe, M. Trau, A.I. Cassady, L. Grøndahl, Poly (3-hydroxybutyrate-co-3-hydroxyvalerate) composite biomaterials for bone tissue regeneration: In vitro performance assessed by osteoblast proliferation, osteoclast adhesion and resorption, and macrophage proinflammatory response, Journal of Biomedical Materials Research Part A: An Official Journal of The Society for Biomaterials, The Japanese Society for Biomaterials, and The Australian Society for Biomaterials and the Korean Society for Biomaterials 82(3) (2007) 599-610.

[18] H.J. Lee, S.E. Kim, H.W. Choi, C.W. Kim, K.J. Kim, S.C. Lee, The effect of surface-modified nano-hydroxyapatite on biocompatibility of poly (ε-caprolactone)/hydroxyapatite nanocomposites, European Polymer Journal 43(5) (2007) 1602-1608.

[19] K.-W. Lee, S. Wang, M.J. Yaszemski, L. Lu, Physical properties and cellular responses to crosslinkable poly (propylene fumarate)/hydroxyapatite nanocomposites, Biomaterials 29(19) (2008) 2839-2848.

[20] S.S. Ray, M. Okamoto, Polymer/layered silicate nanocomposites: a review from preparation to processing, Progress in Polymer Science 28(11) (2003) 1539-1641.

[21] K.S. Katti, A.H. Ambre, N. Peterka, D.R. Katti, Use of unnatural amino acids for design of novel organomodified clays as components of nanocomposite biomaterials, Philosophical Transactions of the Royal Society a-Mathematical Physical and Engineering Sciences 368(1917) (2010) 1963-1980.

[22] A.H. Ambre, K.S. Katti, D.R. Katti, Nanoclay based composite scaffolds for bone tissue engineering applications, Journal of Nanotechnology in Engineering and Medicine 1(3) (2010) 031013.

[23] A. Ambre, K.S. Katti, D.R. Katti, In situ mineralized hydroxyapatite on amino acid modified nanoclays as novel bone biomaterials, Materials Science & Engineering C-Materials for Biological Applications 31(5) (2011) 1017-1029.

[24] A.H. Ambre, D.R. Katti, K.S. Katti, Nanoclays mediate stem cell differentiation and mineralized ECM formation on biopolymer scaffolds, Journal of Biomedical Materials Research Part A 101(9) (2013) 2644-2660.

[25] A.J. Mieszawska, J.G. Llamas, C.A. Vaiana, M.P. Kadakia, R.R. Naik, D.L. Kaplan, Clay enriched silk biomaterials for bone formation, Acta Biomaterialia 7(8) (2011) 3036-3041.

[26] C. Viseras, C. Aguzzi, P. Cerezo, A. Lopez-Galindo, Uses of clay minerals in semisolid health care and therapeutic products, Applied Clay Science 36(1-3) (2007) 37-50.

[27] W.F. Lee, Y.T. Fu, Effect of montmorillonite on the swelling behavior and drug-release behavior of nanocomposite hydrogels, Journal of Applied Polymer Science 89(13) (2003) 3652-3660.

[28] Y. Dong, S.-S. Feng, Poly (d, l-lactide-co-glycolide)/montmorillonite nanoparticles for oral delivery of anticancer drugs, Biomaterials 26(30) (2005) 6068-6076.

[29] M.I. Carretero, Clay minerals and their beneficial effects upon human health. A review, Applied Clay Science 21(3-4) (2002) 155-163.

[30] J.P. Zheng, C.Z. Wang, X.X. Wang, H.Y. Wang, H. Zhuang, K. De Yao, Preparation of biomimetic three-dimensional gelatin/montmorillonite–chitosan scaffold for tissue engineering, Reactive and Functional Polymers 67(9) (2007) 780-788.

[31] D. Depan, A.P. Kumar, R.P. Singh, Cell proliferation and controlled drug release studies of nanohybrids based on chitosan-g-lactic acid and montmorillonite, Acta Biomaterialia 5(1) (2009) 93-100.

[32] S.I. Marras, K.P. Kladi, I. Tsivintzelis, I. Zuburtikudis, C. Panayiotou, Biodegradable polymer nanocomposites: The role of nanoclays on the thermomechanical characteristics and the electrospun fibrous structure, Acta Biomaterialia 4(3) (2008) 756-765.

[33] R. Langer, Tissue engineering: a new field and its challenges, Pharmaceutical research 14(7) (1997) 840.

[34] L. Cen, W.E.I. Liu, L.E.I. Cui, W. Zhang, Y. Cao, Collagen tissue engineering: development of novel biomaterials and applications, Pediatric research 63(5) (2008) 492-496.

[35] J.F. Mano, G.A. Silva, H.S. Azevedo, P.B. Malafaya, R.A. Sousa, S.S. Silva, L.F. Boesel, J.M. Oliveira, T.C. Santos, A.P. Marques, Natural origin biodegradable systems in tissue engineering and regenerative medicine: present status and some moving trends, Journal of the Royal Society Interface 4(17) (2007) 999-1030.

[36] M. Kikuchi, H.N. Matsumoto, T. Yamada, Y. Koyama, K. Takakuda, J. Tanaka, Glutaraldehyde cross-linked hydroxyapatite/collagen self-organized nanocomposites, Biomaterials 25(1) (2004) 63-69.

[37] H.-W. Kim, H.-J. Gu, H.-H. Lee, Microspheres of collagen-apatite nanocomposites with osteogenic potential for tissue engineering, Tissue Engineering 13(5) (2007) 965-973.

[38] J. Venugopal, S. Low, A.T. Choon, T.S. Sampath Kumar, S. Ramakrishna, Mineralization of osteoblasts with electrospun collagen/hydroxyapatite nanofibers, Journal of Materials Science: Materials in Medicine 19(5) (2008) 2039-2046.

[39] A. Lode, A. Bernhardt, M. Gelinsky, Cultivation of human bone marrow stromal cells on three-dimensional scaffolds of mineralized collagen: influence of seeding density on colonization, proliferation and osteogenic differentiation, Journal of tissue engineering and regenerative medicine 2(7) (2008) 400-407.

[40] M. Ngiam, S. Liao, A.J. Patil, Z. Cheng, C.K. Chan, S. Ramakrishna, The fabrication of nano-hydroxyapatite on PLGA and PLGA/collagen nanofibrous composite scaffolds and their effects in osteoblastic behavior for bone tissue engineering, Bone 45(1) (2009) 4-16.

[41]   S. Sotome, T. Uemura, M. Kikuchi, J. Chen, S. Itoh, J. Tanaka, T. Tateishi, K. Shinomiya, Synthesis and in vivo evaluation of a novel hydroxyapatite/collagen–alginate as a bone filler and a drug delivery carrier of bone morphogenetic protein, Materials Science and Engineering: C 24(3) (2004) 341-347.

[42]   S.-W. Tsai, F.-Y. Hsu, P.-L. Chen, Beads of collagen–nanohydroxyapatite composites prepared by a biomimetic process and the effects of their surface texture on cellular behavior in MG63 osteoblast-like cells, Acta biomaterialia 4(5) (2008) 1332-1341.

[43]   J.H. Lee, T.G. Park, H.S. Park, D.S. Lee, Y.K. Lee, S.C. Yoon, J.-D. Nam, Thermal and mechanical characteristics of poly (L-lactic acid) nanocomposite scaffold, Biomaterials 24(16) (2003) 2773-2778.

[44]   H. Liu, E.B. Slamovich, T.J. Webster, Less harmful acidic degradation of poly (lactic-co-glycolic acid) bone tissue engineering scaffolds through titania nanoparticle addition, International journal of nanomedicine 1(4) (2006) 541.

[45]   H. Liu, E.B. Slamovich, T.J. Webster, Increased osteoblast functions on nanophase titania dispersed in poly-lactic-co-glycolic acid composites, Nanotechnology 16(7) (2005) S601.

[46]   E. Nejati, H. Mirzadeh, M. Zandi, Synthesis and characterization of nano-hydroxyapatite rods/poly (l-lactide acid) composite scaffolds for bone tissue engineering, Composites Part A: Applied Science and Manufacturing 39(10) (2008) 1589-1596.

[47]   M.C. Serrano, R. Pagani, M. Vallet-Regı, J. Pena, A. Ramila, I. Izquierdo, M.T. Portolés, In vitro biocompatibility assessment of poly (ε-caprolactone) films using L929 mouse fibroblasts, Biomaterials 25(25) (2004) 5603-5611.

[48] L. Shor, S. Güçeri, X. Wen, M. Gandhi, W. Sun, Fabrication of three-dimensional polycaprolactone/hydroxyapatite tissue scaffolds and osteoblast-scaffold interactions in vitro, Biomaterials 28(35) (2007) 5291-5297.

[49] C. Erisken, D.M. Kalyon, H. Wang, Functionally graded electrospun polycaprolactone and β-tricalcium phosphate nanocomposites for tissue engineering applications, Biomaterials 29(30) (2008) 4065-4073.

[50] J.M. Karp, M.S. Shoichet, J.E. Davies, Bone formation on two-dimensional poly (DL-lactide-co-glycolide)(PLGA) films and three-dimensional PLGA tissue engineering scaffolds in vitro, Journal of Biomedical Materials Research Part A: An Official Journal of The Society for Biomaterials, The Japanese Society for Biomaterials, and The Australian Society for Biomaterials and the Korean Society for Biomaterials 64(2) (2003) 388-396.

[51] M.V. Jose, V. Thomas, K.T. Johnson, D.R. Dean, E. Nyairo, Aligned PLGA/HA nanofibrous nanocomposite scaffolds for bone tissue engineering, Acta biomaterialia 5(1) (2009) 305-315.

[52] V.J. Chen, P.X. Ma, Nano-fibrous poly (L-lactic acid) scaffolds with interconnected spherical macropores, Biomaterials 25(11) (2004) 2065-2073.

[53] D. Verma, K. Katti, D. Katti, Bioactivity in in situ hydroxyapatite–polycaprolactone composites, Journal of Biomedical Materials Research Part A: An Official Journal of The Society for Biomaterials, The Japanese Society for Biomaterials, and The Australian Society for Biomaterials and the Korean Society for Biomaterials 78(4) (2006) 772-780.

[54] Y. Lei, B. Rai, K.H. Ho, S.H. Teoh, In vitro degradation of novel bioactive polycaprolactone—20% tricalcium phosphate composite scaffolds for bone engineering, Materials Science and Engineering: C 27(2) (2007) 293-298.

[55]   K.M. Kim, G.R.D. Evans, Tissue engineering: the future of stem cells, Top Tissue Eng 2 (2005) 1-21.

[56]   J.M. Polak, A.E. Bishop, Stem cells and tissue engineering: past, present, and future, Annals of the New York Academy of Sciences 1068(1) (2006) 352-366.

[57]   D. Marolt, M. Knezevic, G. Vunjak-Novakovic, Bone tissue engineering with human stem cells, Stem cell research & therapy 1(2) (2010) 1-11.

[58]   R. Florencio-Silva, G.R.d.S. Sasso, E. Sasso-Cerri, M.J. Simões, P.S. Cerri, Biology of bone tissue: structure, function, and factors that influence bone cells, BioMed research international 2015 (2015).

[59]   P. Ducy, R. Zhang, V. Geoffroy, A.L. Ridall, G. Karsenty, Osf2/Cbfa1: a transcriptional activator of osteoblast differentiation, cell 89(5) (1997) 747-754.

[60]   T. Komori, H. Yagi, S. Nomura, A. Yamaguchi, K. Sasaki, K. Deguchi, Y. Shimizu, R.T. Bronson, Y.H. Gao, M. Inada, Targeted disruption of Cbfa1 results in a complete lack of bone formation owing to maturational arrest of osteoblasts, cell 89(5) (1997) 755-764.

[61]   T. Komori, Runx2, a multifunctional transcription factor in skeletal development, Journal of cellular biochemistry 87(1) (2002) 1-8.

[62]   K. Nakashima, X. Zhou, G. Kunkel, Z. Zhang, J.M. Deng, R.R. Behringer, B. De Crombrugghe, The novel zinc finger-containing transcription factor osterix is required for osteoblast differentiation and bone formation, Cell 108(1) (2002) 17-29.

[63]   B.F. Boyce, D.E. Hughes, K.R. Wright, L. Xing, A. Dai, Recent advances in bone biology provide insight into the pathogenesis of bone diseases, Laboratory investigation; a journal of technical methods and pathology 79(2) (1999) 83-94.

[64] J.C. Crockett, D.J. Mellis, D.I. Scott, M.H. Helfrich, New knowledge on critical osteoclast formation and activation pathways from study of rare genetic diseases of osteoclasts: focus on the RANK/RANKL axis, Osteoporosis International 22(1) (2011) 1-20.

[65] X. Feng, J.M. McDonald, Disorders of bone remodeling, Annual review of pathology 6 (2011) 121.

[66] L.F. Bonewald, The amazing osteocyte, Journal of bone and mineral research 26(2) (2011) 229-238.

[67] S.C. Manolagas, Choreography from the tomb: an emerging role of dying osteocytes in the purposeful, and perhaps not so purposeful, targeting of bone remodeling, IBMS BoneKEy 3 (2006) 5.

[68] K. Müller, E. Bugnicourt, M. Latorre, M. Jorda, Y. Echegoyen Sanz, J.M. Lagaron, O. Miesbauer, A. Bianchin, S. Hankin, U. Bölz, Review on the processing and properties of polymer nanocomposites and nanocoatings and their applications in the packaging, automotive and solar energy fields, Nanomaterials 7(4) (2017) 74.

[69] D. Sikdar, S.M. Pradhan, D.R. Katti, K.S. Katti, B. Mohanty, Altered phase model for polymer clay nanocomposites, Langmuir 24(10) (2008) 5599-5607.

[70] D. Sikdar, D.R. Katti, K.S. Katti, B. Mohanty, Influence of backbone chain length and functional groups of organic modifiers on crystallinity and nanomechanical properties of intercalated clay-polycaprolactam nanocomposites, International Journal of Nanotechnology 6(5-6) (2009) 468-492.

[71] K.S. Katti, A.H. Ambre, N. Peterka, D.R. Katti, Use of unnatural amino acids for design of novel organomodified clays as components of nanocomposite biomaterials, Philosophical Transactions of the Royal Society A: Mathematical, Physical and Engineering Sciences 368(1917) (2010) 1963-1980.

[72] A.H. Ambre, D.R. Katti, K.S. Katti, Biomineralized hydroxyapatite nanoclay composite scaffolds with polycaprolactone for stem cell-based bone tissue engineering, Journal of Biomedical Materials Research Part A 103(6) (2015) 2077-2101.

[73] K.S. Katti, A.H. Ambre, S. Payne, D.R. Katti, Vesicular delivery of crystalline calcium minerals to ECM in biomineralized nanoclay composites, Materials Research Express 2(4) (2015) 045401.

[74] L. Grgurevic, G.L. Christensen, T.J. Schulz, S. Vukicevic, Bone morphogenetic proteins in inflammation, glucose homeostasis and adipose tissue energy metabolism, Cytokine & growth factor reviews 27 (2016) 105-118.

[75] M.R. Urist, Bone: formation by autoinduction, Science 150(3698) (1965) 893-899.

[76] A.H. Reddi, Role of morphogenetic proteins in skeletal tissue engineering and regeneration, Nature Biotechnology 16(3) (1998) 247-252.

[77] S. Vukicevic, H. Oppermann, D. Verbanac, M. Jankolija, I. Popek, J. Curak, J. Brkljacic, M. Pauk, I. Erjavec, I. Francetic, The clinical use of bone morphogenetic proteins revisited: a novel biocompatible carrier device OSTEOGROW for bone healing, International orthopaedics 38(3) (2014) 635-647.

[78] P. Hernigou, I. Guissou, Y. Homma, A. Poignard, N. Chevallier, H. Rouard, C.H. Flouzat Lachaniette, Percutaneous injection of bone marrow mesenchymal stem cells for ankle non-unions decreases complications in patients with diabetes, International orthopaedics 39(8) (2015) 1639-1643.

[79] D.O. Wagner, C. Sieber, R. Bhushan, J.H. Borgermann, D. Graf, P. Knaus, BMPs: From Bone to Body Morphogenetic Proteins, Science Signaling 3(107) (2010) 6.

[80] T. Katagiri, N. Takahashi, Regulatory mechanisms of osteoblast and osteoclast differentiation, Oral Diseases 8(3) (2002) 147-159.

[81] C. Thouverey, J. Caverzasio, Focus on the p38 MAPK signaling pathway in bone development and maintenance, Bonekey Reports 4 (2015) 8.

[82] N. Itasaki, S. Hoppler, Crosstalk Between Wnt and Bone Morphogenic Protein Signaling: A Turbulent Relationship, Developmental Dynamics 239(1) (2010) 16-33.

[83] Y. Chen, H.C. Whetstone, A. Youn, P. Nadesan, E.C.Y. Chow, A.C. Lin, B.A. Alman, beta-catenin signaling pathway is crucial for bone morphogenetic protein 2 to induce new bone formation, Journal of Biological Chemistry 282(1) (2007) 526-533.

[84] M. Zhang, Y. Yan, Y.B. Lim, D.Z. Tang, R. Xie, A. Chen, P. Tai, S.E. Harris, L.P. Xing, Y.X. Qin, D. Chen, BMP-2 Modulates beta-Catenin Signaling Through Stimulation of Lrp5 Expression and Inhibition of beta-TrCP Expression in Osteoblasts, Journal of Cellular Biochemistry 108(4) (2009) 896-905.

[85] L.J. Yang, K. Yamasaki, Y. Shirakata, X.J. Dai, S. Tokumaru, Y. Yahata, M. Tohyama, Y. Hanakawa, K. Sayama, K. Hashimoto, Bone morphogenetic protein-2 modulates Wnt and frizzled expression and enhances the canonical pathway of Wnt signaling in normal keratinocytes, Journal of Dermatological Science 42(2) (2006) 111-119.

[86] G.M. Boland, G. Perkins, D.J. Hall, R.S. Tuan, Wnt 3a promotes proliferation and suppresses osteogenic differentiation of adult human mesenchymal stem cells, Journal of Cellular Biochemistry 93(6) (2004) 1210-1230.

[87] K. Fujita, S. Janz, Attenuation of WNT signaling by DKK-1 and -2 regulates BMP2-induced osteoblast differentiation and expression of OPG, RANKL and M-CSF, Molecular Cancer 6 (2007).

[88] J. Bolander, Y.C. Chai, L. Geris, J. Schrooten, D. Lambrechts, S.J. Roberts, F.P. Luyten, Early BMP, Wnt and Ca2+/PKC pathway activation predicts the bone forming capacity of periosteal cells in combination with calcium phosphates, Biomaterials 86 (2016) 106-118.

[89] I.H. Kalfas, Principles of bone healing, Neurosurgical focus 10(4) (2001) 1-4.

[90] R. Dimitriou, E. Tsiridis, P.V. Giannoudis, Current concepts of molecular aspects of bone healing, Injury 36(12) (2005) 1392-1404.

[91] T. Onishi, Y. Ishidou, T. Nagamine, K. Yone, T. Imamura, M. Kato, T.K. Sampath, P. Ten Dijke, T. Sakou, Distinct and overlapping patterns of localization of bone morphogenetic protein (BMP) family members and a BMP type II receptor during fracture healing in rats, Bone 22(6) (1998) 605-612.

[92] I.H.A. Ali, D.P. Brazil, Bone morphogenetic proteins and their antagonists: current and emerging clinical uses, British journal of pharmacology 171(15) (2014) 3620-3632.

[93] P. Kloen, M. Di Paola, O. Borens, J. Richmond, G. Perino, D.L. Helfet, M.J. Goumans, BMP signaling components are expressed in human fracture callus, Bone 33(3) (2003) 362-371.

[94] P. Kloen, D. Lauzier, R.C. Hamdy, Co-expression of BMPs and BMP-inhibitors in human fractures and non-unions, Bone 51(1) (2012) 59-68.

[95]   R. Fu, S. Selph, M. McDonagh, K. Peterson, A. Tiwari, R. Chou, M. Helfand, Effectiveness and harms of recombinant human bone morphogenetic protein-2 in spine fusion: a systematic review and meta-analysis, Annals of internal medicine 158(12) (2013) 890-902.

[96]   M.C. Simmonds, J.V.E. Brown, M.K. Heirs, J.P.T. Higgins, R.J. Mannion, M.A. Rodgers, L.A. Stewart, Safety and effectiveness of recombinant human bone morphogenetic protein-2 for spinal fusion: a meta-analysis of individual-participant data, Annals of internal medicine 158(12) (2013) 877-889.

[97]   S. Govender, C. Csimma, H.K. Genant, A. Valentin-Opran, Y. Amit, R. Arbel, H. Aro, D. Atar, M. Bishay, M.G. Borner, P. Chiron, P. Choong, J. Cinats, B. Courtenay, R. Feibel, B. Geulette, C. Gravel, N. Haas, M. Raschke, E. Hammacher, D. van der Velde, P. Hardy, M. Holt, C. Josten, R.L. Ketterl, B. Lindeque, G. Lob, H. Mathevon, G. McCoy, D. Marsh, R. Miller, E. Munting, S. Oevre, L. Nordsletten, A. Patel, A. Pohl, W. Rennie, P. Reynders, P.M. Rommens, J. Rondia, W.C. Rossouw, P.J. Daneel, S. Ruff, A. Ruter, S. Santavirta, T.A. Schildhauer, C. Gekle, R. Schnettler, D. Segal, H. Seiler, R.B. Snowdowne, J. Stapert, G. Taglang, R. Verdonk, L. Vogels, A. Weckbach, A. Wentzensen, T. Wisniewski, B.S. Grp, Recombinant human bone morphogenetic protein-2 for treatment of open tibial fractures - A prospective, controlled, randomized study of four hundred and fifty patients, Journal of Bone and Joint Surgery-American Volume 84A(12) (2002) 2123-2134.

[98]   G.E. Friedlaender, C.R. Perry, J.D. Cole, S.D. Cook, G. Cierny, G.F. Muschler, G.A. Zych, J.H. Calhoun, A.J. LaForte, S. Yin, Osteogenic protein-1 (bone morphogenetic protein-7) in the treatment of tibial nonunions - A prospective, randomized clinical trial comparing rhOP-1 with fresh bone autograft, Journal of Bone and Joint Surgery-American Volume 83A (2001) S151-S158.

[99]   P.V. Giannoudis, N.K. Kanakaris, R. Dimitriou, I. Gill, V. Kolimarala, R.J. Montgomery, The Synergistic Effect of Autograft and BMP-7 in the Treatment of Atrophic Nonunions, Clinical Orthopaedics and Related Research 467(12) (2009) 3239-3248.

[100] M. Pecina, L. Giltaij, S. Vukicevic, Orthopaedic applications of osteogenic protein-1 (BMP-7), International orthopaedics 25(4) (2001) 203.

[101] R. Bilic, P. Simic, M. Jelic, R. Stern-Padovan, D. Dodig, H.P. van Meerdervoort, S. Martinovic, D. Ivankovic, M. Pecina, S. Vukicevic, Osteogenic protein-1 (BMP-7) accelerates healing of scaphoid non-union with proximal pole sclerosis, International orthopaedics 30(2) (2006) 128-134.

CHAPTER 2. TISSUE-ENGINEERED INTERLOCKING SCAFFOLD BLOCKS FOR THE REGENERATION OF BONE

This chapter describes the development of a tissue-engineered interlocking block for accelerated bone regeneration. The contents of this chapter have been published in Krishna Kundu, Dinesh R. Katti, and Kalpana S. Katti, "Tissue-engineered interlocking scaffold blocks for the regeneration of bone", Journal of The Minerals, Metals & Materials Society 72 (4) (2020) 1443-1457.

2.1. Introduction

Bone defects have a significant impact on a patient's quality of life. Bone-related complications including musculoskeletal pathologies such as fractures, low back pain, scoliosis, osteoporosis, bone infection or tumors, congenital disabilities, and oral and maxillofacial pathologies, as well as rheumatic diseases like osteoarthritis are increasing in number every year[1]. Annually, bone defect injuries cost approximately $19 billion, and it is predicted that by 2025, the cost will increase to $25.3 billion[2]. Also, bone is the second most transplanted tissue after blood[3]. Recent studies in bone defect treatment include an array of techniques such as allografts, autografts, gene therapy, and tissue engineering scaffolds [4]. The implantation of metallic/ceramic-based implants to assist bone regeneration remains a popular treatment. Both autografts and allografts suffer from severe limitations such as limited availability, increased risk of infection, donor site morbidity, and insufficient transplant integration. Another major problem in orthopedic and trauma surgery is the delayed healing of critical-size defects. An orthotropic defect in bone that does not heal without surgical intervention is termed as "critical size defect." Classically, a critical-sized bone defect (CSBD) is defined as the smallest bone defect that will not heal spontaneously during the lifetime of the human or animal[5]. Medically, CSBD has been

referred to as a defect that has less than 10% bony regeneration during the lifetime of the human or animal or duration of the experiment[6]. The size of this defect is usually at least two times the diameter of the bone[7].

Many putty-type and paste-like formulations are available commercially for filling bone defects. These products although being highly effective for filling small bone defects, do not bear the load and are not effective for non-union 'critical-size defects.' Commercially available bone grafts are mainly ceramic based. These grafts are derived from synthetic or naturally occurring minerals. Because of the similar mineral composition as bone, these graft materials show excellent osteoconductivity and osteoinductivity. But, these ceramic-based grafts are often brittle and weak under tension and shear[8]. After implantation, mechanical properties frequently decrease by 30-40% within a couple of months of implantation. An interconnected microporous (pore with diameters > 100 μm) structure is required for the grafts for bone regeneration which allows proliferation and differentiation of osteoblast cells, as well as vascularization[9, 10]. Ceramic based available bone grafts have a microporous structure with a pore diameter of fewer than 100 μm. These grafts have different resorption rates[11], and the degrading structures can compromise the intrinsic strength of the bone[12].

In recent years, tissue engineering and regenerative medicine have shown promise for bone reconstitution, with the possibility to circumvent the complications associated with traditional techniques[13-16]. Indeed, a potential solution to fix these problems is the development of engineered structures through the combination of scaffolds, cells, and soluble/mechanical factors. The use of cell-based regeneration therapy was introduced in the early 1990s [17]. Cells-scaffold interaction is very crucial for the regeneration processes, as cells required an appropriate three-dimensional environment to form tissue. Optimization of the various properties of the scaffold

from the nanoscale to macroscale is necessary to provide the cells with proper biophysical and biochemical stimuli for tissue engineering. The integration of these properties is one of the challenges in the field of tissue engineering.

Bone is a nanocomposite with a complex hierarchical structure that results in organized architectures spanning from nanoscale to macroscale [18-20]. Its complex hierarchical structure[21] provides unique mechanical properties of strength, regeneration, and toughness, which is required for structural support and movement. In prior studies, we reported a three-tier hierarchy of collagen molecules in bone and their role on the mechanical behavior of bone [22-24]. Considering its complex hierarchical structure and mechanical strength, designing a scaffold for bone regeneration is challenging. Scaffolds with interconnected porous structures with the appropriate mechanical strength, modulus, and toughness are required [17, 25, 26] as also the need for an appropriate biomechanical load at the defect site. Biocompatible polymers reinforced with inorganic fillers that form nanocomposites can provide appropriate mechanical properties. The properties of the polymer composite can be altered depending on the nature of the inorganic fillers. For tissue engineering purposes, inorganic fillers are also added to improve cell adhesion, cell-scaffold interaction, and facilitate tissue formation. HAP has been extensively used for bone tissue engineering[27] since the mineral phase of the bone matrix has a similar composition[28]. Synthetic HAP can form a chemical bond with the host tissue and provides a greater advantage in clinical applications compared to most other bone substitutes such as allografts or metallic implants[29]. Synthetic HAP has excellent osteoconductive and osteoinductive capabilities and exhibits slow biodegradability and biocompatibility[30, 31]. Because of its biocompatibility with soft tissue such as skin and muscle, it is ideal for bone repair, bone augmentation, coating for bone implants, and dental implants[32-36]. However, poor load-bearing properties restrict its use mainly

to low load-bearing applications. Nanocrystalline HAP powders exhibit enhanced mechanical properties, better bioactivity because of the higher surface area.[31, 37] Sodium montmorillonite (Na-MMT) clay, a layered silicate with trace elements as ionic constituents, is used in polymer-clay nanocomposites (PCNs) for its high reinforcing capability.[38, 39] Na-MMT nanoclay also has a positive effect on cell behavior [40-44]. Thus, MMT nanoclay useful for the design of biodegradable scaffolds for bone tissue engineering. MMT nanoclays enhance mechanical properties, cell attachment, and increase biodegradability. Polycaprolactone (PCL) exhibits ease in processing, adequate mechanical properties, solubility in common organic solvents, biocompatibility, biodegradability which are very important for bone tissue engineering applications.[45] Our prior studies used amino acid modified nanoclays to prepare mineralized HAP [46-48]. Besides enhancing the mechanical properties of the scaffolds the nanoclays also enabled differentiation of human mesenchymal stem cells into osteoblastic lineages without the help of differentiating media [43].

Mesenchymal stem cells (MSCs) have the potential for tissue engineering applications because they can proliferate in an undifferentiated state while maintaining the ability to differentiate into different cell lines[49]. Many studies are reported and are underway in elucidating the mechanisms of osteogenic differentiation of MSCs. Osteoblasts induce the osteogenic differentiation of MSCs not only by hormones or cytokines but also by a direct cell-to-cell interaction[50, 51]. Also, the cell-cell interactions through cadherins are critically involved in bone remodeling, including osteoblast differentiation.[52] Also popular is the use of bone morphogenic proteins (BMPs) in support of bone regeneration [53].

BMPs were first discovered in 1965[54, 55]. They are naturally occurring molecules that enhance bone formation. There are more than 20 BMPs that have been discovered [56, 57]. Among

them, BMP-2 and BMP-7 are the most influential inducers of cartilage and bone formation [58-60]. BMPs induced this effect via two types of serine/threonine kinase receptors: BMPs bind the type II receptor, which subsequently activates the type I receptor by a direct association [61]. Signals from the activated type I receptor are transmitted to the nucleus through various mediator molecules, most importantly, through the formation of SMADs complexes, which induced the Runx2 expression [61, 62]. Eventually, Runx2 stimulates the osteogenic differentiation of MSCs [60, 61]. RUNX2 is a key transcription factor commonly associated with the differentiation of osteoblasts. SMADs are a family of structurally similar proteins that are the signal transducers, which are critically important for regulating cell development and growth. For bone regeneration, bone morphogenetic protein-2 (BMP-2) is the most potent osteoinductive factor for faster recovery of bone defects.[63] But, its clinical application requires supraphysiological BMP doses that increase inappropriate adipogenesis and cyst-like bone formation. [64]Therefore, recent promising alternative strategies are focused on promoting the osteogenic activity of BMPs while simultaneously downregulation their adverse effects. Recent studies suggest important roles of tribbles homologs proteins in development and cellular differentiation.[65] Tribbles homolog 3 dissociated from BMPs receptor in response to stimulation of BMPs. Tribbles homolog 3 (Trb3) helps to degrades Smad ubiquitin regulatory factor 1 (Smurf1), which is considered a negative regulator for Smads dependent pathway. The role of PPARγ in BMP-induced differentiation of MSCs is rather exciting. It has been shown in the recent study that osteogenic BMPs up-regulate the PPARγ level[66]. The recent research also showed that PPARγ enhanced ALP activity significantly. Overexpression of PPARγ induced the adipogenic differentiation of MSCs. One recent study confirmed that PPARγ with BMPs promoted both osteogenic and adipogenic differentiation of MSCs[67]. A recent study showed that Trb3 bind and suppress peroxisome

proliferator-activated receptor-γ (PPARγ), a master regulator of adipogenesis.[68] Thus, adverse adipogenesis can be reduced by targeting Trb3. Trb3 can also enhance BMP-2 induced osteogenesis. [68] Upon BMP stimulation, however, BMP efficacy is greatly reduced due to the enhanced expression of natural BMP antagonists to auto-regulate endogenous BMP-2 levels. Thus, the potency of Trb3 in BMP treatments can be enhanced by inhibiting the expression of BMP antagonists such as noggin. Augmentation of Trb3 expression combined with the employment of noggin suppression can increase bone formation by activation of the Smad pathway and suppression of PPARγ.

In this study, we specifically target the problem of fast tissue regeneration in large nonunion bone defects with two technologies. The first is a scaffold design that uses interconnected small blocks intended to shorten the bone formation time, and the second is the use of coatings of BMP-2 and BMP-7 on the interconnected blocks.

2.2. Materials and methods

2.2.1. Modification of MMT clay

The detailed procedure for the modification of Na-MMT clay is described elsewhere.[46], [48] Briefly, the 5-aminovaleric acid solution was added to preheated (60°C) MMT suspension, and the mixture solution was kept for stirring. After one hour, the obtained slurry was centrifuged and washed to remove chloride ions followed by drying at 70°C, grinding, and sieving to obtain a fine powder. Na-MMT clay (SWy-2) was procured from Clay Minerals Society. The 5-aminovaleric acid was obtained from Sigma-Aldrich.

2.2.2. Preparation of in situ HAPclay

We have followed the procedure described in previous studies to prepare in situ HAP clay.[43, 48] In brief, the organically modified MMT clay powder was dissolved into Na$_2$HPO$_4$

solution (23.8 mM) by stirring at room temperature for 2 hours. Further, 39.8 mM of $CaCl_2$ solution was added, and this suspension was stirred vigorously for 8 hours (pH 7.4). The precipitate obtained was allowed to settle for twelve hours, followed by centrifuging and drying ($70^{\circ}C$), and is subsequently ground and sieved to obtain a fine powder. The compounds Na_2HPO_4 and $CaCl_2$ were purchased from J.T. Baker.

2.2.3. Design of the interlocking scaffold blocks

Two types of scaffolds 'blocks' were fabricated. A simple block refers to a cube of scaffold without any interlocking edges and sides. The other kind was the interlocking blocks that fit into each other for filling a larger space. The specific design of the interlocked blocks resulted from the need to achieve the following characteristics: (1) small size that offered large surface area to volume without sacrificing ability to handle easily, (2) a single block with both male and female interlocking parts, (3) allow interlocking in XY plane and stacking in z plane through vertical notches with grooves and (4) to achieve rounded shapes at interlocking in order to reduce stress concentrators and reduce breaking during assembly. Design of molds for both types of blocks (simple and interlocked) was made using on Solidworks and 3D printed using polymethylmethacrylate (PMMA) polymer with a Formlabs Form 2 3D Printer (Fig. 2.1A-B). We used 3D printed molds to prepare simple scaffold blocks and interlocking scaffold blocks using PCL/in-situ HAP clay. The dimensions of simple scaffold blocks and interlock scaffold blocks are shown in Fig. 2.1C-D. Fig. 2.1E-F shows a two-block assembly, four-block assembly, eight-block assembly, and eight interlock assembly, respectively. Fig. 2.1G represents the cylindrical scaffold.
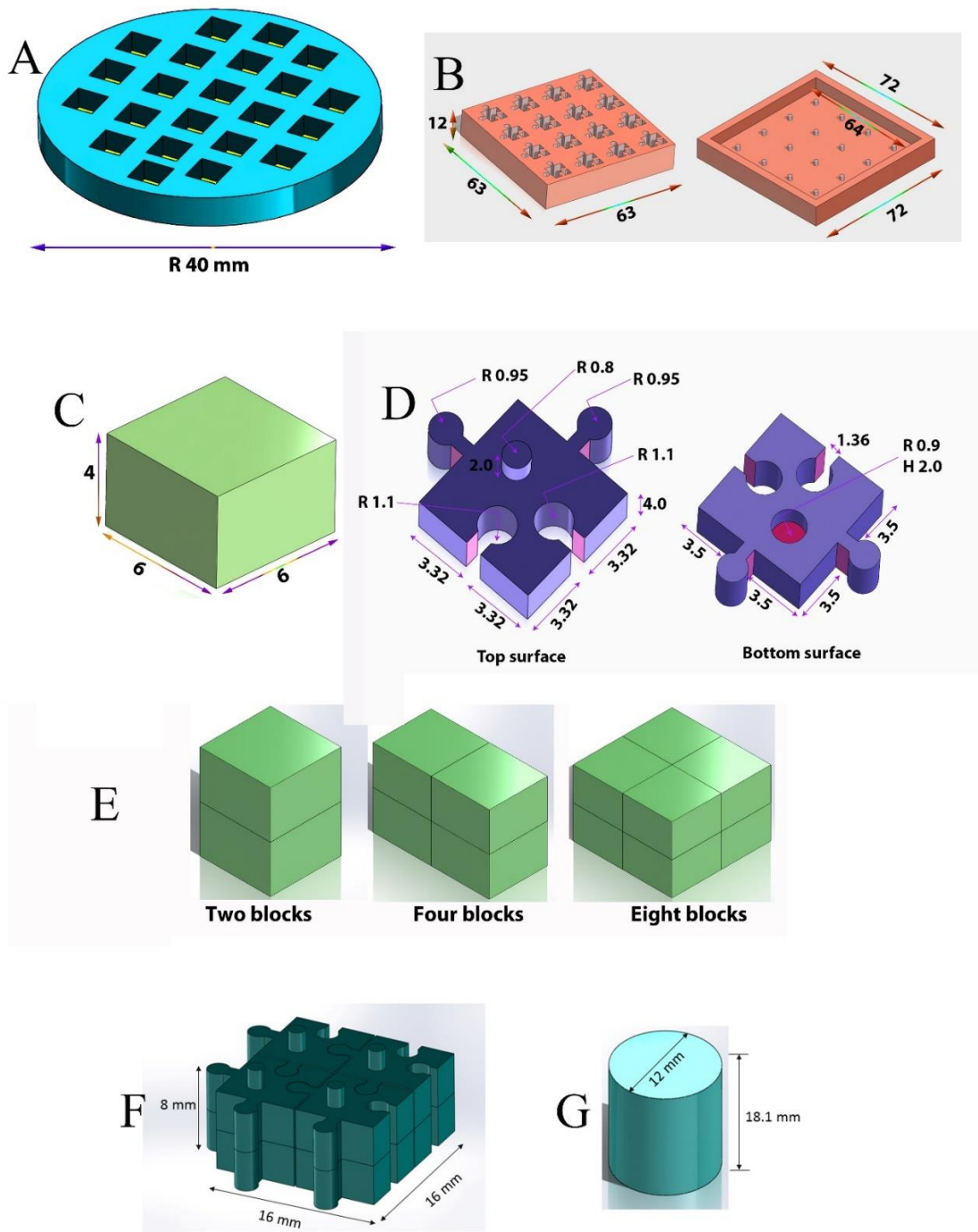
Fig. 2.1. (A) Mold for simple scaffold blocks. (B) Mold for interlocking scaffold blocks. (C) Schematic of a single scaffold block. (D) Schematic of interlocking scaffold blocks. (E) Schematic of assembly of two blocks, four blocks, and eight blocks. (F) Schematic of assembly of eight interlocking blocks. (G) Schematic of the cylindrical scaffold.

2.2.4. Preparation of PCL/in situ HAPclay scaffolds

3D PCL/in situ HAPClay scaffolds were prepared according to the procedure described in earlier studies[69, 70]. The 3D PCL scaffolds were prepared with ten wt. % in situ HAP clay. In a typical procedure, the PCL solution was prepared by dissolving 3.6 g of polymer in 40 ml of 1,4-dioxane. Another solution was prepared by dissolving 0.4 g of prepared in situ HAPclay in 20 ml of 1,4-dioxane, followed by sonicating for 18 minutes. Freshly prepared in situ HAPclay solution was added to the polymer solution and stirred for 2 hours. Then, the polymer HAPclay solution was poured into the 3D printed molds. Further, the freeze extraction method was used to obtain 3D scaffolds. The polymer PCL and solvent 1, 4-dioxane, were purchased from Sigma Aldrich.

2.2.5. Preparation of scaffold sample for cell culture

PCL/ in situ HAPclay scaffolds were placed in a UV sterilization chamber for 45 minutes. Following this, samples were immersed in 100 % ethanol for 24 hours for sterilization, followed by washing with PBS. BMP 2 (Genscript) and BMP 7 (Biovision) solution were prepared by dissolving in cell culture grade water at a concentration of 1μg/ml. Sterilized samples (blocks) were immersed into the freshly made 1:1 BMP-2 and BMP-7 solution for 24 hours. After 24 hours, BMP-2 and BMP-7 coated samples were kept in the cell culture media for 24 hours before their use for cell culture experiments. Initially, a combination of 5 X 10^4 osteoblast cells (hFOB) and 5 X 10^4 MSCs were seeded on each scaffold. On the second day, a scaffold block sandwich was prepared by placing one scaffold on top of another scaffold. Uncoated scaffolds were used as control throughout the experiment.

2.2.6. Cell lines and culture medium

The human osteoblast cell line (hFOB 1.19) was obtained from ATCC. The culture media consisted of 90% HyQ Dulbecco's Modified Eagle medium DMEM-12(1:1) from Hyclone, 10%

fetal bovine serum (FBS) from ATCC, and 0.6% antibiotic solution (G418) from JR scientific. Human bone marrow mesenchymal stem cells (MSCs) were obtained from Lonza and maintained in MSCGM™ Bulletkit™ medium. The Bulletkit™ medium was prepared by adding MSCGM™ SingleQuots™ (Lonza) to MSCBM™ (Lonza). All the cells were maintained at 37^oC and 5% CO_2 in a humidified incubator.

2.2.7. The release profile of BMP's

BMP 2 and BMP 7 solutions were prepared by dissolving in cell culture grade water at a concentration of 1µg/ml. Sterilized PCL/ in situ HAPclay scaffolds (blocks) were immersed into the freshly made 1:1 BMP-2 and BMP-7 solution for 24 hours. Each BMP's coated scaffold was incubated in phosphate-buffered saline at 37^oC, 5% CO_2 under humidified conditions (PBS, 1.0 ml). The supernatant was collected at every 24h intervals, and the fresh PBS was added. The amount of BMP's release was obtained by incubating with p-nitrophenyl phosphate (250uL) at room temperature for 60 min. 3N NaOH (70mL) was further added to the wells, and absorbance readings were taken at 405 nm using a microplate spectrophotometer (Bio-Rad, Benchmark Plus). The standard plot was prepared, and the release profile of BMP's was obtained by comparing it with the standard plot.

2.2.8. WST-1 assay

WST-1 assay (Roche, IN) has been used to study the cell viability and proliferation of both monoculture and co-culture of cells in 3D scaffolds. The WST-1 assay was performed in single block scaffolds and multi-block sandwich scaffolds seeded with MSCs and human hFOBs(1:1). The WST-1 assay was used to perform cell viability as per the manufacturer's protocol. Briefly, cells were cultured on scaffolds/ scaffold blocks for 3, 5, and 7 days. Following this, cell-seeded scaffolds/ scaffold blocks were removed from the culture medium, washed with PBS and then

placed in a new 24-well plate with a solution comprising of 450 ul of DMEM and 50 ul of WST-1 reagent per well, and then incubated for 4 hours in standard humidified condition. After 4 hours, scaffolds were removed from the 24-well plates and the intensity of yellow color, which directly represents the number of live cells (slightly red-colored solution turns yellow as metabolically active cells cleave the tetrazolium salts of WST-1 reagent to formazan), was quantitatively measured at 450 nm using a microplate spectrophotometer (Bio-Rad, Benchmark Plus).

2.2.9. Alkaline phosphate assay

PCL/in situ HAPclay single block scaffolds and multi-block sandwich scaffolds blocks seeded with MSCs and hFOBs were incubated at 37°C, 5% CO_2 under humidified conditions for 3, 5 and 7 days. These samples were washed with PBS after incubation and transferred to wells of 24-well plates, and 850mL Triton X-100 (1 v/v % solution) was added to each well. Cell lysates (250mL) obtained after subjecting the immersed samples to two freeze-thaw cycles (27^{0}C to 37^{0}C) were transferred to new 24-well plates and incubated with p-nitrophenyl phosphate (250uL) at room temperature for 60 min. 3N NaOH (70mL) was further added to the wells, and absorbance readings were taken at 405 nm using a microplate spectrophotometer (Bio-Rad, Benchmark Plus).

2.2.10. Alizarin red staining

PCL/in situ HAPclay single block scaffolds and multi-block sandwich scaffolds blocks seeded with hFOBs were incubated at 37°C, 5% CO_2 under humidified conditions for 3, 5, and 7 days and then washed with PBS before fixing with 2.5% glutaraldehyde overnight. PBS was further used to wash the fixed samples. Further, the samples were stained with Alizarin Red S dye (2 g/100 mL deionized water and pH 4.15). After washing stained samples with cell culture grade water, in order to remove excess dye, images were captured using a confocal microscope.

2.2.11. Immunocytochemistry assay

PCL/in situ HAPclay scaffold blocks seeded with hFOBs and human MSCs were incubated at 37°C, 5% CO_2 under humidified conditions for 3, 5, and 7 days. The samples were washed with PBS, fixed using paraformaldehyde for 10 minutes, then again washed with PBS. The PBS washed sample was kept in bovine serum albumin (BSA), followed by adding collagen-specific primary antibody. This was followed by washing the sample with PBS and the secondary antibody for 45 minutes. After washing with PBS, the sample was stained with 4′,6-diamidino-2-phenylindole (DAPI), a fluorescent stain that binds strongly to adenine–thymine rich regions in DNA and thus commonly used for staining nuclei for imaging. As DAPI can pass through an intact cell membrane, it can be used to stain both live and fixed cells, but it passes through the membrane-less efficiently in live cells, and therefore the effectiveness of the stain is reduced significantly for dead cells. The images were captured using a confocal microscope.

2.2.12. Fourier Transform Infrared Spectroscopy (FTIR)

Initially, 5×10^4 osteoblast cells and 5×10^4 MSCs were seeded on each scaffold. On the second day, a scaffold sandwich was prepared by placing one scaffold on top of another scaffold. Uncoated scaffolds were used as control throughout the experiment. At day three, five, and seven, cells seeded scaffolds were washed with PBS, and the cells from the interface were collected using the cell scraper. Harvested cells were seeded on the ZnSe window and maintained for 24 hours. A ZnSe window (range of 7400-650 cm^{-1}) with attached cells was washed using PBS and kept in 4% paraformaldehyde for 10 minutes, followed by washing with PBS. The FTIR experiments were conducted using a NEXUS TM 870 FTIR spectrometer from Nicolet. We used a KBr beam splitter and acquired spectra at a resolution of 4 cm^{-1} in the transmission mode.

2.2.13. Scanning electron microscopy

SEM imaging was used to study the morphology of the cells at interfaces in a two-block scaffold. The PCL/in situ HAPclay scaffolds/ scaffold blocks seeded with hFOBs and MSCs and scaffold sandwiches were incubated at 37°C, 5% CO_2 under humidified conditions for 3, 5 and 7 days. The samples were washed with PBS, fixed using glutaraldehyde (2.5%), and subsequently dehydrated using ethanol series (10% v/v, 30% v/v,50% v/v, 70% v/v, and 100%) followed by drying with hexamethyldisilazane. Following this, the scaffold blocks were taken apart, coated with a conducting coating of Au-Pd and the interface between the blocks was imaged using the SEM.

2.2.14. Mechanical properties

Compressive mechanical properties of cylindrical scaffold samples (~ 13 mm diameter and 12 mm length) and interlock scaffold assembly (~ 13 mm diameter and 12 mm length) were determined using EZ-X Series Universal Electromechanical Test Frames (Shimadzu, EZ-LX HS). A constant deformation rate of 1 mm/min was applied for up to 10% strain in each test sample. Following this, the load and corresponding displacement data were recorded. Triplicate sample sets were used for this experiment. The slope of the initial linear region of the stress-strain curve was used for calculating the compressive elastic moduli of scaffold samples.

2.2.15. Statistical analysis

For conducting statistical analysis, two-way ANOVA followed by Tukey's post hoc multiple comparison test was used. Data were considered significantly different when probability values obtained were less than 0.05 ($P < 0.05$). Quantitative data were expressed as a mean ± standard deviation. Triplicate samples were used for performing all the experiments.

2.3. Results and discussion

2.3.1. Release kinetics of BMP's

Fig. 2.2 represents the percentage of cumulative content of released BMP's over time from the scaffold. We have observed an initial burst of release in the first 24 hours; about 46% of BMP's release occurred in the first 24 hours. Then a slower released was observed. After 72 hours, about 60% of BMP's release was observed from the scaffold.
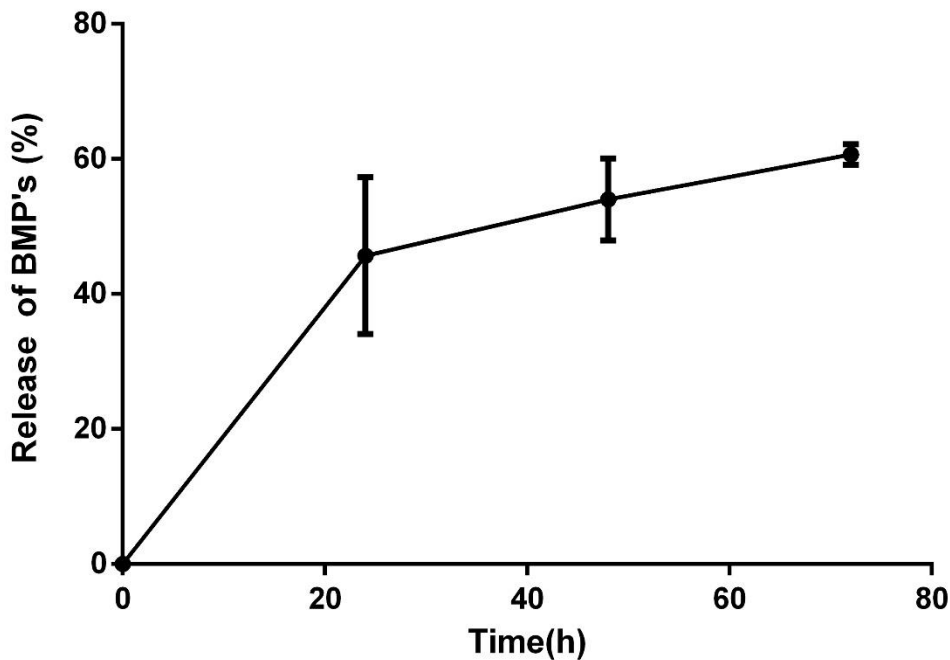
Fig. 2.2. Cumulative Percentage release of BMP's overtime from the scaffold in PBS.

2.3.2. Cell viability in interlocked blocks

The WST-1 assay was performed to evaluate cell viability and proliferation of both MSCs and hFOBs on the scaffold constructs. Initially, we compared cell growth and viability of monoculture (only MSCs) system at days 3, 5, and 7 on the single block (Fig. 2.3A). The highest cell growth was observed at day seven on the single block with the combination of BMP-2 and BMP-7. Further, we compared cell growth and viability of co-culture (MSCs and hFOBs) system at days 3, 5, and 7 on a single block (Fig. 2.3B). We have observed an increase in cell viability

over time. The highest cell growth was observed at day seven on the single block with the combination of BMP-2 and BMP-7. We also compared the effect of co-culture (Fig. 2.3C). We observed a significant increase in cell viability and proliferation with co-culture. Additionally, we compared cell growth and viability of the co-culture system at days 3, 5, and 7 on two-block, four-block, and an eight-block sandwich (Fig. 2.3D). We observed that the increase in the number of blocks did not affect cell viability and proliferation. We also compared the cell growth and viability of the co-culture system at days 3, 5 and 7 on equal volume cylindrical scaffold without any growth factors, the cylindrical scaffold with growth factors and interlock blocks with growth factors (Fig. 2.3E). We observed a significant increase in cell viability and proliferation with interlock blocks with or without growth factors as compared to that of the cylindrical scaffold with similar cell seeding density. As all of the compared samples have equal volume, the surface area plays an important role in improving cell viability and proliferation. Overall, the interlock designed scaffold block has significantly improved cell viability which is further enhanced with the use of BMP coatings.
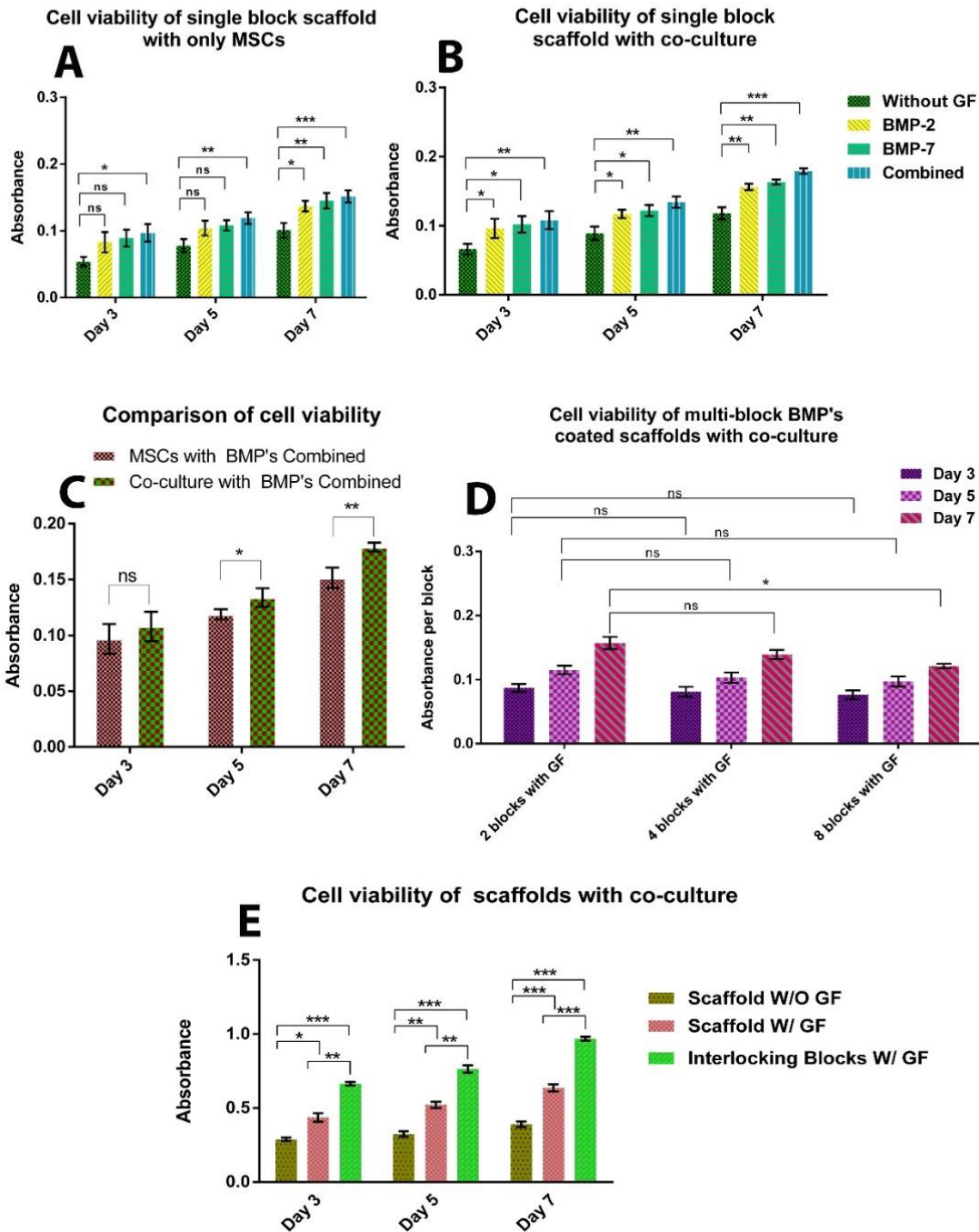
Fig. 2.3. A) Cell viability of single scaffold block seeded with MSCs. B) Cell viability of single scaffold block seeded with MSCs and osteoblast cells. C) Comparison of cell viability of scaffold seeded with only MSCs and co-culture. D) Comparison of cell viability of multi-block scaffolds seeded with MSCs and osteoblast cells and coated with BMPs. E) Comparison of cell viability in equal volume of interlocking scaffolds assembly with cylindrical scaffold. (Two way anova followed by post hoc tukey test p* < 0.05, p* *< 0.01, p*** <0.001, n = 3.)

2.3.3. Osteogenic differentiation of MSCs

Osteogenic differentiation of MSCs was assessed using alkaline phosphatase (ALP) assay, as ALP is an osteogenic marker[71]. At first, we performed ALP assay on MSCs seeded single block scaffolds system at days 3, 5, and 7 (Fig. 2.4A). We observed a significant increase in ALP levels at day seven compared to day three and day 5 with the combination of BMP-2 and BMP-7. We also compared the ALP activity of co-culture (MSCs and hFOBs) at days 3, 5 and 7 on a single block (Fig. 2.4B). We observed an increase in ALP activity over time. The highest ALP activity was observed on day seven on the single block with the combination of BMP-2 and BMP-7. We also compared the effect of co-culture (Fig. 2.4C) on the ALP activity. Intracellular ALP levels were found to increase when MSCs were co-cultured with hFOBs, suggesting that osteoblasts influenced osteogenesis in MSCs. It has been reported in the literature that osteoblast cells induce osteoblastic differentiation of MSCs[72]. Further, we compared the ALP activity of the co-culture system at days 3, 5, and 7 on two-block, four-block, and an eight-block sandwich (Fig. 2.4D). We observed that an increase in the number of blocks has minimal effect on the ALP activity. The ALP activity of co-culture system at days 3, 5 and 7 on equal volume, cylindrical scaffold without any growth factors, cylindrical scaffold with growth factors and interlock blocks with growth factors (Fig. 2.4E) was also compared. We observed a significant increase in the ALP activity with interlock blocks compared with the cylindrical scaffold with similar cell seeding density. The presence of BMPs enhanced this characteristic. Hence it appears that interlocking mechanisms and their enabled large surface area enhanced the osteogenic differentiation of MSCs which was again additionally enhanced with the BMPs.
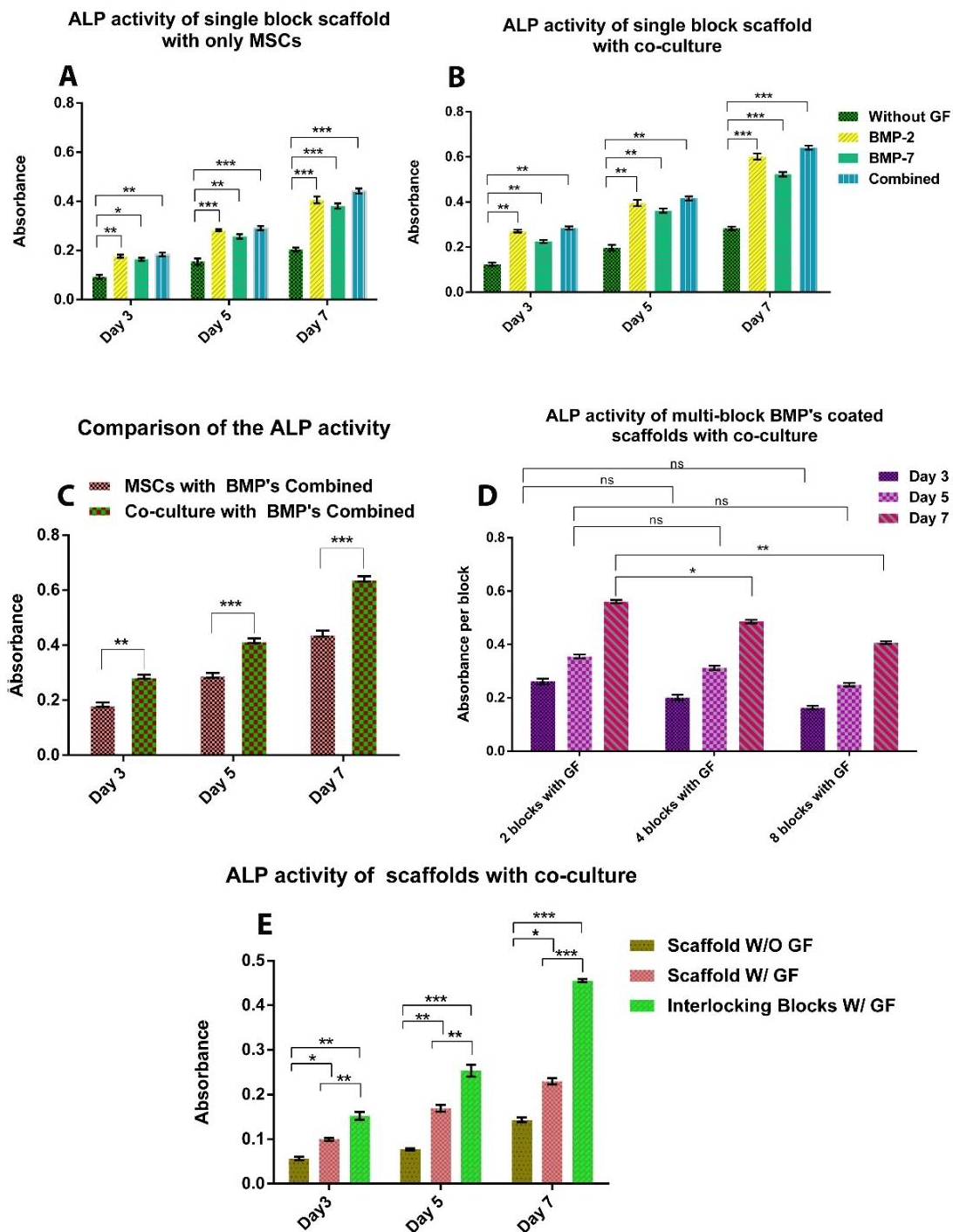
Fig. 2.4. A) ALP activity of single scaffold block seeded with MSCs. B) ALP activity of single scaffold block seeded with MSCs and osteoblast cells. C) Comparison of ALP activity of scaffold seeded with only MSCs and co-culture. D) Comparison of ALP activity of multi-block scaffolds seeded with MSCs and osteoblast cells and coated with BMPs. E) Comparison of ALP activity in equal volume of interlocking scaffolds assembly with cylindrical scaffold. (Two way anova followed by post hoc tukey test p* < 0.05, p* *< 0.01, p*** <0.001, n = 3.)

2.3.4. Bone mineralization

The Alizarin red S staining was performed to evaluate the formation of the mineralized extracellular matrix on the scaffolds. The formation of intense red color with Alizarin red S indicates the formation of the mineralized extracellular matrix (ECM) through interaction with the calcium of ECM. The formation of mineralized ECM on MSC seeded PCL/in-situ HAPclay composites has been reported previously[69]. First, we performed Alizarin red S staining assay on single block scaffolds system seeded with MSCs and hFOBs at days 3, 5, and 7 (Fig. 5I) to observe the effect of BMPs on ECM formation. We have observed that over time, ECM formation increased in every group of the scaffold. The least amount of ECM formation was observed with the scaffold block without any growth factor, and the maximum amount of ECM formation was found with the combination of BMP-2 and BMP-7. For the scaffold block without any growth factor, no ECM formation was observed at day 3. The addition of the BMPs resulted in a significant amount of ECM formation was seen at the same time scale of 3 days. The result suggests that BMP-2 and BMP-7 have a significant influence on the formation of ECM. We also observed the ECM formation on the interface of the 8-blocks scaffold sandwich coated with BMP-2 and BMP-7(Fig. 2.5II) and similarly at the 8-blocks scaffold seeded with MSCs and hFOBs. We also observed the ECM formation on 8-interlock blocks scaffold sandwich seeded with MSCs and hFOBs coated with BMP-2 & BMP-7(Fig. 2.5III). In all cases, ECM formation progressed from day 3 to 7.
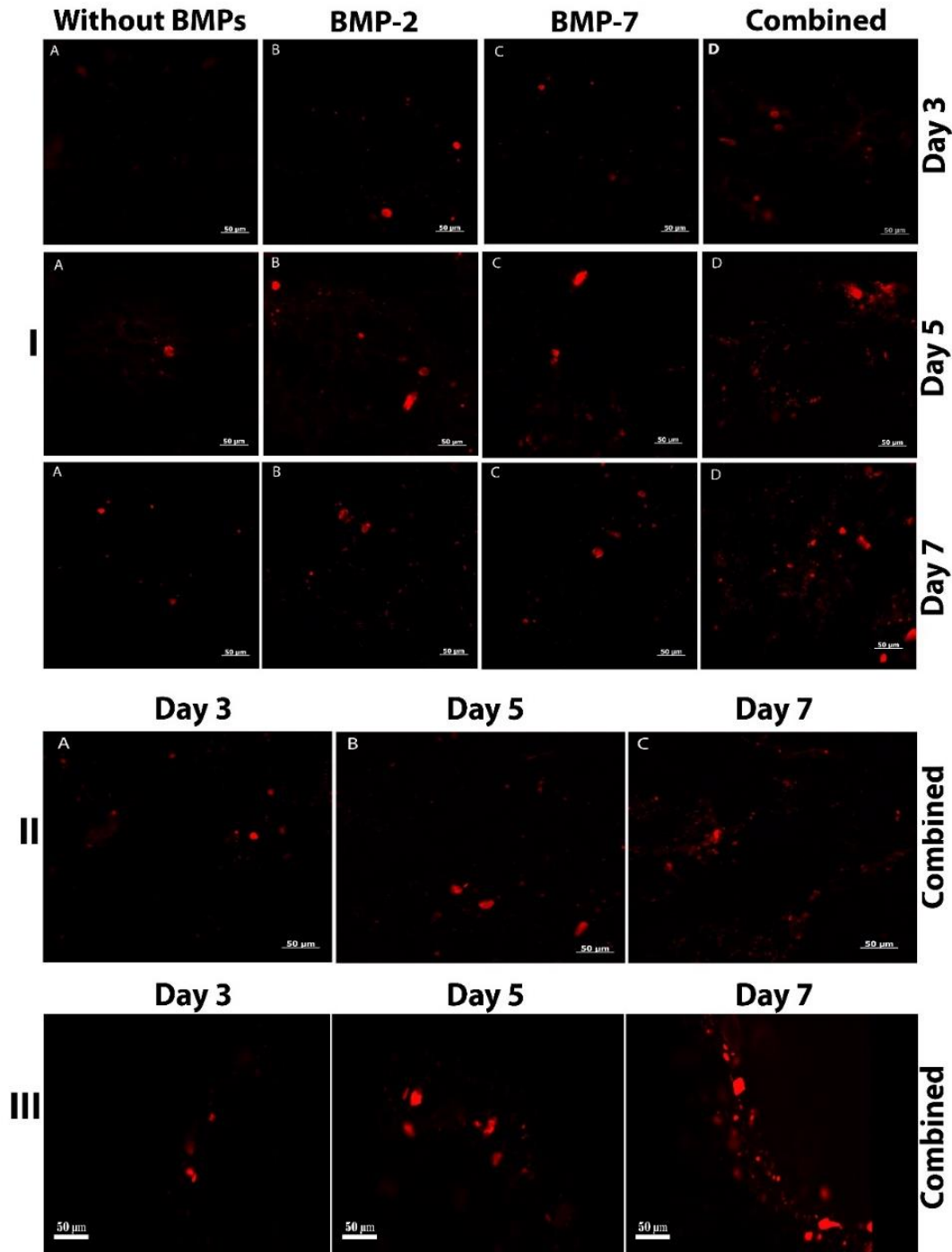
Fig. 2.5. I) Confocal microscope image of Alizarin Red S stained PCL/*in situ* HAPclay single block scaffolds. (A= scaffold block without any growth factor, B= scaffold block coated with BMP-2, C= scaffold block coated with BMP-7, D= scaffold block coated with BMP-2+ BMP-7). II) Confocal microscope image of Alizarin Red S stained PCL/*in situ* HAPclay 8-blocks scaffold coated with BMP-2 and 7 at the interface (A= at day 3, B= at day 5, C= at day 7). III) Confocal microscope image of Alizarin Red S stained PCL/*in situ* HAPclay interlock Scaffold blocks coated with BMP-2 and BMP-7 (A= at day 3, B= at day 5, C= at day 7)

2.3.5. Collagen and collagen fibril formation

An immunocytochemistry assay was performed to evaluate the formation of the collagen. During osteogenic differentiation, MSCs express collagen as an essential part of ECM[73]. We compared the effect of BMPs on single block scaffold seeded with MSCs and hFOBs on collagen formation at day 3, 5, 7, and 11 (Fig. 2.6). The intense staining of the fibril structure indicates the formation of the collagen. We observed that collagen formation increases over time. We did not observe any collagen formation before day five, but the fibril-like structure was observed at day 11 with BMPs coated scaffold. We did not observe significant collagen formation before day 11 on the sample without growth factor. These results suggest that BMPs have a vital role in the formation of collagen.
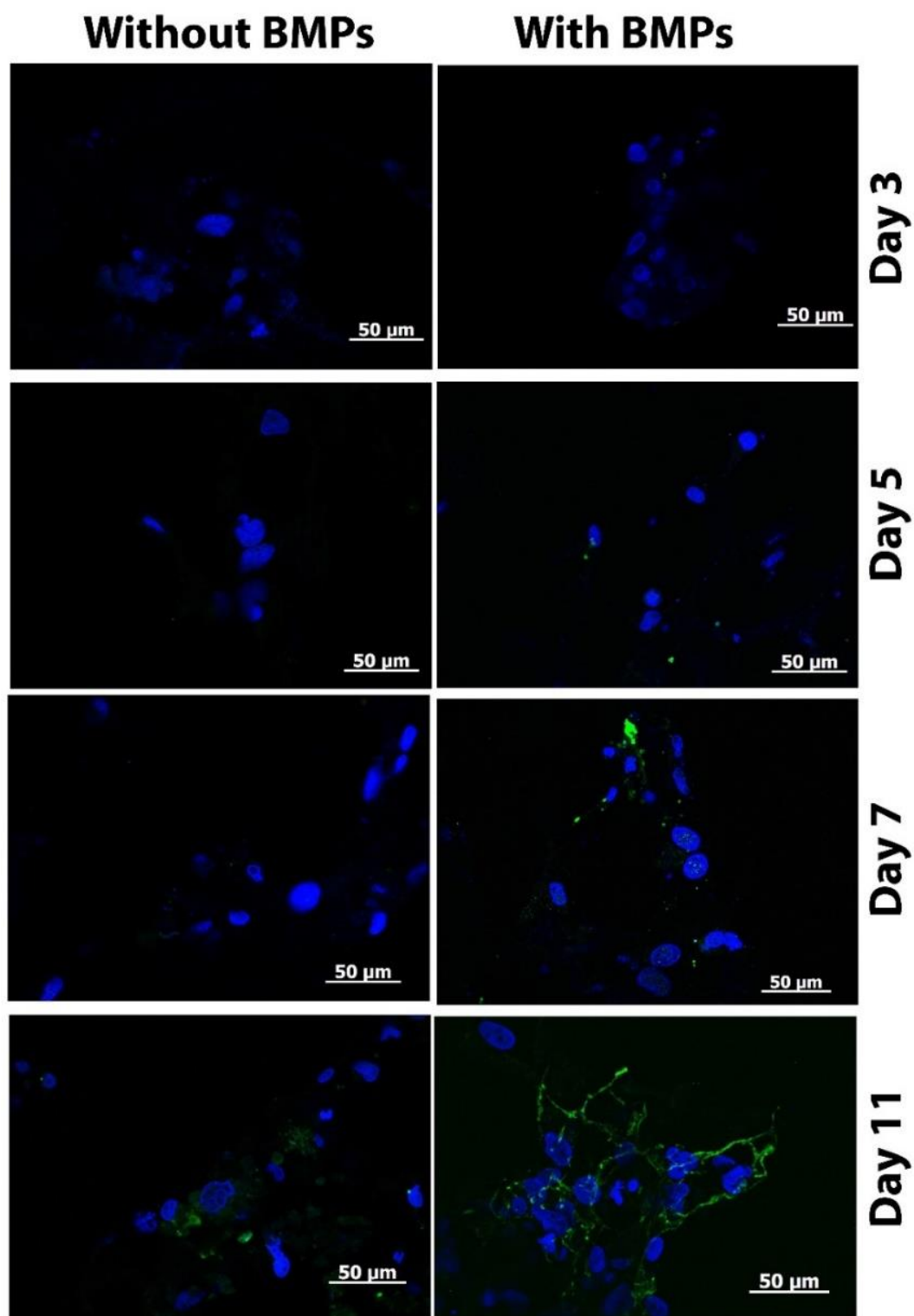
Fig. 2.6. Confocal microscope image of PCL/in situ HAPclay single blocks scaffold. Nuclei were stained with DAPI. Anti-Rabbit Col-1 primary antibody was used with Goat anti-rabbit IgG (H+L) AF 488 (green) secondary antibody.

2.3.6. Molecular changes to phosphate in bone mineral

The main constituents of the cell are membrane lipids and phospholipids, glycolipids, proteins, glycoproteins, phosphoproteins, nucleic acids DNA and RNA, carbohydrates, and small metabolites that are all IR active[74]. Table 2.1 summarizes the band wavenumber and their assignments observed in the FTIR analysis. We compared the effect of BMPs on the two-block scaffold sandwich seeded with MSCs and hFOBs at day 3, 5, 7. FTIR spectra (Fig. 2.7A-C) reveal the presence of DNA, proteins, lipids, and fatty acids. FTIR bands in the region of 1700 cm^{-1} to 900 cm^{-1} arise from C=O, CH_2, CH_3, C-O-C, and O-P-O, phosphodiester stretching bands region for absorbances due to C-C and C-O in deoxyribose of DNA, and the ribose of the RNA, groups or linkages, belonging to phospholipids, proteins, carbohydrates, and amino acids [75-78]. Overall no significant shifts were observed in the characteristic bands in the spectra between BMP coated and uncoated samples. At day 5 and 7(Fig. 2.7A and B), changes to the intensity of the phosphate band were observed that were particularly pronounced at day 7 (Fig. 2.7C). Overall, the results reveal that coating with BMPs results in increasing the intensity of the phosphate band. Osteogenic differentiation is enhanced through BMP treatment [79] and thus increase in phosphate intensity.

Table 2.1. Assignments of vibrational modes observed in the FTIR spectra of co-culture of MSCs and hFOBs cells with and without BMP's.

Band position (cm^{-1})	Band assignment [74-79]
3285-3291	N-H stretch
2954-2957	CH$_3$ asymmetric stretch
2924	CH$_2$ asymmetric stretch
2853-2854	CH$_2$ symmetric stretch
1735	C=O stretch
1652-1653	Amide I
1539-1541	Amide II
1449-1456	CH$_2$, CH$_3$ deformation modes
1396-1400	COO– symmetric stretch
1235-1242	PO2− asymmetric stretch
1085-1092	PO$_2^-$ symmetric stretch
968-972	PO$_2^-$ symmetric stretch
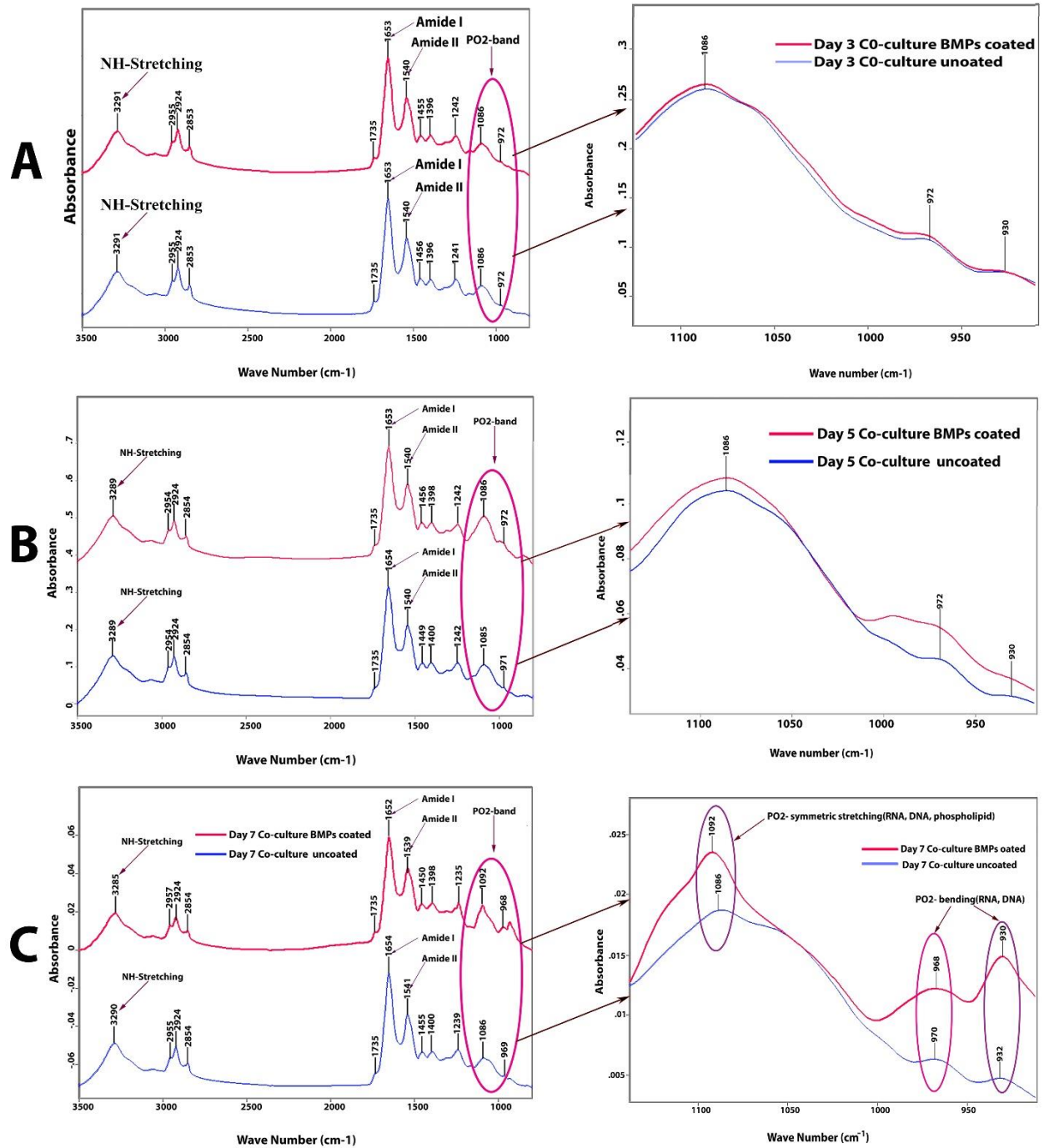
Fig. 2.7.A) FTIR spectra of Osteoblasts and MSCs co-culture at day 3. B) FTIR spectra of Osteoblasts and MSCs co-culture at day 5. C) FTIR spectra of Osteoblasts and MSCs co-culture at day 7.

2.3.7. Block interface cell morphology

In order to investigate the morphology of cells at the interface upon culturing on two-block sandwich PCL/in situ HAPclay scaffolds, SEM imaging was performed. Figure 8A shows the SEM images of the cell-seeded (MSCs and hFOBs) PCL/in situ HAPclay scaffold interface after seven days. As seen, cells aggregate and adhere to the surface of the scaffolds. After seven days, cells spread, and a flattened morphology is observed, suggesting good anchoring to the scaffold (Fig. 2.8).
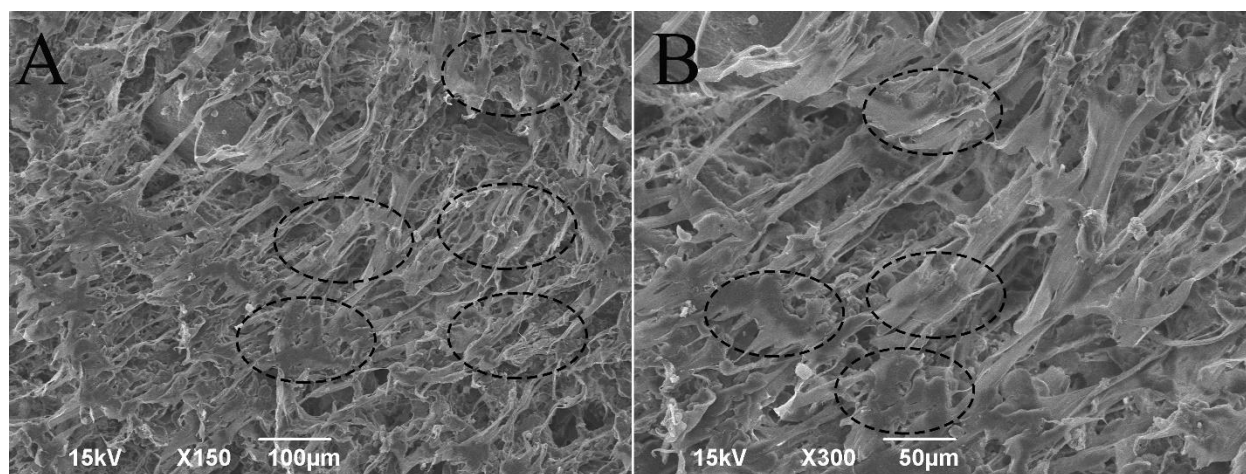
Fig. 2.8. SEM micrographs of 2-block scaffold system at day 7 (Black circles/ellipses represent cells).

2.3.8. Mechanical properties of interlocked assemblies

Compression tests were performed to investigate the change in elastic modulus of the interlock scaffold assembly as compared with the cylindrical scaffold. Fig. 2.9A shows the comparative stress-strain plot of cylindrical scaffold and interlock scaffold, indicating that they are quite similar. Fig. 2.9. shows a comparative plot of elastic moduli of cylindrical scaffold and interlock scaffold. We have found that change in the modulus is not significant between the two. This indicates that the interlocking mechanisms are able to maintain the mechanical integrity of the scaffold. The ease of assembly, followed by enhanced cellular growth, ECM, and bone

formation, is not followed by compromised mechanical behavior with the use of interlock assembly.
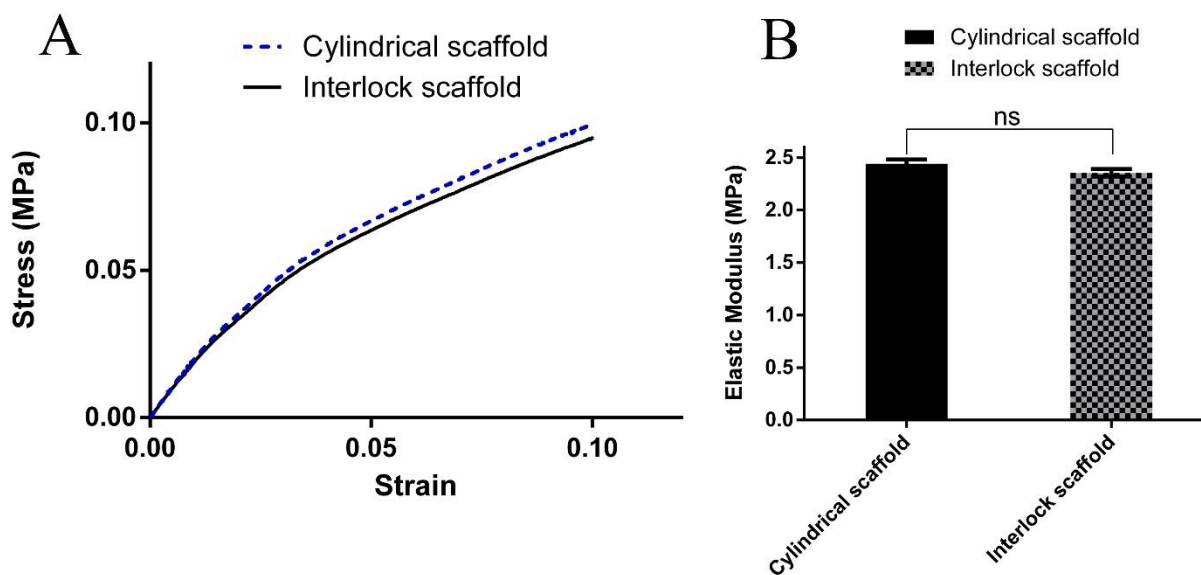
Fig. 2.9. Compressive mechanical properties: A) Representative stress-strain curves obtained for cylindrical scaffold and interlocking scaffolds assembly. B) Compressive elastic moduli of cylindrical scaffold and interlocking scaffolds assembly.

2.4. Conclusions

We report the design of a mechanically stable interlock scaffold that can fill large bone defects. These interlocking assemblies are made using blocks that offer ease of assembly and potential for achieving a myriad of shapes. Bone mineralization on large cylindrical scaffolds is often a process that takes over twenty days[43, 80], and hence the applicability of tissue-engineered scaffolds for nonunion defects remains limited for practical applications. Calcium deposition, the first indicator of initiation of bone mineralization followed by subsequent ECM formation and mineralized fibril structures, is initiated at day 3 in the block systems with additional help from the BMP-2 and BMP-7 coating. The addition of BMP-2 and BMP-7 was found to aid cell viability on scaffold interlocking-blocks. Also, the number of viable cells in scaffold interlocking-blocks with BMP-2 and BMP-7 was higher than the scaffold without any growth factor. Further, the

intracellular ALP levels increased with interlocking blocks coated with BMPs indicating enhanced the osteogenic differentiation of MSCs. An immunocytochemistry assay was also performed to evaluate the formation of the collagen in the scaffold. BMPs coated co-culture scaffold constructs showed fiber-like collagen formation as opposed to control. Changes to the phosphate vibration are observed in the FTIR spectra, suggesting increased ECM formation in the BMPs coated scaffolds arising from improved osteogenic differentiation. The improved cell growth, initiation of mineralization and an effective reduction in time duration of bone growth in defects from over twenty days to less than five days is enabled with use of a unique interlocking scaffold system that is made up of small blocks that fit in XY and Z planes to fill any shape of a non union defect. These interlocking blocks assemble into a structure for which the mechanical integrity of a single scaffold is maintained. Thus a novel scaffold interlocking-block BMP coated scaffold system is presented for accelerated bone growth with co-culture of MSCs and osteoblast cells.

2.5. Acknowledgments

2.6. References

[1]   R. Agarwal, A.J. García, Biomaterial strategies for engineering implants for enhanced osseointegration and bone repair, Advanced drug delivery reviews 94 (2015) 53-62.

[2]   A. Lee, Osteoporosis Education: An Insight into Risk Factors & Prevention, (2018).

[3]   H. Shegarfi, O. Reikeras, Bone transplantation and immune response, Journal of
        Orthopaedic Surgery 17(2) (2009) 206-211.

[4]   O. Ashman, A.M. Phillips, Treatment of non-unions with bone defects: Which option and
        why?, Injury-International Journal of the Care of the Injured 44 (2013) S43-S45.

[5]   J.F. Keating, A. Simpson, C.M. Robinson, The management of fractures with bone loss,
        Journal of Bone and Joint Surgery-British Volume 87B(2) (2005) 142-150.

[6]   Z. Gugala, S. Gogolewski, Regeneration of segmental diaphyseal defects in sheep tibiae
        using resorbable polymeric membranes: A preliminary study, Journal of Orthopaedic
        Trauma 13(3) (1999) 187-195.

[7]   A. Nauth, M.D. McKee, T.A. Einhorn, J.T. Watson, R. Li, E.H. Schemitsch, Managing
        Bone Defects, Journal of Orthopaedic Trauma 25(8) (2011) 462-466.

[8]   S. Zwingenberger, C. Nich, R.D. Valladares, Z. Yao, M. Stiehler, S.B. Goodman,
        Recommendations and considerations for the use of biologics in orthopedic surgery,
        BioDrugs 26(4) (2012) 245-256.

[9]   P.S. Eggli, W. Müller, R.K. Schenk, Porous hydroxyapatite and tricalcium phosphate
        cylinders with two different pore size ranges implanted in the cancellous bone of rabbits.
        A comparative histomorphometric and histologic study of bony ingrowth and implant
        substitution, Clinical orthopaedics and related research (232) (1988) 127-138.

[10]   J.C. Le Huec, T. Schaeverbeke, D. Clement, J. Faber, A. Le Rebeller, Influence of
        porosity on the mechanical resistance of hydroxyapatite ceramics under compressive
        stress, Biomaterials 16(2) (1995) 113-118.

[11]   S. Wenisch, J.P. Stahl, U. Horas, C. Heiss, O. Kilian, K. Trinkaus, A. Hild, R. Schnettler, In vivo mechanisms of hydroxyapatite ceramic degradation by osteoclasts: fine structural microscopy, Journal of Biomedical Materials Research Part A: An Official Journal of The Society for Biomaterials, The Japanese Society for Biomaterials, and The Australian Society for Biomaterials and the Korean Society for Biomaterials 67(3) (2003) 713-718.

[12]   J.S. Carson, M.P.G. Bostrom, Synthetic bone scaffolds and fracture repair, Injury 38(1) (2007) S33-S37.

[13]   A.G. Mikos, S.W. Herring, P. Ochareon, J. Elisseeff, H.H. Lu, R. Kandel, F.J. Schoen, M. Toner, D. Mooney, A. Atala, Engineering complex tissues, Tissue engineering 12(12) (2006) 3307-3339.

[14]   E.A.A. Neel, W. Chrzanowski, V.M. Salih, H.-W. Kim, J.C. Knowles, Tissue engineering in dentistry, Journal of dentistry 42(8) (2014) 915-928.

[15]   G. Bouët, D. Marchat, M. Cruel, L. Malaval, L. Vico, In vitro three-dimensional bone tissue models: from cells to controlled and dynamic environment, Tissue Engineering Part B: Reviews 21(1) (2014) 133-156.

[16]   J. Henkel, M.A. Woodruff, D.R. Epari, R. Steck, V. Glatt, I.C. Dickinson, P.F.M. Choong, M.A. Schuetz, D.W. Hutmacher, Bone regeneration based on tissue engineering conceptions—a 21st century perspective, Bone research 1 (2013) 216.

[17]   R. Langer, J.P. Vacanti, TISSUE ENGINEERING, Science 260(5110) (1993) 920-926.

[18]   J.D. Currey, THE EFFECT OF POROSITY AND MINERAL-CONTENT ON THE YOUNGS MODULUS OF ELASTICITY OF COMPACT-BONE, Journal of Biomechanics 21(2) (1988) 131-139.

[19]   J.D. Currey, Materials science - Hierarchies in biomineral structures, Science 309(5732)
       (2005) 253-254.

[20]   J.D. Currey, The structure and mechanics of bone, Journal of Materials Science 47(1)
       (2012) 41-54.

[21]   S. Weiner, W. Traub, Bone structure: from angstroms to microns, The FASEB journal
       official publication of the Federation of American Societies for Experimental Biology 6(3)
       (1992) 879-85.

[22]   S.M. Pradhan, K.S. Katti, D.R. Katti, Multiscale Modeling of Collagen Fibril in Bone at
       Various Crosslink Densities: An Insight into Its Deformation Mechanisms, Cmes-
       Computer Modeling in Engineering & Sciences 98(2) (2014) 181-201.

[23]   S.M. Pradhan, K.S. Katti, D.R. Katti, Structural Hierarchy Controls Deformation Behavior
       of Collagen, Biomacromolecules 13(8) (2012) 2562-2569.

[24]   S. Pradhan, D. Katti, K. Katti, Steered Molecular Dynamics Study of Mechanical
       Response of Full Length and Short Collagen Molecules, Journal of Nanomechanics and
       Micromechanics 1(3) (2011) 104-110.

[25]   V. Karageorgiou, D. Kaplan, Porosity of 3D biomaterial scaffolds and osteogenesis,
       Biomaterials 26 (2005) 5474-5491.

[26]   H.D. W, Scaffolds in tissue engineering bone and cartilage, 21(24) (2000) 2529.

[27]   M.P. Ginebra, T. Traykova, J.A. Planell, Calcium phosphate cements as bone drug
       delivery systems: A review, Journal of Controlled Release 113(2) (2006) 102-110.

[28]   L.L. Hench, J.M. Polak, Third-generation biomedical materials, Science 295(5557) (2002)
       1014+1016-1017.

[29]   T.W. Bauer, R.C.T. Geesink, R. Zimmerman, J.T. McMahon, Hydroxyapatite-coated femoral stems. Histological analysis of components retrieved at autopsy, Journal of Bone and Joint Surgery - Series A 73(10) (1991) 1439-1452.

[30]   G.E. Poinern, R.K. Brundavanam, N. Mondinos, Z.T. Jiang, Synthesis and characterisation of nanohydroxyapatite using an ultrasound assisted method, Ultrasonics Sonochemistry 16(4) (2009) 469-474.

[31]   R.Z. Lê Geros, Elsevier Scientific Direct 14 (1993) 65-88.

[32]   S.V. Dorozhkin, Calcium orthophosphate-based biocomposites and hybrid biomaterials, Journal of Materials Science 44(9) (2009) 2343-2387.

[33]   S.V. Dorozhkin, Calcium orthophosphate cements for biomedical application, Journal of Materials Science 43(9) (2008) 3028-3057.

[34]   M.P. Ginebra, M. Espanol, E.B. Montufar, R.A. Perez, G. Mestres, New processing approaches in calcium phosphate cements and their applications in regenerative medicine, Acta Biomaterialia 6(8) (2010) 2863-2873.

[35]   M. Bohner, Design of ceramic-based cements and putties for bone graft substitution, European Cells and Materials 20 (2010) 1-12.

[36]   A.J.W. Johnson, B.A. Herschler, Acta Biomater. 7 (2011) 16-30.

[37]   S.I. Stupp, G.W. Ciegler, Organoapatites: Materials for artificial bone. I. Synthesis and microstructure, Journal of Biomedical Materials Research 26(2) (1992) 169-183.

[38]   E.P. Giannelis, Polymer layered silicate nanocomposites, Advanced Materials 8(1) (1996) 29-&.

[39]   S.S. Ray, M. Okamoto, Polymer/layered silicate nanocomposites: a review from preparation to processing, Progress in Polymer Science 28(11) (2003) 1539-1641.

[40]   D. Depan, A.P. Kumar, R.P. Singh, Cell proliferation and controlled drug release studies of nanohybrids based on chitosan-g-lactic acid and montmorillonite, Acta Biomaterialia 5(1) (2009) 93-100.

[41]   K.S. Katti, D.R. Katti, R. Dash, Synthesis and characterization of a novel chitosan/montmorillonite/hydroxyapatite nanocomposite for bone tissue engineering, Biomedical Materials 3(3) (2008) 12.

[42]   A.J. Mieszawska, J.G. Llamas, C.A. Vaiana, M.P. Kadakia, R.R. Naik, D.L. Kaplan, Clay enriched silk biomaterials for bone formation, Acta Biomaterialia 7(8) (2011) 3036-3041.

[43]   A.H. Ambre, D.R. Katti, K.S. Katti, Nanoclays mediate stem cell differentiation and mineralized ECM formation on biopolymer scaffolds, Journal of Biomedical Materials Research Part A 101(9) (2013) 2644-2660.

[44]   A.K. Gaharwar, S.M. Mihaila, A. Swami, A. Patel, S. Sant, R.L. Reis, A.P. Marques, M.E. Gomes, A. Khademhosseini, Bioactive Silicate Nanoplatelets for Osteogenic Differentiation of Human Mesenchymal Stem Cells, Advanced Materials 25(24) (2013) 3329-3336.

[45]   M.A. Woodruff, D.W. Hutmacher, The return of a forgotten polymer-Polycaprolactone in the 21st century, Progress in Polymer Science 35(10) (2010) 1217-1256.

[46]   K.S. Katti, A.H. Ambre, N. Peterka, D.R. Katti, Use of unnatural amino acids for design of novel organomodified clays as components of nanocomposite biomaterials, Philosophical Transactions of the Royal Society a-Mathematical Physical and Engineering Sciences 368(1917) (2010) 1963-1980.

[47] A.H. Ambre, Nanoclay Based Composite Scaffolds For Bone Tissue Engineering Applications, Journal of Nanotechnology for Engineering and Medicine, ASME, 2010, p. 031013.

[48] A. Ambre, K.S. Katti, D.R. Katti, In situ mineralized hydroxyapatite on amino acid modified nanoclays as novel bone biomaterials, Materials Science & Engineering C-Materials for Biological Applications 31(5) (2011) 1017-1029.

[49] Y.F. Shi, G.Z. Hu, J.J. Su, W.Z. Li, Q. Chen, P.S. Shou, C.L. Xu, X.D. Chen, Y. Huang, Z.X. Zhu, X. Huang, X.Y. Han, N.X. Xie, G.W. Ren, Mesenchymal stem cells: a new strategy for immunosuppression and tissue repair, Cell Research 20(5) (2010) 510-518.

[50] L.C. Gerstenfeld, J. Cruceta, C.M. Shea, K. Sampath, G.L. Barnes, T.A. Einhorn, Chondrocytes provide morphogenic signals that selectively induce osteogenic differentiation of mesenchymal stem cells, Journal of Bone and Mineral Research 17(2) (2002) 221-230.

[51] J.M. Dayer, P. Isler, L.P. Nicod, ADHESION MOLECULES AND CYTOKINE PRODUCTION, American Review of Respiratory Disease 148(6) (1993) S70-S74.

[52] R. Civitelli, CELL-CELL COMMUNICATION IN BONE, Calcified Tissue International 56 (1995) S29-S31.

[53] D. Chen, M. Zhao, G.R. Mundy, Bone morphogenetic proteins, Growth Factors 22(4) (2004) 233-241.

[54] M.R. Urist, Bone: Formation by Autoinduction, Science 150(3698) (1965) 893.

[55] U.A. Stock, J.P. Vacanti, Tissue engineering: Current state and prospects, Annual Review of Medicine 52 (2001) 443-451.

[56] E. Kessler, K. Takahara, L. Biniaminov, M. Brusel, D.S. Greenspan, Bone Morphogenetic Protein-1: The Type I Procollagen C-Proteinase, Science 271(5247) (1996) 360.

[57] J.M. Wozney, V. Rosen, A.J. Celeste, L.M. Mitsock, M.J. Whitters, R.W. Kriz, R.M. Hewick, E.A. Wang, NOVEL REGULATORS OF BONE-FORMATION - MOLECULAR CLONES AND ACTIVITIES, Science 242(4885) (1988) 1528-1534.

[58] S.N. Lissenberg-Thunnissen, D.J.J. de Gorter, C.F.M. Sier, I.B. Schipper, Use and efficacy of bone morphogenetic proteins in fracture healing, International Orthopaedics 35(9) (2011) 1271-1280.

[59] J.Z. Li, H. Li, T. Sasaki, D. Holman, B. Beres, R.J. Dumont, D.D. Pittman, G.R. Hankins, G.A. Helm, Osteogenic potential of five different recombinant human bone morphogenetic protein adenoviral vectors in the rat, Gene Therapy 10(20) (2003) 1735-1743.

[60] K.S. Lee, H.J. Kim, Q.L. Li, X.Z. Chi, C. Ueta, T. Komori, J.M. Wozney, E.G. Kim, J.Y. Choi, H.M. Ryoo, S.C. Bae, Runx2 is a common target of transforming growth factor beta 1 and bone morphogenetic protein 2, and cooperation between Runx2 and Smad5 induces osteoblast-specific gene expression in the pluripotent mesenchymal precursor cell line C2C12, Molecular and Cellular Biology 20(23) (2000) 8783-8792.

[61] A.H. Reddi, Role of morphogenetic proteins in skeletal tissue engineering and regeneration, Nature Biotechnology 16(3) (1998) 247-252.

[62] M. Kretzschmar, J. Massague, SMADs: mediators and regulators of TGF-beta signaling, Current Opinion in Genetics & Development 8(1) (1998) 103-111.

[63] B. Bragdon, O. Moseychuk, S. Saldanha, D. King, J. Julian, A. Nohe, Bone morphogenetic proteins: a critical review, Cellular signalling 23(4) (2011) 609-620.

[64]   K. Shahlaie, K.D. Kim, Occipitocervical fusion using recombinant human bone morphogenetic protein-2: adverse effects due to tissue swelling and seroma, Spine 33(21) (2008) 2361-2366.

[65]   J. Fan, J. Pi-Anfruns, M. Guo, D.C.S. Im, Z.-K. Cui, S. Kim, B.M. Wu, T.L. Aghaloo, M. Lee, Small molecule-mediated tribbles homolog 3 promotes bone formation induced by bone morphogenetic protein-2, Scientific reports 7(1) (2017) 7518.

[66]   Y. Peng, Q. Kang, H.W. Cheng, X.M. Li, M.H. Sun, W. Jiang, H.H. Luu, J.Y. Park, R.C. Haydon, T.C. He, Transcriptional characterization of bone morphogenetic proteins (BMPs)-mediated osteogenic signaling, Journal of Cellular Biochemistry 90(6) (2003) 1149-1165.

[67]   Q. Kang, W.X. Song, Q. Luo, N. Tang, J.Y. Luo, X.J. Luo, J. Chen, Y. Bi, B.C. He, J.K. Park, W. Jiang, Y. Tang, J.Y. Huang, Y.X. Su, G.H. Zhu, Y. He, H. Yin, Z.M. Hu, Y. Wang, L. Chen, G.W. Zuo, X.C. Pan, J.K. Shen, T. Vokes, R.R. Reid, R.C. Haydon, H.H. Luu, T.C. He, A Comprehensive Analysis of the Dual Roles of BMPs in Regulating Adipogenic and Osteogenic Differentiation of Mesenchymal Progenitor Cells, Stem Cells and Development 18(4) (2009) 545-U33.

[68]   Y. Takahashi, N. Ohoka, H. Hayashi, R. Sato, TRB3 suppresses adipocyte differentiation by negatively regulating PPARγ transcriptional activity, Journal of lipid research 49(4) (2008) 880-892.

[69]   A.H. Ambre, D.R. Katti, K.S. Katti, Biomineralized hydroxyapatite nanoclay composite scaffolds with polycaprolactone for stem cell-based bone tissue engineering, Journal of Biomedical Materials Research Part A 103(6) (2015) 2077-2101.

[70] D.R. Katti, A. Sharma, A.H. Ambre, K.S. Katti, Molecular interactions in biomineralized hydroxyapatite amino acid modified nanoclay: In silico design of bone biomaterials, Materials Science & Engineering C-Materials for Biological Applications 46 (2015) 207-217.

[71] Y. Gotoh, K. Hiraiwa, M. Nagayama, INVITRO MINERALIZATION OF OSTEOBLASTIC CELLS DERIVED FROM HUMAN BONE, Bone and Mineral 8(3) (1990) 239-250.

[72] L.D.K. Buttery, S. Bourne, J.D. Xynos, H. Wood, F.J. Hughes, S.P.F. Hughes, V. Episkopou, J.M. Polak, Differentiation of osteoblasts and in vitro bone formation from murine embryonic stem cells, Tissue Engineering 7(1) (2001) 89-99.

[73] C. Karlsson, C. Brantsing, T. Svensson, H. Brisby, J. Asp, T. Tallheden, A. Lindahl, Differentiation of human mesenchymal stem cells and articular chondrocytes: Analysis of chondrogenic potential and expression pattern of differentiation-related transcription factors, Journal of Orthopaedic Research 25(2) (2007) 152-163.

[74] G. Bellisola, C. Sorio, Infrared spectroscopy and microscopy in cancer research and diagnosis, American Journal of Cancer Research 2(1) (2012) 1-21.

[75] S. Rehman, Z. Movasaghi, J.A. Darr, I.U. Rehman, Fourier transform infrared spectroscopic analysis of breast cancer tissues; identifying differences between normal breast, invasive ductal carcinoma, and ductal carcinoma in situ of the breast, Applied Spectroscopy Reviews 45(5) (2010) 355-368.

[76] G.I. Dovbeshko, V.I. Chegel, N.Y. Gridina, O.P. Repnytska, Y.M. Shirshov, V.P. Tryndiak, I.M. Todor, G.I. Solyanik, Surface enhanced IR absorption of nucleic acids from tumor cells: FTIR reflectance study, Biopolymers 67(6) (2002) 470-486.

[77] G.I. Dovbeshko, N.Y. Gridina, E.B. Kruglova, O.P. Pashchuk, FTIR spectroscopy studies of nucleic acid damage, Talanta 53(1) (2000) 233-246.

[78] L. Chiriboga, P. Xie, H. Yee, V. Vigorita, D. Zarou, D. Zakim, M. Diem, Infrared spectroscopy of human tissue. I. Differentiation and maturation of epithelial cells in the human cervix, Biospectroscopy 4(1) (1998) 47-53.

[79] A.T. Mehlhorn, P. Niemeyer, K. Kaschte, L. Muller, G. Finkenzeller, D. Hartl, N.P. Sudkamp, H. Schmal, Differential effects of BMP-2 and TGF-β1 on chondrogenic differentiation of adipose derived stem cells, Cell proliferation 40(6) (2007) 809-823.

[80] K.S. Katti, A.H. Ambre, S. Payne, D.R. Katti, Vesicular delivery of crystalline calcium minerals to ECM in biomineralized nanoclay composites, Materials Research Express 2(4) (2015).

CHAPTER 3. INITIAL UPSURGE OF BMPS ENHANCES LONG-TERM OSTEOGENESIS IN *IN-VITRO* BONE REGENERATION

This chapter describes the mechanisms of the BMPs associated with bone tissue formation and the effect of BMPs on the nanomechanical properties of the newly formed tissue. The contents of this chapter have been published in Krishna Kundu, Sharad V. Jaswandkar, Dinesh R. Katti, and Kalpana S. Katti, "Initial upsurge of BMPs enhances long-term osteogenesis in in-vitro bone regeneration", Materialia 26 (2022) 101576.

3.1. Introduction

Bone is a highly vascularized and dynamic natural nanocomposite that is constantly remodeled throughout an individual's lifespan. Each year, more than four million bone grafting procedures are performed worldwide, making it the second most transplanted tissue after blood[1, 2]. In contrast to other tissues and organs, bone tissue usually has better self-healing ability. The damaged part can regain its original structure and mechanical strength without leaving fibrotic scars. However, when the range of bone defects exceeds the critical-size defect (CSD), bone defects cannot heal by themselves and require reasonable clinical intervention[3]. Large-sized bone defects can be caused by trauma, developmental deformity, tumor resection, and infection, which are common issues in clinical treatment[4].

Bone regeneration is a complex process involving various growth factors, including bone morphogenetic proteins (BMPs), vascular endothelial growth factor (VEGF), insulin-like growth factor (IGF), and a few others[5]. Among these, BMPs are the most important osteogenic growth factors shown to induce bone formation by inducing mesenchymal stem cells (MSCs) toward osteoblastic differentiation[6]. The BMPs are multi-functional growth factors that play a vital role in embryonic development and adult homeostasis by morphogenesis, differentiation, proliferation,

and apoptosis of various types of cells in the body. BMPs are mostly known for cartilage and bone formation. In 1965, Urist reported that bioactive components in the demineralized bone matrix induce bone formation[7]. BMPs signaling occurs through both canonical Smad-dependent pathways (BMP ligands, receptors, and Smads) and non-canonical Smad-independent signaling pathways (p38 mitogen-activated protein kinase pathway, MAPK). Both canonical Smad-dependent pathways and non-canonical Smad-independent signaling pathways express Runx2 gene expression to control osteogenesis[8-10].

For the treatment of the non-unions, BMPs are considered a favorable approach because they are considered the most potent toward bone regeneration[11]. There are fifteen different BMPs are found in mammals; among them, rhBMP-2 and rhBMP-7 are FDA approved. BMP-2 and BMP-7 have been tested in several preclinical studies showing the ability to induce bone regeneration[12-14] and evaluated in clinical trials to treat various bone disorders such as non-unions, open fractures, and osteonecrosis[15-19]. Clinical trials results suggested that BMP-2 and BMP-7 are safe, significantly reduced the frequency of bone grafting procedures and effective in non-union bone defect[15, 18, 20].

The Wnt and bone morphogenic protein (BMP) signaling pathways are important for many biological events and complement each other for bone regeneration[21]. BMP-2 induces Wnt and activates the β-catenin signaling pathway during endochondral ossification, and the β-catenin signaling pathway regulates the early phases of chondrogenesis and osteogenesis[22]. BMP-2 promotes osteogenic differentiation by increasing the expression of LRP-5 and stabilizing β-catenin through the downregulation of β-Trcp[23, 24]. A substantial reduction of osteogenesis occurs with β-catenin deficiency. The function of BMP-2 toward bone formation is inhibited by

DKK-1 overexpression[22, 25, 26]. Overall, the Wnt/ β-catenin pathway is found to be very crucial for osteogenesis and bone mass formation along with BMP signaling pathway.

Numerous scaffolds have been developed for bone tissue engineering applications[27]. 3D porous scaffolds with the appropriate mechanical properties are required for bone tissue engineering[28, 29]. The scaffolds serve as mechanical support during tissue growth, and their porous structure provides nutrient supply and helps waste removal[29]. Biocompatible polymers reinforced with hydroxyapatite (HAP) are extensively used in bone tissue engineering because of the similar compositions of the mineral phase of the bone[30]. HAP enhanced cell attachment, cell proliferation, and osteogenic differentiation of stem cells[31, 32]. Inorganic fillers are also used to improve the mechanical properties of the scaffold to facilitate bone tissue formation[33]. Montmorillonite (MMT) nano-clay is used as an inorganic filler to enhance the mechanical properties of the scaffold[34]. Along with the mechanical properties of the scaffold, MMT nano-clay also improves cell adhesion cell proliferation[35-37]. Interlocking block scaffolds provide a large surface area, facilitating cell proliferation and osteogenic differentiation of mesenchymal stem cells (MSCs)[38].

Dual growth factor delivery on bone regeneration significantly improves vascular growth and bone growth[39]. The combination of BMP-2 with BMP-7 was shown to enhance bone morphogenesis[40]. Therefore, developing a scaffold that could deliver a combination of BMP-2 with BMP-7 in a time-dependent manner would be a viable bone graft for bone healing. In the previous study, we found that a combination of BMP-2 and BMP-7 enhanced osteogenic differentiation, accelerated mineralization, shortened collagen formation time[38]. Based on observations in the previous study, we hypothesized that cells seeded scaffolds exhibit mechanics changes over time due to the maturation of ECM. To this end, we evaluated nanomechanical

75

properties of the cells seeded scaffolds using Berkovich indenter tip and correlated mechanical properties changes with mRNA expression of bone-related genes, confocal and SEM imaging.

3.2. Materials and methods

3.2.1. Modification of MMT clay

Na-MMT clay (SWy-2) was received from the Clay Minerals Society (Wyoming). The Na-MMT clay is modified with 5-aminovaleric acid described in detail in previous studies [41, 42]. In brief, preheated (60°C) 5-aminovaleric acid solution was added to preheated (60°C) MMT suspension and kept for stirring for one hour. After one hour, the obtained slurry was separated using a centrifuge followed by drying at 70°C, grinding, and sieving to obtain a fine powder. The 5-aminovaleric acid was purchased from Sigma-Aldrich.

3.2.2. Preparation of in situ HAPclay

The in situ HAP clay was prepared following the detailed steps described in previous studies[36, 43, 44]. Briefly, amino acid modified Na-MMT clay powder was poured into Na_2HPO_4 (J.T. Baker) solution and kept for stirring for 2 hours. Then, $CaCl_2$ (J.T. Baker) solution was added to the clay, Na_2HPO_4 suspension, and kept for stirring for 8 hours at pH 7.4. The precipitate obtained was separated using a centrifuge followed by drying at 70°C, grinding, and sieving to obtain a fine powder.

3.2.3. Preparation of PCL/in situ HAPclay scaffolds

3D porous PCL/in situ HAPClay scaffolds were prepared following the steps described in detail in previous studies[34, 38]. In brief, the PCL (Sigma Aldrich) solution was prepared by dissolving 3.6 g (90%) of polymer in 40 ml of 1,4-dioxane (Sigma Aldrich). Another solution was prepared by dispersing 0.4 g (10%) of *in situ* HAPclay in 20 ml of 1,4-dioxane. The *in situ* HAPclay suspension was sonicated for 18 minutes for better dispersion of *in situ* HAPclay in

dioxane. Sonicated *in situ* HAPclay solution was added to the polymer solution and kept for stirring for 2 hours. Then, the polymer HAPclay solution was poured into the 3D-printed molds. Designing and preparation of 3D printed mold described in the previous study[38]. Further, the freeze extraction method was used to obtain 3D scaffolds.

3.2.4. Preparation of scaffold sample for cell culture

PCL/ in situ HAPclay scaffolds were sterilized using a UV sterilization chamber for 45 minutes, followed by immersing in 100 % ethanol for 24 hours. Then the sterilized were washed in PBS to remove the ethanol from the scaffolds. BMP 2 (Genscript) and BMP 7 (Biovision) solutions were prepared by following the manufacturer's protocol at a concentration of 1μg/ml. Sterilized scaffolds were immersed into the freshly made 1:1 BMP-2 and BMP-7 solution for 24 hours. After 24 hours, BMP-2 and BMP-7 coated samples were kept in the cell culture media for 24 hours before using them for cell culture experiments. Initially, a combination of 5 X 10^4 osteoblast cells (hFOB) and 5 X 10^4 MSCs were seeded on each scaffold.

3.2.5. Cell lines and culture medium

The human osteoblast cell line (hFOB 1.19) was purchased from ATCC. The culture media consisted of 90% HyQ Dulbecco's Modified Eagle medium DMEM-12(1:1) from Hyclone, 10% fetal bovine serum (FBS) from ATCC, and 0.6% antibiotic solution (G418) from JR scientific. Human mesenchymal stem cells (MSCs) were purchased from Lonza and maintained in MSCGM™ Bulletkit™ medium. The Bulletkit™ medium was prepared by adding MSCGM™ SingleQuots™ (Lonza) to MSCBM™ (Lonza). We maintained cells at 37°C and 5% CO_2 in a humidified incubator.

3.2.6. ELISA assays

The amount of BMP-2 and BMP-7 released in the PBS were determined using the ELISA assay kits (BMP-2 Invitrogen kit, BMP-7 Invitrogen kit) following the manufacturers' instructions. We collected the supernatant at every 24hr interval followed by adding fresh PBS.

3.2.7. DNA quantification

Cell viability was performed by measuring DNA content according to the manufacturers' protocol (AccuBlue® Broad Range dsDNA Quantitation Kits). Briefly, the cell-seeded scaffolds were washed with PBS, and each scaffold was digested in 500 µl of cell lysis TE buffer. Then, scaffolds were kept at -80 °C followed by three freeze-thaw cycles at −80 °C and 37 °C. Further, the cells supernatants were collected after centrifugation. Finally, 10 µl of each diluted sample was mixed with 200 µl of working solution and incubated for 30 min at room temperature in the dark. The fluorescence was measured at 350 nm excitation/460 nm emission using a fluorescence microplate reader (BioTek).

3.2.8. Scanning electron microscopy

The tissue-cultured scaffold samples were washed with PBS and fixed with 2.5% glutaraldehyde followed by ethanol series treatment (10%, 30%, 50%, 70%, and 100% v/v) for dehydration. The samples were dried using hexamethyldisilazane after alcohol treatment. The samples were then carbon-coated and mounted on SEM stubs for observation using the JEOL JSM 6490LV scanning electron microscope.

3.2.9. Gene expression studies

Total RNA from the cell-seeded scaffolds was isolated and quantified using Direct-zol RNA MiniPrep kit (Zymo Research) and Nanodrop ND 2000 (Nanodrop products), respectively. Then, cDNA was prepared using 2 µg/µl of RNA, random primers, and M-MLV reverse

transcriptase (Promega) in PCR thermal cycler (Applied Biosystems). Real-time polymerase chain reaction (PCR) experiment was performed using a 7500 Fast Real-Time PCR system (Applied Biosystems). Forward primer, reverse primer, SYBR Green dye, and cDNA were added to make a final volume of 20 µl and run using a thermal profile with a holding stage (2 min at 50 °C, 10 min at 95 °C) and a cycling stage (40 cycles of 15 s at 95 °C, and 1 min at 60 °C). The mRNA expressions of Runt Related Transcription Factor 2 (RUNX2), Osteopontin (OPN), Osteocalcin (OCN), Bone sialoprotein (BSP), Alkaline phosphatase (ALP), LRP5, Wnt5a, and β-catenin were quantified and normalized to housekeeping gene glyceraldehyde-3-phosphate-dehydrogenase (GAPDH). For all the genes 2D 0 days sample were used as a control. Target gene expressions were analyzed using the comparative C_t method ($2^{-\Delta\Delta Ct}$). The sequence of primers used is shown in Table 3.1.

Table 3.1. The sequence of primers used for the quantitative real-time PCR experiment.

Gene	Forward primer	Reverse primer
GAPDH	5'-CATCTTCTTTTGCGTCGCCA-3'	5'-TTAAAAGCAGCCCTGGTGACC-3'
RUNX2	5'- GTC TCA CTG CCT CTC ACT TG-3'	5'- CAC ACA TCT CCT CCC TTC TG-3'
OPN	5'- CCAAGCGTGGAAACACACAGCC-3'	5'- GGCTTTGGAACTCGCCTGACTG-3'
OCN	5'-GTG ACG AGT TGG CTG ACC-3'	5'-TGG AGA GGA GCA GAA CTG G-3'
BSP	5'-CCA GAC CAT TGA CAA CTA CC-3'	5'-CAG GCG AGA CAG ATT TGC-3'
ALP	5'-TCAACACCAACGTGGCTAAG -3'	5'-CACAATGCCCACAGATTTCC-3'
VEGF	5'-GAC AAG AAA ATC CCT GTGGGC-3'	5'- AAC GCG AGT CTG TGT TTT TGC-3'
LRP5	5'-GTTCGGTCTGACGCAGTACA-3'	5'-GTCCATCACGAAGTCCAGGT-3'
Wnt-5a	5'-TCT CAG CCC AAG CAA CAA GG-3'	5'-GCC AGC ATC ACA TCA CAA CAC-3'
β-catenin	5'-GGC AGC AAC AGT CTT ACC -3'	5'- TCC ACA TCC TCT TCC TCA -3'

3.2.10. Analysis of nanomechanical response

Displacement controlled nanoindentation experiments on the hydrated scaffolds, cell-seeded scaffolds without BMPs coating, and cell-seeded scaffolds with BMPs coating in cell culture medium were performed using Berkovich diamond indenter fluid tip (three-sided

pyramidal; 100-200 nm tip radius) using Hysitron Triboscope nanomechanical instrument (Minneapolis, MN) equipped with multimode AFM (nanoscope IIIa controller and J-type piezo scanner system) (Veeco Metrology, Santa Barbara, CA). Cell-seeded porous scaffolds were placed inside the custom-designed 3D printed holder and flushed with cell culture medium for the experiment. Subsequently, samples were placed onto the nanoindentation sample stage, and the whole tip-sample-fluid assembly was heated and maintained at 37°C. For the entire duration of the experiments, extreme care was taken to ensure that the scaffolds were wholly immersed in the cell culture medium. Indentation experiments were performed at maximum indentation depths of 500, 1000, and 2000 nm, respectively, at loading and unloading rates of 25 nm/s.

The load-displacement curve of each test was carefully analyzed to separate scaffolds, cells, and mineralized ECM indentation responses. Contact stiffness was calculated by applying power-law fit to the initial unloading portion of the load-displacement curve and analytically differentiating the power-law relation, following the Oliver-Pharr method [45]. Reduced modulus was calculated from the stiffness and contact area measurements using Hysitron analysis software. The elastic modulus for each indent was further determined from reduced modulus and is given by the following relation:

$$\frac{1}{E_r} = \frac{(1 - \vartheta^2)}{E_s} + \frac{(1 - \vartheta_i^2)}{E_i}$$

where, E_r=reduced elastic modulus; E_s=elastic modulus of sample; E_i=elastic modulus of indenter; ϑ_i= Poisson's ratio of indenter; ϑ_s= Poisson's ratio of the sample. In this work, we used the diamond indenter tip of elastic modulus 1141 GPa and Poisson's ratio of 0.07. Using Poisson's ratio of 0.5, as also commonly used in literature, we calculated elastic moduli of biological cells. In this work, all the experiments are performed under fully immersed conditions. For all the samples, at least 30 indents were made under each set of experimental conditions. We used

triplicate samples in the experiments to ensure repeatability and reproducibility. In this work, at a particular depth, variation in elastic properties arises due to the presence of different constituents (porous scaffolds, cells, and mineralized ECM) possessing different physical/biological characteristics, thereby expected to exhibit their unique mechanical behavior. Under such a scenario, a range of modulus values was plotted to indicate the difference in elastic properties of cells, cell scaffolds, and Mineralized ECM.

3.2.11. Alizarin red staining and quantification assay

Cell-seeded scaffolds were fixed with 4% paraformaldehyde for 30 mins and washed with PBS three times (5 min each wash) to remove the residual fixative agent. Further, scaffolds were stained with Alizarin Red S dye (2 g/100 mL deionized water, pH = 4.10 to 4.15 and kept for 2 min 30 sec. After 2 min 30 sec, the scaffold was washed using cell culture grade water many times to remove excess dye. Z-stacks of the samples were obtained using a Zeiss Axio Observer Z1 microscope equipped with an LSM700 laser-scanning module. Images were taken using a 639 nm laser light source. For image analysis, Imaris software was used.

3.2.12. Statistical analysis

All the experiments were carried out in triplicates (n = 3) unless otherwise mentioned, and the data are presented as Mean value of triplicates ± standard derivation. The statistical significance (p-value) between the two groups is done using Student's unpaired *t-test. In contrast,* multiple comparisons are made using two-way ANOVA followed by an appropriate *post hoc* test (GraphPad Prism v8.4.2). Differences between the two groups were considered statistically significant when probability, $*p < 0.05$.

3.3. Results and discussion

3.3.1. Release kinetics of BMPs

The amount of BMP-2 and BMP-7 released from the scaffolds is measured by ELISA assay. Fig. 3.1A represents the percentage of cumulative content of released BMP-2 and BMP-7 over time from the scaffolds. We observed an initial burst of release in the first 24 h; about 40% of BMP-2 and BMP-7 releases occurred in the first 24 hr, followed by a slower release. Finally, after 15-day for BMP-7 and after 16-day for BMP-2, complete release was observed from the scaffolds.
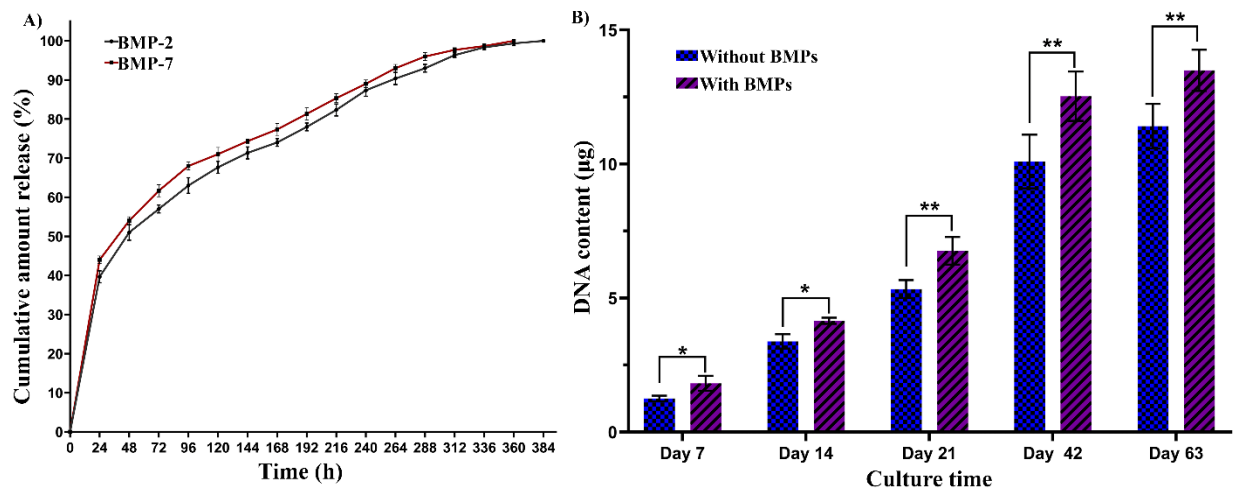
Fig. 3.1. Cumulative percentage release of BMP-2 and BMP-7 over time from the scaffolds in PBS (A), The proliferation of hMSCs and hFOB (DNA content) on BMPs coated and without BMPs scaffold samples at day-7, day-14, day-21, day-42, and day-63 (B). $*p < 0.05$, $**p < 0.01$, and $***p < 0.001$ indicate a significant difference between BMPs coated and without BMPs scaffold samples.

3.3.2. Coating with the BMPs enhanced the proliferation of hMSCs and hFOB

The hMSCs and hFOB were cultured on scaffolds for 63 days on both without BMPs and with BMPs coated nanoclay based porous scaffolds. The DNA quantification data showed a steady increase in DNA content in both culturing conditions over time. However, the amount of DNA was significantly higher in BMPs coated scaffolds than without BMPs scaffolds, as shown in Fig.

3.1B. In addition, the cell proliferation with BMPs coated samples showed an increase in DNA content, with some statistical significance ($*p < 0.05$) compared to day-7 without BMPs samples, indicating the effect of BMPs on hMSCs and hFOB proliferation. In contrast, at day-21 and later, BMPs coated samples exhibited a large increase in cell proliferation at statistically significant levels ($**p < 0.01$).

3.3.3. Cell morphology

SEM micrographs of dry PCL/in situ HAPclay scaffold are shown in Fig. 3.2(A–C). The images indicate interconnecting porous microstructure. These scaffolds seem to have pore sizes in the range of less than 10 µm–300 µm. SEM micrographs of PCL/in situ HAPclay scaffold seeded with human MSCs and osteoblast cells for nine weeks are shown in Fig. 3.2(D–I). These images indicate attachment, spreading of cells on the scaffold, and formation of mineralized extracellular matrix (ECM) by the cells on these composite scaffolds. The red arrows indicate the mineralization on the scaffolds seeded with human MSCs and osteoblast cells. In addition, SEM micrographs show enhanced ECM formation on BMPs coated samples Fig. 3.2(G-I) compared with uncoated samples Fig. 3.2(D-F), indicating the effect of BMPs on mineralization.
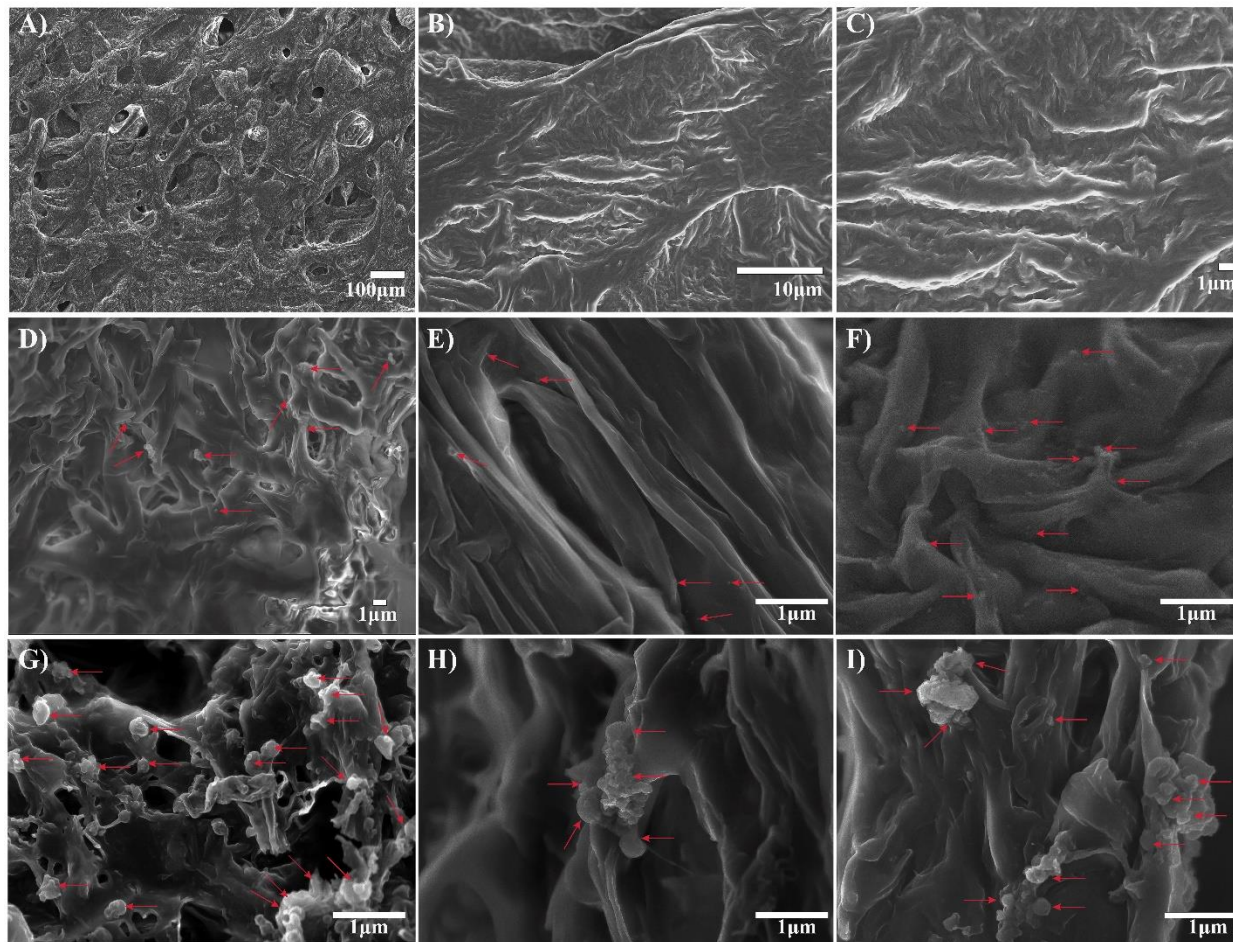
Fig. 3.2. SEM micrographs of PCL/ in situ HAPclay scaffolds (A-C) showing the interconnecting porous structure of the scaffold, SEM micrographs of hMSCs and hFOB cultured on bone-mimetic nanoclay scaffolds after 63 days indicating cell attachment, spreading, and mineralization on (D-F) without BMPs coated and (G-I) BMPs coated scaffold.

3.3.4. Osteogenic differentiation of hMSCs and hFOB and ECM formation on nanoclay-based scaffolds amplified by BMPs.

To evaluate the effect of BMPs on ECM formation on MSCs and hFOB cells seeded nanoclay-based scaffolds, we examined the expressions of ECM formation-related genes (OPN, OCN, and BSP). OPN, OCN, and BSP are bone markers, and the expression of these markers increases during osteoblast maturation and ECM formation. Fig. 3.3(A-C) represents the quantitative real-time PCR of OPN, OCN, and BSP expression, respectively. We found increased gene expression levels of ECM formation-related markers over time for both, without, and with

BMPs coated scaffolds. However, a significant increase in ECM-related markers was observed with BMPs coated scaffolds. After 63-days almost ~2-fold increase in OPN level (A), ~2.5-fold increase in OCN level (B), and ~1.5-fold increase in BSP level (C) was observed in BMPs coated scaffolds compared with without BMPs coated scaffolds. They indicated the effect of BMPs on mineralization. To evaluate the effect of BMPs on osteogenic differentiation on MSCs and hFOB cells seeded nanoclay-based scaffolds, we examined the expressions of osteogenic differentiation-related genes (ALP and Runx2). Fig. 3.3(D, E) represents the quantitative real-time PCR of ALP and Runx2 expression, respectively. ALP is an osteogenic marker, indicating the early stage of osteoblastic differentiation, while Runx2 is a transcription factor that regulates osteoblastic differentiation. In the early stage of differentiation of MSCs, Runx2 has been shown to promote the differentiation of mesenchymal cells into osteoblasts; however, with the maturation of osteoblast, levels of Runx2 reduce. ALP expression has also been shown to downregulate during the maturation of osteoblasts and the formation of an extracellular matrix (ECM). We observed an increase in ALP and Runx2 expression at 7-days and 14-days, indicating osteogenic differentiation of MSCs for both samples. Later, at 21-days, 43-days, and 63-days, the expressions of ALP and Runx2 were downregulated, indicating the maturation of osteoblast and ECM formation. With BMPs at 7-days and 14-days, we observed a ~3-fold increase in Runx2 (D) and ALP (E) levels compared with uncoated samples, indicating osteogenic differentiation of MSCs amplified by BMPs. Fig. 3.3(F) illustrates the effect of BMPs on Runx2 level elevation through the Smad-dependent pathway. Then, an elevated level of Runx2 enhanced the osteogenic differentiation of MSCs and pre-osteoblast to mature osteoblast and enhanced bone formation[46]. With the maturation of osteoblast, the Runx2 level decreased[47]. Our results suggest the elevation of the Runx2 in the early stage is related to the osteogenic differentiation of MSCs and hFOB. Later on,

attenuation of the Runx2 level is associated with the maturation of the osteoblast and ECM formation. Fold increase in gene expression levels with BMPs coated samples is shown in Table 3.2.

Table 3.2. Relative gene expression levels as a function of culture time for scaffolds without BMPs and with BMPs. Values in the bracket indicates folds increase in gene expression compared with scaffolds without BMPs.

Gene / Culture time	OPN	OCN	BSP	ALP	Runx2	Wnt-5a	LRP-5	β-catenin
Without BMPs scaffolds								
Day 7	1.61	1.70	1.72	1.49	1.65	1.01	1.56	1.63
Day 14	2.76	2.61	2.87	2.52	3.50	1.49	2.08	2.04
Day 21	3.40	3.05	4.03	1.98	2.80	1.36	1.91	1.87
Day 42	4.34	3.92	4.77	1.57	2.23	1.19	1.70	1.66
Day 63	4.91	4.46	5.63	1.24	1.27	0.79	1.38	1.46
Without BMPs scaffolds								
Day 7	2.53 (**1.58**)	3.25 (**1.91**)	2.72 (**1.59**)	6.26 (**4.20**)	6.29 (**3.81**)	1.72 (**1.71**)	2.25 (**1.44**)	3.03 (**1.86**)
Day 14	5.35 (**1.94**)	5.64 (**2.16**)	5.16 (**1.80**)	7.91 (**3.13**)	11.57 (**3.30**)	3.16 (**2.12**)	3.74 (**1.80**)	5.29 (**2.59**)
Day 21	6.85 (**2.02**)	7.57 (**2.48**)	6.37 (**1.58**)	4.22 (**2.13**)	6.52 (**2.33**)	2.57 (**1.89**)	3.11 (**1.63**)	3.14 (**1.68**)
Day 42	8.24 (**1.90**)	9.09 (**2.32**)	7.57 (**1.59**)	2.60 (**1.66**)	3.82 (**1.71**)	2.18 (**1.84**)	2.68 (**1.58**)	2.61 (**1.57**)
Day 63	8.91 (**1.82**)	10.58 (**2.37**)	9.12 (**1.62**)	1.81 (**1.46**)	2.34 (**1.85**)	1.87 (**2.36**)	2.42 (**1.75**)	2.27 (**1.56**)
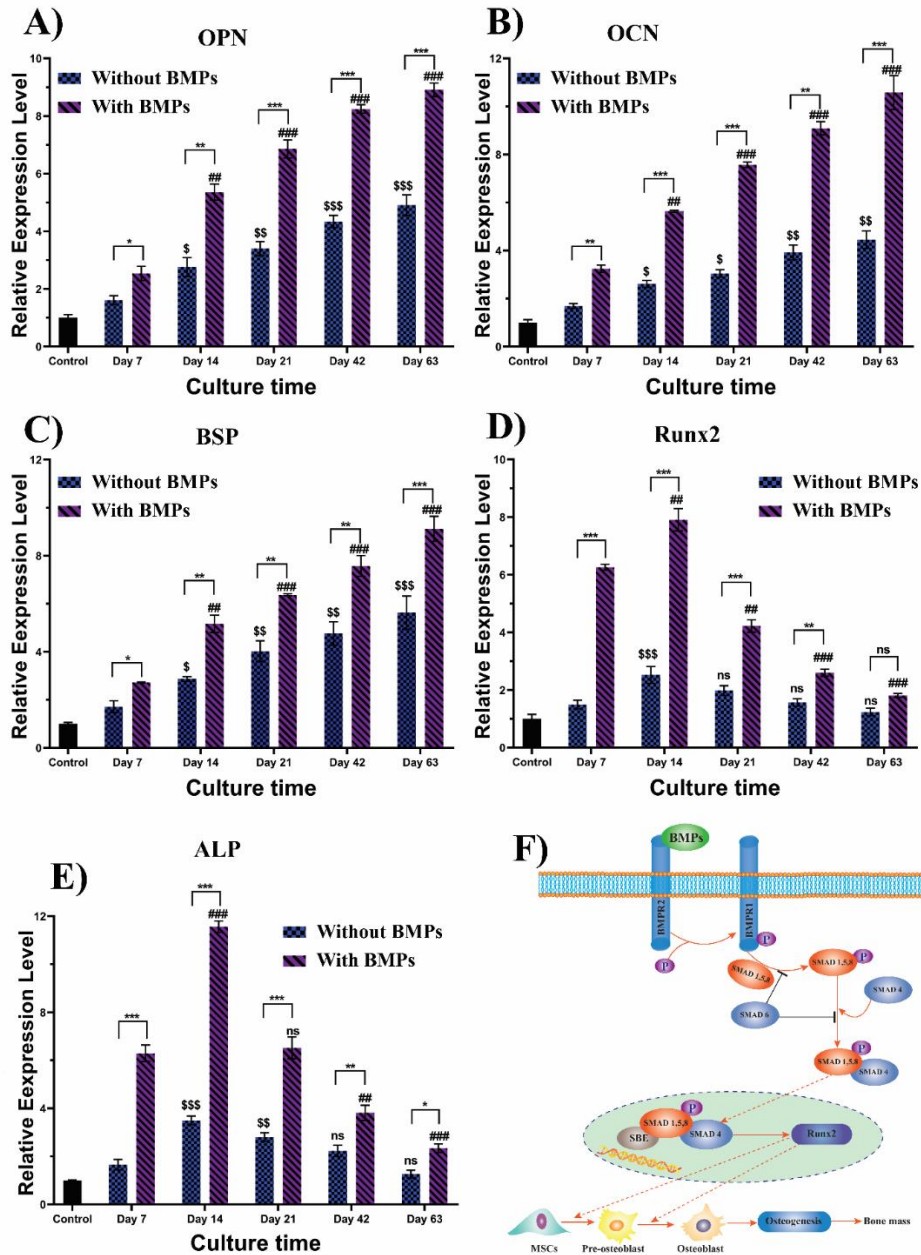
Fig. 3.3. Osteogenic differentiation of hMSCs and hFOB and ECM formation on nanoclay-based scaffolds. Quantitative real-time PCR of gene expression for ECM formation-related markers A) OPN, B) OCN, and C) BSP. Quantitative real-time PCR of gene expression for osteogenic differentiation-related markers D) Runx2, and E) ALP. BMPs induced osteogenesis pathway F) illustrating how BMPs upregulate Runx2, and enhanced osteogenesis. $*p < 0.05$, $**p < 0.01$, $***p < 0.001$ indicate a significant difference between BMPs coated scaffold and without BMPs coated scaffolds at 7-days, 14-days, 21-days, 42-days, and 63 days. $^{\$}p < 0.05$, $^{\$\$}p < 0.01$, $^{\$\$\$}p < 0.001$ indicate a significant difference between without BMPs 7-days with 14-days, 21-days, 42-days and 63-days. $^{\#}p < 0.05$, $^{\#\#}p < 0.01$, $^{\#\#\#}p < 0.001$ indicate a significant difference between with BMPs 7-days with 14-days, 21-days, 42-days, and 63 days.

3.3.5. Osteogenesis in nanoclay-based scaffolds is mediated by the Wnt/β-catenin signaling pathway, enhanced by BMPs.

The Wnt/β-catenin signaling pathway plays a very important role in osteogenesis. To evaluate the effect of BMPs on the Wnt/β-catenin signaling pathway during osteogenesis on the nanoclay-based scaffolds, we analyzed the expressions of Wnt/β-catenin pathway-related genes (LRP5, Wnt5a, and β-catenin) in both scaffold systems. Fig. 3.4(A) describes the Wnt-5 expression level on with/without BMPs coated scaffolds over time. We observed a ~1.7-fold increase at day 7 and ~1.8-fold increase at day 14 in Wnt-5a expression level on BMPs coated samples compared with uncoated samples; then, for both samples, expression level decreases. Fig. 3.4(B) describes the LRP-5 expression level on with/without BMPs coated scaffolds over time. We found a ~1.5-fold increase at day 7 and ~1.8-fold increase at day 14 in LRP-5 expression level on BMPs coated samples compared with uncoated samples; then, for both samples, expression level decreases. Fig. 3.4(C) describes the β-catenin expression level over time with/without BMPs coated scaffolds. We observed a ~1.8-fold increase at day 7 and a ~2.5-fold increase at day 14 in β-catenin expression level on BMPs coated samples compared with uncoated samples for both samples, then, for both samples, expression level decreases. Fig. 3.4(D) describes the effect of BMPs on activation of the Wnt/β-catenin signaling pathway and upregulation of Wnt-related factors and ultimately enhance the osteogenic differentiation and bone formation. The activated Wnt/β-catenin pathway inhibits cytoplasmic degradation of β-catenin while promoting nuclear translocation of β-catenin, upregulating the bone-specific genes. β-catenin regulates the early stages of osteogenic differentiation and reduces bone maturation. We observed upregulated expressions of Wnt-related factors (LRP5, Wnt5a, β-catenin) at 7-days and 14-days while the expressions of all genes evaluated went down at 21-days and later on, indicating the maturation of bone. The number of

fold increase in gene expression levels with BMPs coated sample compared with uncoated samples

is shown in Table 3.2.
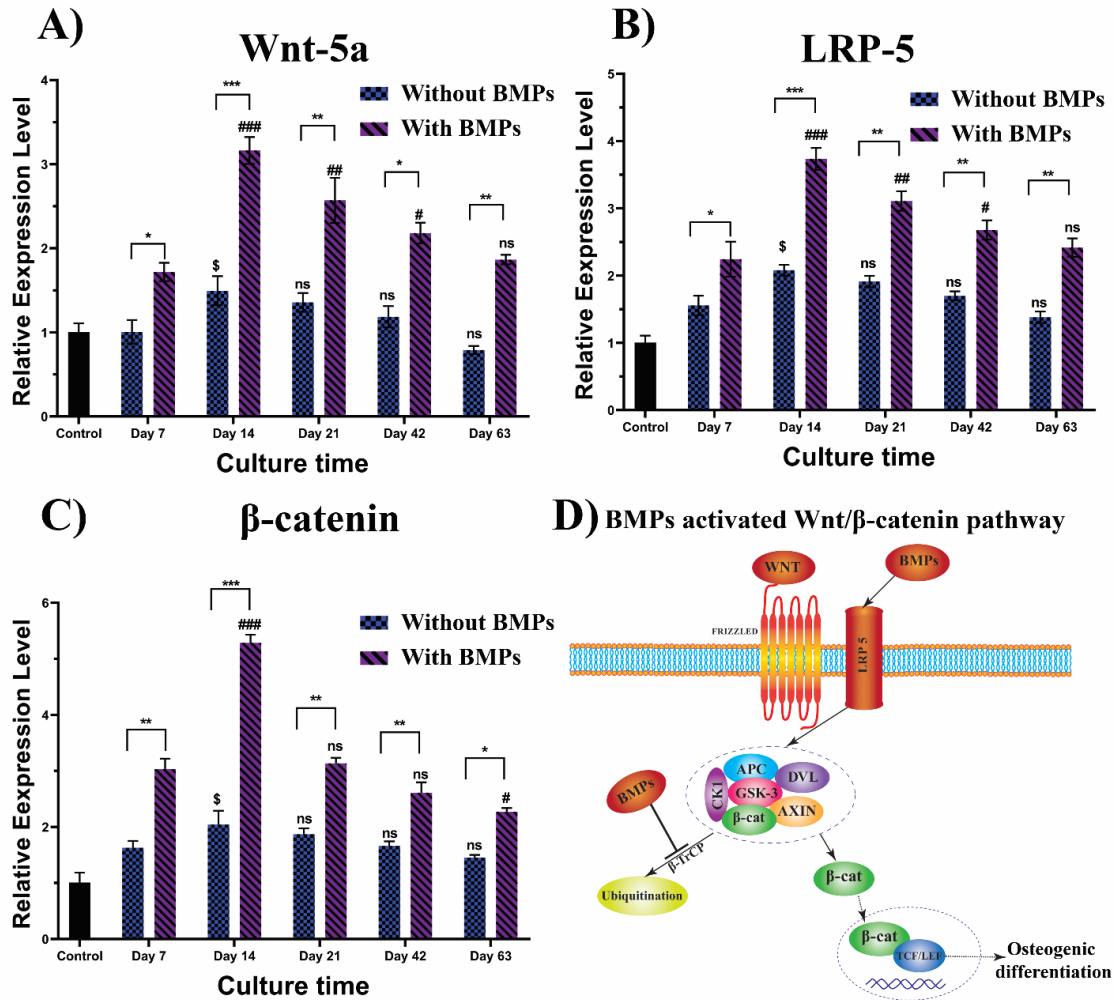
Fig. 3.4. Osteogenesis in nanoclay-based scaffolds is mediated by Wnt/β-catenin signaling pathway, enhanced by BMPs. A) Quantitative real-time PCR of gene expression for Wnt-related factors LRP-5, B) Quantitative real-time PCR of gene expression for Wnt-related factors Wnt5a, and C) Quantitative real-time PCR of gene expression for Wnt-related factors β-catenin. Wnt-pathway D) illustrating how BMPs induced Wnt-pathay by inhibiting ubiquitination of β-catenin, and ehnaced osteogenesis. $*p < 0.05$, $**p < 0.01$, $***p < 0.001$ indicate a significant difference between BMPs coated scaffold and without BMPs coated scaffolds at 7-days, 14-days, 21-days, 42-days, and 63 days. $^\$p < 0.05$, $^{\$\$}p < 0.01$, $^{\$\$\$}p < 0.001$ indicate a significant difference between without BMPs 7-days with 14-days, 21-days, 42-days, and 63-days. $^\#p < 0.05$, $^{\#\#}p < 0.01$, $^{\#\#\#}p < 0.001$ indicate a significant difference between with BMPs 7-days with 14-days, 21-days, 42-days, and 63-days.

3.3.6. Mineralized bone nodule formation is enhanced in the BMPs coated samples.

To assess the effect of BMPs on mineralization, we performed an Alizarin Red S assay. Scaffolds seeded with hMSCs and hFOB (without BMPs), scaffolds seeded with hMSCs, and hFOB coated with BMP-2 and BMP-7 (with BMPs) at one week, three weeks, six weeks, and nine weeks samples were stained with Alizarin Red S; the results are shown in Fig. 3.5. Positive Alizarin Red S staining was observed for all the samples, indicating mineralized nodule formation. A significant difference in mineralization was observed between without BMPs and with BMPs samples. For all the samples, mineralized nodule formation increases over time. At nine weeks, maximum mineralized ECM formation was observed with BMPs coated samples, whereas the least amount of ECM formation was observed at one week with no BMPs coated samples. In Fig. 3.5, the 3D view shows how ECM formation increased in each sample with time progression. A significant increase in ECM formation was observed from three weeks to six weeks and six weeks to nine weeks for both samples. Thus, the Alizarin Red S assay data indicates that BMPs enhance the mineralized bone nodule formation.
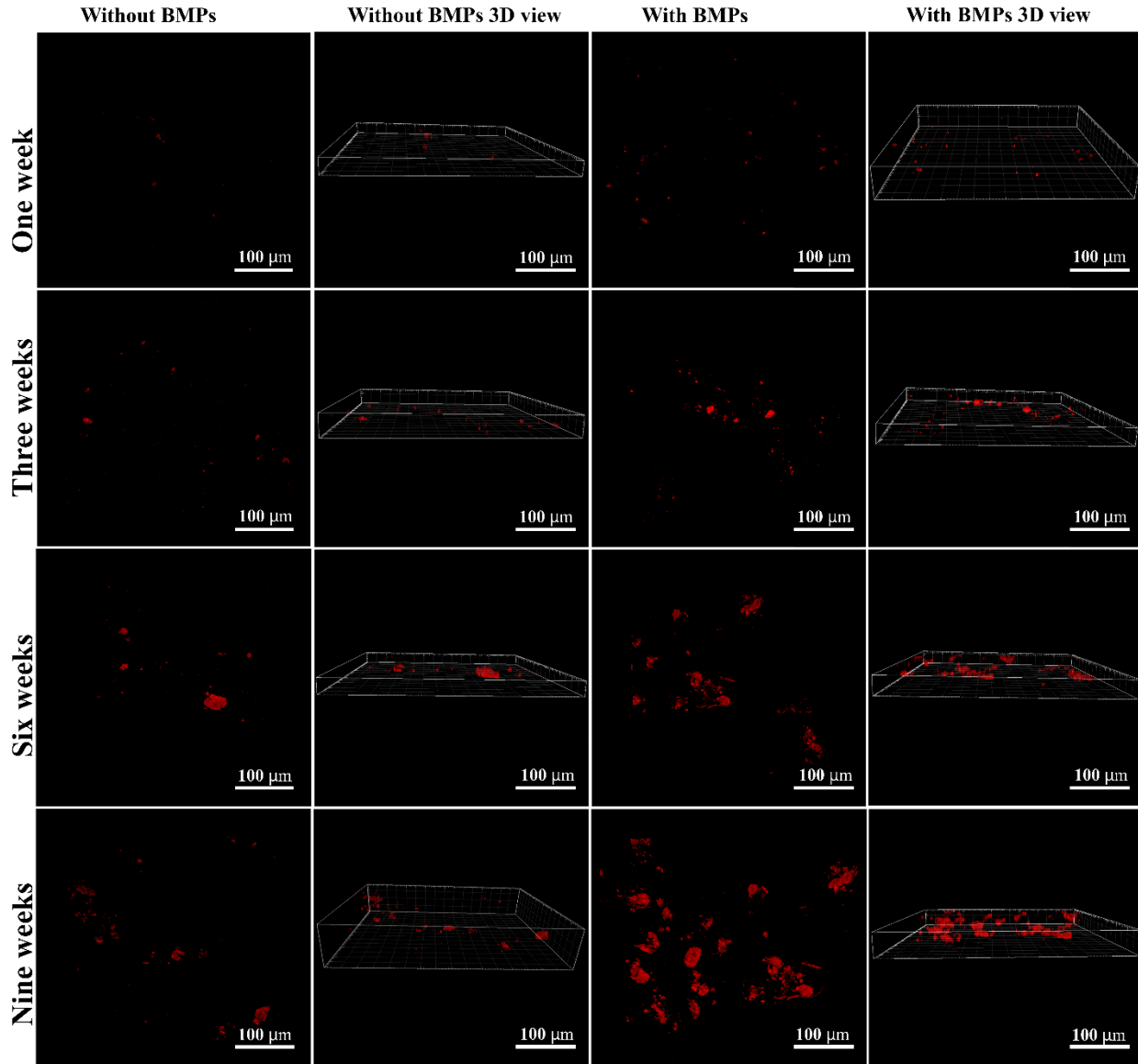
Fig. 3.5. Effect of BMPs on mineralization. Alizarin Red S-stained scaffolds seeded with hMSCs and hFOB (without BMPs), scaffolds seeded with hMSCs, and hFOB coated with BMP-2 and BMP-7 (with BMPs) at one week, three weeks, six weeks, and nine weeks. 3D view showing the amount of mineralized ECM formation on each scaffold. Bar = 100 μm.

3.3.7. Mechanical properties of the scaffolds decrease with the hydration period progression.

First, we investigated the mechanical properties of scaffolds in a hydrated state using instrumented indentation, focusing on the effect of hydration time on elastic modulus and indentation hardness. Here the depth-controlled nanoindentation tests were performed on scaffolds that had been hydrated for various periods, with indentation depths of 500 nm, 1000 nm, and 2000

nm. Fig. 3.6 (B-D) represents the load-displacement indentation curves for hydrated scaffolds at various indentation depths. In contrast, Fig. 3.6 (E-G) display Young's modulus and indentation hardness for the hydrated scaffold as a function of imposed indentation depth and hydration period. It can be seen from Fig. 3.6 (B-D) that the maximum indentation loads for scaffold hydrated for a similar period increases with the increasing indentation depth. However, the maximum indentation load for equivalent indentation depths decreases as the scaffold hydrates. In general, wet environments alter the mechanical characteristics of polymers, owing to the plasticizing effect of water[48]. Earlier studies from our group have shown that organomodified nanoclay particles alter the crystallinity of polymer nanocomposites. Adding HAP nanoparticles to PCL composite scaffolds changes the degradation rate [49-51]. It has also been observed that the incorporation of calcium phosphate-based nanoparticles also impacts polymer chain configuration [51]. The gradual decrease in the PCL/in situ HAPclay scaffold's mechanical properties observed here, therefore, can be attributed to its degradation in an aqueous environment from one week to nine weeks of hydration. The elastic modulus and indentation hardness corresponding to each indentation represented the local behavior of the scaffold around the indented site. The interspersed lamellar structure with interconnected porosities is an intrinsic feature of PCL composite scaffolds containing in situ HAPclay[34]. Therefore, the range of elastic modulus and indentation hardness of the scaffolds in the hydrated condition obtained here fluctuated moderately. It has also been observed that the scaffolds' elastic modulus and indentation hardness decreases as the depth of the applied indentation increases. The material behavior observed here could be due to the indentation size effect (ISE) induced by intrinsic structural characteristics of materials, which causes hardness and elastic modulus to decrease as indentation depth increases. Several reasons for ISE have been proposed in recent decades, including the well-known strain gradient plasticity hypothesis[52],

contact surface variation[53], dislocation nucleation[54], and microfracture mechanisms [55]. However, in this case, the SEM images (Fig. 3.2 (A-C)) for the scaffold demonstrate that the porous scaffold structure contains small nano-pores and macroscopic defects such as big macro-pores. Therefore, when the penetrating indenter travels a greater depth in the scaffold, it is more likely to encounter a large sub-surface macro-pore or voids, causing a more rise in depth of penetration at a lower indentation load and thus affecting a larger area of contact, resulting in a lower modulus value. In contrast, the low penetration depth resulted in a smaller contact area; therefore, the modulus calculated would be on the higher side, as shown in our results. At the 500 nm penetration depth, the indenter captures the indentation response of a relatively small layer of scaffold surface; therefore, it appears that it is capturing the mechanical properties of the mixture of scaffold constituents. As a result, the elastic modulus value achieved here by 500 nm indentation depth is larger than the elastic modulus values acquired here by 1000 nm and 2000 nm indentation depth. However, indentation depths of 1000 nm and 2000 nm penetrate deeper into the scaffold and capture the impacts of the porosity on the mechanical properties of the scaffold, resulting in capturing the bulk properties of the scaffold system. In addition, all the unloading curves demonstrate considerable hysteresis compared to the loading curves in load-displacement plots, demonstrating that large plastic deformation occurs during the nanoindentation process.
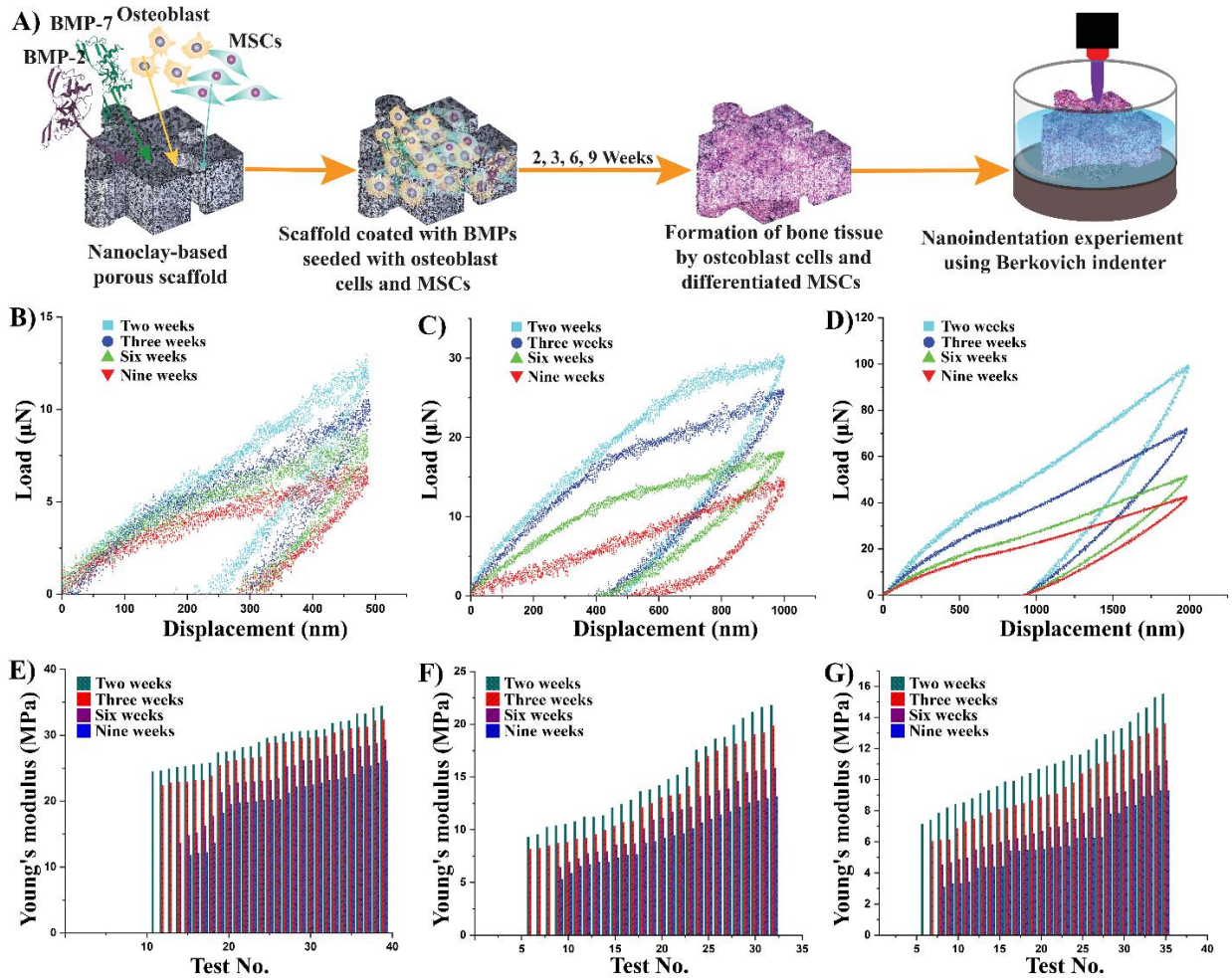
Fig. 3.6. A) Schematic showing steps of coating with BMP-2/BMP-7, co-culture hMSCs/hFOB followed by the workflow of nanoindentation experiment. Initially, BMP-2/-7 coated scaffolds are seeded with hMSCs and hFOB. Further, the change in nanomechanical properties of the cells seeded scaffolds was determined using a Berkovich diamond indenter fluid tip using Hysitron Triboscope nanomechanical instrument. Typical nanoindentation load–depth curves of hydrated scaffolds at 500 nm (B), 1000 nm (C), and 2000 nm (D) indentation depths. (E), (F) and (G) represent the elastic modulus (E) as a function of indentation depth of 500 nm, 1000 nm, and 2000 nm, respectively.

3.3.8. Mechanical properties of the cells seeded scaffolds increase over time.

Fig. 3.7. (A-F) shows a typical load-displacement indentation graph for scaffolds seeded with hMSCs and hFOB without BMPs. The elastic modulus values derived from load-displacement plots for indentation depths of 500 nm, 1000 nm, and 2000 nm are shown in Fig. 3.6 (G) (H) and (I), respectively. As illustrated in Fig. 3.7 (A-F) for scaffolds seeded with hMSCs and

hFOB, the maximum indentation load and elastic modulus at 500 nm, 1000 nm, and 2000 nm indentation depth increase over time as the cells in the scaffolds start forming ECM and maturation of ECM occurred from one week to nine weeks. However, as the indentation depths increase, the elastic modulus decreases for the scaffolds cell-seeded for an equal period of time. The data points in Fig. 3.7 (G) (H) and (I) show that the elastic modulus of the scaffold varied substantially across all indentation depths. Considering that each scaffold constituent is distributed randomly throughout the whole scaffold volume, the lower values of elastic modulus mainly indicate the region of the clay matrix with a low proportion of hard inclusions. Conversely, higher elastic modulus values mainly indicate the region of the clay matrix with a large proportion of small hard inclusions. Because most biological samples, particularly biological cells and tissues, are neither ideal solids nor ideal liquids, they display both elastic and viscous responses and are hence referred to as viscoelastic[56]. Based on the wide range of elastic moduli values obtained for all indentation depths, three distinct zones of indentation response may be identified: soft, semi-hard, and hard. The elastic modulus in the range of 2.5 MPa to 7 MPa represents the microscopic mechanical behavior of bone cells on a scaffold (porous matrix) tested for all indentation depths. The soft region demonstrated here shows a soft cellular material like deformation response, consistent with the previously described cell indentation results[57]. Furthermore, the intermediate range of elastic modulus (15 to 50 MPa for 500 nm and 1000 indentation depth, and 12 to 18 MPa for 2000 indentation depth) represents a mechanical characteristic of a mixed zone made up of cell scaffold matrix and small-sized hard mineral inclusions (semi-hard region). The elastic moduli values in the semi-hard region represent the transition region between the soft cellular matrix and stiff mineral matrix. Finally, the higher range of elastic moduli (35 to 85 MPa for 500 nm and 1000 indentation depth, and 22 to 35 MPa for 2000 indentation depth) represents a scaffold matrix zone

that exhibits stiff deformation behavior of large-sized rigid minerals inclusions. Considering the mineral formation over time (shown in Fig. 3.5) in conjunction with the elastic modulus values presented in Fig. 3.7, we can conclude that small rigid mineral inclusion in the scaffold matrix at the microscopic scale can substantially influence the overall bulk mechanical characteristics of the scaffold system. The elastic modulus values obtained from nanoindentation of BMP coated scaffold shows a trend similar to that of BMP uncoated scaffold, where maximum indentation load and elastic modulus for all indentation depths increased over time as the cells in the scaffolds began to form ECM and maturation of ECM occurred from one week to nine weeks. Fig. 3.8 (A–F) represents typical load-displacement graphs for nanoindentation on scaffolds seeded with hMSCs and hFOB with BMPs.
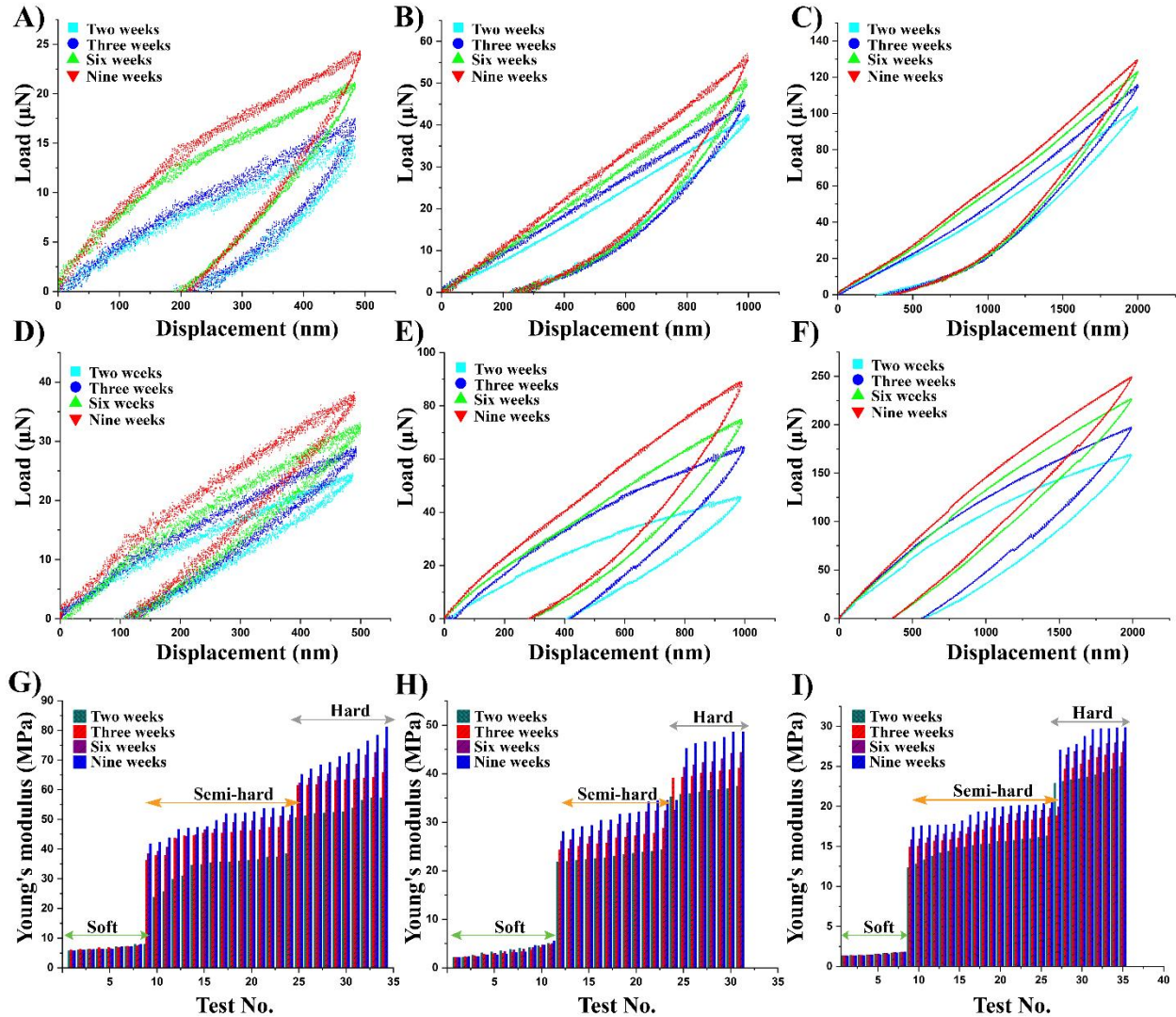
Fig. 3.7. Nanoindentation load-displacement curves, elastic modulus (E) of scaffolds seeded with hMSCs and hFOB. Representative nanoindentation load-displacement curves from semi-hard areas of cells seeded scaffolds at indentation depths of 500 nm, 1000 nm, and 2000 nm are shown in (A), (C), and (C), respectively. The representative nanoindentation load-displacement curves from the hard regime of cells seeded scaffolds at indentation depths of 500 nm, 1000 nm, and 2000 nm are shown in (D), (E), and (F), respectively. The elastic modulus values at 500 nm, 1000 nm, and 2000 nm indentation depths are shown in (G), (H), and (I), respectively.

Fig. 3.8 (G) (H) and (I) show the elastic modulus values derived from load-displacement plots of nanoindentation tests for indentation depths of 500 nm, 1000 nm, and 2000 nm, respectively. Fig. 3.8 (A-F) shows that for scaffolds seeded with hMSCs and hFOB with BMPs, the peak indentation load and elastic modulus for all indentation depth (500 nm, 1000 nm, and

97

2000 nm) increase with time as the cells in the scaffolds continues to generate ECM over time. Here, similar to scaffolds seeded without BMPs, a wide range of elastic modulus of the scaffold is observed (for all indentation depths), indicating three different indentation response zones: soft, semi-hard, and hard. The soft material zone identified here has an elastic modulus ranging from 3 MPa to 7.5 MPa, representing the microscopic mechanical behavior of bone cells on a porous scaffold matrix. Furthermore, the intermediate elastic modulus range (35 to 100 MPa for 500 nm and 1000 indentation depth, and 18 to 28 MPa for 2000 indentation depth) constitutes a mechanically distinctive semi-hard zone. Lastly, in the hard regime, the range of elastic modulus (85 to 190 MPa for 500 nm and 1000 indentation depth, and 40 to 55 MPa for 2000 indentation depth) observed characterizes the scaffold matrix made up of very stiff minerals inclusions. The semi-hard and hard regions report a nearly two-fold increase in the elastic modulus in scaffold coated with BMPs compared with scaffold uncoated with BMPs at nine weeks.
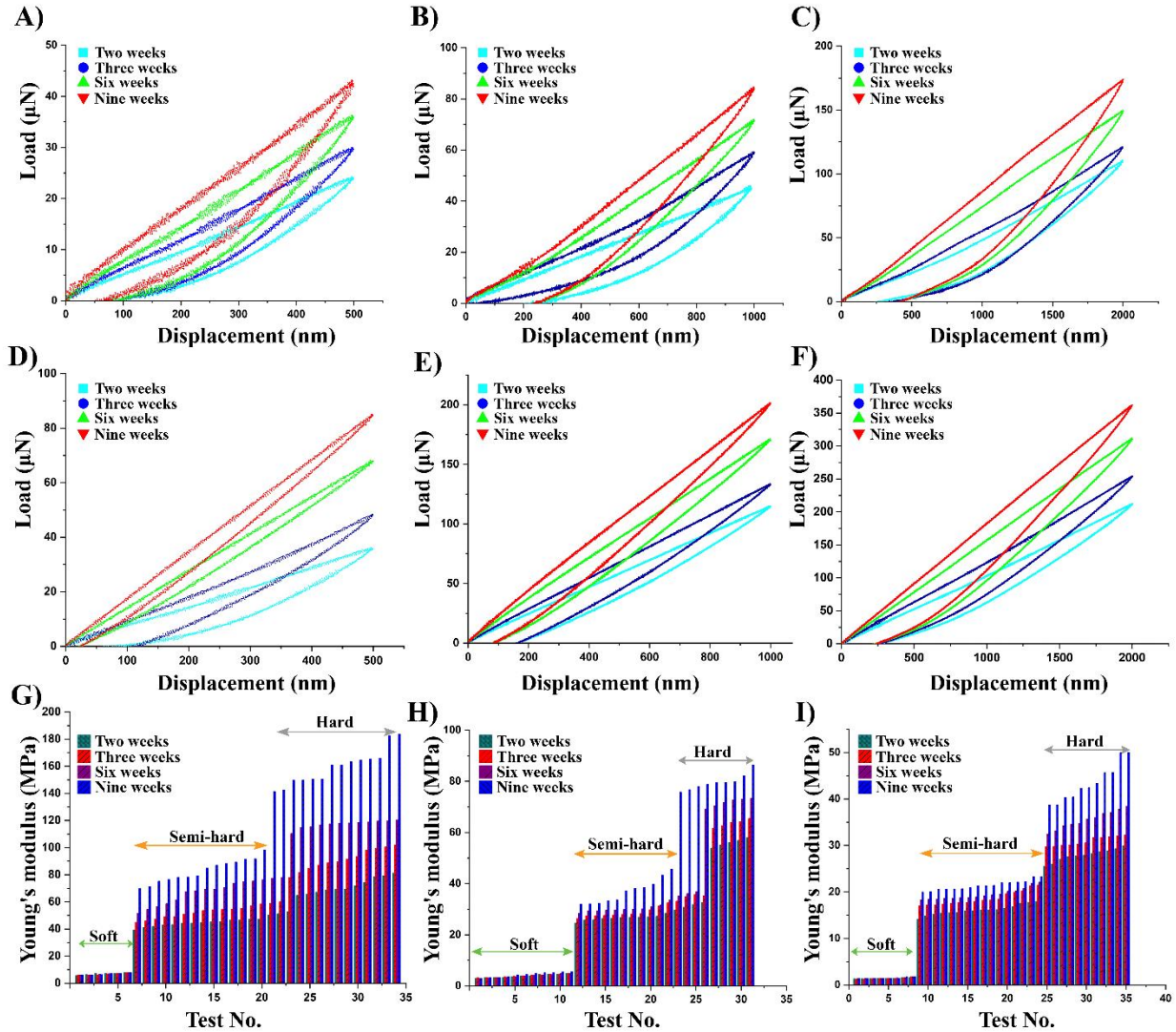
Fig. 3.8. Nanoindentation load-displacement curves, elastic modulus (E) of scaffolds seeded with hMSCs and hFOB coated with BMP-2 and BMP-7. Representative nanoindentation load-displacement curves from semi-hard areas of cell-seeded scaffolds at indentation depths of 500 nm, 1000 nm, and 2000 nm are shown in (A), (B), and (C), respectively. Representative nanoindentation load-displacement curves from the hard regime of cells seeded scaffolds are shown in (D), (E), and (F) for the indentation depths of 500 nm, 1000 nm, and 2000 nm, respectively. The elastic modulus values at 500 nm, 1000 nm, and 2000 nm indentation depths are shown in (G), (H), and (I), respectively.

Fig. 3.9 (A-C) summarizes the young's modulus values determined from nanoindentation tests performed on hydrated scaffolds, cell-seeded scaffolds without BMPs, and cell-seeded scaffolds with BMPs at indentation depths of 500 nm, 1000 nm, and 2000 nm. A 67.4%, 24.5% and 12.3% increase in elastic modulus of semi-hard regions is observed with the addition of BMPs

99

at 500 nm, 1000 nm and 2000 nm indentation (Table 3.3). A 120.4%, 69.2% and 54.2% increase in elastic modulus of hard regions is observed with the addition of BMPs at 500 nm, 1000 nm and 2000 nm indentation (Table 3.3). The values presented here are an average of over 100 nanoindentation test data points for each indentation depth, with standard deviations indicating the range of values where the elastic modulus converges. To begin, in the case of hydrated scaffolds, the elastic modulus values consistently decreased with increasing hydration period for all indentation depths. Thus, the results presented here greatly accord with our previous studies on the degradation of the scaffold in aquatic environments[49], where the degradation of the scaffold and reduction of mechanical integrity is suggested to result in substantially reduced compressive strength and modulus over time. As shown in Fig. 3.9, for the cell-seeded scaffold with and without BMPs, the elastic modulus values increased with time (from one week to nine weeks) for all indentation depths. However, the cell-seeded scaffold with BMPs showed significantly higher elastic modulus and improved mechanical strength than those without BMPs over time. A 120% increase in elastic modulus at 500 nm indentation on scaffolds coated with BMPs indicates more ECM formation, significantly enhancing the overall mechanical characteristics of scaffolds over time, making them more suitable for possible uses in critical bone defect treatment. In addition, for a given indentation depth, peak loads increase over time for both BMP coated and uncoated scaffolds. The peak loads for hard regions in BMP coated scaffolds are significantly higher (~201 µN) as compared to uncoated scaffolds (~89 µN) at 1000 nm after 9 weeks. Significant increases are also observed in other regions. Simultaneously, elastic modulus at 9 weeks increases for BMP coated scaffolds from ~47 MPa to 80 MPa for hard regions at 1000nm (Table 3.4).
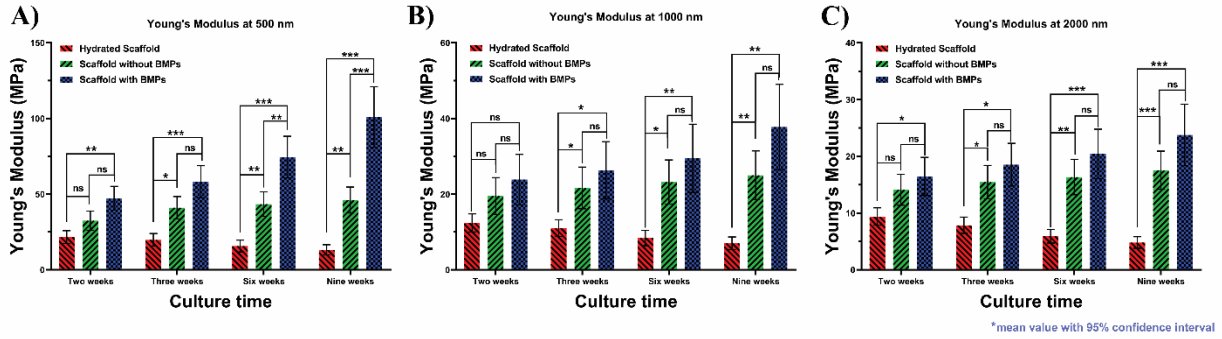
Fig. 3.9. Elastic modulus (E) of the hydrated scaffold, scaffolds seeded with hMSCs and hFOB, scaffolds seeded with hMSCs and hFOB coated with BMP-2 and BMP-7 at two weeks, three weeks, six weeks, and nine weeks (A), (B), and (C) at indentation depths of 500 nm, 1000 nm, and 2000 nm, respectively. $*p < 0.05$, $**p < 0.01$, and $***p < 0.001$ indicate a significant difference between BMPs coated and without BMPs scaffold samples.

This is consistent with increased mineralized nodule formations and ECM formations shown in Fig. 3.5. These, in turn, result from enhanced osteogenic differentiation of osteoblasts mediated by the Wnt/β-catenin signaling pathway, enhanced by BMPs. Thus, the cascade of events initiated by the BMPs impacts bone growth at time intervals much longer than the BMP presence in the scaffolds.

Table 3.3. Quantitative representation of Elastic modulus observed during nanoindentation of scaffolds without BMPs and with BMPs.

Without BMPs scaffolds				With BMPs scaffolds			
Semi-hard regions **Elastic modulus (MPa)**				**Semi-hard regions** **Elastic modulus (MPa)**			
Indentation Depth (nm) / **Culture time (Weeks)**	**500**	**1000**	**2000**	**Indentation Depth (nm)** / **Culture time (Weeks)**	**500**	**1000**	**2000**
Two	33.87	21.57	14.87	**Two**	45.53	27.80	16.10
Three	44.38	24.65	16.98	**Three**	52.84	30.21	18.58
Six	46.61	27.66	17.95	**Six**	70.19	31.48	19.52
Nine	49.44	29.63	19.06	**Nine**	82.75	36.88	21.40
At nine weeks % increase in modulus compared with uncoated					**67.39**	**24.47**	**12.32**
Hard regions **Elastic modulus (MPa)**				**Hard regions** **Elastic modulus (MPa)**			
Indentation Depth (nm) / **Culture time (Weeks)**	**500**	**1000**	**2000**	**Indentation Depth (nm)** / **Culture time (Weeks)**	**500**	**1000**	**2000**
Two	53.57	36.37	23.81	**Two**	71.85	55.98	28.36
Three	63.17	40.12	25.81	**Three**	91.22	63.57	31.18
Six	67.89	42.83	27.39	**Six**	117.29	71.72	36.16
Nine	72.33	47.07	28.83	**Nine**	159.38	79.64	44.45
At nine weeks % increase in modulus compared with uncoated					**120.35**	**69.20**	**54.22**

Table 3.4. Quantitative representation of peak load observed during nanoindentation of scaffolds without BMPs and with BMPs.

Without BMPs scaffolds				With BMPs scaffolds			
Semi-hard regions Peak load (µN)				Semi-hard regions Peak load (µN)			
Culture time (Weeks) \ Indentation Depth (nm)	500	1000	2000	Culture time (Weeks) \ Indentation Depth (nm)	500	1000	2000
Two	15.51	42.45	103.61	Two	24.13	46.08	110.66
Three	17.47	46.08	115.98	Three	29.89	59.04	121.12
Six	21.15	51.15	123.15	Six	36.29	71.86	149.56
Nine	24.25	57.14	129.59	Nine	42.98	84.49	173.68
At nine weeks % increase in modulus compared with uncoated					72.24	47.86	34.02
Hard regions Peak load (µN)				Hard regions Peak load (µN)			
Culture time (Weeks) \ Indentation Depth (nm)	500	1000	2000	Culture time (Weeks) \ Indentation Depth (nm)	500	1000	2000
Two	24.61	45.77	169.01	Two	35.93	114.89	212.28
Three	29.06	64.67	197.11	Three	48.46	133.29	254.14
Six	33.15	74.91	226.78	Six	67.85	171.18	311.29
Nine	38.22	89.08	249.21	Nine	85.03	201.39	361.78
At nine weeks % increase in modulus compared with uncoated					122.48	126.08	45.17

3.4. Conclusion

In this study, we report changes to nanomechanical properties of scaffolds over a period of nine weeks during osteogenesis with the influence of BMPs on nanoclay interlocking scaffolds. The changes in the elastic modulus of the scaffolds are measured with the formation of ECM over time. The mechanical properties observed at different indentation depths (500 nm-2000 nm) are measured using displacement controlled nanoindentation. Furthermore, the indentation results showed that scaffolds degrade in culture media and the elastic modulus reduces over time. In contrast, in cells seeded scaffolds, the cells form ECM, and elastic modulus increases over time.

In addition, BMP-2/BMP-7 coated scaffolds showed higher elastic modulus values (with as much as 120% increase) indicating enhanced ECM formation in BMPs coated samples. BMPs enhanced cell proliferation is observed in the nanoclay based scaffold. Gene expression studies indicate a significant increase in the bone related protein and osteogenesis with BMPs coated samples compared to without BMPs samples, indicating that BMPs play an essential role in osteogenesis and ECM formation. In addition, alizarin Red S staining images show a significant increase in the mineralized bone nodules with BMPs coated samples compared with without BMPs samples suggesting that BMPs play a crucial role in mineralized ECM formation. The BMP release experiments indicate that 100% release occurs at about 2.3 weeks. Interestingly, the data obtained on mechanical properties as well as gene expressions indicate substantial increase at well past the 2.3-week period.

In summary, we report changes in the nanomechanical properties during osteogenesis and bone tissue formation in BMP coated porous scaffolds over extended time periods up to nine weeks. Furthermore, the results indicate that the formation of ECM enhances the elastic modulus of the scaffolds. The role of BMPs in ECM formation lasts much longer (at nine weeks) than the release rate in the scaffolds (100% at 2.3 weeks). Thus, BMPs play a crucial role on initial stages of osteogenesis in the scaffolds. This study provides valuable insight into the mechanisms of the BMPs associated with bone tissue formation through the activation of the Wnt/β-catenin signaling pathway and upregulation of Wnt-related factors. Thus, an initial burst of BMPs can influence long term bone formation without the need for continuous BMP release. Hence this study has potential therapeutic applications for bone regeneration.

3.5. Acknowledgements

3.6. References

[1]   D.J. Prolo, J.J. Rodrigo, Contemporary bone graft physiology and surgery, Clinical Orthopaedics and Related Research® 200 (1985) 322-342.

[2]   A.S. Brydone, D. Meek, S. Maclaine, Bone grafting, orthopaedic biomaterials, and the clinical need for bone engineering, Proceedings of the Institution of Mechanical Engineers, Part H: Journal of Engineering in Medicine 224(12) (2010) 1329-1343.

[3]   J.O. Hollinger, J.C. Kleinschmidt, The critical size defect as an experimental model to test bone repair materials, The Journal of craniofacial surgery 1(1) (1990) 60-68.

[4]   T.A. McCall, D.S. Brokaw, B.A. Jelen, D.K. Scheid, A.V. Scharfenberger, D.C. Maar, J.M. Green, M.R. Shipps, M.B. Stone, D. Musapatika, Treatment of large segmental bone defects with reamer-irrigator-aspirator bone graft: technique and case series, Orthopedic Clinics 41(1) (2010) 63-73.

[5]   N.T. Bennett, G.S. Schultz, Growth factors and wound healing: biochemical properties of growth factors and their receptors, The American Journal of Surgery 165(6) (1993) 728-737.

[6]   D.J. Baylink, R.D. Finkelman, S. Mohan, Growth factors to stimulate bone formation, Journal of Bone and Mineral Research 8(S2) (1993) S565-S572.

[7]   M.R. Urist, Bone: Formation by Autoinduction, Science 150(3698) (1965) 893.

[8]   D.O. Wagner, C. Sieber, R. Bhushan, J.H. Borgermann, D. Graf, P. Knaus, BMPs: From Bone to Body Morphogenetic Proteins, Science Signaling 3(107) (2010) 6.

[9]   T. Katagiri, N. Takahashi, Regulatory mechanisms of osteoblast and osteoclast differentiation, Oral Diseases 8(3) (2002) 147-159.

[10] C. Thouverey, J. Caverzasio, Focus on the p38 MAPK signaling pathway in bone development and maintenance, Bonekey Reports 4 (2015) 8.

[11] A. Oryan, S. Alidadi, A. Moshiri, A. Bigham-Sadegh, Bone morphogenetic proteins: A powerful osteoinductive compound with non-negligible side effects and limitations, Biofactors 40(5) (2014) 459-481.

[12] D.S. Keskin, A. Tezcaner, P. Korkusuz, F. Korkusuz, V. Hasirci, Collagen-chondroitin sulfate-based PLLA-SAIB-coated rhBMP-2 delivery system for bone repair, Biomaterials 26(18) (2005) 4023-4034.

[13] J.N. Zara, R.K. Siu, X.L. Zhang, J. Shen, R. Ngo, M. Lee, W.M. Li, M. Chiang, J. Chung, J. Kwak, B.M. Wu, K. Ting, C. Soo, High Doses of Bone Morphogenetic Protein 2 Induce Structurally Abnormal Bone and Inflammation In Vivo, Tissue Engineering Part A 17(9-10) (2011) 1389-1399.

[14] H.S. Yang, W.G. La, S.H. Bhang, T.J. Lee, M. Lee, B.S. Kim, Apatite-Coated Collagen Scaffold for Bone Morphogenetic Protein-2 Delivery, Tissue Engineering Part A 17(17-18) (2011) 2153-2164.

[15]   S. Govender, C. Csimma, H.K. Genant, A. Valentin-Opran, Y. Amit, R. Arbel, H. Aro, D. Atar, M. Bishay, M.G. Borner, P. Chiron, P. Choong, J. Cinats, B. Courtenay, R. Feibel, B. Geulette, C. Gravel, N. Haas, M. Raschke, E. Hammacher, D. van der Velde, P. Hardy, M. Holt, C. Josten, R.L. Ketterl, B. Lindeque, G. Lob, H. Mathevon, G. McCoy, D. Marsh, R. Miller, E. Munting, S. Oevre, L. Nordsletten, A. Patel, A. Pohl, W. Rennie, P. Reynders, P.M. Rommens, J. Rondia, W.C. Rossouw, P.J. Daneel, S. Ruff, A. Ruter, S. Santavirta, T.A. Schildhauer, C. Gekle, R. Schnettler, D. Segal, H. Seiler, R.B. Snowdowne, J. Stapert, G. Taglang, R. Verdonk, L. Vogels, A. Weckbach, A. Wentzensen, T. Wisniewski, B.S. Grp, Recombinant human bone morphogenetic protein-2 for treatment of open tibial fractures - A prospective, controlled, randomized study of four hundred and fifty patients, Journal of Bone and Joint Surgery-American Volume 84A(12) (2002) 2123-2134.

[16]   G.M. Calori, L. Tagliabue, L. Gala, M. d'Imporzano, G. Peretti, W. Albisetti, Application of rhBMP-7 and platelet-rich plasma in the treatment of long bone non-unions A prospective randomised clinical study on 120 patients, Injury-International Journal of the Care of the Injured 39(12) (2008) 1391-1402.

[17]   G.E. Friedlaender, C.R. Perry, J.D. Cole, S.D. Cook, G. Cierny, G.F. Muschler, G.A. Zych, J.H. Calhoun, A.J. LaForte, S. Yin, Osteogenic protein-1 (bone morphogenetic protein-7) in the treatment of tibial nonunions - A prospective, randomized clinical trial comparing rhOP-1 with fresh bone autograft, Journal of Bone and Joint Surgery-American Volume 83A (2001) S151-S158.

[18]   M.F. Swiontkowski, H.T. Aro, S. Donell, J.L. Esterhai, J. Goulet, A. Jones, P.J. Kregor, L. Nordsletten, G. Paiement, A. Patel, Recombinant human bone morphogenetic protein-2 in open tibial fractures - A subgroup analysis of data combined from two prospective randomized studies, Journal of Bone and Joint Surgery-American Volume 88A(6) (2006) 1258-1265.

[19]   W. Sun, Z.R. Li, F.Q. Gao, Z.C. Shi, Q.D. Zhang, W.S. Guo, Recombinant Human Bone Morphogenetic Protein-2 in Debridement and Impacted Bone Graft for the Treatment of Femoral Head Osteonecrosis, Plos One 9(6) (2014) 6.

[20]   M.D. McKee, Recombinant human bone morphogenic protein-7 - Applications for clinical trauma, Journal of Orthopaedic Trauma 19(10) (2005) S26-S28.

[21]   N. Itasaki, S. Hoppler, Crosstalk Between Wnt and Bone Morphogenic Protein Signaling: A Turbulent Relationship, Developmental Dynamics 239(1) (2010) 16-33.

[22]   Y. Chen, H.C. Whetstone, A. Youn, P. Nadesan, E.C.Y. Chow, A.C. Lin, B.A. Alman, beta-catenin signaling pathway is crucial for bone morphogenetic protein 2 to induce new bone formation, Journal of Biological Chemistry 282(1) (2007) 526-533.

[23]   M. Zhang, Y. Yan, Y.B. Lim, D.Z. Tang, R. Xie, A. Chen, P. Tai, S.E. Harris, L.P. Xing, Y.X. Qin, D. Chen, BMP-2 Modulates beta-Catenin Signaling Through Stimulation of Lrp5 Expression and Inhibition of beta-TrCP Expression in Osteoblasts, Journal of Cellular Biochemistry 108(4) (2009) 896-905.

[24]   L.J. Yang, K. Yamasaki, Y. Shirakata, X.J. Dai, S. Tokumaru, Y. Yahata, M. Tohyama, Y. Hanakawa, K. Sayama, K. Hashimoto, Bone morphogenetic protein-2 modulates Wnt and frizzled expression and enhances the canonical pathway of Wnt signaling in normal keratinocytes, Journal of Dermatological Science 42(2) (2006) 111-119.

[25] G.M. Boland, G. Perkins, D.J. Hall, R.S. Tuan, Wnt 3a promotes proliferation and suppresses osteogenic differentiation of adult human mesenchymal stem cells, Journal of Cellular Biochemistry 93(6) (2004) 1210-1230.

[26] K. Fujita, S. Janz, Attenuation of WNT signaling by DKK-1 and -2 regulates BMP2-induced osteoblast differentiation and expression of OPG, RANKL and M-CSF, Molecular Cancer 6 (2007).

[27] E.C. Rodríguez-Merchán, Bone Healing Materials in the Treatment of Recalcitrant Nonunions and Bone Defects, International Journal of Molecular Sciences 23(6) (2022) 3352.

[28] A.J. Salgado, O.P. Coutinho, R.L. Reis, Bone tissue engineering: state of the art and future trends, Macromolecular bioscience 4(8) (2004) 743-765.

[29] V. Karageorgiou, D. Kaplan, Porosity of 3D biomaterial scaffolds and osteogenesis, Biomaterials 26(27) (2005) 5474-5491.

[30] G. Wei, P.X. Ma, Structure and properties of nano-hydroxyapatite/polymer composite scaffolds for bone tissue engineering, Biomaterials 25(19) (2004) 4749-4757.

[31] L. Xia, K. Lin, X. Jiang, B. Fang, Y. Xu, J. Liu, D. Zeng, M. Zhang, X. Zhang, J. Chang, Effect of nano-structured bioceramic surface on osteogenic differentiation of adipose derived stem cells, Biomaterials 35(30) (2014) 8514-8527.

[32] H. Yanagida, M. Okada, M. Masuda, M. Ueki, I. Narama, S. Kitao, Y. Koyama, T. Furuzono, K. Takakuda, Cell adhesion and tissue response to hydroxyapatite nanocrystal-coated poly (L-lactic acid) fabric, Journal of bioscience and bioengineering 108(3) (2009) 235-243.

[33] K. Rezwan, Q.Z. Chen, J.J. Blaker, A.R. Boccaccini, Biodegradable and bioactive porous polymer/inorganic composite scaffolds for bone tissue engineering, Biomaterials 27(18) (2006) 3413-3431.

[34] A.H. Ambre, D.R. Katti, K.S. Katti, Biomineralized hydroxyapatite nanoclay composite scaffolds with polycaprolactone for stem cell-based bone tissue engineering, Journal of Biomedical Materials Research Part A 103(6) (2015) 2077-2101.

[35] A.H. Ambre, K.S. Katti, D.R. Katti, Nanoclay based composite scaffolds for bone tissue engineering applications, Journal of Nanotechnology in Engineering and Medicine 1(3) (2010) 031013.

[36] A. Ambre, K.S. Katti, D.R. Katti, In situ mineralized hydroxyapatite on amino acid modified nanoclays as novel bone biomaterials, Materials Science & Engineering C-Materials for Biological Applications 31(5) (2011) 1017-1029.

[37] A.H. Ambre, D.R. Katti, K.S. Katti, Nanoclays mediate stem cell differentiation and mineralized ECM formation on biopolymer scaffolds, Journal of Biomedical Materials Research Part A 101(9) (2013) 2644-2660.

[38] K. Kundu, D.R. Katti, K.S. Katti, Tissue-Engineered Interlocking Scaffold Blocks for the Regeneration of Bone, JOM 72(4) (2020) 1443-1457.

[39] R. Subbiah, A. Cheng, M.A. Ruehle, M.H. Hettiaratchi, L.E. Bertassoni, R.E. Guldberg, Effects of controlled dual growth factor delivery on bone regeneration following composite bone-muscle injury, Acta Biomaterialia 114 (2020) 63-75.

[40] P. Yilgor, R.A. Sousa, R.L. Reis, N. Hasirci, V. Hasirci, Effect of scaffold architecture and BMP-2/BMP-7 delivery on in vitro bone regeneration, Journal of Materials Science: Materials in Medicine 21(11) (2010) 2999-3008.

[41] K.S. Katti, D.R. Katti, A.H. Ambre, Asme, UNNATURAL AMINO ACIDS MODIFIED CLAYS FOR DESIGN OF SCAFFOLDS FOR BONE TISSUE ENGINEERING, Nemb2010: Proceedings of the Asme First Global Congress on Nanoengineering for Medicine and Biology - 2010 (2010) 227-228.

[42] K.S. Katti, A.H. Ambre, N. Peterka, D.R. Katti, Use of unnatural amino acids for design of novel organomodified clays as components of nanocomposite biomaterials, Philosophical Transactions of the Royal Society a-Mathematical Physical and Engineering Sciences 368(1917) (2010) 1963-1980.

[43] A.H. Ambre, D.R. Katti, K.S. Katti, Biomineralized hydroxyapatite nanoclay composite scaffolds with polycaprolactone for stem cell-based bone tissue engineering, Journal of Biomedical Materials Research - Part A (2015).

[44] K. Kundu, A. Afshar, D.R. Katti, M. Edirisinghe, K.S. Katti, Composite nanoclay-hydroxyapatite-polymer fiber scaffolds for bone tissue engineering manufactured using pressurized gyration, Composites Science and Technology 202 (2021) 108598.

[45] W.C. Oliver, G.M. Pharr, An improved technique for determining hardness and elastic modulus using load and displacement sensing indentation experiments, Journal of materials research 7(6) (1992) 1564-1583.

[46] M.S. Rahman, N. Akhtar, H.M. Jamil, R.S. Banik, S.M. Asaduzzaman, TGF-β/BMP signaling and other molecular events: regulation of osteoblastogenesis and bone formation, Bone research 3(1) (2015) 1-20.

[47] T. Komori, Regulation of osteoblast differentiation by Runx2, Osteoimmunology, Springer2009, pp. 43-49.

[48]   E.S. Sandhurst, S.V. Jaswandkar, K. Kundu, D.R. Katti, K.S. Katti, H. Sun, D. Engebretson, K.R. Francis, Nanoarchitectonics of a Microsphere-Based Scaffold for Modeling Neurodevelopment and Neurological Disease, ACS Applied Bio Materials (2022).

[49]   A. Sharma, M.D.S. Molla, K.S. Katti, D.R. Katti, Multiscale models of degradation and healing of bone tissue engineering nanocomposite scaffolds, Journal of Nanomechanics and Micromechanics 7(4) (2017) 04017015.

[50]   D. Sikdar, D. Katti, K. Katti, B. Mohanty, Effect of organic modifiers on dynamic and static nanomechanical properties and crystallinity of intercalated clay–polycaprolactam nanocomposites, Journal of applied polymer science 105(2) (2007) 790-802.

[51]   C.X.F. Lam, M.M. Savalani, S.-H. Teoh, D.W. Hutmacher, Dynamics of in vitro polymer degradation of polycaprolactone-based scaffolds: accelerated versus simulated physiological conditions, Biomedical materials 3(3) (2008) 034108.

[52]   W.D. Nix, H. Gao, Indentation size effects in crystalline materials: a law for strain gradient plasticity, Journal of the Mechanics and Physics of Solids 46(3) (1998) 411-425.

[53]   A. Iost, R. Bigot, Indentation size effect: reality or artefact?, Journal of Materials Science 31(13) (1996) 3573-3577.

[54]   M.F. Horstemeyer, M.I. Baskes, S.J. Plimpton, Length scale and time scale effects on the plastic flow of fcc metals, Acta Materialia 49(20) (2001) 4363-4374.

[55]   M.V. Swain, Fracture Mechanics of Ceramics, Vol. 6, Edited by RC Bradt, AG Evans, FF Lange and DPH Hasselman, Plenum Press, New York (1983) 355-69.

[56]   S.-Y. Tee, A. Bausch, P.A. Janmey, The mechanical cell, Current biology: CB 19(17) (2009) R745.

[57] R. Khanna, K.S. Katti, D.R. Katti, Experiments in nanomechanical properties of live osteoblast cells and cell–biomaterial interface, Journal of Nanotechnology in Engineering and Medicine 2(4) (2011).

CHAPTER 4. COMPOSITE NANOCLAY-HYDROXYAPATITE-POLYMER FIBER SCAFFOLDS FOR BONE TISSUE ENGINEERING MANUFACTURED USING PRESSURIZED GYRATION

This chapter describes the fabrication and characterization of polymer nanoclay composite fiber prepared by the pressure gyration method for bone tissue engineering application. The contents of this chapter have been published in Krishna Kundu, Ayda Afshar, Dinesh R. Katti, Mohan Edirisinghe, Kalpana S. Katti, "Composite nanoclay-hydroxyapatite-polymer fiber scaffolds for bone tissue engineering manufactured using pressurized gyration", Composites Science and Technology 202 (2021) 108598.

4.1. Introduction

While numerous operational techniques such as bone autografts, allografts and biomaterial implantation with biocompatible, osteointegrative and osteoconductive properties are available, they have significant limitations[1]. Post-surgery, autografts are often accompanied with nerve damage, infections, morbidity, scarring and chronic pain[2–4]. Additionally, allografts have the potential for disease conductivity, infection, and incite immune reactions following the implant rejection. Researchers have attempted to overcome these complications using natural or synthetic biomaterials. Moreover, the alternative to traditional bone grafting therapies is the use of an engineered scaffold designed to support cell migration, regeneration, and proliferation[5–7]. Cellular growth and attachment are largely dependent on both the size and density of the pores within a scaffold, which, depending on the materials and applications, must be carefully controlled to specific parameters. One of the main reasons why porosity is important is that cellular networks rely on interconnected pathways for nutrient transportation and cell proliferation, imitating the structure of the native extracellular matrix (ECM) environment[8–12]. Scaffolds are intended to

serve as fillers that occupy bone defects or available space in damaged organs/ tissues, and their resorption activity enables them to provide a basis for new tissue growth that will replace the scaffolds[13–15]. A multifunctional scaffold must be produced that can modulate the balance between bone resorption and bone regeneration to repair bone defects[16]. The demand for developing new bioactive scaffolds is growing, which can promote the formation of functional tissues by directing stem cell differentiation. Often critical-sized-bone-defects or defects that lack the ability to heal spontaneously without medical intervention are at least two times the diameter of the bone[17]. Such defects require filling with scaffold systems that are also able to bear load[18]. Putty-type materials are required for filling around the larger scaffolds. The nanocomposite fiber materials presented here are good candidates for use as packing cement around scaffolds for large and critical-sized defects as well as novel candidates for filling smaller bone defects.

Polymeric fibers have been extensively used to prepare porous polymer scaffolds for tissue engineering applications in the form of woven and nonwoven fibers[19,20], often for non-union and non load-bearing applications. There are several techniques to prepare nanofibers, such as phase separation[21], template synthesis[22], self-assembly[23], and electrospinning[24,25]. Usually, spinning techniques are used to prepare nonwoven polymer fibers using polymer solutions or melt[26,27]. The spinning technique can produce the fibers in the nano- to micrometer range, resembles the collagen fibers in the extracellular matrix (ECM)[28–30]. These fibers have a high surface-area-to-volume ratio, a low density, and a high surface volume[31]. Among these techniques, electrospinning is the most popular technique. Still, it has several drawbacks, such as a low production rate, utilization of very high voltage, and sensitivity to the dielectric constant of the polymer solution. Those drawbacks demand a novel, cost-effective technique to fabricate

nanofibers with a high production rate[32]. Typically, pressurized gyration generates fibers with the combination of centrifugal and dynamic fluid flow forces which act against surface tension. As the pressurized gyration consists of simultaneous centrifugal spinning and solution blowing, fibers size, diameter, morphology is greatly influenced by the rotation speed, and pressure of the process[32,33]. Polymer concentration and the evaporation rate of the solvent determine the yield and the quality of the fibers. This technique has been widely used to prepare nanofibers from various polymers for different applications, such as drug delivery and tissue engineering[32–35].

Some of the most striking characteristics of nanofibers is their high surface to volume ratio and high porosity, which makes it a robust and desirable candidate for bone tissue regeneration[36–38]. With remarkable interconnectivity between fiber pores, they are able to shape highly porous mesh networks, making them an attractive option for a host of advanced healthcare applications[39–42]. Many therapeutic agents can be individually or simultaneously incorporated with fibers for bone tissue regeneration. Clay/copolymer nanocomposite films are commonly used in bone regeneration applications because they provide mechanical support and the aspect ratio, the degree of intercalation/exfoliation and the ionic strength of the clay can be adjusted according to the drug properties prior to the addition of the clay to the copolymer matrices. To some extent, their morphology replicates that of the native extracellular matrix (ECM), which is prolific to faster tissue regeneration[43,44]. In general, if the physical interaction between the drug and the fibrous scaffold is optimized to tailor the average pore size of the target drug, higher drug loading efficiency can be achieved. In order to achieve a preferred fiber diameter for drug delivery applications, it is important to optimize the spinning parameters.

Among various polymers, PCL is a semi-crystalline and hydrophobic polymer which has gained attention in musculoskeletal tissue engineering because of its biocompatibility, and superior

mechanical properties[45]. It can be used to produce a wide range of scaffolding materials[46]. Some of the problems associated with PCL, however, include its slow *in vivo* degradation rate and lack of bioactive characteristics[47]. The degradation properties of PCL can be enhanced by integrating nanoparticles such as hydroxyapatite, silica, magnetic nanoparticles, and clays into polymer scaffolds[48–50] or by combining PCL with other rapidly degrading polymers.

In the cell-based regeneration therapy, cells-scaffold interaction is very important for the new tissue formations, as cells require a three-dimensional environment with proper stimuli to form tissue. After the introduction of the cell-based regeneration therapy in the early 1990s[51], numerous works have been done to optimize the various properties of the scaffold to provide the appropriate environment for the cells with adequate biophysical and biochemical stimuli to accelerate the regeneration process. One of the major challenges in the field of tissue engineering is to incorporate these properties into the scaffold. Different inorganic fillers are added to the scaffold to improve cell adhesion, cell-scaffold interaction, and facilitate tissue formation for tissue engineering purposes. Hydroxyapatite (HAP) nano-clay has a strong resemblance to the mineral bone; it provides adequate calcification sites while increasing biocompatibility and osteoconductivity of the scaffold[52–55]. Synthetic HAP can form a chemical bond with the host tissue and offers a greater benefit in clinical applications compared to most other bone substitutes such as allografts or metallic implants. HAP has been reported to enhance osteoblast cell attachment and proliferation, which is a highly desired characteristic for bone defect fillers and to promote bone growth when placed in differentiated bone cells[56–58]. The addition of HAP to polymeric fibers is crucial for bone tissue engineering. Synthetic HAP has excellent osteoconductive and osteoinductive abilities and exhibits slow biodegradability and

biocompatibility[59]. The biocompatibility with soft tissue such as skin and muscles makes it ideal for bone regeneration, bone augmentation, bone-implant coating, and dental implants[18].

There are other trace elements, such as sodium, magnesium, silicon, which are also used in the scaffold with HAP to improve bioactivity, cell attachment, cell differentiation, bone formation, and mineralization[60–63]. Sodium montmorillonite (Na-MMT) clay is the most commonly used layered silicate for the preparation of polymer-clay nanocomposites for its high surface-to-volume ratio and high aspect ratio at low filler content ($> 5\%$), which helps to establish better interaction with the polymer matrix and to enhance the mechanical properties[64–66]. The nanometer thickness of the MMT layer provides a high aspect ratio that can also be beneficial in obtaining cellular response that favours tissue formation as nanoscale features facilitate cell adhesion and increase the biodegradability of the scaffold[66–68].

Mesenchymal stem cells (MSCs) have been considered as the cell source for tissue-engineering applications due to their ease of isolation, ability to proliferate in an undifferentiated state[69], capability of differentiating into different cell lineages including bone[70,71], ligament[72], adipose[73], cartilage[74,75], and muscle[76]. In several studies, MSCs have been seeded on the porous scaffold and implanted on the animal model to achieve the direct repair of bone defects[77,78]. Co-culture of osteoblast cells with MSCs induce the osteogenic differentiation of MSCs[18]. Osteoblast cells enhance the osteogenic differentiation by a direct cell-to-cell interaction[79,80] and are critically involved in bone remodeling[81].

In this study, we investigate the feasibility of fiber-based nanoclay scaffolds for bone tissue engineering applications. We observed the effect of HAP-Clay in polymeric fibers scaffold in terms of cell viability, cell proliferation, osteogenesis, mineral depositions, and collagen fiber formations, which are the essential elements of bone regeneration.

4.2. Materials and methods

4.2.1. Modification of MMT clay

The detailed procedure for the modification of Na-MMT clay is described elsewhere[82–85]. Briefly, 5-aminovaleric acid solution was added to preheated (60°C) MMT suspension, and the mixture solution was kept for stirring. After one hour, the obtained slurry was centrifuged and washed to remove chloride ions followed by drying at 70°C, grinding, and sieving to obtain a fine powder. Na-MMT clay (SWy-2) was procured from Clay Minerals Society. The 5-aminovaleric acid was obtained from Sigma-Aldrich.

4.2.2. Preparation of in situ HAPclay

We have followed the procedure described in previous studies [82–85] to prepare *in situ* HAP clay. Briefly, the organically modified MMT clay powder was dissolved into Na_2HPO_4 solution by stirring at room temperature (xx ^{o}C) for 2 hours. Further, $CaCl_2$ solution was added, and this suspension was stirred vigorously for 8 hours (pH 7.4). The precipitate obtained settled in 12 hours, was centrifuged and dried (70°C). Subsequently, it was ground and sieved to obtain a fine powder. The compounds Na_2HPO_4 and $CaCl_2$ were purchased from J.T. Baker.

4.2.3. Preparation of polymer and clay solution

Polycaprolactone (PCL, M_w 800 00 gmol^{-1}) was purchased from Sigma-Aldrich (Poole, UK). Multiple polycaprolactone (PCL) solutions were prepared at different concentrations. As a result of preliminary testing, it was found that 15 w/v% PCL in chloroform produced the optimal fiber yield. Therefore, 15 w/v% PCL in chloroform was prepared and served as a control sample. Different HAP MMT-Clay and MMT-Clays concentrations (2 w/w % and 5 w/w %) were loaded into PCL polymer solution followed by stirring for 24 h using magnetic stirrers to obtain a homogeneous solution.

4.2.4. Pressurized gyration

Pressurized gyration is a simple technique for mass production of fibers and fibrous structures with controllable fiber size and fiber size distribution with high yield. The setup consists of an aluminum cylindrical vessel (60 mm diameter, 35 mm height) with a total of 24 orifices on the wall of the vessel, each orifice is 0.5 mm in diameter. The vessel top is connected to a DC motor that generates a maximum speed of 36 000 rpm, and the bottom is connected to a constant nitrogen gas stream (N_2) that generates pressure between 0.1 – 0.3 MPa. The fibers produced by this technique depend on rotational speed of the vessel, air pressure and the concentration of polymer solution. The polymer solution is placed into the vessel before spinning. High speed and high-pressure cause fibers to erupt, elongate, and thin. As the fibers thin, the solvent evaporates from the fiber strand. In this study, we report the creation of PCL fibers incorporated with HAP MMT nanoclays. The maximum rotation speed was used as it increases the centrifugal force, and as such, the fibers leave at greater kinetic energy and thinness. When increasing pressure, in general fibers are manufactured thinner due to the gas pressure providing a greater elongation power. However, increased pressure (gas flow) can also increase evaporation which can lead to thicker fibers due to increase in polymer concentration and higher solution viscosity.

4.2.5. Preparation of fiber scaffold

The polymer composite fibers samples from the pressurized gyration method were received from Edirisinghe-lab, Mechanical Engineering, UCL. A 3D cylindrical scaffold of dimension 3 mm (height) X 10 mm (diameter) was prepared by pressing 0.065g of fibers (Fig. 4.1) and subsequently these were used them for cell culture experiments.
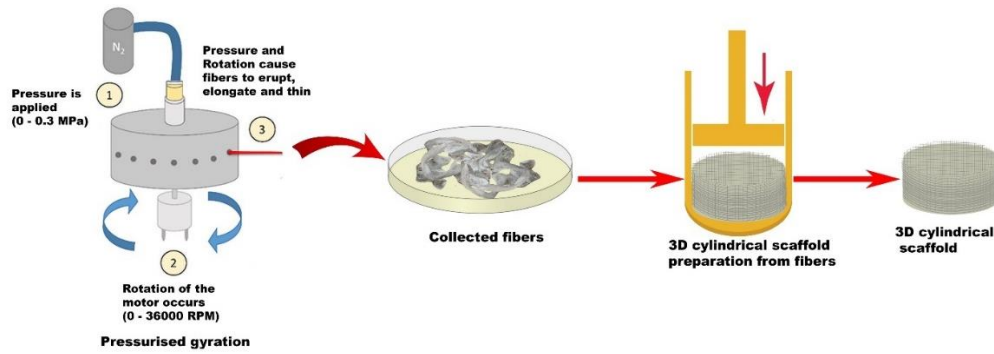
Fig. 4.1. Schematic diagram illustrating the pressurized gyration set up and 3 key phases and 3D scaffold preparation from polymer composite fibers generated by pressurized gyration.

4.2.6. Scaffolds for cell culture experiments

3D scaffold samples were kept in UV for 45 mins for sterilization. After that, sample were immersed in 100 % ethanol for 24 h. Then, samples were washed with PBS and kept in the cell culture media for 24 hours prior to using them for cell culture experiments. Initially, 5×10^4 osteoblast cells and 5×10^4 MSCs were seeded on each scaffold.

4.2.7. Cell line and culture medium

The human osteoblast cell line (hFOB 1.19) was obtained from ATCC and maintained in a media consist of 90% HyQ Dulbecco's Modified Eagle medium DMEM-12(1:1) from Hyclone, 10% FBS from ATCC and 0.6% G418 solution (antibiotic) from JR scientific. Human bone marrow Mesenchymal stem cells (MSCs) were obtained from Lonza and maintained in MSCGM™ Bulletkit™ medium. The Bulletkit™ medium was prepared by adding MSCGM™ SingleQuots™ (Lonza) to MSCBM™ (Lonza). All the cells were maintained at 37$^\text{o}$C and 5% CO2 in a completely humidified incubator.

4.2.8. Surface morphology of fibers

The surface morphology of the nanoclays containing PCL fibers were studied using scanning electron microscopy (SEM) using a Hitachi HN004, which operated at an accelerating voltage of 5kV. Before analysis, samples were pre-coated with gold sputter using Quorum Q1500R

ES for 90 seconds. For diameter, an average of 100 fiber strand readings was measured at random using ImageJ software. The average fiber diameter was created and plotted on histograms using OriginPro (Origin Lab Corporation, Northampton, MA, USA).

4.2.9. WST-1 assay

WST-1 assay was performed in scaffolds seeded with MSCs and human osteoblast cells (1:1). WST-1 (Roche, IN) assay was used to perform cell viability as per the manufacturer's protocol. Briefly, cells were cultured on scaffolds for 7, 14, and 21 days. Following which, cell-seeded scaffolds were removed from the culture medium, washed with PBS, and then placed in a new 48-well plate with a solution comprising 450 ml of DMEM and 50 ml of WST-1 reagent per well before incubating for 4 h in standard humidified condition. After 4 h, scaffolds were removed from the 48-well plates and the intensity of yellow color, which directly represents the number of live cells (slightly red-colored solution turns yellow as metabolically active cells cleave the tetrazolium salts of WST-1 reagent to formazan), was read at 450 nm using a microplate spectrophotometer (Bio-Rad, Benchmark Plus).

4.2.10. Alkaline phosphate assay

3D fiber scaffolds seeded with human osteoblast cells were incubated at 37ºC, 5% CO_2 under humidified conditions for 7, 14, 21 days. These samples were washed with PBS after incubation, transferred to unused wells of 48-well plates, and 850mL Triton X-100 (1 v/v %solution) was added to each well containing the samples. Cell lysates (250mL) obtained after subjecting the immersed samples to two freeze-thaw cycles (27^0C to 37^0C) were transferred to new 48-well plates and incubated with p-nitrophenyl phosphate (250mL) at room temperature for 60 min. 3N NaOH (70mL) was further added to the wells and absorbance readings will be taken at 405 nm using a microplate spectrophotometer (Bio-Rad, Benchmark Plus).

4.2.11. Alizarin red staining

3D fiber scaffolds seeded with MSCs and human osteoblast cells were incubated at 37ºC, 5% CO_2 under humidified conditions for 7, 14 and 21 days and were then washed with PBS before fixing with 4% paraformaldehyde for 15 min. PBS was used to wash the fixed samples. Further 2% Alizarin Red S (ARS) staining solution of 50 µL was dropped on the washed scaffold and kept for 150 s. After 150 s, the scaffold was washed using PBS many times in order to remove the unbound stain and dried at room temperature for imaging. Images were captured using an inverted microscope at 20× magnification. For quantification, stained samples were immersed into 700 µL of 10% acetic acid solution and incubated at room temperature for 5 min to solubilize the stain and absorbance of the released Alizarin Red S stain was measured at 405 nm.

4.2.12. Immunocytochemistry assay

3D fiber scaffolds seeded with MSCs and human osteoblast cells were incubated at 37ºC, 5% CO_2 under humidified conditions for 21 days. Cell-seeded scaffolds were washed in PBS and fixed in 4% paraformaldehyde (PFA) for 30 min, followed by permeabilizing with 0.2% TritonX-100 in PBS for 5 min. Further, the samples were blocked with 0.2% fish skin gelatin (FSG) for 45 min, followed by incubation with the primary antibody overnight at 4 °C. Collagen I (Abcam) antibody was diluted in a blocking buffer (0.2% FSG in PBS with 0.02% Tween20) at a dilution of 1:100. Finally, Alexa Flour 488/647 conjugated secondary antibodies corresponding specifically to the origin of the used primary antibody was added at 1:250 dilution and incubated for 45 min at 25 °C. The nuclei were counterstained with DAPI. The stained samples were observed under a confocal microscope (Zeiss Axio Observer Z1 LSM 700)

4.2.13. Scanning Electron Microscopy (SEM) and SEM-EDS (Energy Dispersive Spectroscopy)

3D fiber scaffolds seeded with MSCs and human osteoblast cells were incubated at 37°C, 5% CO_2 under humidified conditions for 21 days. The samples were washed with PBS, fixed using glutaraldehyde (2.5%), subsequently dehydrated using ethanol series (10% v/v, 30% v/v, 50% v/v, 70% v/v, and 100%) and then dried with hexamethyldisilazane. SEM imaging was then performed on the dried samples after coating them with gold and mounting them on the SEM sample stubs. SEM-EDS experiments were also performed on these scaffolds.

4.2.14. Statistical analysis

Two-way ANOVA followed by Tukey's post hoc multiple comparison test was used for statistical analysis. Data were considered significantly different when the probability values obtained were< 0.05 ($P< 0.05$). Quantitative data were expressed as a mean ± standard deviation. Triplicate samples were used for performing all the experiments.

4.3. Results and discussion

4.3.1. Microstructures of the polymer fibers

The PCL solutions were spun consecutively at 36 000 rpm at different pressures (no applied pressure, i.e. no gas flow and therefore gyration only, 0.1 MPa, 0.2 MPa, 0.3 MPa) and also varying the concentration of MMT-Clay and HAP MMT-Clay (2 w/w % and 5 w/w %) to identify the effects of pressure and concentration on the microstructure of the fibers. The PCL fiber microstructures are characterized using scanning electron microscopy (SEM). (Fig. 4.2). The fiber size also increased with increase in the nano-clay concentration. Interestingly, the formation of pores within fibers was observed to increase at higher HAP and MMT loading. The SEM images emphasized the alignment of PCL/ MMT and PCL/ HAP fibers. The morphology reveals non-

uniformity of fiber diameter across the fiber surface. PCL MMT-Clay fibers are observed as dark regions within the fiber strands, and PCL HAP MMT-Clay fibers are detected as blocks attached to the fiber pores. We also observe that the increase in the concentration of MMT-Clay (Fig. 4.2 a,b,c) results in increase of the diameter of the fiber from 1.07 µm ± 452 nm to 3.21 µm ± 2.57 µm, and increases roughness of the fibers. It was also found that the increase in the gas pressure greatly affects fiber diameter. In pressurize gyration, a gradient in the pressure results in the acceleration of the polymer solution out from the orifices. Therefore, an increase in gas pressure causes jet elongation resulting in fiber thinning; hence at higher gas pressures, usually thinner fibers are achieved. For the same concentration (5 w/w %) of the MMT-Clay (Fig. 4.2 b,c), with the reduction of pressure from 0.3 MPa to pressureless, the diameter of the fibers increases from 2.01 µm ± 1.38 µm to 3.21 µm ± 2.57. Similar effects of pressure and concentration were observed with HAP MMT-Clay. With the increase in the concentration from 2% to 5%; an increase in the diameter of the fibers from 1.34 µm ± 767 nm to 3.24 µm ± 3.68 µm (Fig. 4.2 d,e,f) is observed resulting in the formation of thick HAP-Clay blocks embedded in the submicron fibrous structure and decrease in the pressure from 0.3 MPa to pressureless, at the same concentration (5%) results in increase the diameter of the fibers from 2.95 µm ± 1.85 µm to 3.24 µm ± 3.68 µm(Fig. 4.2 e,f).
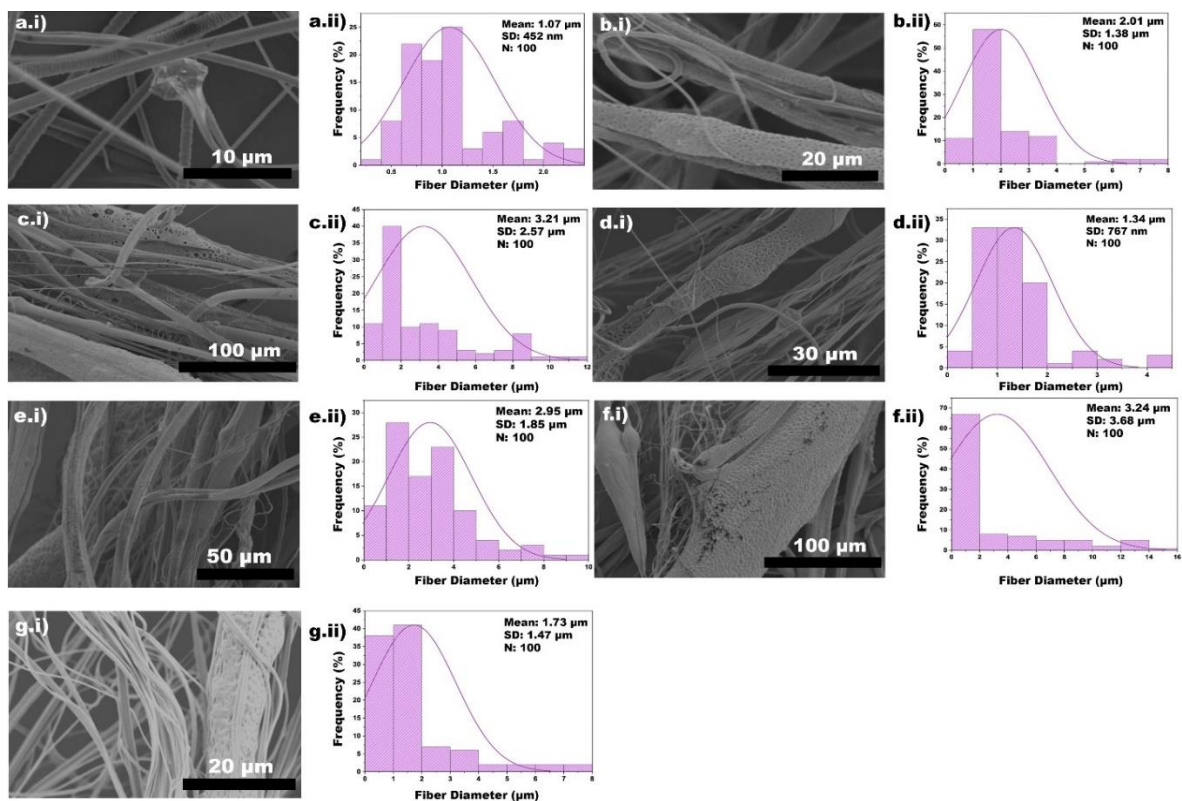
Fig. 4.2. SEM images of 15 w/v% PCL/ chloroform incorporated with: a.i) 2 w/w % MMT-Clay (0.3MPa), b.i) 5 w/w % MMT-Clay (0.3MPa), c.i) 5 w/w % MMT-Clay (no applied pressure), d.i) 2 w/w % HAP MMT-Clay (0.3MPa), e.i) 5 w/w % HAP MMT-Clay (0.3MPa), f.i) 5 w/w % HAP MMT-Clay (0 MPa), g.i) PCL/ chloroform (no applied pressure), and a.ii, b.ii, c.ii, d.ii, e.ii, f.ii, g.ii) respective fiber diameter distributions-all spun at 36,000 rpm.

4.3.2. Cell viability

The WST-1 assay was performed to evaluate cell viability and proliferation of both MSCs and osteoblasts on the scaffolds to evaluate the biocompatibility of synthesized polymer fiber scaffolds over 21 days. The cell viability measured using the absorbance at 450 nm is proportional to the amount of dehydrogenase activity in the cells[86]. Fig. 4.3 represents the cell viability of different fiber scaffolds seeded with MSCs and osteoblasts for 7 days, 14 days, and 21 days. We observed an increase in cell viability over time for all the three different scaffold systems. As compared to the control group (PCL fiber scaffolds), no significant increase in the cell viability was observed with PCL MMT-Clay fiber scaffolds at day 7 and day 14; however, at day 21 a

significant increase was observed with PCL MMT-Clay fiber scaffolds. Compared to the control group (PCL fiber scaffolds), a significant increase in the cell viability was observed with PCL HAP MMT-Clay fiber over a period of 21 days. We also compared PCL HAP MMT-Clay fiber scaffolds with scaffolds PCL MMT-Clay fiber scaffolds and observed a significant increase in cell viability over the period of 21 days. Collectively, the addition of HAP-Clay in the PCL fibers immensely enhanced the cell viability of the scaffolds.
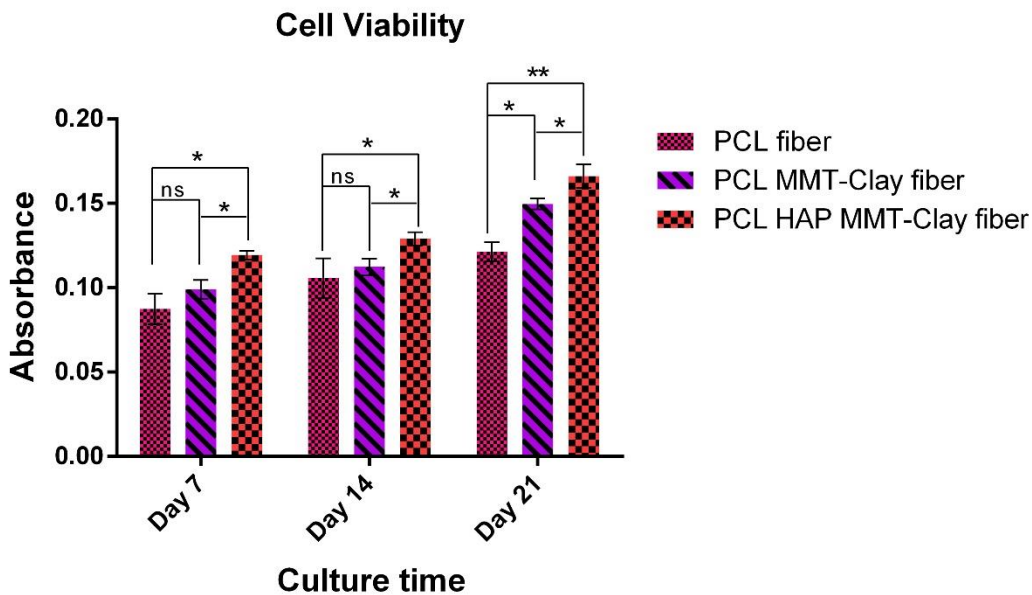
Fig. 4.3. Cell viability of scaffolds seeded with MSCs and osteoblast cells. (Two-way anova followed by post hoc tukey test p* < 0.05, p* *< 0.01, p*** <0.001, n = 3.)

4.3.3. Osteogenic differentiation

Osteogenic differentiation of MSCs was assessed using the alkaline phosphatase (ALP) assay. Fig. 4.4 represents the ALP activity of different fiber scaffolds seeded with MSCs and osteoblasts for 7 days, 14 days, and 21 days. Initially, we observed an increase in ALP activity over 14 days for all the three different scaffold systems. This was followed by a gradual decline during the study period for all the samples. Compared to the control group (PCL fiber scaffolds), no significant increase in the ALP activity was observed with PCL MMT-Clay fiber scaffolds and

PCL HAP MMT-Clay fiber scaffolds at day 7; however, at day 14 a significant increase was observed with both PCL MMT-Clay fiber scaffolds and PCL HAP MMT-Clay fiber scaffolds. We also compared PCL HAP MMT-Clay fiber scaffolds with scaffolds PCL MMT-Clay fiber scaffolds; at day 7 no significant increase in ALP activity was observed; however, a significant increase with PCL HAP MMT-Clay fiber scaffolds was seen at day 14. The initial increase in the ALP activity till 14 days indicates that, initially, the rate of differentiation of MSCs into osteoblast phenotype was higher. The decrease in ALP activity indicates the fewer number of MSCs differentiated into osteoblast phenotype. It has been reported that the ALP activity of MSCs decreases during osteogenic differentiation[87]. Results indicate that HAP-Clay in the PCL fibers very significantly enhanced the ALP activity of the scaffolds.
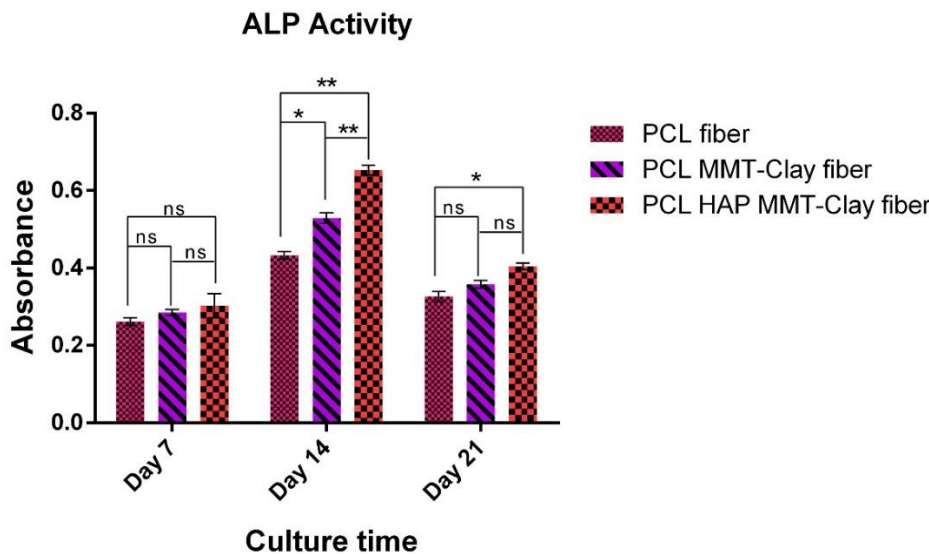
Fig. 4.4. ALP activity of scaffolds seeded with MSCs and osteoblast cells. (Two-way anova followed by post hoc tukey test $p^* < 0.05$, $p^{**} < 0.01$, $p^{***} < 0.001$, n = 3.)

4.3.4. Bone mineralization

The Alizarin red S (ARS) staining was performed to check the formation of the mineralized extracellular matrix (ECM) on the polymeric fiber scaffolds (Fig. 4.5). The red color formation with Alizarin red S indicates the deposition of the inorganic matrix by cells cultured on scaffolds.

Prior studies have shown calcium deposition increases over time in PCL/ in situ HAP clay scaffold seeded with MSCs over 23 days[88]. As seen in Fig. 4.5, ARS staining showed dispersed and limited calcium deposition at 7 days, while enhanced calcium deposition was observed at 21 days (Fig. 4.5a), which was further confirmed by quantification of the released ARS (Fig. 4.5b).

Over time, calcium deposition increases in all the fiber scaffold systems. Compared to the control group (PCL fiber scaffolds), no significant increase in the calcium deposition was observed with PCL MMT-Clay fiber scaffolds and PCL HAP MMT-Clay fiber scaffolds at day 7. However, at day 14 and day 21, significant increase with both PCL MMT-Clay fiber scaffolds and PCL HAP MMT-Clay fiber scaffolds was observed. A significant increase in the mineral deposition was observed with PCL HAP MMT-Clay fiber scaffolds in comparison with PCL MMT-Clay fiber scaffolds. Hence, the addition of HAP-Clay in the PCL fibers enhanced the mineral deposition of the scaffolds.
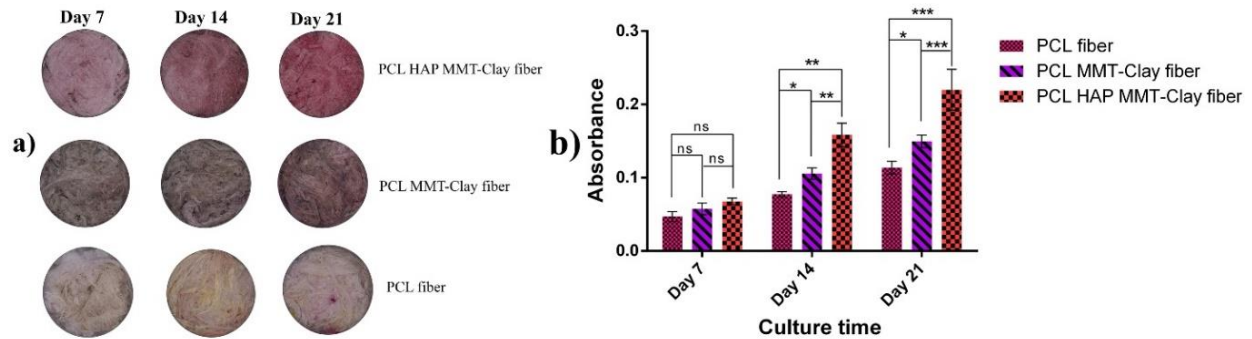
Fig. 4.5. Alizarin Red S staining (a) and quantification absorbance assay (b) of scaffolds seeded with MSCs and osteoblast cells.

4.3.5. Collagen and collagen fibril formation

Immunocytochemistry assay was performed to evaluate the formation of collagen. The appearance of green color indicates the formation of the collagen by primary- secondary antigen-antibody interaction. A prior study,[18] reported that well defined fibril structure of collagen is observed in 11 days for PCL/in situ HAP clay scaffolds seeded with MSCs and osteoblast cells

129

coated with bone morphogenic proteins. Fig. 4.6. shows confocal microscope images of PCL fibers scaffold, PCL MMT-Clay fibers scaffold, PCL HAPMMT-Clay fibers scaffold seeded with MSCs and osteoblasts at day 21. We observed the least collagen formation in scaffolds with PCL fibers, and the highest with PCL HAP MMT-Clay fibers. Thus it appears that HAP-Clay particles actively induce collagen formation.
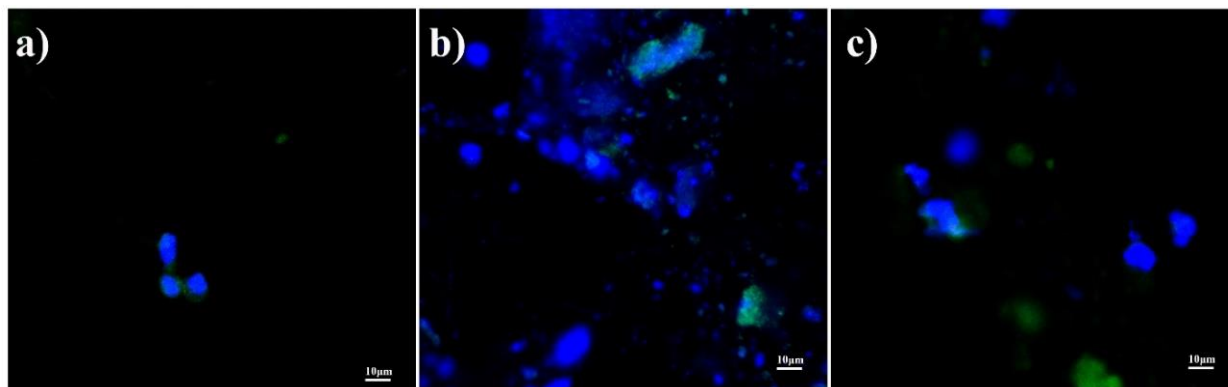
Fig. 4.6. Confocal microscope image of a) PCL fiber, b) PCL MMT-Clay fiber, c) PCL HAP MMT-Clay fiber scaffolds seeded with MSCs & osteoblasts at day 21. Nuclei were stained with DAPI (blue). Anti-rabbit Col-1 primary antibody was used with goat anti-rabbit IgG (H + L) AF 488 (green) secondary-antibody.

4.3.6. Scanning Electron Microscopy (SEM) studies

In order to investigate the morphology of cells at the different fiber scaffolds, SEM imaging was performed. Fig. 4.7 shows the SEM images of a) PCL fibers, b) PCL MMT-Clay fibers, c) PCL HAP MMT-Clay fiber scaffolds seeded with MSCs and osteoblasts at day 21. As seen, a flattened morphology of the cells was observed in the surface of the fibers indicated with red circles/ellipses; More cells were observed with PCL HAP MMT-Clay fiber scaffolds.
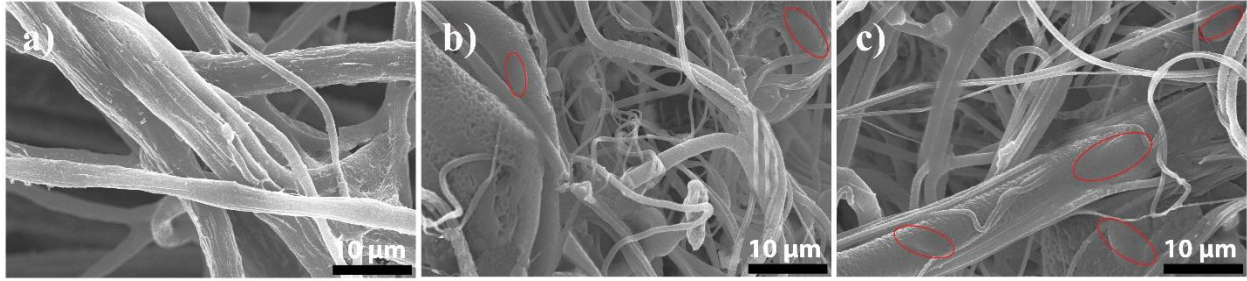
Fig. 4.7. SEM micrographs of a) PCL fiber, b) PCL MMT-Clay fiber, c) PCL HAP MMT-Clay fiber scaffolds seeded with MSCs and osteoblasts at day 21 (red circles/ellipses represent flattened cells on the surface of the fibers).

4.3.7. Elemental composition of nanocomposite fibers

As determined by EDS, fiber samples indicate elemental constituents of carbon, sodium, silicon, chloride, gold, and calcium. The source of the sodium and chloride in the spectrum is the entrapped NaCl in the fibers from the cell culture medium, and the source of the gold is the coating. The elemental spectrum of the PCL MMT-Clay fibers is shown in Fig. 4.8a. The presence of Si in this spectrum indicates the dispersion of the clay particles (montmorillonite) in the fibers. The elemental spectrum of the PCL HAP MMT-Clay fibers is shown in Fig. 4.8b. The presence of Si and Ca in this spectrum indicates the dispersion of the HAP-clay particles in the fibers. The results indicate the formation of composites of PCL with HAP MMT-Clay through the pressurized gyration method. indicates the dispersion of the clay particles (montmorillonite) in the fibers. The elemental spectrum of the PCL HAP MMT-Clay fibers is shown in Fig. 4.8b. The presence of Si and Ca in this spectrum indicates the dispersion of the HAP-clay particles in the fibers. The results indicate the formation of composites of PCL with HAP MMT-Clay through the pressurized gyration method.
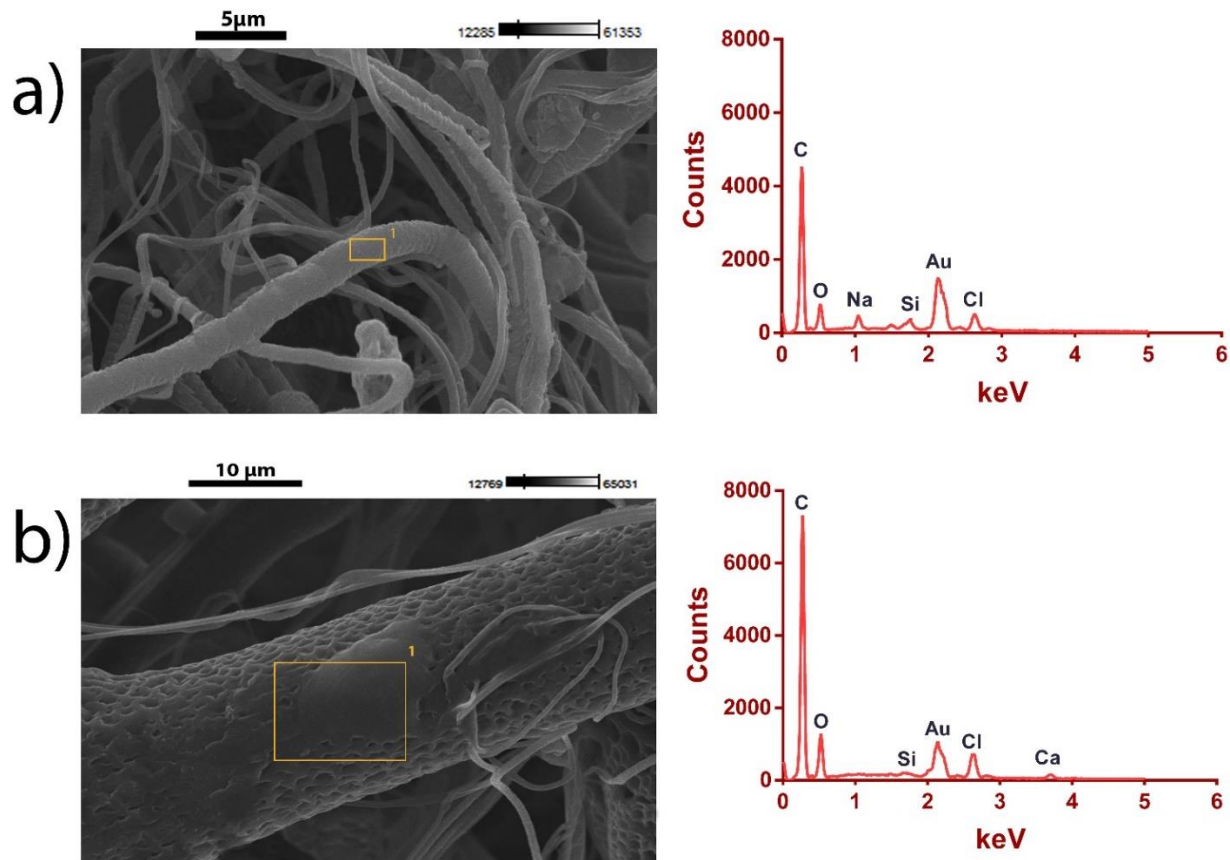
Fig. 4.8. Elemental spectra of a) PCL MMT-Clay fiber, b) PCL HAP MMT-Clay fiber, yellow boxes shown in left-hand side images represent the spots from which localized elemental data were obtained during SEM-EDS experiments.

4.4. Conclusions

This comprehensive investigation demonstrates novel methods in fabrication of HAP nanoclay PCL composite fibers for use in bone tissue regeneration applications. Using a pressurized gyration setup, we fabricated PCL fibers incorporated with nano HAP MMT-Clay and nano MMT-Clay at 2 w/w% and 5 w/w%. The results demonstrated that the polymer fiber scaffolds as prepared are biocompatible, cells were able to thrive and differentiate on the fiber scaffolds. Calcium deposition and collagen formation, the main components of ECM formation, were also observed. The addition of HAP-Clay was found to enhance the cell viability and proliferation, on PCL fiber scaffolds. Further, the intracellular ALP levels increased with PCL HAP MMT-Clay

fiber scaffold, indicating enhancement of the osteogenic differentiation of MSCs. Immunocytochemistry was also performed to evaluate the formation of the collagen in the PCL fiber scaffolds. PCL HAP MMT-Clay fibers scaffold showed enhanced collagen formation as opposed to control, PCL fiber scaffolds. Compressed pellets of the nanoclay HAP polymer fibers fabricated here have potential applications as fillers for non-union bone defects as well as their use as 'cement' for non-union scaffold preparations for bone tissue regeneration.

4.5. Acknowledgements

4.6. References

[1] Z. Sheikh, N. Hamdan, Y. Ikeda, M. Grynpas, B. Ganss, M. Glogauer, Natural graft tissues and synthetic biomaterials for periodontal and alveolar bone reconstructive applications: a review, Biomater. Res. 21(9) (2017) 1-20.

[2] G. Fernandez de Grado, L. Keller, Y. Idoux-Gillet, Q. Wagner, A.M. Musset, N. Benkirane-Jessel, F. Bornert, D. Offner, Bone substitutes: a review of their characteristics, clinical use, and perspectives for large bone defects management, J. Tissue Eng. 9 (2018) 1-18.

[3] S. Titsinides, G. Agrogiannis, T. Karatzas, Bone grafting materials in dentoalveolar reconstruction: A comprehensive review, Jpn. Dent. Sci. Rev. 55 (2019) 26–32.

[4] H.-S. Sohn, J.-K. Oh, Review of bone graft and bone substitutes with an emphasis on fracture surgeries, Biomater. Res. 23(9) (2019) 1-7.

[5]   I. Bružauskaitė, D. Bironaitė, E. Bagdonas, E. Bernotienė, Scaffolds and cells for tissue regeneration: different scaffold pore sizes—different cell effects, Cytotechnology. 68 (2016) 355–369.

[6]   M. Rasoulianboroujeni, N. Kiaie, F.S. Tabatabaei, A. Yadegari, F. Fahimipour, K. Khoshroo, L. Tayebi, Dual Porosity Protein-based Scaffolds with Enhanced Cell Infiltration and Proliferation, Sci. Rep. 8 (2018) 14889.

[7]   M. Ansari, Bone tissue regeneration: biology, strategies and interface studies, Prog. Biomater. 8 (2019) 223–237.

[8]   Y. Wang, W. Cui, X. Zhao, S. Wen, Y. Sun, J. Han, H. Zhang, Bone remodeling-inspired dual delivery electrospun nanofibers for promoting bone regeneration, Nanoscale. 11 (2019) 60–71.

[9]   Y.F. Goh, I. Shakir, R. Hussain, Electrospun fibers for tissue engineering, drug delivery, and wound dressing, J. Mater. Sci. 48 (2013) 3027–3054.

[10]   A. Ali, S. Bano, S.S. Poojary, D. Kumar, Y.S. Negi, Effect of incorporation of montmorillonite on Xylan/Chitosan conjugate scaffold, Colloids Surfaces B Biointerfaces. 180 (2019) 75–82.

[11]   S.E. Enderami, S.F. Ahmadi, R.N. Mansour, S. Abediankenari, H. Ranjbaran, M. Mossahebi-Mohammadi, R. Salarinia, H. Mahboudi, Electrospun silk nanofibers improve differentiation potential of human induced pluripotent stem cells to insulin producing cells, Mater. Sci. Eng. C. 108 (2020) 110398.

[12]   T. Ghassemi, A. Shahroodi, M.H. Ebrahimzadeh, A. Mousavian, J. Movaffagh, A. Moradi, Current concepts in scaffolding for bone tissue engineering, Arch. Bone Jt. Surg. 6 (2018) 90–99.

[13] S. Stratton, N.B. Shelke, K. Hoshino, S. Rudraiah, S.G. Kumbar, Bioactive polymeric scaffolds for tissue engineering, Bioact. Mater. 1 (2016) 93–108.

[14] J.-H. Zeng, S.-W. Liu, L. Xiong, P. Qiu, L.-H. Ding, S.-L. Xiong, J.-T. Li, X.-G. Liao, Z.-M. Tang, Scaffolds for the repair of bone defects in clinical studies: a systematic review, J. Orthop. Surg. Res. 13(33) (2018) 1-14.

[15] A. Sharikova, Z.I. Foraida, L. Sfakis, L. Peerzada, M. Larsen, J. Castracane, A. Khmaladze, Characterization of nanofibers for tissue engineering: Chemical mapping by Confocal Raman microscopy, Spectrochim. Acta Part A Mol. Biomol. Spectrosc. 227 (2020) 117670.

[16] Haryanto, S. Kim, J.H. Kim, J.O. Kim, S. Ku, H. Cho, D.H. Han, P. Huh, Fabrication of poly(ethylene oxide) hydrogels for wound dressing application using E-beam, Macromol. Res. 22 (2014) 131–138.

[17] A. Nauth, M.D. McKee, T.A. Einhorn, J.T. Watson, R. Li, E.H. Schemitsch, Managing bone defects, J. Orthop. Trauma. 25 (2011) 462–466.

[18] K. Kundu, D.R. Katti, K.S. Katti, Tissue-Engineered Interlocking Scaffold Blocks for the Regeneration of Bone, JOM. 72 (2020) 1443–1457.

[19] M. Van Lieshout, G. Peters, M. Rutten, F. Baaijens, A knitted, fibrin-covered polycaprolactone scaffold for tissue engineering of the aortic valve, Tissue Eng. 12 (2006) 481–487.

[20] D. Li, T. Wu, N. He, J. Wang, W. Chen, L. He, C. Huang, H.A. EI-Hamshary, S.S. Al-Deyab, Q. Ke, X. Mo, Three-dimensional polycaprolactone scaffold via needleless electrospinning promotes cell proliferation and infiltration, Colloids Surfaces B Biointerfaces. 121 (2014) 432–443.

[21] J. Zhao, W. Han, H. Chen, M. Tu, R. Zeng, Y. Shi, Z. Cha, C. Zhou, Preparation, structure and crystallinity of chitosan nano-fibers by a solid–liquid phase separation technique, Carbohydr. Polym. 83 (2011) 1541–1546.

[22] S.L. Tao, T.A. Desai, Aligned Arrays of Biodegradable Poly(ε-caprolactone) Nanowires and Nanofibers by Template Synthesis, Nano Lett. 7 (2007) 1463–1468.

[23] L.E.R. O'Leary, J.A. Fallas, E.L. Bakota, M.K. Kang, J.D. Hartgerink, Multi-hierarchical self-assembly of a collagen mimetic peptide from triple helix to nanofibre and hydrogel, Nat. Chem. 3 (2011) 821–828.

[24] P. Sofokleous, E. Stride, M. Edirisinghe, Preparation, Characterization, and Release of Amoxicillin from Electrospun Fibrous Wound Dressing Patches, Pharm. Res. 30 (2013) 1926–1938.

[25] U.E. Illangakoon, H. Gill, G.C. Shearman, M. Parhizkar, S. Mahalingam, N.P. Chatterton, G.R. Williams, Fast dissolving paracetamol/caffeine nanofibers prepared by electrospinning, Int. J. Pharm. 477 (2014) 369–379.

[26] G. Narayanan, B.S. Gupta, A.E. Tonelli, Poly(ε-caprolactone) nanowebs functionalized with α- And γ-cyclodextrins, Biomacromolecules. 15 (2014) 4122–4133.

[27] J. Ren, K.A. Blackwood, A. Doustgani, P.P. Poh, R. Steck, M.M. Stevens, M.A. Woodruff, Melt-electrospun polycaprolactone strontium-substituted bioactive glass scaffolds for bone regeneration, J. Biomed. Mater. Res. Part A. 102 (2014) 3140–3153.

[28] D. Sankar, K.T. Shalumon, K.P. Chennazhi, D. Menon, R. Jayakumar, Surface plasma treatment of poly(caprolactone) micro, nano, and multiscale fibrous scaffolds for enhanced osteoconductivity, Tissue Eng. - Part A. 20 (2014) 1689–1702.

[29] W. Liu, S. Thomopoulos, Y. Xia, Electrospun Nanofibers for Regenerative Medicine, Soft Fibrillar Materials: Fabrication and Applications, Chapter 9 (2013) 265–295.

[30] V. Beachley, E. Katsanevakis, N. Zhang, X. Wen, A Novel Method to Precisely Assemble Loose Nanofiber Structures for Regenerative Medicine Applications, Adv. Healthc. Mater. 2 (2013) 343–351.

[31] C.J. Luo, S.D. Stoyanov, E. Stride, E. Pelan, M. Edirisinghe, Electrospinning versus fibre production methods: From specifics to technological convergence, Chem. Soc. Rev. 41 (2012) 4708–4735.

[32] H. Alenezi, M.E. Cam, M. Edirisinghe, Experimental and theoretical investigation of the fluid behavior during polymeric fiber formation with and without pressure, Appl. Phys. Rev. 6 (2019) 041401.

[33] S. Mahalingam, G.G. Ren, M.J. Edirisinghe, Rheology and pressurised gyration of starch and starch-loaded poly(ethylene oxide), Carbohydr. Polym. 114 (2014) 279–287.

[34] B.T. Raimi-Abraham, S. Mahalingam, P.J. Davies, M. Edirisinghe, D.Q.M. Craig, Development and Characterization of Amorphous Nanofiber Drug Dispersions Prepared Using Pressurized Gyration, Mol. Pharm. 12 (2015) 3851–3861.

[35] B.T. Raimi-Abraham, S. Mahalingam, M. Edirisinghe, D.Q.M. Craig, Generation of poly(N-vinylpyrrolidone) nanofibres using pressurised gyration, Mater. Sci. Eng. C. 39 (2014) 168–176.

[36] P. Prabhu, Nanofibers for Medical Diagnosis and Therapy, in: A. Barhoum, M. Bechelany, A.S.H. Makhlouf (Eds.), Handb. Nanofibers, Springer International Publishing, Cham. (2019) 831–867.

[37]   A. Memic, T. Abudula, H.S. Mohammed, K. Joshi Navare, T. Colombani, S.A. Bencherif, Latest Progress in Electrospun Nanofibers for Wound Healing Applications, ACS Appl. Bio Mater. 2 (2019) 952–969.

[38]   S.P. Miguel, R.S. Sequeira, A.F. Moreira, C.S.D. Cabral, A.G. Mendonça, P. Ferreira, I.J. Correia, An overview of electrospun membranes loaded with bioactive molecules for improving the wound healing process, Eur. J. Pharm. Biopharm. 139 (2019) 1–22.

[39]   A. Barhoum, K. Pal, H. Rahier, H. Uludag, I.S. Kim, M. Bechelany, Nanofibers as new-generation materials: From spinning and nano-spinning fabrication techniques to emerging applications, Appl. Mater. Today. 17 (2019) 1–35.

[40]   S. Ahn, H.A.M. Ardoña, P.H. Campbell, G.M. Gonzalez, K.K. Parker, Alfalfa Nanofibers for Dermal Wound Healing, ACS Appl. Mater. Interfaces. 11 (2019) 33535–33547.

[41]   I.S. Kurtz, J.D. Schiffman, Current and emerging approaches to engineer antibacterial and antifouling electrospun nanofibers, Materials (Basel). 11 (2018) 1059.

[42]   S. Nemati, S. jeong Kim, Y.M. Shin, H. Shin, Current progress in application of polymeric nanofibers to tissue engineering, Nano Converg. 6 (2019) 1–16.

[43]   F. Paladini, M. Pollini, Antimicrobial silver nanoparticles for wound healing application: Progress and future trends, Materials (Basel). 12 (2019) 2540.

[44]   S. Ahn, C.O. Chantre, A.R. Gannon, J.U. Lind, P.H. Campbell, T. Grevesse, B.B. O'Connor, K.K. Parker, Soy Protein/Cellulose Nanofiber Scaffolds Mimicking Skin Extracellular Matrix for Enhanced Wound Healing, Adv. Healthc. Mater. 7 (2018) 1701175.

[45]   J. Ko, N.K. Mohtaram, F. Ahmed, A. Montgomery, M. Carlson, P.C.D. Lee, S.M. Willerth, M.B.G. Jun, Fabrication of poly (ε-caprolactone) microfiber scaffolds with varying topography and mechanical properties for stem cell-based tissue engineering applications, J. Biomater. Sci. Polym. Ed. 25 (2014) 1–17.

[46]   M.J. Mochane, T.S. Motsoeneng, E.R. Sadiku, T.C. Mokhena, J.S. Sefadi, Morphology and properties of electrospun PCL and its composites for medical applications: A mini review, Appl. Sci. 9 (2019) 2205.

[47]   S.Y. Reyes-López, D. Cornejo-Monroy, G. González-García, A Novel Route for the Preparation of Gold Nanoparticles in Polycaprolactone Nanofibers, J. Nanomater. 2015 (2015) 1–7.

[48]   D. Chuan, R. Fan, Y. Wang, Y. Ren, C. Wang, Y. Du, L. Zhou, J. Yu, Y. Gu, H. Chen, G. Guo, Stereocomplex poly(lactic acid)-based composite nanofiber membranes with highly dispersed hydroxyapatite for potential bone tissue engineering, Compos. Sci. Technol. 192 (2020) 108107.

[49]   Y.S. Cho, M. Quan, S.H. Lee, M.W. Hong, Y.Y. Kim, Y.S. Cho, Assessment of osteogenesis for 3D-printed polycaprolactone/hydroxyapatite composite scaffold with enhanced exposure of hydroxyapatite using rat calvarial defect model, Compos. Sci. Technol. 184 (2019) 107844.

[50]   P. Melo, A.M. Ferreira, K. Waldron, T. Swift, P. Gentile, M. Magallanes, M. Marshall, K. Dalgarno, Osteoinduction of 3D printed particulate and short-fibre reinforced composites produced using PLLA and apatite-wollastonite, Compos. Sci. Technol. 184 (2019) 107834.

[51]   R. Langer, J.P. Vacanti, Tissue engineering, Science. 260 (1993) 920–926.

[52] S. Bose, S. Dasgupta, S. Tarafder, A. Bandyopadhyay, Microwave-processed nanocrystalline hydroxyapatite: Simultaneous enhancement of mechanical and biological properties, Acta Biomater. 6 (2010) 3782–3790.

[53] G.E. Poinern, R.K. Brundavanam, N. Mondinos, Z.T. Jiang, Synthesis and characterisation of nanohydroxyapatite using an ultrasound assisted method, Ultrason. Sonochem. 16 (2009) 469–474.

[54] R.Z. LeGeros, Calcium phosphate-based osteoinductive materials, Chem. Rev. 108 (2008) 4742–4753.

[55] M.P. Ginebra, M. Espanol, E.B. Montufar, R.A. Perez, G. Mestres, New processing approaches in calcium phosphate cements and their applications in regenerative medicine, Acta Biomater. 6 (2010) 2863–2873.

[56] R. Nawang, M.Z. Hussein, K.A. Matori, C.A. Che Abdullah, M. Hashim, Physicochemical properties of hydroxyapatite/montmorillonite nanocomposite prepared by powder sintering, Results Phys. 15 (2019) 102540.

[57] A.H. Ambre, D.R. Katti, K.S. Katti, Biomineralized hydroxyapatite nanoclay composite scaffolds with polycaprolactone for stem cell-based bone tissue engineering, J. Biomed. Mater. Res. - Part A. 103 (2015) 2077–2101.

[58] G. Wu, F. Huang, Y. Huang, Y. Chen, L. Zheng, H. Wang, Y. Xie, Bone inductivity comparison of control versus non-control released rhBMP2 coatings in 3D printed hydroxyapatite scaffold, J. Biomater. Appl. 34 (2020) 1254–1266.

[59] B. Huang, C. Vyas, J.J. Byun, M. El-Newehy, Z. Huang, P. Bártolo, Aligned multi-walled carbon nanotubes with nanohydroxyapatite in a 3D printed polycaprolactone scaffold stimulates osteogenic differentiation, Mater. Sci. Eng. C. 108 (2020) 110374.

[60] S. Bose, G. Fielding, S. Tarafder, A. Bandyopadhyay, Understanding of dopant-induced osteogenesis and angiogenesis in calcium phosphate ceramics, Trends Biotechnol. 31 (2013) 594–605.

[61] S. Bose, G. Fielding, S. Tarafder, A. Bandyopadhyay, Trace element doping in calcium phosphate ceramics to understand osteogenesis and angiogenesis, Trends Biotechnol. 18 (2013) 1199–1216.

[62] C. Dai, H. Guo, J. Lu, J. Shi, J. Wei, C. Liu, Osteogenic evaluation of calcium/magnesium-doped mesoporous silica scaffold with incorporation of rhBMP-2 by synchrotron radiation-based μCT, Biomaterials. 32 (2011) 8506–8517.

[63] S. Bose, S. Tarafder, A. Bandyopadhyay, Effect of Chemistry on Osteogenesis and Angiogenesis Towards Bone Tissue Engineering Using 3D Printed Scaffolds, Ann. Biomed. Eng. 45 (2017) 261–272.

[64] V. Mittal, Polymer layered silicate nanocomposites: A review, Materials (Basel). 2 (2009) 992–1057.

[65] S. Sinha Ray, M. Okamoto, Polymer/layered silicate nanocomposites: A review from preparation to processing, Prog. Polym. Sci. 28 (2003) 1539–1641.

[66] K.S. Katti, D.R. Katti, R. Dash, Synthesis and characterization of a novel chitosan/montmorillonite/ hydroxyapatite nanocomposite for bone tissue engineering, Biomed. Mater. 3 (2008) 034122.

[67] A.J. Mieszawska, J.G. Llamas, C.A. Vaiana, M.P. Kadakia, R.R. Naik, D.L. Kaplan, Clay enriched silk biomaterials for bone formation, Acta Biomater. 7 (2011) 3036–3041.

[68]   A.H. Ambre, D.R. Katti, K.S. Katti, Nanoclays mediate stem cell differentiation and mineralized ECM formation on biopolymer scaffolds, J. Biomed. Mater. Res. Part A. 101A (2013) 2644–2660.

[69]   Y. Shi, G. Hu, J. Su, W. Li, Q. Chen, P. Shou, C. Xu, X. Chen, Y. Huang, Z. Zhu, X. Huang, X. Han, N. Xie, G. Ren, Mesenchymal stem cells: a new strategy for immunosuppression and tissue repair, Cell Res. 20 (2010) 510–518.

[70]   D.J. Prockop, Marrow stromal cells as stem cells for nonhematopoietic tissues, Science. 276 (1997) 71–74.

[71]   S.E. Haynesworth, J. Goshima, V.M. Goldberg, A.I. Caplan, Characterization of cells with osteogenic potential from human marrow, Bone. 13 (1992) 81–88.

[72]   G.H. Altman, R.L. Horan, I. Martin, J. Farhadi, P.R.H. Stark, V. Volloch, J.C. Richmond, G. Vunjak-Novakovic, D.L. Kaplan, Cell differentiation by mechanical stress, FASEB J. 16 (2002) 1–13.

[73]   J.N. Beresford, J.H. Bennett, C. Devlin, M.E. Owen, Evidence for an inverse relationship between the differentiation of adipocytic and osteogenic cells, Bone Miner. 17 (1992) 198.

[74]   S. Wakitani, T. Goto, S.J. Pineda, R.G. Young, J.M. Mansour, A.I. Caplan, V.M. Goldberg, Mesenchymal cell-based repair of large, full-thickness defects of articular cartilage., J. Bone Jt. Surg. 76 (1994) 579–592.

[75]   B. Johnstone, T.M. Hering, A.I. Caplan, V.M. Goldberg, J.U. Yoo, In vitro chondrogenesis of bone marrow-derived mesenchymal progenitor cells, Exp. Cell Res. 238 (1998) 265–272.

[76]   S. Wakitani, T. Saito, A.I. Caplan, Myogenic cells derived from rat bone marrow mesenchymal stem cells exposed to 5-azacytidine, Muscle Nerve. 18 (1995) 1417–1426.

[77] H. Petite, V. Viateau, W. Bensaïd, A. Meunier, C. de Pollak, M. Bourguignon, K. Oudina, L. Sedel, G. Guillemin, Tissue-engineered bone regeneration, Nat. Biotechnol. 18 (2000) 959–963.

[78] E. Kon, A. Muraglia, A. Corsi, P. Bianco, M. Marcacci, I. Martin, A. Boyde, I. Ruspantini, P. Chistolini, M. Rocca, R. Giardino, R. Cancedda, R. Quarto, Autologous bone marrow stromal cells loaded onto porous hydroxyapatite ceramic accelerate bone repair in critical-size defects of sheep long bones, J. Biomed. Mater. Res. 49 (2000) 328–337.

[79] L.C. Gerstenfeld, J. Cruceta, C.M. Shea, K. Sampath, G.L. Barnes, T.A. Einhorn, Chondrocytes Provide Morphogenic Signals That Selectively Induce Osteogenic Differentiation of Mesenchymal Stem Cells, J. Bone Miner. Res. 17 (2002) 221–230.

[80] J.M. Dayer, P. Isler, L.P. Nicod, Adhesion molecules and cytokine production, Am. Rev. Respir. Dis. 148 (1993) S70–S74.

[81] R. Civitelli, Cell-Cell Communication in Bone, Calcif. Tissue Int. 56 (1995) S29–S31.

[82] K.S. Katti, A.H. Ambre, N. Peterka, D.R. Katti, Use of unnatural amino acids for design of novel organomodified clays as components of nanocomposite biomaterials, Philos. Trans. R. Soc. A Math. Phys. Eng. Sci. 368 (2010) 1963–1980

[83] A.H. Ambre, K.S. Katti, D.R. Katti, Nanoclay Based Composite Scaffolds for Bone Tissue Engineering Applications, J. Nanotechnol. Eng. Med. 1 (2010) 031013.

[84] K.S. Katti, D.R. Katti, A.H. Ambre, Unnatural amino acids modified clays for design of scaffolds for bone tissue engineering, in: Proc. ASME 1st Glob. Congr. Nanoeng. Med. Biol. NEMB2010, American Society of Mechanical Engineers Digital Collection. (2010) 227–228.

[85] A. Ambre, K.S. Katti, D.R. Katti, In situ mineralized hydroxyapatite on amino acid modified nanoclays as novel bone biomaterials, Mater. Sci. Eng. C. 31 (2011) 1017–1029.

[86] A.H. Cory, T.C. Owen, J.A. Barltrop, J.G. Cory, Use of an aqueous soluble tetrazolium/formazan assay for cell growth assays in culture, Cancer Commun. 3 (1991) 207–212.

[87] L.-Y. Sun, D.-K. Hsieh, P.-C. Lin, H.-T. Chiu, T.-W. Chiou, Pulsed electromagnetic fields accelerate proliferation and osteogenic gene expression in human bone marrow mesenchymal stem cells during osteogenic differentiation, Bioelectromagnetics. 31 (2009) 209–219.

[88] S. Kar, H. Jasuja, D.R. Katti, K.S. Katti, Wnt/β-Catenin Signaling Pathway Regulates Osteogenesis for Breast Cancer Bone Metastasis: Experiments in an In Vitro Nanoclay Scaffold Cancer Testbed, ACS Biomater. Sci. Eng. 6 (2020) 2600–2611.

CHAPTER 5. AMINOACIDS MODIFIED NANOCLAYS AS A COMPONENT OF HAP/PCL NANOCOMPOSITE SCAFFOLDS AS CANCER TESTBED: IN-VITRO AND IN-SILICO STUDY

This chapter describes the in-silico design of the unnatural amino acids modified clays and discusses the potential of these nano clay incorporated polymer scaffolds as cancer testbeds. The contents of this chapter are going to be submitted for publication. The article is coauthored by Krishna Kundu, Hanmant Gaikwad, Sharad V Jaswandkar, Dinesh R. Katti, and Kalpana S. Katti.

5.1. Introduction

Langer and Vacanti described tissue engineering nearly 29 years ago in 1993 as an interdisciplinary field of research that applies both engineering principles and life science processes and phenomena to the production of biological substitutes that repair, maintain, or enhance tissue function.[1] The tissue engineering discipline largely relies on porous 3D scaffolds to offer the appropriate microenvironment for optimal tissue and organ regeneration.[2] These scaffolds, which are often seeded with cells and relevant growth factors, serve as tissue development templates. The core emphasis of tissue engineering is the development of biocompatible materials with suitable mechanical properties that facilitate tissue growth, differentiation, and regeneration.[3] Therefore, over the last three decades, significant efforts have been devoted to developing composite systems using polymers and nanoscale fillers that can satisfy requirements such as biocompatibility, biodegradability, surface properties, and mechanical properties needed for materials used in tissue engineering.[4-7] The first work on polymer-based nanocomposites was published in 1965, and it investigated the adsorption of methyl methacrylate-based polymer chains on the montmorillonite (MMT) clay surface. [8] Later, research was undertaken on the amalgamation of clays in different polymeric matrix types such as

thermosets,[9] thermoplastics,[10] and elastomers[11]. Furthermore, Toyota's research group made the first successful effort to make nylon-6/silicate clay nanocomposites in 1995, which fueled the development of sophisticated polymeric/nanoclay composites fabrication for medicinal applications.[12] PCNs are nanocomposites made of clay particles with at least one dimension in the nanoscale range spread in a polymer matrix. Compared to neat polymers and polymers with micron-sized fillers, PCNs exhibit considerable improvements in their properties such as mechanical strength[13, 14], thermal stability[15], decreased gas permeability [16], decreased ionic conductivity [17], and effects on the degradability of biodegradable polymers [18]. Previously, the molecular architectures of intercalated nanocomposites were explored using the molecular dynamics (MD) approach[19, 20]. Our previous simulation-based investigation on PCNs demonstrated an altered phase theory concept. According to the findings, the atomic-scale interactions between clay and Polymer in PCNs result in an "altered polymer phase" with different elastic properties than the neat polymer.[20] This altered polymeric phase caused the increase in mechanical characteristics of PCNs. Our prior simulation study on PCNs also discovered that the properties of the clay and polymer, as well as their interactions at the interfaces, alter the properties of polymer and clay, which has a major impact on the mechanical behavior of PCNs.[21]

Nano-sized montmorillonite (MMT) clay is a crucial component of PCNs, accounting for their greatly improved characteristics. Sodium montmorillonite (Na-MMT) is a layered silicate from the 2: 1 phyllosilicate family.[22-24] In each layer of MMT, one octahedral alumina sheet is located between two tetrahedral silica sheets. Each layer has a thickness in the nanometer scale and a lateral size in the micrometer range. Isomorphic substitutions occur in Na-MMT layers, generating a negative charge that is adjusted by exchangeable cations such as calcium, sodium,

146

and magnesium in the interlayer space. Pure MMT clay is hydrophilic by nature and can be modified organophilic by substituting the cations in the interlayer with cationic surfactants like alkylphosphonium or alkylammonium ions. Cationic surfactants also may increase spacing between interlayers, enhancing polymeric species' intercalation in the interlayer.[22-24] MMT possesses therapeutic qualities, including the capability to adsorb bacterial toxins and dietary toxins linked with gastrointestinal distress.[25] Although MMT clay has medicinal qualities and multiple studies reported the use of MMT clay for drug release and drug delivery applications, numerous studies have also been reported demonstrating the utilization of MMT for structural applications in biomaterials. Some investigations on the utilization of chitosan and MMT have described the construction of chitosan–MMT nanocomposite films with increased tensile strength.[26-28] The presence of MMT clay enhanced the thermal properties and increased the elastic modulus and hardness of exfoliated–intercalated chitosan–MMT nanocomposites.[29] Lin et al. created chitosan–clay nanocomposites that improved tensile strength while decreasing in vitro degradation.[29] Electrospinning has also been used to create poly- (3-caprolactone)–MMT nanocomposites that showed enhanced stiffness compared to neat poly-(3-caprolactone) without a noticeable drop in polymer ductility. Gelatin–MMT–chitosan scaffold developed by Zheng et al. presented an enhancement in the mechanical properties and the degradation rate due to the addition of MMT clay.[30] In prior research, we developed chitosan–MMT–hydroxyapatite (HAP) nanocomposite that showed a considerable increase in nanomechanical performance in comparison to chitosan–MMT and chitosan–HAP composites.[31] Clay modification is crucial in the preparation of nanocomposites since it can impact the properties of the resulting nanocomposites. The interaction among the polymer and the functional groups of the modifier employed for clay modifications influence the extent of polymer intercalation in the

147

interlayer gap of clay. Molecular dynamics simulations based on modeling studies on PCNs have highlighted the significance of interactions between polymers, clay, and organic modifiers on the crystallinity and nanomechanical characteristics of PCNs.[20] Our earlier simulation-based research on amino acids and intercalate clays demonstrated that amino acids could intercalate clays and that chain length and modifier functionality influence the clay's intercalation.[32] Furthermore, we discovered that organic modifiers influence the nanomechanical characteristics and crystallinity of the formed PCNs.[33] Therefore, it is critical to utilize a suitable modifier to get the desired characteristics in the composites. Non-genetically coded amino acids can be natural or synthetic.[34] They can be utilized as chiral building blocks, molecular scaffolds in the production of combinatorial libraries, and molecular probes in studying biological systems.[35] Our previous experimental study on Sodium montmorillonite (Na-MMT) clay modification with amino acids revealed that d-spacing changes in Na-MMT clay are favorable for bone biomaterials applications.[19] There is still a lot of room to use MMT clay's structural features as a biomaterial by altering the interlayer gap between clay sheets while maintaining or enhancing biocompatibility. We modified the MMT clay with three unnatural amino acids in the current study. The X-ray diffraction (XRD) technique was used to study d-spacing changes in clay by amino acid intercalations. The FTIR was utilized to characterize the modified Na-MMT clay, while the cell culture experiments were employed to assess the modified MMT clay's biocompatibility. Further, a molecular dynamic simulation of intercalated MMT clays illustrates the atomic scale interaction between unnatural amino acids and clay sheets that is responsible for the modified d-spacing in MMT clays.

5.2. Materials and methods

5.2.1. Modification of MMT clay

Na-MMT clay (SWy-2) was purchased from the Clay Minerals Society (Wyoming). The received Na-MMT clay is modified with 5-aminovaleric acid, 2-aminopimelic acid, 4-(4-Aminophenyl) butyric acid described in detail in previous studies [36, 37]. In brief, preheated (60°C) amino acids solution was added to the oven (60oC) MMT suspension and stirred for one hour. After one hour, the slurry was separated using a centrifuge, followed by drying at 70°C, grinding, and sieving to obtain a fine powder. All of the amino acids were purchased from Sigma-Aldrich.

5.2.2. Preparation of in situ HAPclay

The *in-situ* HAP clay was prepared following the detailed steps described in previous studies[38-40]. Briefly, amino acid-modified Na-MMT clay was mixed into Na_2HPO_4 (J.T. Baker) solution and stirred for 2 hours. Thereafter, $CaCl_2$ (J.T. Baker) solution was added to the clay mixture and stirred for another 8 hours while maintaining the pH at 7.4. Then, the precipitate was separated by centrifuging followed by drying at 70°C, grinding, and sieving to obtain a fine in-situ HAP clay powder.

5.2.3. Preparation of PCL/in situ HAPclay scaffolds

3D porous polymer HAPClay scaffolds were prepared using the steps described broadly in previous studies[41, 42]. In brief, the PCL (Sigma Aldrich) solution was prepared by dissolving 3.6 g (90%) of polymer in 40 ml of 1,4-dioxane (Sigma Aldrich) for stirring for 3 hours. Another solution was prepared by dispersing 0.4 g (10%) of *in situ* HAPclay in 20 ml of 1,4-dioxane and sonicating for 18 minutes. Then, in situ HAPclay solution was poured into polymer solution and

stirred for another 2 hours. Then, prepared polymer HAPclay solution was poured into tube followed by freeze extraction to prepare ~90% porous PCL/in situ HAPClay scaffolds.

5.2.4. Preparation of scaffold sample for cell culture

PCL/ in situ HAPclay scaffolds were sterilized by keeping scaffolds under UV sterilization chamber for 45 minutes, followed by keeping in 100 % ethanol for 24 hours. Sterilized scaffolds were washed in PBS to remove all the ethanol from the scaffolds. Then, scaffold samples were kept in the cell culture media for 24 hours before using them for cell culture experiments. Initially, 5×10^4 mesenchymal stem cells (MSCs) were seeded on each scaffold and cultured for 23 days, followed by sequential culture of 5×10^4 MCF-7 for another 15 days.

5.2.5. Cell lines and culture medium

Human mesenchymal stem cells (MSCs) were purchased from Lonza and maintained in MSCGM™ Bulletkit™ medium. The Bulletkit™ medium was prepared by adding MSCGM™ SingleQuots™ (Lonza) to MSCBM™ (Lonza). Human breast cancer cell MCF-7 were purchased from ATCC and maintained in in Eagle's Minimum Essential Medium (EMEM). The EMEM was prepared by adding 10% FBS, 0.01 mg/mL human recombinant insulin, and 1% P/S in 90% EMEM. We maintained cells at 37°C and 5% CO_2 in a humidified incubator.

5.2.6. XRD characterization

An X-ray diffractometer (Rigaku) was used to obtain XRD data on powdered clay samples. The *d*-spacing of the clay structure was calculated from the XRD data using Bragg's diffraction law. A scan range of 2θ =2–30° and scan rate of 2°min−1 were used. Powdered MMT clay and modified clay samples were placed in an aluminum mount prior to performing the XRD scan.

5.2.7. Scanning electron microscopy

Scanning electron microscope was used to study the microstructure of various amino acid-modified nanoclay polymer scaffolds. The samples were gold-coated and mounted on SEM stubs for observation using the JEOL JSM 6490LV scanning electron microscope.

5.2.8. Fourier transform infrared spectroscopy (FTIR)

The FTIR experiments were conducted using a NEXUS TM 870 FTIR spectrometer from ThermoNicolet with a KBr beam splitter. KBr windows were used to place the powder samples, followed by placing them in the universal sample holder for conducting the FTIR experiments and acquired spectra at a resolution of 4 cm^{-1} in the transmission mode at a mirror velocity of 0.158 cm s-1.

5.2.9. Molecular model construction and simulation details

This study used the MD technique to build an organically modified clay model. In this collaborative work, Hanmant Gaikwad build and analyzed the model. The 6×3 Na-MMT clay model was used here, used in several previous studies [43, 44]. The Na-MMT clay model comprises two-layer clay sheets and has a tetrahedral-octahedral-tetrahedral (t-o-t) unit structure. The interface force field (InterfaceFF) parameters[45] were used for the Na-MMT clay model. The initial overall dimensions of a single 6×3 Na-MMT clay (t-o-t) mineral layer were 31.68 Å $\times$ 27.44 Å $\times$ 6.56 Å. In each unit cell, one of every four Al^{3+} ions was replaced by Mg^{2+} or Fe^{3+} ions, resulting in isomorphous substitution. This isomorphic substitution was balanced by introducing positively charged Na$^+$ ions in the interlayer space. Further, these Na cations were removed and replaced by the modifier to modify the MMT clay model. This study used 2-Aminopimelic acid and 4-Aminophenyl butyric acid as a modifier to build the organically modified MMT (OMMT) clay. The structure of aminopimelic acid and aminophenyl butyric acid has been obtained from the

PubChem database. The protonated molecular models for modifiers were created using Material studio 7.0. In addition, the library of CHARMm36[46] was used to obtain partial charge and force field parameters for amino acid atoms. Seven, eight, nine, ten, eleven, and twelve modifiers were placed between MMT clay sheets to create modified MMT clay models parallel to the clay surface (Fig. 5.4 a-b). After placing the aminopimelic acid and aminophenyl butyric acid molecules inside the intercalated MMT clay model, the initial d-spacing for OMMT clay models was 13.1Å and 12.1 Å, respectively (Fig. 5.4c-d).

All simulations were conducted using the NAMD2.12 software[47], and VMD 1.9.3[48] was used for the visualizations. The simulations were run at North Dakota State University's Center for Computationally Assisted Science and Technology (CCAST), a parallel computing facility. At the initial stage, the conjugate gradient method was used to minimize the OMMT clay model under vacuum conditions (0 K temperature and 0 bar pressure)[49]. Then, the temperature and pressure of the molecule were increased in steps of 100 K and 0.25 bar to 300 K and 1.01325 bar, respectively, using a stepwise approach. The experimental synthesis of OMMT involved raising the system's temperature to 333 K, then lowering it to 300 K. (room temperature). As a result, we increased the temperature of OMMT models in our simulation to 333 K from 300 K at 1 atm pressure, then decreased it to room temperature at 1 atm. Each simulation was run for 100 ps with a 0.5 fs time step. Finally, the equilibrium simulation of the OMMT model was carried out for the NPT ensemble condition (isobaric-isothermal) for another 2 ns at room temperature and pressure. The temperature and pressure were controlled during simulation using Langevin dynamics and Nose Hoover piston methods[50]. For the implementation of Particle Mesh Ewald (PME) electrostatic interactions, molecular dynamic simulations of the OMMT model were performed

with periodic boundary conditions. The switch and cut-off distances used for van der Waals and electrostatic force calculations were 16 Å and 17 Å, respectively.

5.2.10. Mechanical properties

Compressive mechanical properties of the different amino acids modified MMT clay HAP polymer scaffold samples (~ 13 mm diameter and 12 mm length) were determined using EZ-X Series Universal Electromechanical Test Frames (Shimadzu, EZ-LX HS). For the experiment, A constant deformation rate of 1 mm/min was applied for up to 10% strain in each test for all the samples. Triplicate samples were used for this experiment, and corresponding load-displacement data were collected. The slope of the initial linear region of the stress-strain curve was used for calculating the compressive elastic moduli of scaffold samples.

5.2.11. WST-1 assay

WST-1 assay (Roche, IN) has been used to study the cell viability and proliferation of both MSCs and sequential culture of cells in 3D scaffolds per the manufacturer's protocol. Briefly, cells were cultured on scaffolds for 23 days with MSCs and another 15 days with MSCs+ MCF-7. For the experiment, scaffolds were removed from the culture medium, washed with PBS, and then placed in a new 24-well plate with a solution comprising 450 ul of DMEM and 50 ul of WST-1 reagent per well and incubated for 4 hours in standard humidified condition. After 4 hours, scaffolds were removed from the 24-well plates, and the intensity of yellow color, which directly represents the number of live cells (slightly red-colored solution turns yellow as metabolically active cells cleave the tetrazolium salts of WST-1 reagent to formazan), was quantitatively measured at 450 nm using a microplate spectrophotometer (Bio-Rad, Benchmark Plus).

5.2.12. Alizarin red staining (ARS)

Cell-seeded scaffolds were fixed with 4% paraformaldehyde for 45 mins and washed with PBS three times (5 min each wash) to remove the residual fixative agent. Next, Paraformaldehyde fixed scaffolds were stained with Alizarin Red S dye for 2 minutes. The concentration of the dye was 2 g in 100 mL of deionized water, and the final pH was maintained at 4.15. After 2 min, the scaffold was washed using cell culture grade water several times to remove excess dye. Images were obtained using a Zeiss Axio Observer Z1 microscope equipped with an LSM700 laser-scanning module. Images were taken using a 639 nm laser light source. For image analysis, Imaris software was used.

5.2.13. Statistical analysis

All the experiments were carried out in triplicates (n = 3) unless otherwise mentioned, and the data are presented as the Mean value of triplicates ± standard derivation. The statistical significance (p-value) between the two groups is done using Student's unpaired *t-test. In contrast,* multiple comparisons are made using two-way ANOVA followed by an appropriate *post hoc* test (GraphPad Prism v8.4.2). Differences between the two groups were considered statistically significant when probability, $*p < 0.05$.

5.3. Result and discussion

5.3.1. XRD analysis

Fig. 5.1 shows the XRD patterns of MMT clay and MMT clay modified with the three amino acids used in this study. The peak value appears for unmodified MMT clay corresponding to the d_{001} plane at $2\theta = 7.887°$, and d_{001} spacing is observed at 11.200 Å at this 2θ. The peak value appears for MMT clay modified with 5-aminovaleric acid corresponding to the d_{001} plane at $2\theta = 6.842°$, and d_{001} spacing is observed at 12.908 Å at this 2θ. The peak value appears for MMT

clay modified with (±)-2- aminopimelic acid corresponding to the d_{001} plane at $2\theta =6.742°$, and d_{001} spacing is observed at 13.100 Å at this 2θ. The peak value appears for MMT clay modified with 4-(4- Aminophenyl) butyric acid corresponding to the d_{001} plane at $2\theta =6.114°$, and d_{001} spacing is observed at 14.445 Å at this 2θ. Results suggest that the d001 spacing of MMT clay increases with the modification with amino acids because of the formation of an intercalated structure. The highest interlayer spacing is observed with the MMT clay modified with 4-(4-Aminophenyl)butyric acid. The molecule (±)-2- aminopimelic acid has one extra −CH2- and -COOH group compared with 5-aminovaleric acid. The molecule 4-(4-Aminophenyl)butyric acid has a large phenyl group compared with 5-aminovaleric acid and (±)-2- aminopimelic acid. Results suggest that the increase in the d-spacing of MMT clay can be affected by the length of the hydrocarbon chain, type of functional groups, and the position or number of the −COOH and −NH2 groups in the amino acids.
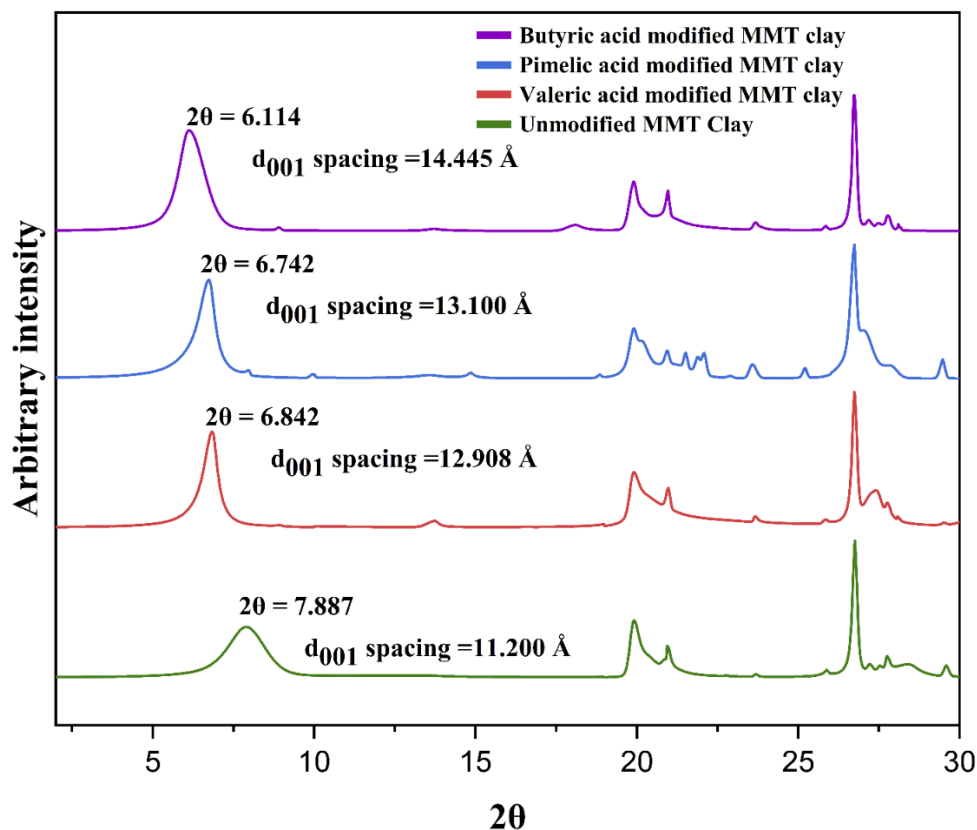
Fig. 5.1. XRD patterns of MMT clay and MMT clay modified with aminovaleric acid, aminopimelic acid, aminophenyl butyric acid.

5.3.2. FTIR analysis

Fig. 5.2 shows the FTIR spectra for MMT clay and MMT clay modified with the three amino acids within the 4000–400 cm−1 range. The corresponding band assignments are given in Table 5.1. A significant difference was observed in the FTIR spectra of the modified clays and the pure MMT clay. The clays modified with amino acids show a shift in the band position corresponding to the structural -OH group compared with pure MMT clay. Band in the range of 2800-3000 cm-1 was observed with modified MMT clay but not with pure MMT clay. These bands are attributed to the C-H stretching bands of the amino acids. MMT clay modified with amino acids showed bands at 1715, 1709, and 1722 cm−1, indicating the amino acids' presence in the modified clays. These bands are attributed to the C=O stretching bands of the carboxylic group in

the amino acid. A previous study reported that C=O stretching bands for unnatural amino acids were observed in the 1725-1735 cm−1 range[37]. There is a shift in the position of the C=O stretching band to a lower wavenumber in the case of MMT clay modified with amino acids, which suggests hydrogen bonding interactions between amino acids and MMT clay. Fig. 5.2 also shows bands observed in the 1550-1300 cm-1 range with amino acids modified MMT clays, but not with pure MMT clay. These bands arise may be due to the N−H vibrations confirming the presence of the amino acids in the MMT clay. Si−O stretching bands were observed at 1031, 1048, 1040, and 1051 cm-1 for MMT clay, aminovaleric acid-modified MMT clay, aminopomelic acid-modified MMT clay, and aminophenyl butyric acid-modified MMT clay, respectively. In addition, a shift in the Si−O stretching vibrations was observed for all the amino acids modified MMT clays. These shifts may be because of the interaction between the protonated amine group and the oxygen of silica tetrahedral. The bands observed at 959, 915, 911, and 916 cm-1 attributed to Al-FeOH deformation, and the bands observed at 799, 795, 795, and 795 cm-1 attributed to Al-OH deformation.

Table 5.1. Assignments of vibrational modes observed in the FTIR spectra of MMT clay and MMT clay modified with different amino acids.

Band position (cm^{-1})				Band assignment
MMT clay	Aminovaleric acid-modified MMT clay	Aminopimelic acid-modified MMT clay	Aminphenyl butyric acid-modified MMT clay	
3568	3614	3619	3603	O−H stretching
-	2932	2924,2858	2814	C−H stretching
-	1715	1709	1722	C=O stretching
1614	-	-	-	H−O−H deformation
-	1499,1400	1450,1340	1503,1399	N−H deformation
1031	1048	1040	1051	Si−O stretching
959	915	911	916	Al−OH deformation
799	795	795	795	Al−FeOH deformation
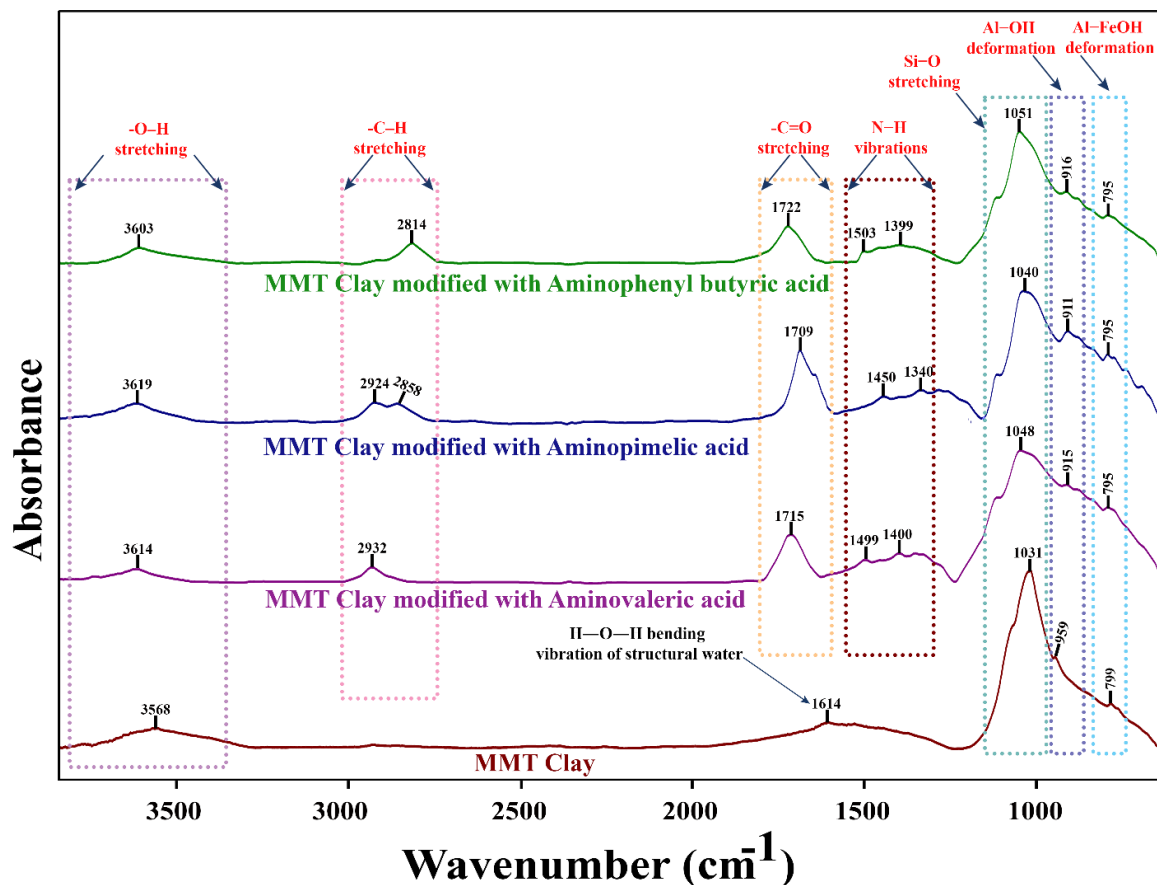
Fig. 5.2. FTIR spectra of MMT clay and MMT clay modified with aminovaleric acid, aminopimelic acid, and aminophenyl butyric acid within the range of 4000–900 cm−1.

5.3.3. Scaffolds microstructure analysis

The SEM micrographs of the various amino acid-modified nanoclay polymer scaffolds are presented in Fig. 5.3. Micrographs demonstrated the microstructure of the scaffolds at different magnifications. All the scaffolds appear porous and have pore sizes varying from ~300 μm to sub-micron size. However, no significant change in the microstructure was observed within the scaffolds prepared with unmodified clay or aminoacid-modified clay scaffolds. SEM micrographs also show interconnectivity among the microstructure, even in the sub-micron size for all scaffolds. For scaffolds to maintain cell differentiation, allow for the entry and exit of nutrients, and remove

metabolic waste, they must have an interconnected microporous structure. Thus, the results suggest that these scaffolds have the potential to be used in tissue engineering applications.
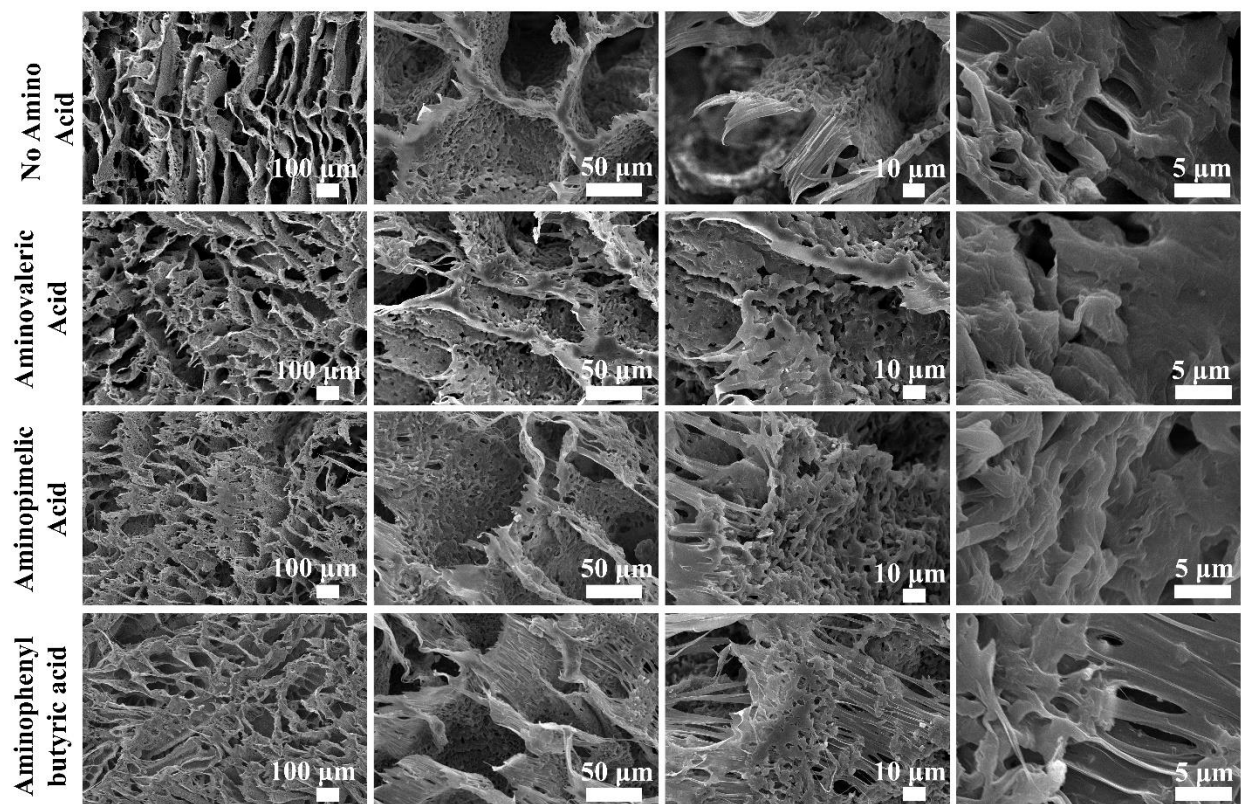
Fig. 5.3. SEM micrographs of PCL/ in situ HAPclay scaffolds

5.3.4. Molecular modeling-based analysis of interactions between MMT clay and unnatural amino acids

Here, in this collaborative work, Hanmant Gaikwad first build the OMMT models to investigate the effect of the number of amino acid molecules on the d-spacing. Here, nine amino acid molecules were considered for molecular interaction. Further calculations based on substituting nine Na cations with nine protonated amino acids in clay interlayer space for charge neutrality based on cation exchange capacity experiments from a prior study[51]. The d-spacing of the equilibrated models was compared to the initial d-spacing of the models; it showed an increment in d-spacing. The final d-spacing for OMMT models modified with aminopimelic acid

and aminophenyl butyric acid increased from 13.1 Å to 13.26 Å and 14.1 Å to 14.68 Å, respectively (Fig. 5.4). The molecular interactions of modified MMT clay with aminopimelic acid and aminophenyl butyric acid modifiers were investigated using MDEnergyTM of NAMD[47]. The molecular interaction of MMT clay with Amino-valeric acid as a modifier has been investigated in prior work.[52] Electrostatic (ELE) and van der Waals (VDW) interactions between modifiers and MMT chains are represented in Table 5.2. The amino acid molecules were examined for their backbone and the functional group to investigate molecular interactions. Strong interaction between clay-backbone and clay-functional groups with aminophenyl butyric acid modifier has been observed, as shown in Table 5.2. However, in the OMMT model with aminopimelic acid modifier, the interaction was observed only for clay-functional groups. Both OMMT models mostly showed electrostatic interaction. The OMMT model with aminophenyl butyric acid modifier was shown a lower electrostatic interaction of functional groups with clay than the clay-backbone. In this model, the benzene ring at the backbone site made a more partially charged backbone than the functional groups. But for the OMMT model with aminopimelic acid modifiers, the partial charges of the atoms in the functional group were higher than those of the carbon and hydrogen atoms in the backbone, resulting in higher electrostatic interactions between clay and functional groups (Fig. 5.5). Compared with electrostatic interaction, less van der Waals (VDW) interaction was observed for both modifiers in clay-backbone and clay-functional groups. For both OMMT models, backbone carbon atoms largely contributed to the high value of VDW interaction at clay –backbone interaction. A significantly less VDW interaction was observed between clay-functional groups for the aminophenyl butyric acid-modified clay model. Still, it played a significant role in the aminopimelic acid-modified clay model. The final OMMT model showed the functional groups COOH and NH3+ of amino acids tilted towards the interlayer clay

sheets (Fig. 5.4a-b). The hydrogen atoms from functional groups and backbone sections showed strong, attractive interaction with the clay sheet. In contrast, carbon atoms from the backbone and oxygen and nitrogen atoms from the functional group showed repulsive interaction for both OMMT models. The aminopimelic acid-modified clay model has two COOH groups in the modifier structure, reflecting a more repulsive interaction for oxygen atoms than the OMMT model for aminophenyl butyric acid. The functional hydrogen atom showed a strong attraction between clay sheets, which bent the functional group towards the clay sheets (Fig. 5.4a-b). It influences the d-spacing between clay sheets. The energy interaction between modifier and clay sheets for aminopimelic acid-modified clay showed a higher value than the OMMT model with aminophenyl butyric acid. The higher backbone length of aminophenyl butyric acid resulted in a stronger backbone –MMT clay interaction than aminopimelic acid and aminovaleric acid for respective OMMT models. These interactions affect the increment in d-spacing compared to the initial d-spacing of the OMMT model. For more energy interaction between clay-modifiers, more tilt was observed for amino acid molecules towards the clay sheet. Hence, the d-spacing for the OMMT model with aminophenyl butyric acid and aminopimelic acid showed an increment of 0.58 Å and 0.16 Å, respectively, compared with its initial model. The interaction between aminopimelic acid, aminophenyl butyric acid, and aminovaleric acid[52] with MMT clay influenced the d-spacing of OMMT models, which were reflected in the experimental d-spacing value evaluated from XRD.

Table 5.2. The non-bonded interaction energies between MMT clay and different constituents of protonated aminophenyl butyric acid, protonated aminopimelic acid, and protonated aminovaleric acid[52]. The negative and positive values of energies represent the attractive and repulsive interactions, respectively.

Non-bonded interaction between	Electrostatic (ELE) energy (Kcal/mol)			Van der Waals (VDW) Energy (Kcal/mol)			Total (ELE+VDW) energy (Kcal/mol)		
	Amino phenyl butyric acid	Amino pimelic acid	Aminov aleric acid	Amino phenyl butyric acid	Amino pimelic acid	Amino valeric acid	Amino phenyl butyric acid	Amino pimelic acid	Amino valeric acid
MMT clay - backbone	-891	-107	-561	-78	-32	-76	-969	-140	-657
MMT clay - backbone C	+215	+690	+535	-64	-28	-70	+151	+662	+465
MMT clay - backbone H	-1106	-798	-1096	-14	-4	-6	-1120	-802	-1102
MMT clay – functional groups	-736	-1601	-907	-7	+118	-65	-743	-1483	-972
MMT clay - COOH	-284	-163	+133	-5	+31	-58	-289	-132	+75
MMT clay - NH3+	-452	-1438	-1040	-2	+87	-7	-454	-1351	-1047
MMT clay -functional-O	+1227	+2670	+2018	+1	+43	-50	+1228	+2714	+1968
MMT clay -functional-N	+1091	+1040	+731	-1	+58	-1	+1090	+1098	+730
MMT clay -functional-C	-826	-1690	-1086	-6	-11	-6	-832	-1701	-1092
MMT clay -COOH functional-H	-684	-1144	-799	-1	-1	-2	-685	-1144	-801
MMT clay -NH3+ functional-H	-1543	-2478	-1771	-1	+29	-6	-1544	-2449	-1777
MMT clay - modifier	-1627	-1709	-1468	-85	+86	-141	-1712	-1623	-1609
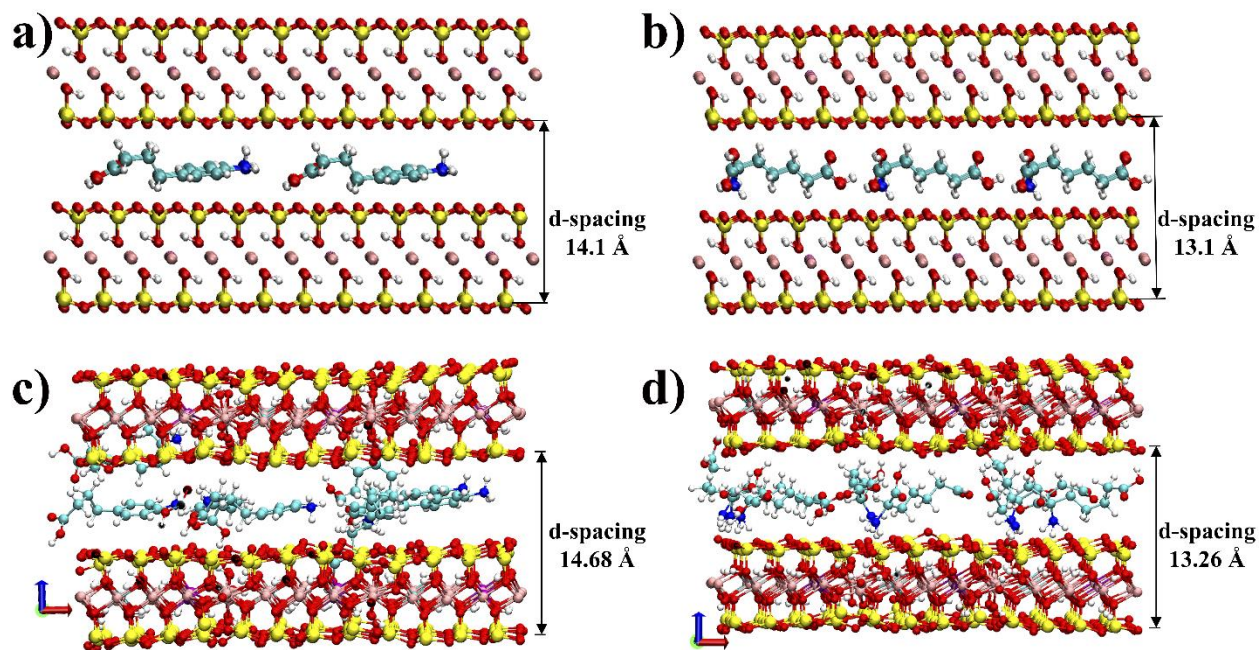
Fig. 5.4. a) Initial orientation of protonated aminophenyl butyric acid parallel to the clay surface b) Initial orientation of protonated aminopimelic acid parallel to the clay surface, final representation of organically modified MMT clay model c) with aminophenyl butyric acid and d) with aminopimelic acid at 1atm pressure and 300K.
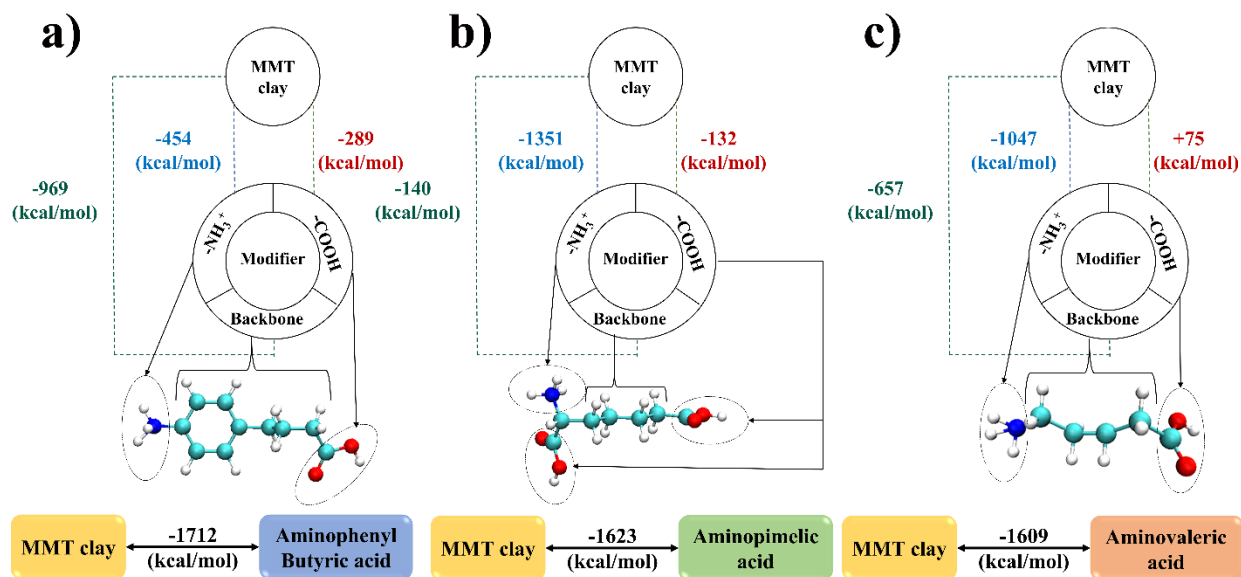
Fig. 5.5. Representation and map of total non-bonded interaction between MMT clay and different constituents of a) aminophenyl butyric acid modifier and b) aminopimelic acid modifier c)aminovaleric acid modifier[52].

163

5.3.5. Mechanical testing

The mechanical properties of any material are strongly influenced by microstructure, porosity, and the reinforcing effect of additives. The stress-strain curves shown in Fig. 5.6a represent the deformation response of nanocomposite scaffolds made from unmodified clay and clay modified with aminophenyl butyric acid, pimelic acid, and valeric acid under compressive loading. According to Fig. 5.6a, each curve possessed initial linear compressive stress regions that grew directly proportional to strain, followed by a region where compressive stress increased nonlinearly with strain due to densification. The initial elastic regime within the 0-0.01 strain range represents the scaffold's elastic response. Later, with further compression, the internal structure of the scaffold starts to collapse as the crushing and compression packs up the porous scaffold microstructure, causing compressive stress to increase nonlinearly as the strain increases in the densification region. As shown in Fig. 5.6a, the scaffold made of MMT clay modified with aminophenyl butyric acid showed the highest compressive strength. The scaffolds of MMT clay modified with aminopimelic acid and amino valeric acid have an intermediate compressive strength, while the scaffold made of unmodified MMT clay has the lowest compressive strength for a similar amount of compression. The compressive modulus values derived from the stress-strain curves of scaffolds made of MMT clay-modified with aminophenyl butyric acid, pimelic acid, valeric acid, and unmodified clay are 7.03±0.58 MPa, 6.04±0.49 MPa, 3.46±0.25 MPa and 2.79±0.23 respectively are shown in the Fig. 5.6b   In a prior experimental and molecular dynamics (MD) simulation-based study, we observed that the interfacial interactions between clay and other constituents had a considerable influence on the mechanical properties of the scaffold[52]. MD simulation observed similar behaviors in the present study while investigating the interaction between MMT clay and unnatural amino acid modifiers. The maximum interaction energy was

found between MMT clay and aminophenyl butyric acid (-1712 kcal/mol), followed by moderate interaction energy between MMT clay and aminopimelic acid (-1623 kcal/mol) as compared to the lowest interaction energy observed between MMT clay and aminovaleric acid (-1609 kcal/mol)[52] in the prior study. The interaction energy between MMT clay and aminobutyric acid is approximately 5.4 % and 6.4 % greater than the interaction energy observed between MMT clay and aminopimelic acid and interaction energy between MMT clay and aminovaleric acid, respectively. Result suggests that the interactions of MMT clay with modifiers are crucial in the mechanical properties of the scaffold system.
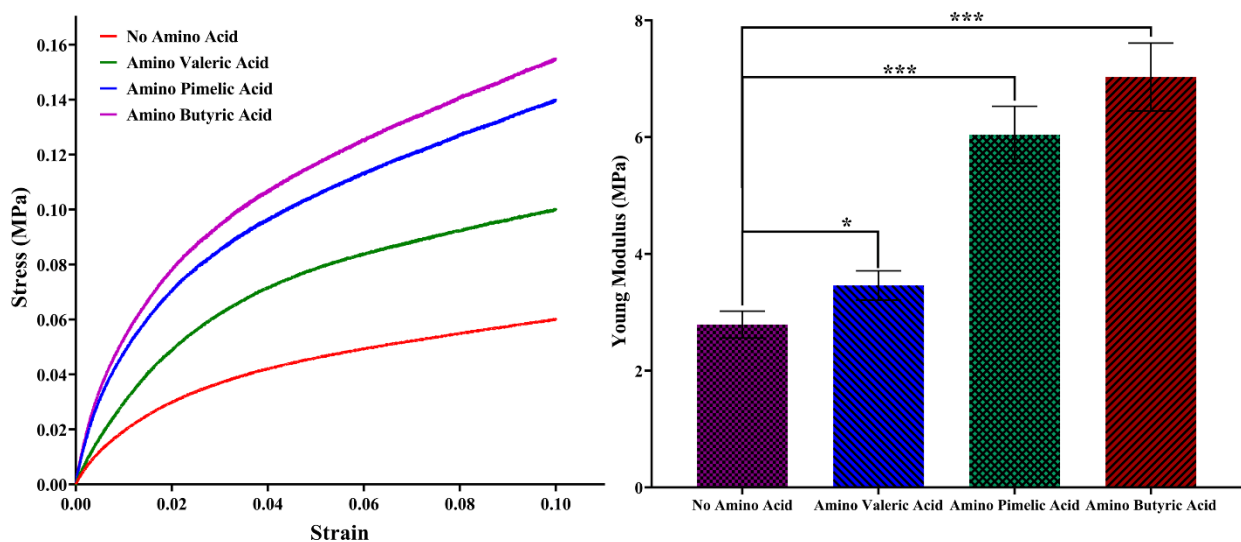
Fig. 5.6. Compressive mechanical properties: a) representative stress-strain curves obtained for different amino acids modified scaffolds. b) Representative compressive elastic moduli of different amino acids modified scaffolds.

5.3.6. Cell viability

The WST-1 assay was performed to evaluate cell viability and proliferation of both the monoculture of MSCs for 23 days and sequential culture of MSCs +MCF-7 for 15 days on the scaffolds to evaluate the biocompatibility of different amino acid-modified scaffolds. The cell viability measured using the absorbance at 450 nm is proportional to the amount of dehydrogenase activity in the cells. Fig. 5.7a shows the cell viability of different amino acid-modified scaffolds

seeded with MSCs for 8 days, 16 days, and 23 days. We observed an increase in cell viability over time for all four scaffold systems. Compared to the control, no amino acid scaffolds significant increase in the cell viability was observed with aminovaleric acid and aminopimelic acid-modified scaffolds; however, no significant difference was observed with aminophenyl butyric acid-modified scaffolds at 23rd days. Fig. 5.7b shows the cell viability of different amino acid-modified scaffolds seeded with MSCs +MCF-7 for 23+5 days, 23+10 days, and 23+15 days. All four scaffold systems observed an increase in cell viability over time. Compared to the control, no amino acid scaffolds significant increase in the cell viability was observed with aminovaleric acid and aminopimelic acid-modified scaffolds; however, no significant difference was observed with aminophenyl butyric acid-modified scaffolds. The result suggests amino acids significantly control cell viability and proliferation of the cells.
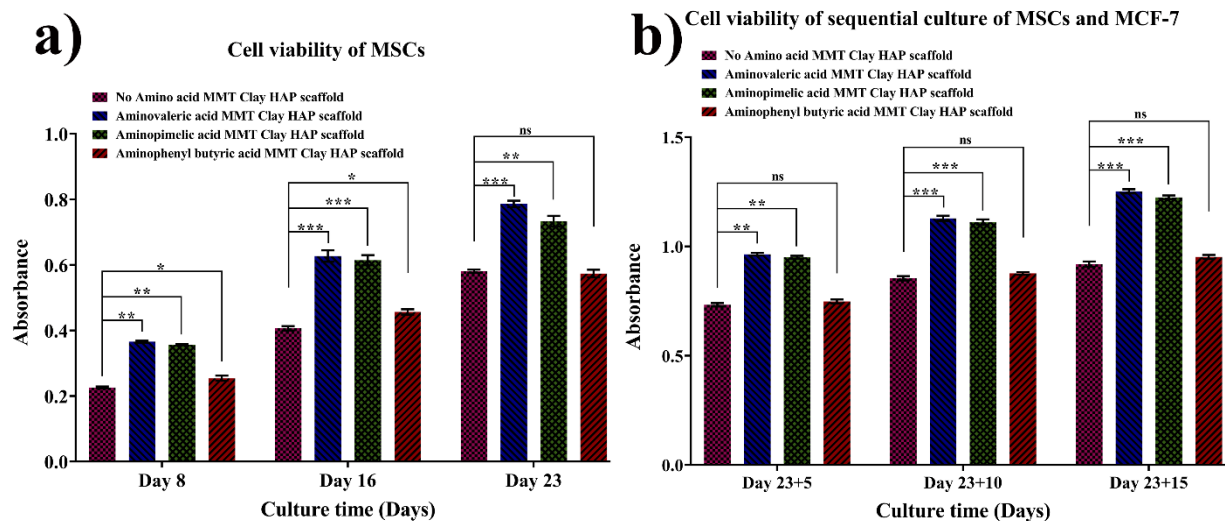
Fig. 5.7. Cell viability of different aminoacids modified scaffolds seeded with a) MSCs and b) sequential culture of MSCs + MCF-7 cells. (Two-way anova followed by post hoc tukey test p* < 0.05, p* *< 0.01, p*** <0.001, n = 3.)

5.3.7. Mineralized bone nodule formation is controlled by amino acid modifier

We performed an Alizarin Red S assay to assess the effect of different amino acids on mineralization. Scaffolds modified with no amino acid used as a control. The results are shown in

Fig. 5.8. Positive Alizarin Red S staining was observed for all the samples, indicating mineralized nodule formation. In both cases, MSCs and sequential culture showed a significant difference in mineralization with different amino acid-modified samples. On the 23rd day, minimum mineralized ECM formation was observed with no amino acid sample, whereas the maximum amount of ECM formation was observed with aminovaleric acid-modified scaffolds. Similar results were observed at 23+15 days with the sequential culture of MSCs and MCF-7. All the samples observed a significant increase in ECM formation from the 23rd day to 23+15 days. Result suggests Mineralized bone nodule formation is enhanced with MCF-7. A previous study suggested that MCF-7 cells are osteoblastic in nature[53]. Thus, the Alizarin Red S assay data indicates that amino acids play a crucial role in mineralized bone nodule formation.
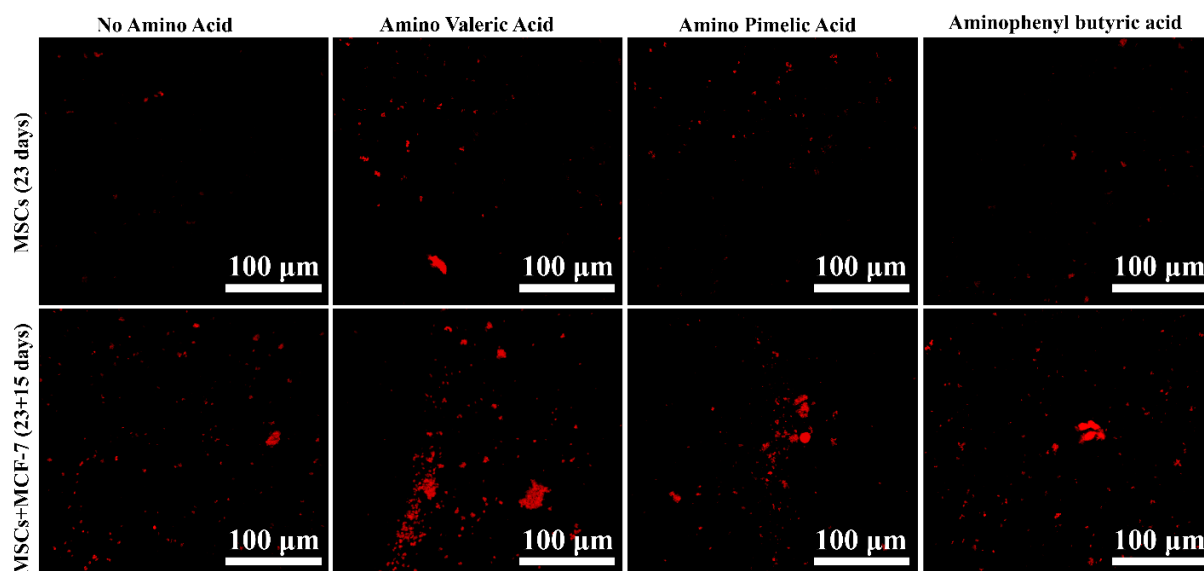
Fig. 5.8. Effect of different amino acids on mineralization. Alizarin Red S-stained different amino acids modified polymer HAP clay scaffolds seeded with hMSCs at 23rd days and hMSCs +MCF-7 at 23rd+15th days, showing the amount of mineralized ECM formation on each scaffold. Bar = 100 μm.

5.4. Conclusion

This comprehensive investigation demonstrates the potential of unnatural amino acid-modified MMT nanoclay polymer scaffolds for tissue engineering applications. The intercalation

of the unnatural amino acids was observed and was confirmed by XRD. XRD results demonstrate that intercalation of the amino acids significantly increases in the d-spacing. FTIR analysis revealed the presence of C=O vibration and -CH vibration band on the modified MMT clay samples, further confirming the intercalation of the amino acids inside the clay sheets. Also, FTIR results showed a significant band shift of the C=O vibration band, suggesting a significant molecular interaction between amino acids and MMT clay. Microstructure analysis revealed the interconnected microporous structure of the scaffolds. Molecular dynamics simulation study results show significant non-bonded interactions between the MMT clay and amino acids. Maximum non-bonded interactions between clay and modifier were observed with aminophenyl butyric acid, and an increase in non-bonded interactions plays a critical role in increasing the final mechanical response of the polymer clay scaffolds. Cell culture experiments revealed the effect of different amino acids on cell proliferation and viability, thus confirming the biocompatibility of the amino acids-modified clay scaffolds. Confocal imaging result suggests that MCF-7 cells are osteoblastic, and a significant increase in the calcium deposition was observed with the sequential culture confirming more bone formation. Thus, this study provides valuable insight into the effects of different amino acids in terms of molecular interactions, mechanical properties, and cellular responses and shows the potential applications of these scaffolds as a biomaterial in tissue engineering applications.

5.5. Acknowledgments

5.6. References

[1]   R. Langer, Tissue engineering, Tissue engineering, Science 260 (1993) 920-926.

[2]   Q.L. Loh, C. Choong, Three-dimensional scaffolds for tissue engineering applications: role of porosity and pore size, (2013).

[3]   F.J. O'Brien, Biomaterials & scaffolds for tissue engineering, Materials today 14(3) (2011) 88-95.

[4]   T.G. Kim, H. Shin, D.W. Lim, Biomimetic scaffolds for tissue engineering, Advanced Functional Materials 22(12) (2012) 2446-2468.

[5]   B. Pei, W. Wang, Y. Fan, X. Wang, F. Watari, X. Li, Fiber-reinforced scaffolds in soft tissue engineering, Regenerative biomaterials 4(4) (2017) 257-268.

[6]   G. Turnbull, J. Clarke, F. Picard, P. Riches, L. Jia, F. Han, B. Li, W. Shu, 3D bioactive composite scaffolds for bone tissue engineering, Bioactive materials 3(3) (2018) 278-314.

[7]   L. Bedian, A.M. Villalba-Rodríguez, G. Hernández-Vargas, R. Parra-Saldivar, H.M.N. Iqbal, Bio-based materials with novel characteristics for tissue engineering applications–A review, International journal of biological macromolecules 98 (2017) 837-846.

[8]   A. Blumstein, Polymerization of adsorbed monolayers. I. Preparation of the clay–polymer complex, Journal of polymer science part A: general papers 3(7) (1965) 2653-2664.

[9]   M.A. Ahmed, U.F. Kandil, N.O. Shaker, A.I. Hashem, The overall effect of reactive rubber nanoparticles and nano clay on the mechanical properties of epoxy resin, Journal of Radiation Research and Applied Sciences 8(4) (2015) 549-561.

[10]   M. Ito, K. Nagai, Thermal aging and oxygen permeation of nylon-6 and nylon-6/montmorillonite composites, Journal of applied polymer science 118(2) (2010) 928-935.

[11]   J. Diez, R. Bellas, C. Ramirez, A. Rodriguez, Effect of organoclay reinforcement on the curing characteristics and technological properties of SBR sulphur vulcanizates, Journal of applied polymer science 118(1) (2010) 566-573.

[12]   A. Okada, M. Kawasumi, A. Usuki, Y. Kojima, T. Kurauchi, O. Kamigaito, Synthesis and properties of nylon-6/clay hybrids, pp. 45-50.

[13]   K. Haraguchi, H.-J. Li, Mechanical properties and structure of polymer− clay nanocomposite gels with high clay content, Macromolecules 39(5) (2006) 1898-1905.

[14]   A. Usuki, N. Hasegawa, M. Kato, S. Kobayashi, Polymer-clay nanocomposites, Inorganic polymeric nanocomposites and membranes (2005) 135-195.

[15]   H.W.P. Carvalho, C.V. Santilli, V. Briois, S.H. Pulcinelli, Polymer–clay nanocomposites thermal stability: experimental evidence of the radical trapping effect, Rsc Advances 3(45) (2013) 22830-22833.

[16]   Y. Cui, S. Kumar, B.R. Kona, D. van Houcke, Gas barrier properties of polymer/clay nanocomposites, Rsc Advances 5(78) (2015) 63669-63690.

[17]   A.J. Bur, Y.-H. Lee, S.C. Roth, P.R. Start, Measuring the extent of exfoliation in polymer/clay nanocomposites using real-time process monitoring methods, Polymer 46(24) (2005) 10908-10918.

[18]   J.K. Pandey, K.R. Reddy, A.P. Kumar, R.P. Singh, An overview on the degradability of polymer nanocomposites, Polymer degradation and stability 88(2) (2005) 234-250.

[19] K.S. Katti, A.H. Ambre, N. Peterka, D.R. Katti, Use of unnatural amino acids for design of novel organomodified clays as components of nanocomposite biomaterials, Philosophical Transactions of the Royal Society A: Mathematical, Physical and Engineering Sciences 368(1917) (2010) 1963-1980.

[20] D. Sikdar, S.M. Pradhan, D.R. Katti, K.S. Katti, B. Mohanty, Altered phase model for polymer clay nanocomposites, Langmuir 24(10) (2008) 5599-5607.

[21] D. Sikdar, K.S. Katti, D.R. Katti, Molecular interactions alter clay and polymer structure in polymer clay nanocomposites, Journal of nanoscience and nanotechnology 8(4) (2008) 1638-1657.

[22] M. Alexandre, P. Dubois, Polymer-layered silicate nanocomposites: preparation, properties and uses of a new class of materials, Materials science and engineering: R: Reports 28(1-2) (2000) 1-63.

[23] S.S. Ray, M. Okamoto, Polymer/layered silicate nanocomposites: a review from preparation to processing, Progress in polymer science 28(11) (2003) 1539-1641.

[24] S. Pavlidou, C.D. Papaspyrides, A review on polymer–layered silicate nanocomposites, Progress in polymer science 33(12) (2008) 1119-1198.

[25] F.-H. Lin, C.-H. Chen, W.T.K. Cheng, T.-F. Kuo, Modified montmorillonite as vector for gene delivery, Biomaterials 27(17) (2006) 3333-3338.

[26] M. Darder, M. Colilla, E. Ruiz-Hitzky, Chitosan–clay nanocomposites: application as electrochemical sensors, Applied Clay Science 28(1-4) (2005) 199-208.

[27] E. Günister, D. Pestreli, C.H. Ünlü, O. Atıcı, N. Güngör, Synthesis and characterization of chitosan-MMT biocomposite systems, Carbohydrate Polymers 67(3) (2007) 358-365.

[28] X. Wang, Y. Du, J. Luo, Biopolymer/montmorillonite nanocomposite: preparation, drug-controlled release property and cytotoxicity, Nanotechnology 19(6) (2008) 065707.

[29] S.F. Wang, L. Shen, Y.J. Tong, L. Chen, I.Y. Phang, P.Q. Lim, T.X. Liu, Biopolymer chitosan/montmorillonite nanocomposites: preparation and characterization, Polymer Degradation and Stability 90(1) (2005) 123-131.

[30] J.P. Zheng, C.Z. Wang, X.X. Wang, H.Y. Wang, H. Zhuang, K. De Yao, Preparation of biomimetic three-dimensional gelatin/montmorillonite–chitosan scaffold for tissue engineering, Reactive and Functional Polymers 67(9) (2007) 780-788.

[31] D.R. Katti, P. Ghosh, S. Schmidt, K.S. Katti, Mechanical properties of the sodium montmorillonite interlayer intercalated with amino acids, Biomacromolecules 6(6) (2005) 3276-3282.

[32] D. Sikdar, D.R. Katti, K.S. Katti, B. Mohanty, Influence of backbone chain length and functional groups of organic modifiers on crystallinity and nanomechanical properties of intercalated clay-polycaprolactam nanocomposites, International Journal of Nanotechnology 6(5-6) (2009) 468-492.

[33] D. Sikdar, D.R. Katti, K.S. Katti, The role of interfacial interactions on the crystallinity and nanomechanical properties of clay–polymer nanocomposites: a molecular dynamics study, Journal of applied polymer science 107(5) (2008) 3137-3148.

[34] J.S. Ma, Unnatural amino acids in drug discovery, Chimica oggi 21(6) (2003) 65-68.

[35] D.A. Dougherty, Unnatural amino acids as probes of protein structure and function, Current opinion in chemical biology 4(6) (2000) 645-652.

[36] K.S. Katti, D.R. Katti, A.H. Ambre, Asme, UNNATURAL AMINO ACIDS MODIFIED CLAYS FOR DESIGN OF SCAFFOLDS FOR BONE TISSUE ENGINEERING, Nemb2010: Proceedings of the Asme First Global Congress on Nanoengineering for Medicine and Biology - 2010 (2010) 227-228.

[37] K.S. Katti, A.H. Ambre, N. Peterka, D.R. Katti, Use of unnatural amino acids for design of novel organomodified clays as components of nanocomposite biomaterials, Philosophical Transactions of the Royal Society a-Mathematical Physical and Engineering Sciences 368(1917) (2010) 1963-1980.

[38] A.H. Ambre, D.R. Katti, K.S. Katti, Biomineralized hydroxyapatite nanoclay composite scaffolds with polycaprolactone for stem cell-based bone tissue engineering, Journal of Biomedical Materials Research - Part A (2015).

[39] A. Ambre, K.S. Katti, D.R. Katti, In situ mineralized hydroxyapatite on amino acid modified nanoclays as novel bone biomaterials, Materials Science & Engineering C-Materials for Biological Applications 31(5) (2011) 1017-1029.

[40] K. Kundu, A. Afshar, D.R. Katti, M. Edirisinghe, K.S. Katti, Composite nanoclay-hydroxyapatite-polymer fiber scaffolds for bone tissue engineering manufactured using pressurized gyration, Composites Science and Technology 202 (2021) 108598.

[41] A.H. Ambre, D.R. Katti, K.S. Katti, Biomineralized hydroxyapatite nanoclay composite scaffolds with polycaprolactone for stem cell-based bone tissue engineering, Journal of Biomedical Materials Research Part A 103(6) (2015) 2077-2101.

[42] K. Kundu, D.R. Katti, K.S. Katti, Tissue-Engineered Interlocking Scaffold Blocks for the Regeneration of Bone, Jom 72(4) (2020) 1443-1457.

[43] D.R. Katti, Z.R. Patwary, K.S. Katti, Modelling clay–fluid interactions in montmorillonite clays, Environmental Geotechnics 4(5) (2016) 322-338.

[44] D. Sikdar, D.R. Katti, K.S. Katti, A molecular model for ε-caprolactam-based intercalated polymer clay nanocomposite: integrating modeling and experiments, Langmuir 22(18) (2006) 7738-7747.

[45] H. Heinz, H. Koerner, K.L. Anderson, R.A. Vaia, B.L. Farmer, Force field for mica-type silicates and dynamics of octadecylammonium chains grafted to montmorillonite, Chemistry of materials 17(23) (2005) 5658-5669.

[46] B. Brooks, M. Karplus, Harmonic dynamics of proteins: normal modes and fluctuations in bovine pancreatic trypsin inhibitor, Proceedings of the National Academy of Sciences 80(21) (1983) 6571-6575.

[47] J.C. Phillips, R. Braun, W. Wang, J. Gumbart, E. Tajkhorshid, E. Villa, C. Chipot, R.D. Skeel, L. Kale, K. Schulten, Scalable molecular dynamics with NAMD, Journal of computational chemistry 26(16) (2005) 1781-1802.

[48] W. Humphrey, A. Dalke, K. Schulten, VMD: visual molecular dynamics, Journal of molecular graphics 14(1) (1996) 33-38.

[49] M.C. Payne, M.P. Teter, D.C. Allan, T.A. Arias, a.J.D. Joannopoulos, Iterative minimization techniques for ab initio total-energy calculations: molecular dynamics and conjugate gradients, Reviews of modern physics 64(4) (1992) 1045.

[50] Y. Zhang, S.E. Feller, B.R. Brooks, R.W. Pastor, Computer simulation of liquid/liquid interfaces. I. Theory and application to octane/water, The Journal of chemical physics 103(23) (1995) 10252-10266.

[51]   D.R. Katti, A. Sharma, A.H. Ambre, K.S. Katti, Molecular interactions in biomineralized hydroxyapatite amino acid modified nanoclay: In silico design of bone biomaterials, Materials Science & Engineering C-Materials for Biological Applications 46 (2015) 207-217.

[52]   D.R. Katti, A. Sharma, A.H. Ambre, K.S. Katti, Molecular interactions in biomineralized hydroxyapatite amino acid modified nanoclay: in silico design of bone biomaterials, Materials Science and Engineering: C 46 (2015) 207-217.

[53]   S. Kar, H. Jasuja, D.R. Katti, K.S. Katti, Wnt/β-Catenin signaling pathway regulates osteogenesis for breast cancer bone metastasis: Experiments in an in vitro nanoclay scaffold cancer testbed, ACS Biomaterials Science & Engineering 6(5) (2019) 2600-2611.

CHAPTER 6. EFFECT OF DIFFERENT COMPOSITIONS OF BIOACTIVE CERAMICS ON MECHANICAL AND BIOCHEMICAL PROPERTIES OF THE SCAFFOLD TOWARD BONE TISSUE ENGINEERING

This chapter describes the design of the *in situ* hydroxy apatite and tri-calcium phosphate incorporated nano clays polymer scaffolds bone tissue engineering applications. The contents of this chapter are going to be submitted for publication. The article is coauthored by Krishna Kundu, Dinesh R. Katti, and Kalpana S. Katti.

6.1. Introduction

More than 500,000 bone-grafting procedures are estimated to be performed annually in the United States and 2.2 million worldwide [1], with the occurrence rate expected to rise by 13% yearly [2]. Conventional methods for bone regeneration are limited to autografts and allografts transplantations or the implantation of metallic/ceramic-based implants to assist bone regeneration [3, 4]. Although they are considered the "gold standard," they have limited availability, increased risk of infection, donor site morbidity, the need for a second surgery to harvest the graft, and insufficient transplant integration [5-7]. These restrictions have prompted a lot of research and the development of synthetic biomaterials. Synthetic materials are relatively abundant, easy to manufacture and eliminate many of the significant problems associated with autogenous grafts. Calcium phosphate compounds have been studied extensively over the last decade due to their close resemblance to the body's hard tissue mineral component and their excellent biocompatibility [8, 9]. The most widely investigated calcium phosphates are hydroxyapatite (HAP) and b-tricalcium phosphate (b-TCP)[10, 11]. These biomaterials have no immunologic reaction or systemic toxicity[12]. At physiological pH, b-TCP resorbs faster than HAP, making it mechanically weaker [2, 13], and it has the advantage of not lingering in the repair site for long

periods. Biphasic calcium phosphates (BCP) are formed by combining HA with b-TCP, and the ratio of HAP and TCP can be adjusted to alter the BCP's degradation rate [14, 15]. This combination offers advantages over other bioceramics by permitting better control over bioactivity and biodegradation, ensuring the biomaterial's stability while stimulating bone ingrowth. The deterioration of BCP at the implant site gradually releases calcium and phosphorus ions into the biological environment, creating an ideal environment for new bone formation [9][16]. The primary purpose of using BCP is to increase the biological properties of bioceramics, such as bioactivity, bio-resorbability, osteoconductivity, and osteoinductivity, to promote bone tissue production [17]. It should be noted that a slow or fast biodegradation rate can interfere with the rate and pattern of new bone formation. As a result, the fundamental advantage of BCP is the ability to control the composition ratio of the more stable phase to the biodegradable phase to improve the biodegradation rate and increase the bone regeneration process for specific applications. This is accomplished by selecting an optimal composition ratio of HAP and α- or β-TCP, where increasing the latter's ratio improves BCP bioactivity and biodegradability [18-20]. Various researchers have attempted to produce desired biological responses by modifying various parameters during biomaterial manufacturing or by including various biocompatible polymers. However, the biological responses to BCP ceramics differ according to their physical properties and chemical compositions, resulting in varying rates and patterns of bone regeneration. Various researchers have tried to produce desired biological responses by modifying various parameters during biomaterial manufacturing or by including various biocompatible polymers. However, the ideal physicochemical parameters of BCP scaffolds, such as composition ratio, pore size, total porosity, and interconnected porosity, have not yet been thoroughly investigated. In this study, we intended to create a novel scaffold system for bone tissue engineering. Biomineralized HAP

fabrication inside nanoclay interfaces has been investigated in our previous studies, as also the design of polycaprolactone scaffolds with the HAPclay additions.[21] We analyzed the mechanical properties, biocompatibility, and Alkaline Phosphatase Activity to ensure that the scaffold system we developed is mechanically compatible, biocompatible, and enhances bone formation.

6.2. Materials methods

6.2.1. Modification of MMT clay

The detailed procedure for the modification of Na-MMT clay is described elsewhere[22, 23]. Briefly, the 5-aminovaleric acid solution was added to preheated (60°C) MMT suspension, and the mixture solution was kept for stirring. After one hour, the obtained slurry was centrifuged and washed to remove chloride ions, followed by drying at 70°C, grinding, and sieving to obtain a fine powder. Na-MMT clay (SWy-2) was procured from Clay Minerals Society. The 5-aminovaleric acid was obtained from Sigma-Aldrich.

6.2.2. Preparation of *in situ* HAPclay

We have followed the procedure described in previous studies to prepare *in situ* HAP clay.[23, 24]   In brief, the organically modified MMT clay powder was dissolved into Na_2HPO_4 solution (23.8 mM) by stirring at room temperature for 2 hours. Further, 39.8 mM of $CaCl_2$ solution was added, and this suspension was stirred vigorously for 8 hours (pH 7.4). The precipitate obtained was allowed to settle for twelve hours, followed by centrifuging and drying (70°C), and is subsequently ground and sieved to obtain a fine powder. The compounds Na_2HPO_4 and $CaCl_2$ were purchased from JT Baker.

6.2.3. Scaffold preparation

3D polymer scaffolds were prepared with 10 wt. % in situ HAP clay, 10 wt. % TCP, 10 wt. % in situ HAP clay and 5% wt. TCP, 5 wt. % in situ HAP clay and 10% wt. TCP, 10 wt. % in

situ HAP clay and 10% wt. TCP, 15 wt. % in situ HAP clay, 15 wt. % TCP. In a typical procedure, PCL solution was prepared by dissolving the polymer (appropriate wt% in 40 ml of 1,4-dioxane solvent) to achieve different scaffolds. Another solution was prepared by dissolving the required amount of prepared in situ HAPclay and ground TCP in 20 ml of 1,4-dioxane, followed by sonicating for 30 mins. Details of in-situ HAPclay preparation are described in earlier studies.[22, 24, 25] Freshly prepared in situ HAPclay and TCP solution was added to the polymer solution and stirred for 2 hours. The freeze extraction method was used to obtain 3D scaffolds. PCL and 1, 4-dioxane were purchased from Sigma Aldrich. TCP was received from FORTUS medical Inc.

6.2.4. Cell culture experiments

Scaffolds were cut into 3 mm (height) X 12 mm (diameter) small pieces and kept in UV for 45 mins. After that, samples were immersed in 100 % ethanol for 24 h for sterilization. Then, the samples were washed with PBS. Samples were kept in the cell culture media for 24 hours before using them for cell culture experiments. Then, 5 X 104 osteoblast cells were seeded on each scaffold.

6.2.5. Cell line and culture medium

The human osteoblast cell line (hFOB 1.19) was obtained from ATCC and maintained in a media consisting of 90% HyQ Dulbecco's Modified Eagle medium DMEM-12(1:1) from Hyclone, 10% FBS from ATCC, and 0.6% G418 solution (antibiotic) from JR scientific. All the cells were maintained at 37°C and 5% CO_2 in a completely humidified incubator.

6.2.6. Porosity determination

The porosity of the porous polymer scaffolds was determined by measuring the dimensions and mass of the scaffolds and comparing the calculated density with the density of the solid nanocomposites. The apparent density of the scaffolds was calculated as,

$$q = mV^{-1}$$

Where, m is the mass and V is the volume of the porous scaffolds. The porosity of the porous scaffolds was calculated from,

$$\text{Porosity} = 1 - q/q_s$$

Where, q_s is the density of the solid nanocomposite.

6.2.7. Mechanical properties determination

Compressive mechanical properties of scaffold samples (~13 mm diameter and ~12 mm length) were determined using EZ-X Series Universal Electromechanical Test Frames (Shimadzu, EZ-LX HS). Triplicate sample sets were used while performing this experiment. A 1 mm/min constant deformation rate was applied to each test sample for up to 10% strain. The load and corresponding displacement data were recorded. The load-displacement data were used to construct the stress-strain response curves for each sample.

6.2.8. In vitro degradation studies

Accelerated degradation studies were performed on PCL composite scaffolds using sodium hydroxide solution (0.1 M). Scaffold samples (~13 mm diameter and ~ 12 mm thickness) were UV sterilized, immersed in 70 % alcohol overnight, and then washed with PBS. The scaffold samples were transferred to glass vials containing the degradation media (0.1 M NaOH). Each scaffold sample was thus immersed in separate vials containing the degradation media with the caps of these vials tightened properly. These scaffold containing vials were maintained at 37°C during degradation, with degradation media refreshed every seven days. After each degradation period (time point), the scaffolds were removed from the vials, washed carefully with deionized water, and dried at room temperature. The percentage weight loss for the scaffold samples was calculated using the following formula,

$$\text{\% weight loss} = (W_i - W_d)/W_i \text{ x } 100$$

Where, W_i is initial weight of scaffold before degradation, W_d is weight of the degraded scaffold. Data were obtained for triplicate sample sets after each time point in these experiments.

6.2.9. Mechanical properties of the degraded scaffolds in 0.1 M NaOH

The mechanical properties of scaffold samples (~ 13 mm diameter and 12 mm length) were obtained after each degradation period using EZ-X Series Universal Electromechanical Test Frames (Shimadzu, EZ-LX HS). The compressive mechanical tests were performed on undegraded (0 days, control) and degraded (7, 14, and 21 days) PCL/in situ HAPclay composite scaffold samples. A 1 mm/min constant deformation rate was applied to each test sample for up to 10% strain. The load and corresponding displacement data were recorded. The load-displacement data were used to construct the stress-strain response curves for each sample.

6.2.10. WST-1 assay

WST-1 assay was performed in scaffold seeded with human osteoblast cells. The WST-1 (Roche, IN) assay was used to perform cell viability per the manufacturer's protocol. Briefly, cells were cultured on scaffolds for 3, 5, and 7 days. After that, cell-seeded scaffolds were removed from the culture medium, washed with PBS, and then placed in a new 24-well plate with a solution comprising 450 ml of DMEM and 50 ml of WST-1 reagent per well and then incubated for four h in standard humidified condition. After four h, scaffolds were removed from the 24-well plates, and the intensity of yellow color, which directly represents the number of live cells (slightly red colored solution turns yellow as metabolically active cells cleave the tetrazolium salts of WST-1 reagent to formazan), was read at 450 nm using a microplate spectrophotometer (Bio-Rad, Benchmark Plus).

6.2.11. Alkaline phosphate assay

ALP activity assay was performed in scaffold seeded with human osteoblast cells was incubated at 37°C, 5% CO_2 under humidified conditions for 3, 5 and 7 days. These samples were washed with PBS after incubation, transferred to unused wells of 24-well plates and 850mL Triton X-100 (1 v/v %solution) was added to each of the well containing the samples. Cell lysates (250mL) obtained after subjecting the immersed samples to two freeze-thaw cycles (27^0C to 37^0C) was transferred to new 24-well plates and incubated with p-nitrophenyl phosphate (250mL) at room temperature for 60 min. 3N NaOH (70mL) was further added to the wells, and absorbance readings were taken at 405 nm using a microplate spectrophotometer (Bio-Rad, Benchmark Plus).

6.2.12. Statistical analysis

Two-way ANOVA followed by Tukey's post hoc multiple comparison test was used for statistical analysis. Data were considered significantly different when the probability values obtained were< 0.05 (P< 0.05). Quantitative data were expressed as a mean ± standard deviation. Triplicate samples were used for performing all the experiments.

6.3. Results and discussion

6.3.1. Porosity determination

Fig. 6.1 shows the representative percent porosity of the scaffolds with different ceramic content. Maximum porosity was observed with 10% HAP/clay and 10% TCP. Minimum porosity was observed with 10% TCP + 10 % HAP clay. The result suggested that with the decrease of polymer content in the scaffolds, porosity decreases, and porosity increases with the decrease of ceramic content.
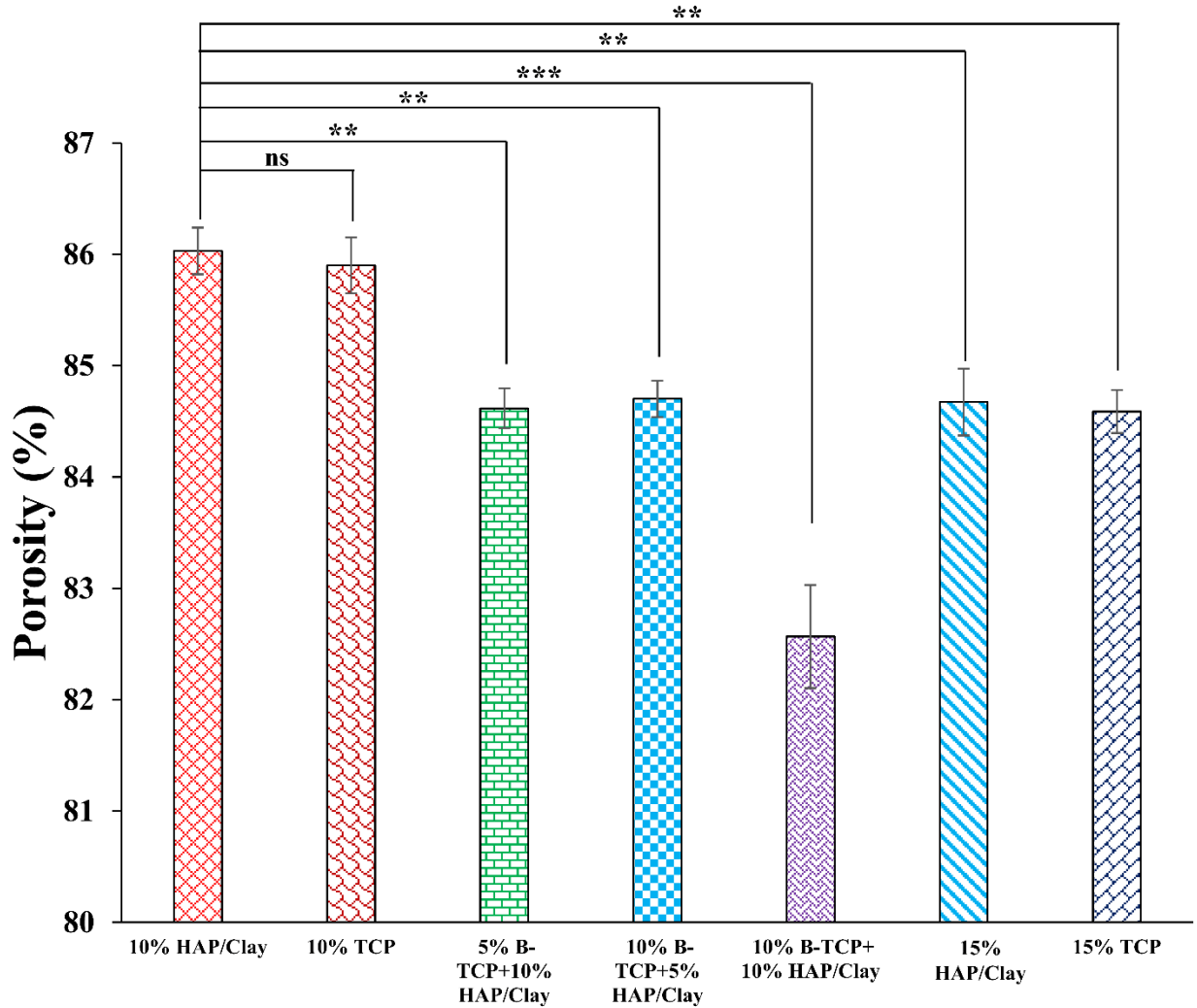
Fig. 6.1. Percent porosity of different PCL Nanocomposite scaffolds.

6.3.2. Mechanical properties

Compressive mechanical properties of scaffold samples were determined using the UTM A-Z test frame. Representative stress-strain responses are shown in Fig. 6.2. A significant increase in the compressive strength was observed with an increase in the ceramic content. Maximum compressive strength was observed with 10% TCP + 10% HAP clay, and minimum compressive strength was observed with 10% HAP clay and 10% TCP scaffolds at 10% strain. Results suggest that with the increase in the ceramic content, scaffolds are becoming stiffer with lower porosity. Fig. 6.3 represents the scaffolds' compressive elastic modulus with different ceramic content

combinations. Maximum elastic modulus was observed with 10% HAP clay + 5% TCP, and the minimum was observed with 10% TCP scaffolds. The result suggests that with the increase in HAP content with TCP, elastic modulus increases; later, with the increase of TCP content, scaffolds become stiffer, and elastic modulus decreases.
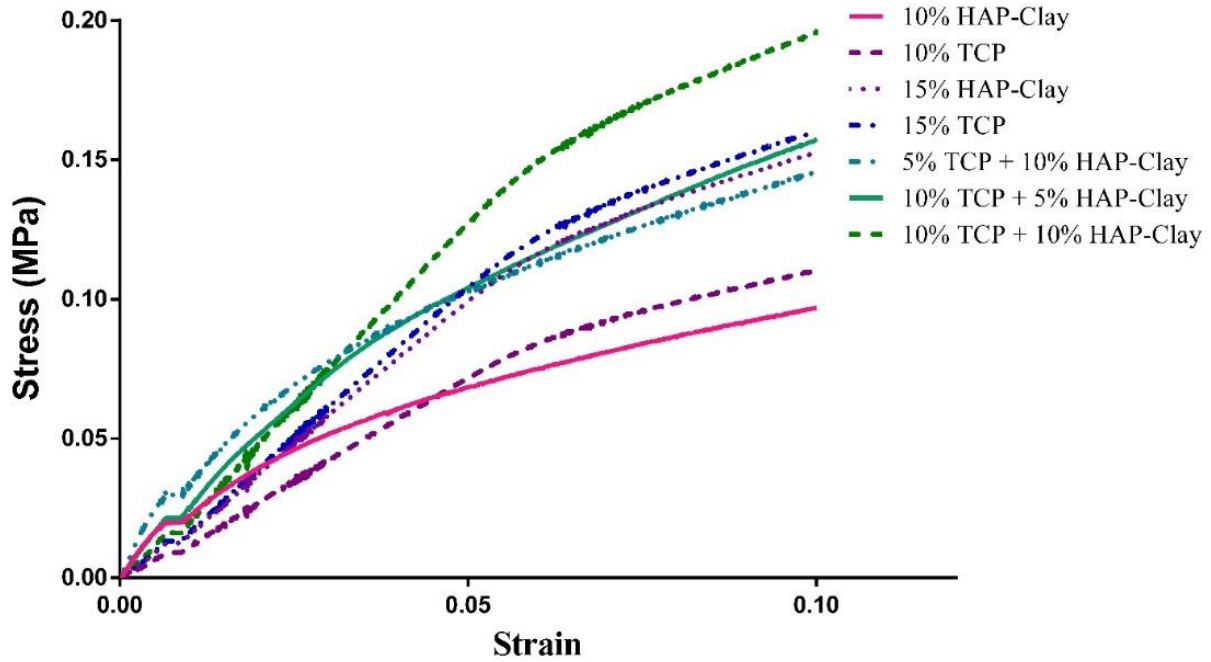

Fig. 6.2. Representative stress-strain curves obtained for PCL/in situ 10% HAPclay scaffolds, PCL + 10% TCP scaffolds, PCL/in situ 15% HAPclay scaffolds, PCL + 15% TCP scaffolds, PCL/in situ 10% HAPclay + 10% TCP scaffolds, PCL/in situ 10% HAPclay + 5% TCP scaffolds, PCL/in situ 5% HAPclay + 10% TCP scaffolds.
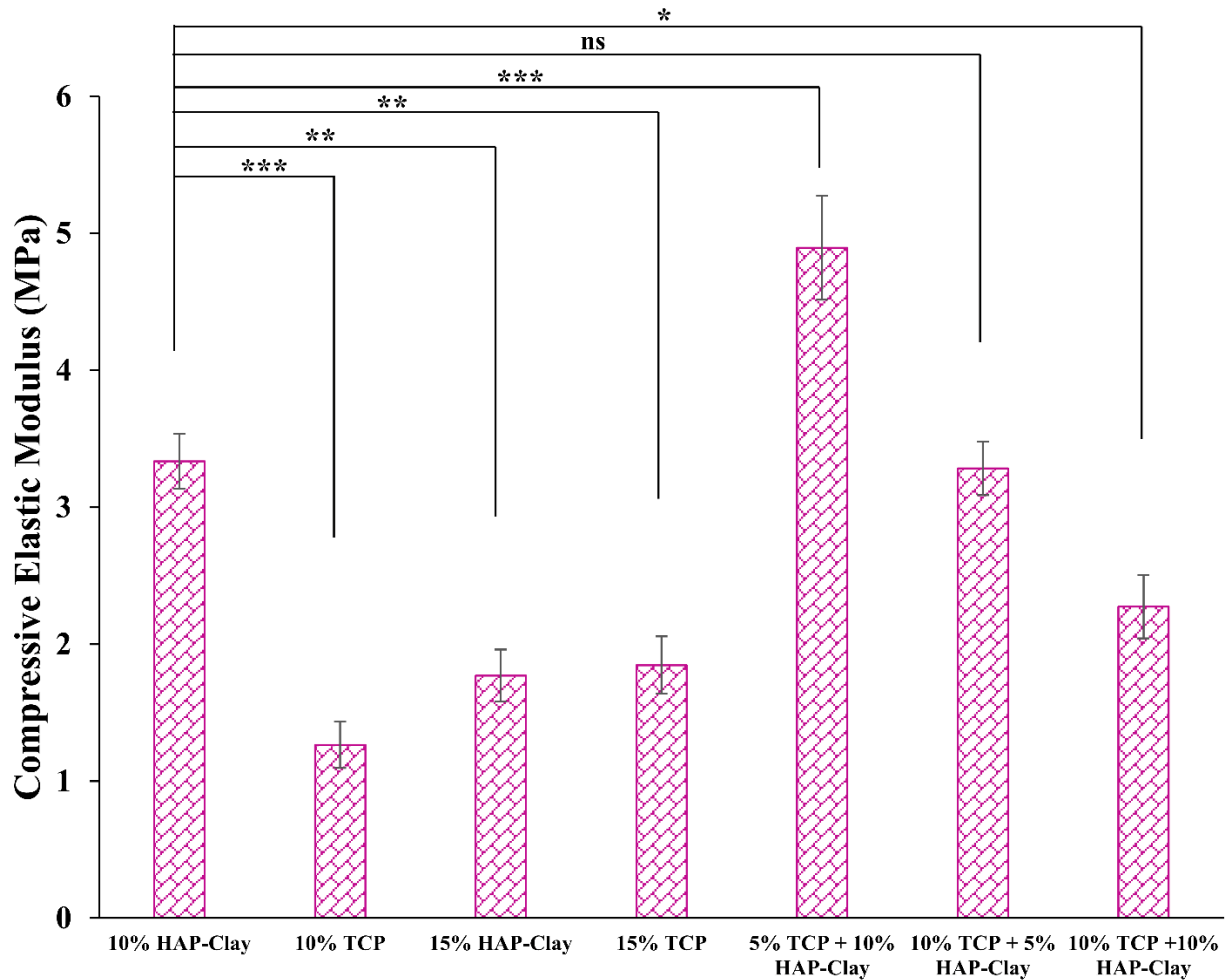
Fig. 6.3. Compressive elastic moduli of different PCL nanocomposite scaffolds.

6.3.3. In vitro degradation

Fig. 6.4 represents the comparative percentage weight loss of PCL composite scaffold with different mineral particle content over time. In vitro accelerated hydrolytic degradation of PCL/in situ HAPclay composite scaffolds was studied under alkaline conditions (0.1 M NaOH). Studies have shown that non-enzymatic hydrolysis of ester linkages in PCL constitutes the first stage of its in vivo degradation, followed by a second stage involving intracellular degradation of decreased molecular weight, hydrolytically cleaved PCL. Using alkaline conditions during degradation studies helps to increase the hydrolytic degradation rate of PCL and thus simultaneously simulates

185

the initial in vivo stage of PCL degradation. The lack of degrading enzymes under normal physiological conditions was another factor responsible for the preference of alkaline conditions for degradation studies. Fig.4 indicates an increase in vitro degradation of PCL scaffolds over 21 days. Changes in the rate of weight loss percentage were observed for scaffolds over the degradation period. Initially, the weight loss percentage was less in every scaffold sample. However, from day 7 to day 14, it was more than day 0 to day seven or day 14 to day 21. Initially, weight loss increased with increased ceramic particles, but from day 14 to day 21, we observed that adding ceramic particles reduced the degradation.
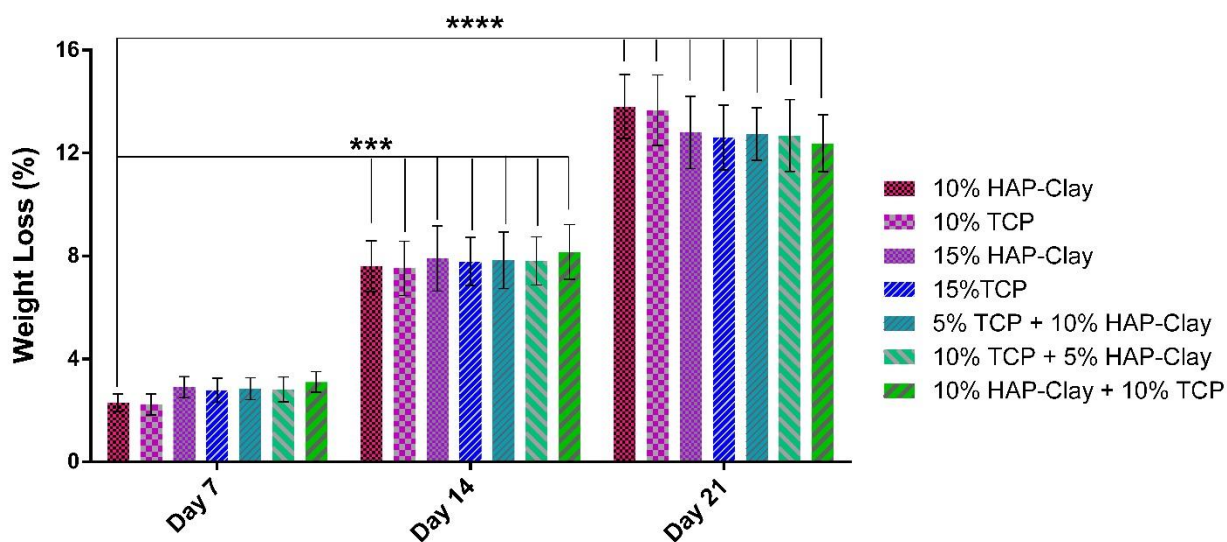

Fig. 6.4. Comparative percentage weight loss of PCL composite scaffolds containing in situ HAP-Clay/TCP from in vitro degradation experiment under accelerated conditions.

6.3.4. Mechanical properties of the degraded scaffolds in 0.1 M NaOH

The mechanical properties of scaffold samples were determined on undegraded (0 days, control) and degraded (7, 14, and 21 days) PCL/in situ HAPclay composite scaffold samples. In addition, the accelerated degradation studies (0.1M NaOH maintained at 37^0C) were carried out on PCL composite scaffolds containing in situ HAPclay/TCP. The stress-strain plots of the undegraded and degraded samples are shown in Fig. 6.5. As seen, the compressive mechanical

properties of the scaffolds decrease with time. A significant drop in the mechanical properties can be observed between 0 to 7 days. Then a gradual decrease in the compressive strength was observed up to 21 days.
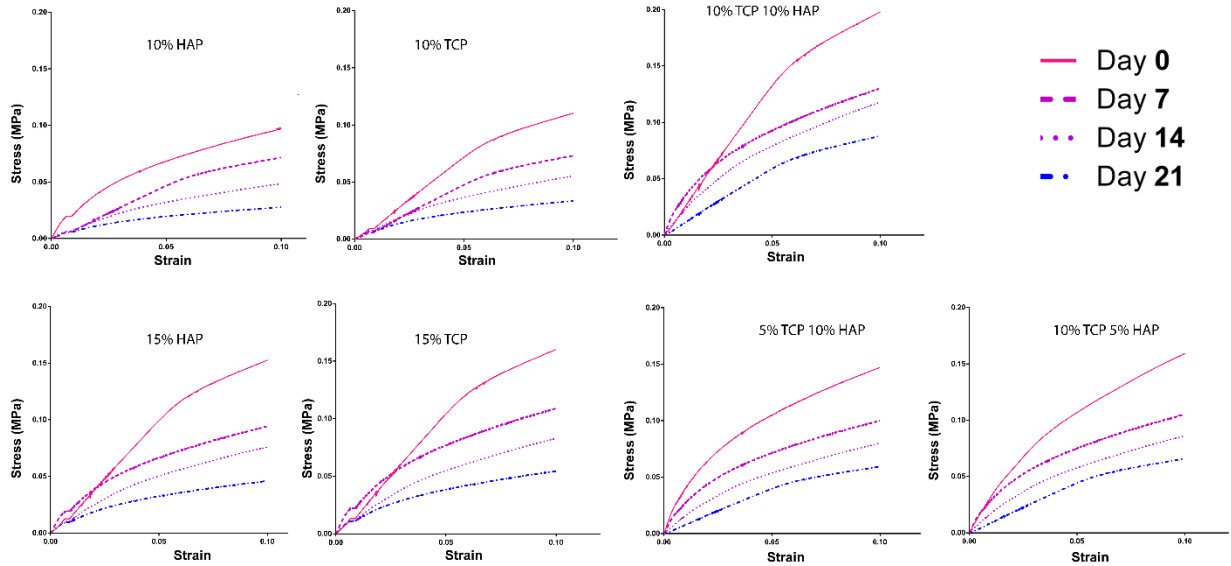

Fig. 6.5. Compressive mechanical properties of undegraded (day 0) and degraded (day 7, 14, and 21) PCL composite scaffolds containing in situ HAPclay/TCP from in vitro degradation experiment under accelerated conditions (0.1M NaOH).

Polymer composite scaffolds degraded, and the mechanical properties of the scaffolds decreased over time. Fig. 6.6 represents the scaffolds' degradation as a time function. We observed a gradual increase of degradation over time for all the scaffolds sample. However, the higher ceramic content showed reduced degradation compared to lower ceramic content scaffolds.
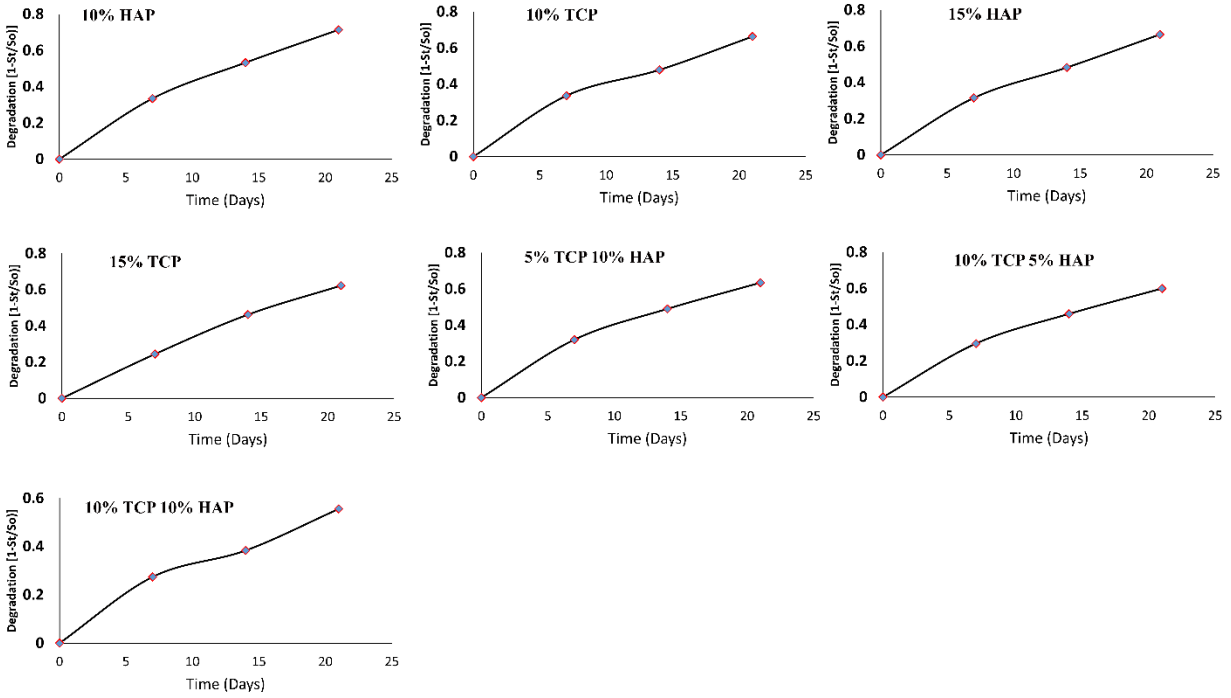
Fig. 6.6. Mechanical property degradation (D) of polymer composite scaffolds in alkaline condition (0.1M NaOH)

6.3.5. WST-1 assay

The WST-1 assay was performed to evaluate the cell viability and proliferation of MSCs and osteoblasts on the scaffold constructs. WST-1 assay results are shown in Fig. 6.7A-E. We observed a steady increase in cell viability over time in all the materials. Fig.6A shows a ~ 1.3-fold increase in cell viability by adding 5% TCP by keeping the HAP content at 10%. However, further addition of TCP to 10% leads to a decrease in cell viability. In Fig. 6.7B, we kept TCP content constant and evaluated the effect of increased HAP content from 5% to 10%. The results showed no significant increase in cell viability by changing HAP content. In addition, we did not observe any change in the cell viability by varying the HAP and TCP content, from 10% to 15% in Fig. 6.7C and D, respectively. The compiled cell viability on day 7 of all materials represents that the scaffolds containing 5% TCP+10% HAP show the highest cell viability and hence could be considered as the best material in terms of cell viability.
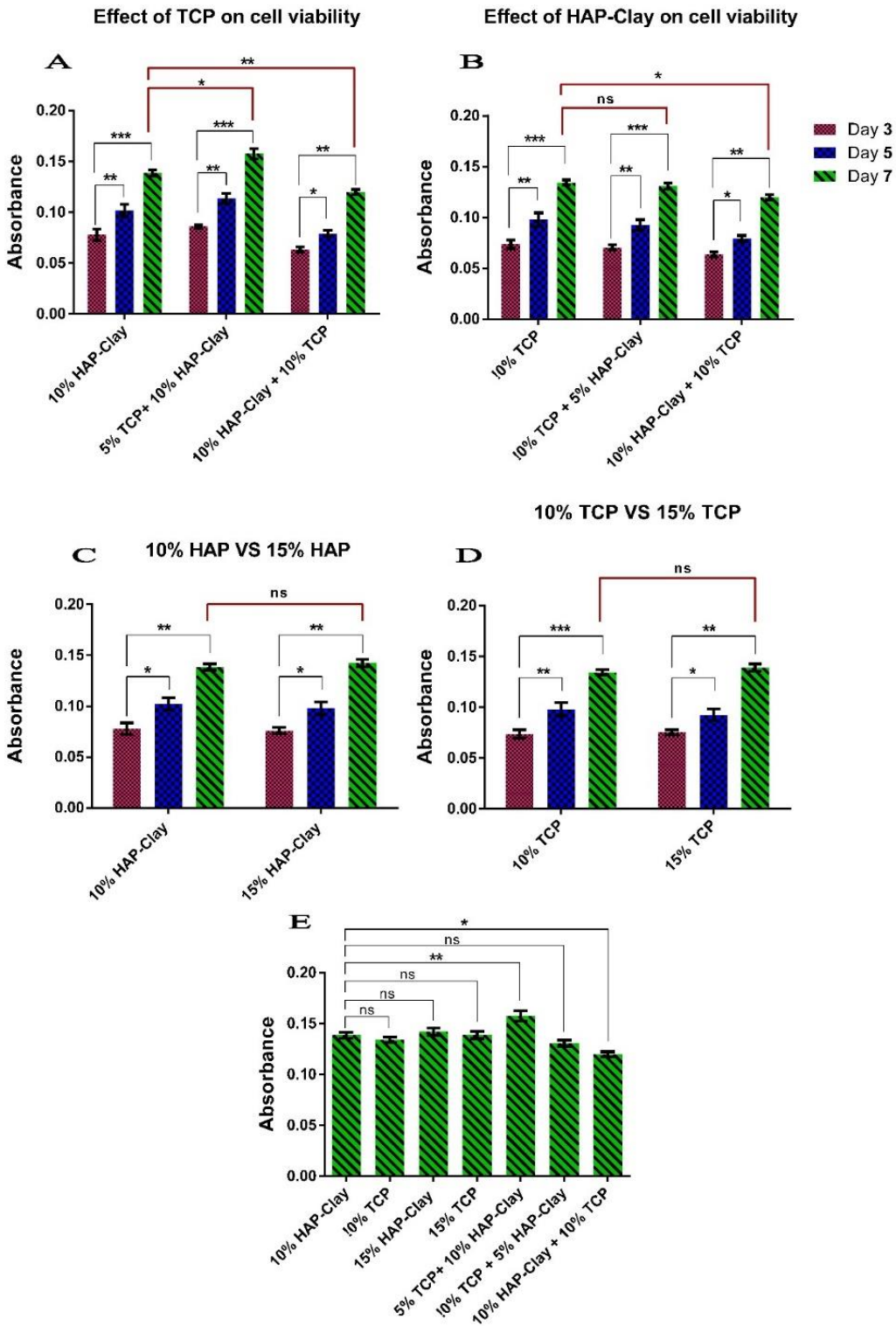
188

Fig. 6.7. Cell viability of scaffold seeded with MSCs and hFOB. Results are shown as mean ± standard deviation. (Two-way ANOVA followed by post hoc Tukey test p* < 0.05, p* *< 0.01, p*** <0.001, n = 3)

6.3.6. Alkaline phosphate assay

Osteogenic differentiation of MSCs was assessed by alkaline phosphatase (ALP) assay as ALP is an osteogenic marker. ALP activity assay results are shown in Fig. 6.8A-E. ALP increases if active bone formation occurs, as ALP is a byproduct of osteoblast activity. Immature osteoblast turned into mature osteoblast and released ALP. Here, we observed an increase in ALP activity over time in all materials. In Fig. 6.8A, with the addition of 5% TCP, ALP activity increases by ~1.2 fold. On the other hand, ALP activity decreases with a further increase in TCP content to 10%. In Fig. 6.8B, we did not observe an increase in ALP activity by varying HAP-Clay content by keeping TCP constant to 10%. Similarly, we did not observe any variation in ALP activity by changing HAP-Clay content and TCP content from 10% to 15%, respectively, in Fig. 6.8C and D. Eventually, we observed the highest ALP activity in scaffolds containing 5% TCP + 10% HAP-Clay on day seven, as shown in Fig. 6.8E.
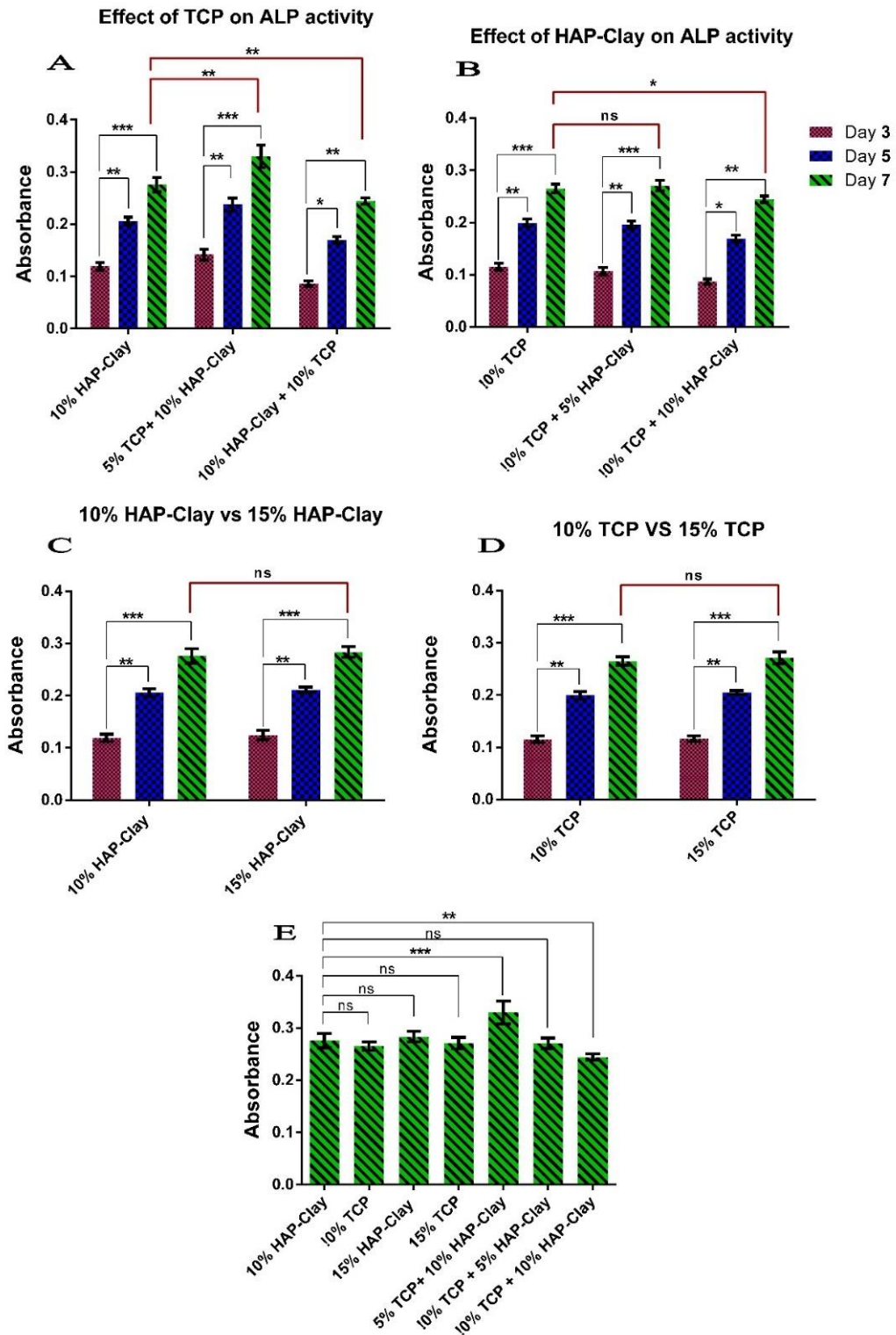
Fig. 6.8. ALP activity of scaffold seeded with MSCs and hFOB. Results are shown as mean ± standard deviation. (Two-way ANOVA followed by post hoc Tukey test p* < 0.05, p* *< 0.01, p*** <0.001, n = 3)

6.4. Conclusion

We have found that porosity decreases with the addition of the mineral particles. Maximum porosity was observed with 10% HAP/Clay, and minimum porosity was observed with 10% TCP and 10% HAP/Clay PCL scaffold. We have found that the compressive strength increases with the addition of the mineral particles. Maximum compressive strength was observed with 10% HAP-Clay + 10% TCP scaffolds. Maximum elastic modulus was observed with 10% HAP-Clay + 5% TCP scaffolds. We have observed that weight loss increases over time for all samples for accelerated degradation. Initially, with a higher content of ceramic particles, weight loss is enhanced, but from day 14 to day 21, it was observed degradation is reduced (lower weight loss) with higher ceramic particles content. We have observed that for accelerated degradation, the compressive mechanical properties of the scaffolds decrease with time. A significant drop in mechanical properties can be observed between 0 to 7 days. Further, cell viability increased over seven days in all samples, and a significant increase has been observed for scaffolds with 5% TCP + 10% HAP-Clay. Over seven days, ALP activity increases in all samples over seven days, and a significant increase has been observed with the scaffolds with 5% TCP + 10% HAP-Clay compared with the control scaffolds (HAP-Clay). From our results, we can conclude that the scaffold system we developed herein with 5% TCP + 10% HAP-Clay has adequate mechanical strength required for bone formation, and is biocompatible and osteogenic.

6.5. Acknowledgments

6.6. References

[1]   P.V. Giannoudis, H. Dinopoulos, E. Tsiridis, Bone substitutes: an update, Injury 36(3) (2005) S20-S27.

[2]   C.G. Finkemeier, Bone-grafting and bone-graft substitutes, JBJS 84(3) (2002) 454-464.

[3]   Z.A.A. Sheikh, M.A. Javaid, M.N. Abdallah, Z. Khurshid, S.Z. Zafar, Dental Biomaterials (Principle and Its Application), (2013).

[4]   R. Dimitriou, E. Jones, D. McGonagle, P.V. Giannoudis, Bone regeneration: current concepts and future directions, BMC medicine 9(1) (2011) 1-10.

[5]   C.M.L. Clokie, H. Moghadam, M.T. Jackson, G.K.B. Sandor, Closure of critical sized defects with allogenic and alloplastic bone substitutes, Journal of Craniofacial Surgery 13(1) (2002) 111-121.

[6]   J. Baumhauer, M.S. Pinzur, R. Donahue, W. Beasley, C. DiGiovanni, Site selection and pain outcome after autologous bone graft harvest, Foot & ankle international 35(2) (2014) 104-107.

[7]   W. Wang, K.W.K. Yeung, Bone grafts and biomaterials substitutes for bone defect repair: A review, Bioactive materials 2(4) (2017) 224-247.

[8]   I. Manjubala, T.P. Sastry, R.V.S. Kumar, Bone in-growth induced by biphasic calcium phosphate ceramic in femoral defect of dogs, Journal of biomaterials applications 19(4) (2005) 341-360.

[9]   D. Tadic, M. Epple, A thorough physicochemical characterisation of 14 calcium phosphate-based bone substitution materials in comparison to natural bone, Biomaterials 25(6) (2004) 987-994.

[10] K.J.L. Burg, S. Porter, J.F. Kellam, Biomaterial developments for bone tissue engineering, Biomaterials 21(23) (2000) 2347-2359.

[11] A.J. Haddad, G.K.B. Sandor, C.M.L. Clokie, Poster 28: Enhanced bone healing in rabbit calvarium using novel bone substitutes, Journal of Oral and Maxillofacial Surgery 61(8) (2003) 96.

[12] C. Suneelkumar, K. Datta, M.R. Srinivasan, S.T. Kumar, Biphasic calcium phosphate in periapical surgery, Journal of Conservative Dentistry: JCD 11(2) (2008) 92.

[13] A. Ogose, T. Hotta, H. Kawashima, N. Kondo, W. Gu, T. Kamura, N. Endo, Comparison of hydroxyapatite and beta tricalcium phosphate as bone substitutes after excision of bone tumors, Journal of Biomedical Materials Research Part B: Applied Biomaterials: An Official Journal of The Society for Biomaterials, The Japanese Society for Biomaterials, and The Australian Society for Biomaterials and the Korean Society for Biomaterials 72(1) (2005) 94-101.

[14] A. Piattelli, A. Scarano, C. Mangano, Clinical and histologic aspects of biphasic calcium phosphate ceramic (BCP) used in connection with implant placement, Biomaterials 17(18) (1996) 1767-1770.

[15] N. Beheshtizadeh, M. Azami, H. Abbasi, A. Farzin, Applying extrusion-based 3D printing technique accelerates fabricating complex biphasic calcium phosphate-based scaffolds for bone tissue regeneration, Journal of Advanced Research (2021).

[16] F. Barrère, C.A. van Blitterswijk, K. de Groot, Bone regeneration: molecular and cellular interactions with calcium phosphate ceramics, International journal of nanomedicine 1(3) (2006) 317.

[17] S.E. Lobo, T.L. Arinzeh, Biphasic calcium phosphate ceramics for bone regeneration and tissue engineering applications, Materials 3(2) (2010) 815-826.

[18] G. Daculsi, R.Z. LeGeros, E. Nery, K. Lynch, B. Kerebel, Transformation of biphasic calcium phosphate ceramics in vivo: ultrastructural and physicochemical characterization, Journal of biomedical materials research 23(8) (1989) 883-894.

[19] S. Mofakhami, E. Salahinejad, Biphasic calcium phosphate microspheres in biomedical applications, Journal of Controlled Release 338 (2021) 527-536.

[20] M. Mohammadi, J.-M. Tulliani, L. Montanaro, P. Palmero, Gelcasting and sintering of hydroxyapatite materials: Effect of particle size and Ca/P ratio on microstructural, mechanical and biological properties, Journal of the European Ceramic Society 41(14) (2021) 7301-7310.

[21] A.H. Ambre, D.R. Katti, K.S. Katti, Biomineralized hydroxyapatite nanoclay composite scaffolds with polycaprolactone for stem cell-based bone tissue engineering, Journal of Biomedical Materials Research Part A 103(6) (2015) 2077-2101.

[22] K.S. Katti, A.H. Ambre, N. Peterka, D.R. Katti, Use of unnatural amino acids for design of novel organomodified clays as components of nanocomposite biomaterials, Philosophical Transactions of the Royal Society a-Mathematical Physical and Engineering Sciences 368(1917) (2010) 1963-1980.

[23] A. Ambre, K.S. Katti, D.R. Katti, In situ mineralized hydroxyapatite on amino acid modified nanoclays as novel bone biomaterials, Materials Science & Engineering C-Materials for Biological Applications 31(5) (2011) 1017-1029.

[24] A.H. Ambre, D.R. Katti, K.S. Katti, Nanoclays mediate stem cell differentiation and mineralized ECM formation on biopolymer scaffolds, Journal of Biomedical Materials Research Part A 101(9) (2013) 2644-2660.

[25] A.H. Ambre, Nanoclay Based Composite Scaffolds For Bone Tissue Engineering Applications, Journal of Nanotechnology for Engineering and Medicine, ASME, 2010, p. 031013.

CHAPTER 7. SUMMARY, CONCLUSIONS AND FUTURE DIRECTIONS

7.1. Summary and conclusions

➢ This dissertation reported the design of a mechanically stable interlock scaffold system for critical-size bone defect repair that offers a large surface area, can be assembled to make any shape and fill any size bone defect, that provides a unique microenvironment that enables improved cell growth, accelerated calcium deposition and collagen production, main components of bone, and an effective reduction in time duration of bone growth in defects. Thus, a novel scaffold interlocking-block BMP-coated scaffold system is presented for accelerated bone growth with the co-culture of MSCs and osteoblast cells.

➢ This dissertation, for the first time, changes to nanomechanical properties of scaffolds over nine weeks during osteogenesis with the influence of BMPs on nanoclay interlocking scaffolds using the quasi-static nanoindentation method were evaluated and found that scaffolds degrade in culture media, and the elastic modulus reduces over time; in contrast, cells start from ECM, and the elastic modulus increases over time. In addition, BMPs play a crucial role in forming more ECM, and enhanced elastic modulus with BMPs coated scaffolds was observed. From immunofluorescence, SEM imaging, and gene expression analysis results, we observed a significant increase in elastic modulus and increased mineralization and bone-related proteins. This research also revealed that BMPs activate the Wnt/β-catenin signaling pathway by upregulating Wnt-related factors. Hence this study has potential therapeutic applications for bone regeneration.

➢ This dissertation, for the first time, reported the fabrication of polymer clay nanocomposite fiber using a pressurized gyration. The microstructure analysis showed that the incorporation of in-situ HAP nano and operating pressure plays an essential role in the

microstructure of the fibers. The results suggested that cells were able to thrive, proliferate, and differentiate. The results also concluded that the incorporation of HAP-Clay enhanced cell viability, proliferation, mineralization, and collagen formation. Thus, this study represents a new opportunity to design manufacturable composite nanoclay polymer fiber for bone tissue engineering applications.

➤ This dissertation also reported the in-silico design of the unnatural amino acids modified clays and fabricated unnatural amino acids modified scaffolds. XRD analysis revealed that modifying clay with unnatural amino acids enhanced the d-spacing and intercalation of the unnatural amino acids into the clay sheet. FTIR analysis revealed a significant band shift of the C=O vibration band, suggesting a significant molecular interaction between amino acids and the MMT clay sheet. A significant difference in the mechanical response of the polymer clay scaffolds was observed, which rose from the difference in nonbonded interactions between the MMT clay and amino acids. The results suggest amino acids-modified scaffolds are biocompatible with bone cells and breast cancer cells. A significant increase in calcium deposition was observed with the sequential culture, confirming that MCF-7 is osteoblastic. Thus, this study provides valuable insight into the effects of different amino acids in terms of molecular interactions, mechanical properties, and cellular responses and shows the potential applications of these scaffolds as a biomaterial in tissue engineering applications.

7.2. Future directions

➤ This dissertation reported the design and development of an interlock scaffold system, a 3D tissue-engineered bone graft, to augment accelerated bone regeneration for critical-size bone defects. This study provides new insight into the crosstalk between bone-regenerating

cells, scaffolds, and bone morphogenic proteins (BMPs). Based on understanding the effect of BMPs on accelerated bone regeneration and its long-term effects, the following suggestions can be made for future research.

➢ This dissertation reported accelerated bone regeneration with an interlocking scaffold system coated with BMPs and seeded with MSCs and osteoblast cells. However, further experiments must be conducted to verify our scaffold system's suitability as a bone graft for accelerated bone regeneration. Besides, the complexity of our system can be increased by incorporating immunological and vascular elements known to have critical roles in bone remodeling. Furthermore, incorporating dynamic fluid flow with the help of a bioreactor would help us to provide a more humanoid microenvironment to understand the role of shear stress on bone regeneration. Also, using patient-derived stem cells in the in vitro model might help us predict the suitability of our developed system as a bone graft.

➢ This dissertation investigated the changes in nanomechanical properties of scaffolds seeded with cells over the osteogenesis progression using the developed interlocking scaffold system. This research also shows that elastic modulus increases with the progression of osteogenesis due to mineralization and bone-related protein formation. Therefore, further studies need to be carried out using both experimental and modeling approaches; developing an FEA model of the scaffold indentation process could provide us great flexibility to understand the variation in indentation response of the materials with changes in the degradation rate, loading rate, indentation depth, tip geometry, and holding time.